The Annual Heat Balance of the Martian Polar Caps from Viking Observations

Thesis by

David A. Paige

In Partial Fulfillment of the Requirements
for the Degree of
Doctor of Philosophy

California Institute of Technology
Pasadena, California

1985

(submitted February 19, 1985)

© 1985

David A. Paige

All Rights Reserved

To Rhea

Acknowledgements

The Viking IRTM observations of the Martian polar regions represent one of the most informative and complete solar system data sets obtained to date. I will be forever grateful to Hugh Kieffer and the IRTM team for allowing me to use these data and to have the great privilege of seeing them in organized form for the very first time.

I also thank Dave Crisp, Frank Palluconi and Richard Zurek for many very helpful discussions and outright assistance. Finally, I thank my thesis advisor Andy Ingersoll, who urged me to go ahead and try to determine the annual radiation budget of the north polar cap when most everyone else I talked to said it couldn't be done!

Abstract

This thesis presents the first measurements of the annual heat budgets of the polar caps of Mars from spacecraft observations. The primary motivation for this work is to understand why seasonal CO_2 frost deposits at the north pole of Mars disappear in the summer, whereas seasonal CO_2 deposits near the south pole do not. This behavior is not expected to first order because both Martian poles receive the same total amount of sunlight at the top of the atmosphere over the course of a year. Understanding why the Martian north and south polar caps behave in an asymmetric fashion is important because the vapor pressures of permanent polar CO_2 deposits determine the planet-wide surface pressures of CO_2 gas, which is the dominant constituent of the Martian atmosphere.

Annual radiation budgets for the core regions of the north and south polar caps are determined from solar reflectance and infrared emission observations obtained by the Infrared Thermal Mappers (IRTMs) aboard the two Viking orbiters. The results show that the absence of CO_2 frost at the north pole during summer is primarily due to an asymmetry in the rates of CO_2 frost sublimation at surface in the north and south during spring. Further analysis traces this difference to seasonal frost reflectivities being approximately 20% lower in the north than in the south during late spring. It is shown that seasonal frost deposits at the poles demonstrate a remarkable tendency to not become darker when contaminated with dust, and to become brighter with increasing rates of solar illumination. Since peak solar illumination rates are presently higher at the south pole than the north pole because of the large eccentricity of Mars' orbit, the tendency for the frost to become brighter with increasing rates of solar illumination explains the asymmetry. The tendency for the frost to not become darker when contaminated by dust explains why the seasonal behavior of the Martian polar caps is highly repeatable from year to year despite interannual variations in the occurrence of Martian global dust storms.

It is suggested that the unexpected properties of Martian seasonal frost deposits revealed by the results of this study are caused by the tendency for dust particles within the frost to absorb solar radiation, sublimate the solid CO_2 that supports them and sink into the frost. If the current behavior of Martian CO_2 frost is an indicator to past events, then interactions between dust and frost have exerted a powerful stablizing influence on the Martian climate system.

TABLE OF CONTENTS

Acknowledgements iv

Abstract v

List of Figures x

List of Tables xiii

Chapter 1. Introduction 1

References 9

Chapter 2. The Annual Heat Balance of the Martian Polar Caps From Viking Observations

1. Introduction 11
2. Polar Heat Balance 12
3. Radiation Budget Measurements 14
4. Smaller Heat Balance Quantities 25
5. North Polar Subsurface Heat Conduction and Permanent CO_2 Reservoir 28
6. South Polar Subsurface Heat Conduction and Permanent CO_2 Reservoir 33
7. Annual Behavior of CO_2 Frost 38
8. Simplified Polar Radiative Model 41
9. Discussion 46
10. Conclusions 50

References 51

Chapter 3. An Analysis of IRTM Polar Night Observations

1. Introduction 53

2. Coincident Brightness Temperatures 59

3. Low Brightness Temperatures 72

4. Dust Storm Brightness Temperatures 84

6. Conclusions 91

References 92

Chapter 4. A New Theory for the Asymmetric Behavior of the Martian Polar Caps 94

References 114

Appendix 1. Polar Radiation Budgets from IRTM Observations

1. Bolometric Emission Rates 115

2. Planetary Albedos 120

References 151

Appendix 2. A 10-Layer One-Dimensional Polar Radiative Model

1. Overview 152

2. Solar Heating 155

2.1 Near IR CO_2 Absorption 155

2.2 Broad-Band Solar Scattering 156

2.3 Surface and Atmospheric Solar Heating Rates 156

3. Infrared Cooling 156

3.1 The 15 μ Band of CO_2 157

3.2 Two-Stream δ-Eddington Code for IR Scattering 161

3.3 Mie Calculations 165

3.4 IR Spectral Intervals 181

4. Dynamics, etc. 182

5. IRTM Brightness Temperatures 184

References 191

Appendix 3. 10-Layer Model Calculations of the Parameter f 193

References 207

LIST OF FIGURES

Chapter 2

2-1 The north and south study regions. 13

2-2 IRTM spectral response. 16

2-3 North study region annual behavior. 18

2-4 South study region annual behavior. 20

2-5 Bidirectional reflectance plots. 24

2-6 North study region subsurface temperatures. 32

2-7 Hypothetical south study region behavior. 36

2-8 Simplified polar radiative model results. 44

2-9 Inferred study region surface albedos. 48

Chapter 3

3-1 IRTM low brightness temperature map. 54

3-2 Hunt's CO_2 cloud modeling results. 57

3-3 Study region brightness temperatures. 60

3-4 Calculated greybody emissivity effects. 62

3-5 Required variation of ε_{S11} vs. ε_{S20}. 63

3-6 Polar radio occultation data. 65

Appendix 1

A1-1 North study region brightness temperatures. 118

A1-2 South study region brightness temperatures. 119

A1-3 through A1-11 Bi-Directional reflectance plots. 123

A1-12 North study region albedos. 149

A1-13 South study region albedos. 150

Appendix 2

A2-1 Model layer structure. 154

A2-2 5, 10, 20, and 40 layer temperature profiles. 158

A2-3 CO_2 15 μ equivalent width comparison. 160

A2-4 Mie parameters for montmorillonite 219b. 167

A2-5 Mie parameters for basalt. 172

A2-6 Mie parameters for water ice. 177

A2-7 IRTM 15 μ channel weighting functions. 185

A2-8 Scattering code comparisons. 189

Appendix 3

A3-1 Aerosol vertical distributions. 200

A3-2 Calculated values of f. 201

LIST OF TABLES

Chapter 2

2-1 Simplified Radiative Model Input Parameters. 47

Chapter 3

3-1 10-layer Model Input Parameters. 77

Chapter 4

4-1 Calculated Martian Surface Pressures 111

Appendix 1

A1-1 IRTM Bolometric Spectral Model. 116

Appendix 2

A2-1 Summary of Mie Calculations. 166

Appendix 3

A3-1 Fixed Model Input Parameters. 195

A3-2 Parameter Sets A, B, and C. 196

Chapter 1

INTRODUCTION

The Martian polar caps are important manifestations of the seasons and climate of Mars. They are major storehouses of volatiles; they exert a powerful influence on the global climate; they may contain a valuable record of Mars' past climatic history. Every quantitative study of the behavior of the Martian polar caps has dealt with at least some aspect of their annual heat balance. The first and most important of these was by Leighton and Murray (1966).

Leighton and Murray's work was based on two observational constraints. The first was that the polar caps are observed to advance and retreat with the Martian seasons. They advance during fall and winter and retreat during spring and summer, leaving permanent or residual caps near both poles at the end of summer. The second was that the Martian atmosphere is composed primarily of CO_2 gas (Kaplan et al., 1964), with a surface pressure of a few millibars (Kliore et al., 1965). The temperature of CO_2 frost in solid-vapor equilibrium with such an atmosphere is between 140 K and 150 K, depending on the exact value of the CO_2 partial pressure. By ignoring possible radiative and dynamic effects of the Martian atmosphere and by assuming surface radiative properties do not vary with time, it is possible to write a simple equation for the annual heat balance at either of the Martian poles:

$$\overline{F_{Solar}}(1 - A_s) = \varepsilon_s \sigma T_s^4 \tag{1.1}$$

where $\overline{F_{Solar}}$ is the annually averaged polar insolation (the flux of incident solar energy), A_s is the surface albedo (reflectivity), ε_s is the surface greybody emissivity, σ is the Stefan-Boltzmann constant and T_s is the surface temperature. A_s, ε, and T_s were not known to Leighton and Murray, but when reasonable values of $0.6 \le A_s \le 0.7$ and $0.8 \le \varepsilon_s \le 0.9$ are assumed, equation (1.1) can be satisfied if 140 K < T_s < 150 K. Leighton and Murray postulated that the apparent agreement between the annually averaged temperatures of polar frost deposits from radiative balance and from thermodynamic considerations was no coincidence and proposed that the Martian polar caps were composed primarily of CO_2 frost in solid-vapor equilibrium with CO_2 gas in the Martian atmosphere.

To demonstrate the seasonal behavior of Martian CO_2 frost deposits, Leighton and Murray constructed a global, lunar-like thermal model that calculated Martian diurnal surface and subsurface temperatures as functions of latitude and season. The results showed that, at high latitudes, fall and winter surface temperatures can drop to the point where CO_2 frost would be expected to condense out of the Martian atmosphere. Seasonal frost deposits formed in this manner were shown to sublimate away before the end of summer, thus explaining the seasonal advance and retreat of the Martian polar caps.

One very interesting consequence of the Leighton and Murray model is that the only place where CO_2 frost is expected to be stable throughout the year is right at the poles. This is because annual insolation increases as you move away from the poles, so off-polar permanent CO_2 deposits must have higher annually averaged temperatures than on-polar deposits from equation (1.1). Frost deposits with higher temperatures have higher vapor pressures, so excess CO_2 from off-polar deposits would be expected to migrate to higher and higher latitudes.

The important climatic implication of Leighton and Murray's model is that the mass of the entire Martian atmosphere may be controlled by the vapor pressures of CO_2 frost deposits at the poles. Since vapor pressure is an exponential function of temperature, even modest variations in the various factors that determine the actual annual heat balance at the poles could have dramatic consequences. One important factor that is known to vary is the annual polar insolation. In 1973, Ward showed that the orbital elements of Mars undergo quasi-periodic variations with periods that are similar to those of the earth ($\sim 10^5$ years) but with amplitudes that are many times greater (Ward, 1974). The obliquity of Mars (the angle between its spin axis and its orbit normal) can deviate from its present value of 25° by ±9°. This gives a two-fold variation in the annual insolation at the poles. Layered deposits that are seen in the polar regions have been interpreted to be geologic evidence for quasi-periodic climate variations on Mars (Murray et al., 1972; Carr, 1982).

Leighton and Murray's basic ideas concerning the composition and behavior of the seasonal polar caps on Mars have held up well in the face of new observational evidence. The near infrared spectrometers and infrared radiometers aboard Mariner 7 showed that the seasonal polar caps contain solid CO_2 at temperatures near 145 K to 150 K (Herr and Pimentel, 1969; Neugebauer et al., 1969). The Viking landers have also obtained year-long surface pressure records that show seasonal variations due to the global condensation and sublimation of CO_2 frost that are very similar to those predicted by the Leighton and Murray model (Hess et al., 1979). But as Leighton and Murray first pointed out, it is the behavior of CO_2 frost at the poles that has the greatest impact on the Martian climate, and it is at the poles that the observational evidence first indicated that the behavior of the Martian polar caps may be considerably more complicated than was originally thought.

On the eve of the Viking mission to Mars, the composition of the residual polar caps was very much in doubt, as much of the available observational data were consistent with the hypothesis that they were composed of water ice, which is much less volatile than CO_2 frost under current Martian conditions (Murray and Malin, 1973; Ingersoll, 1974; Briggs, 1974). Published Viking results have settled many of the pre-Viking controversies, but in ways that no one predicted.

In August of 1976, while searching for a suitable landing site for Viking Lander 2 (VL2), the instruments aboard Viking Orbiter 2 (VO-2) observed the north residual polar cap midway through its summer season. The relative clarity of the polar atmosphere during this season allowed the infrared thermal mapper (IRTM) aboard VO-2 to obtain surface brightness temperature measurements of the residual frost deposits. The observed temperatures of 205 K were high enough to completely rule out the presence of CO_2 frost in solid-vapor equilibrium with the atmosphere, leaving water ice as the only other possibility (Kieffer et al., 1976). Simultaneous measurements of large column abundances of water vapor over the cap by the Mars Atmospheric Water Detector (MAWD) provided further confirmation (Farmer et al., 1976).

Soon after both Viking landers had landed safely, the orbital inclination of VO-2 was increased to 80°, which allowed excellent viewing geometry for both polar regions. As luck would have it, both Viking orbiters and the instruments aboard them continued to function long past their original designated lifetimes, amassing huge global data sets with full seasonal coverage. The IRTM instruments obtained a nearly continuous set of high quality, calibrated solar reflectance and thermal emission observations of both polar regions that span an entire Mars year.

In 1979, Kieffer (1979) published an analysis of selected IRTM observations of the retreating south polar cap during the spring and summer seasons. The situation in the south was greatly complicated by the presence of hot dust particles in the south polar atmosphere which prevented direct observations of surface frost temperatures in any of the IRTM infrared channels. In his paper, Kieffer presented several lines of evidence consistent with CO_2 frost remaining on the surface of the south residual cap throughout the summer season, but concluded that the processes that allowed CO_2 to persist in the south remained to be identified.

The Viking observations pose an interesting, and as of yet, unsolved problem: during a Mars year, both poles receive the same total solar insolation, yet the CO_2 frost that accumulates during the fall and winter seasons in the north is sublimated away before the end of summer, whereas CO_2 appears to persist at the south residual cap throughout the year. In view of the extreme sensitivity of the Martian climate system to the annual polar heat balance, identifying which physical processes are responsible for the north-south polar cap asymmetry will be an important step toward understanding the past and present climate on Mars.

Most published explanations for asymmetry in the behavior of CO_2 frost at the poles have attributed it to the timing of global dust storms on Mars. Although the mechanisms for global dust storms generated are not well understood, they are observed to occur preferentially during the southern spring and summer seasons, when Mars is at perihelion (Slipher, 1962, Briggs et al, 1979, Zurek, 1982). At the Second International Colloquium on Mars, Kieffer and Palluconi (1979) suggested that the radiative effects of atmospheric dust raised during global dust storms tend to simultaneously protect sublimating CO_2 frost in the south (Davies, 1979), and retard or possibly even stop the condensation of CO_2 frost in the north (Martin and Kieffer, 1979). Furthermore, they suggested that condensation in the polar night sweeps dust from the atmosphere in the north and deposits it onto the accumulating north seasonal cap (Pollack et al., 1979). Since pure frost reflectivities can be significantly lowered by the incorporation of minute quantities of dust (Toon et al., 1980; Warren and Wiscomb, 1981), north polar seasonal frost deposits might sublimate much faster than their southern counterparts. Kieffer and Palluconi also pointed out that any planet with polar caps composed of the major atmospheric constituent would not be expected to have two permanent polar caps because the cap at the pole with the more favorable annual energy budget should quickly grow at the expense of the other by lowering the total atmospheric pressure.

Other possible explanations for north-south polar cap asymmetries proposed at one time or another include elevation differences between the north and south residual caps (Murray and Malin, 1973), preferential accumulation of drifting snow at the south residual cap (James et al., 1979; Kieffer, 1979) and the radiative effects of north "polar hood" clouds (James and North, 1982) and ozone (Kuhn et al, 1979).

While none of the theoretical or observational work that has been published to date is in direct contradiction to any of the proposed explanations for the north-south polar cap asymmetry, this same work has yet to produce definitive evidence that any of the proposed mechanisms are wholly or partially responsible for the observed asymmetry. The primary goal of this study is to find the definitive evidence and explain the asymmetry.

The data used in this study consist primarily of the IRTM solar reflectance and infrared emission observations of the north and south residual polar caps. These data show complex spectral and temporal structure due to a variety of factors. The most important are the seasonally dependant rates of insolation at the poles, the composition of the surface and the properties and of aerosol particles that are suspended in the north and south polar atmospheres throughout much of the year.

Chapter 2 presents the initial approach to the asymmetry problem employed in this study. Because of the complexity of the IRTM polar data, it was decided to not use them as surrogate measures of surface or atmospheric properties, but as nearly direct measures of the total fluxes of solar and infrared radiation at the top of the atmosphere at the poles. The methods that were used to determine annual polar radiation budgets from the IRTM observations are described in Appendix 1. As will be described in Chapter 2, the net flux of energy at the top of the atmosphere is a key element of the heat balance at the Martian poles and even approximate knowledge of the quantity can be used to place powerful constraints on the behavior of CO_2 frost on the surface and in the atmosphere. Full seasonal coverage obtained by IRTM made it possible to determine the behavior of CO_2 frost at both poles throughout a Martian year and to identify the seasons in which this behavior was most asymmetric.

Chapter 2 also presents an analysis of late spring season radiation budget results with the aid of a simplified polar radiative model. This model was distilled from a more complete 10-layer one-dimensional polar thermal equilibrium model that is described in Appendix 2. The main goal of this part of Chapter 2 is to better understand the relative importance of surface albedo and dust opacity in determining CO_2 sublimation rates during the spring seasons and to use the radiation budget data to constrain these quantities during late spring north and south poles.

Chapter 3 presents an analysis of IRTM polar night observations. The goal of this study is to explain the structure of these observations and to achieve a qualitative understanding of the surface and atmospheric properties that determine the rates of CO_2 accumulation during the polar and winter seasons. Chapter 3 also investigates the hypothesis that significant quantities of dust are incorperated into the condensing north seasonal polar cap during global dust storms.

Chapter 4 examines the hypothesis that the present asymmetrical behavior of seasonal CO_2 frost is due to to the preferential occurrence of

Martian global dust storms during southern spring and summer and presents a new theory based on the observations presented in this thesis that could have important implications for our current understanding of the Martian climate.

(Chapter 2 is an expanded version of a Research Article co-authored by Andrew P. Ingersoll that will appear in *Science* on June 6, 1985. The remainder of the thesis has not been published.)

REFERENCES

Briggs, G.A. (1974) *Icarus* **23**, 1974.

Briggs, G.A. et al. (1979) *J. Geophys. Res.* **84**, 2795.

Carr, M.H. (1982) *Icarus* **50**, 129.

Davies, D.W. (1979) *J. Geophys. Res.* **84**, 8289.

Farmer, C.B., et al. (1976) *Science* **194**, 1339.

Herr, K.C. and G.C. Pimentel (1969) *Science* **166**, 496.

Hess, S.L., R.M. Henry, and J.E. Tillman (1979) *J. Geophys. Res.* **84**, 2923.

Ingersoll, A.P. (1974) *J. Geophys. Res.* **79**, 3403.

James, P.B. et al. (1979) *J. Geophys. Res.* **84**, 2889.

James, P. and G. North (1982) *J. Geophys. Res.* **87**, 10271.

Kaplan, L.D., G. Munch, and H. Spinard (1964) *Astrophys. J.* **134**, 1.

Kieffer, H.H. et al. (1976) *Science* **194**, 1341.

Kieffer, H.H. (1979) *J. Geophys. Res.* **84**, 8263.

Kieffer, H.H. and F.D. Palluconi (1979) NASA Conference Publication 2072, 45.

Kliore, A. et al. (1965) *Science* **149**, 1243.

Kuhn, W.R. et al., (1979) *J. Geophys. Res.* **84**, 8341.

Leighton, R.B. and B.C. Murray (1966) *Science* **153**, 136.

Martin, T.Z. and H.H. Kieffer (1979) *J. Geophys. Res.* **84**, 2843.

Murray, B.C. et al. (1972) *Icarus* **17**, 328.

Murray, B.C. and M.C. Malin (1973) *Science* **182**, 437.

Neugebauer, G. et al. (1969) *Science* **166**, 98.

Pollack, J.B. et al. (1979) *J. Geophys. Res.* **84**, 2929.

Slipher, E.C. (1962) *The Photographic Story of Mars*, Sky Publishing Co., Cambridge, Mass.

Toon, O.B., J.B. Pollack, W. Ward, J.A. Burns, and K. Kilske (1980) *Icarus* **44**, 552.

Ward, W.R. (1974) *J. Geophys. Res.* **79**, 3375.

Warren., S. G. and W. J. Wiscomb (1981) Abstract for Workshop on Quasi-Periodic Climate Change on Mars and Earth, NASA Ames, Feb., 1981.

Zurek, R.W. (1982) *Icarus* **50**, 288.

CHAPTER 2

THE ANNUAL HEAT BALANCE OF THE MARTIAN POLAR CAPS FROM VIKING OBSERVATIONS

1. Introduction

One of the most interesting results of the Viking mission to Mars was the discovery that the seasonal behavior of CO_2 frost at the Martian poles is not symmetric. In the north, the Viking orbiter summer time observations gave unequivocal evidence for an exposed, permanent water ice polar cap, and the complete absence of solid CO_2 *(1,2)*. In the south, the observations suggest that solid CO_2 remained on the surface through the end of the summer season *(3,4)*. These results were not anticipated, and have important implications for our understanding of the Martian climate system.

On Mars, the temperatures of CO_2 frost deposits are determined by the local partial pressure of CO_2 gas, the dominant constituent of the Martian atmosphere. The partitioning of total available CO_2 between atmosphere and polar caps over climatic time scales is determined by the vapor pressures of the coldest permanent year-long CO_2 deposits on the planet*(5)*. When the annual heat balance at both poles does not favor the stability of permanent CO_2 deposits, the Martian atmosphere may then be in equilibrium with a large reservoir of CO_2 adsorbed onto minerals in a thick, porous, planetwide rubble layer known as the Martian regolith *(6)*. Since the temperatures of stable CO_2 frost deposits are governed by their annual heat balance, the properties and processes that determine the annual heat balance at the Martian poles have a major impact on the composition and mass of the Martian atmosphere *(7)*. Since both poles receive the same total insolation (sunlight incident at the top of the atmosphere) over the course of a year, the present north-south asymmetry in the behavior of CO_2 frost shows that processes generated on Mars itself must play an important role in determining the behavior of the Martian polar caps over climatic time scales. Identifying and understanding these processes will be an important step toward understanding the past and present climate of Mars.

This chapter presents an extensive compilation of Viking Infrared Thermal Mapper (IRTM) solar reflectance and infrared emission observations of the Martian north and south polar regions. The observations span an entire Mars year, and are used to determine annual radiation budgets and heat budgets for the core regions of the north and south permanent or residual polar caps. The results define the current behavior of CO_2 frost at the Martian poles and provide new clues to the properties and processes that may be responsible for this behavior.

2. Polar Heat Balance

The basic principle that underlies heat balance studies is that the total net flux of energy into a system through its boundaries is equal to the rate at which energy is stored inside the system. The systems chosen for this study consist of the atmospheres and seasonal frost deposits within two small regions that correspond geographically to the core areas on the Martian residual polar caps. Fig. 2-1 shows the boundaries of these north and south study regions superposed on the approximate areas of the residual polar caps. The instantaneous heat balance equation for the seasonal frost deposits and atmospheres within either of these regions per unit area can be written:

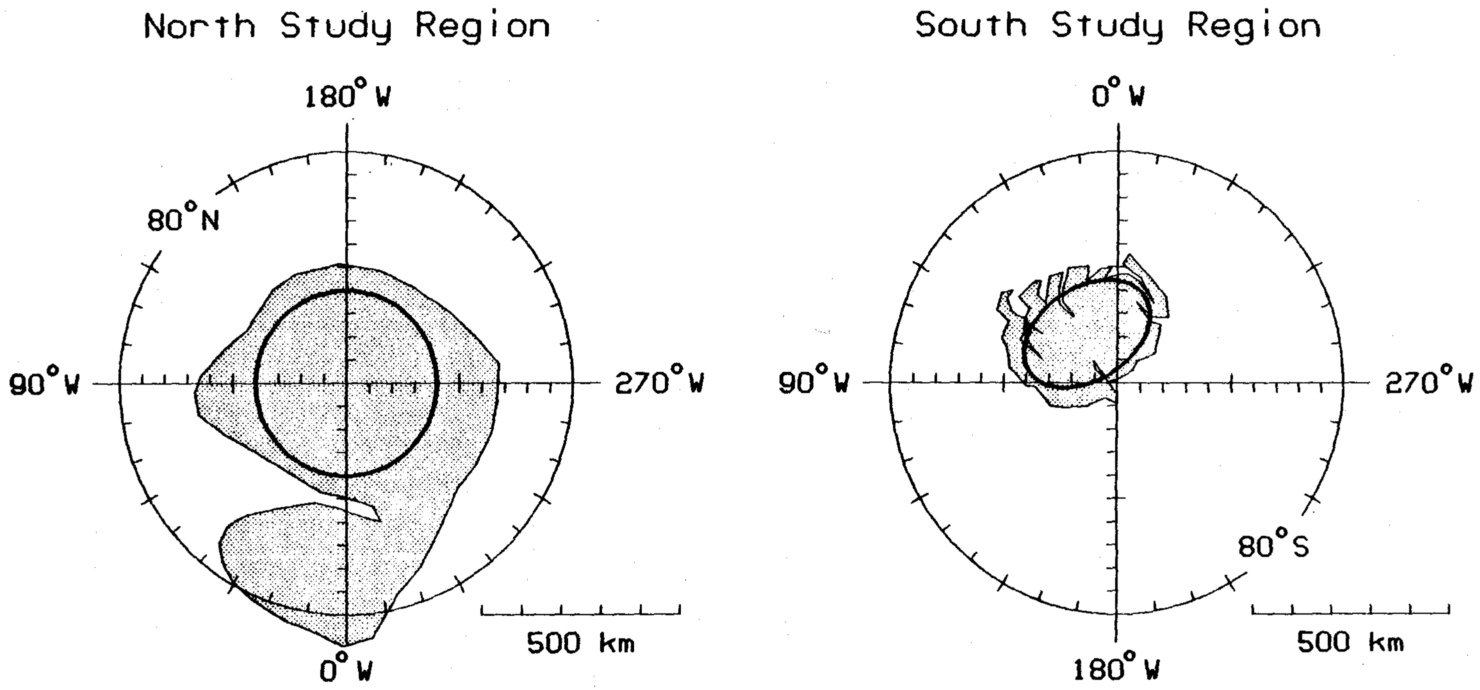

Fig. 2-1. Maps showing the boundaries of the study regions superposed on the approximate areas of the Martian north (left) and south (right) polar caps as they appear during the later summer seasons (shaded).

$$F_{Rad} + F_{Horiz} + F_{Cond} = S_{Atm} + S_{CO_2} \qquad (2.1)$$

where F_{Rad} is the net flux of solar and infrared radiation into the regions at the top of the atmosphere; F_{Horiz} is the net horizontal heat flux into the regions at their boundaries; F_{Cond} is the upward subsurface conductive heat flux into the regions at the top boundaries of the underlying permanent polar caps; S_{Atm} is the rate of total potential energy storage in the atmospheric columns within the regions and S_{CO_2} is the rate of latent heat storage in condensing or sublimating CO_2 condensates within the regions. Terms involving kinetic energy generation, latent heat storage in H_2O condensates and heat flow from the Martian interior are not included in equation (2.1) because their magnitudes are much smaller than the terms listed. The relevance of the heat balance equation to the behavior of seasonal frosts within the north and south study regions lies in the CO_2 latent heat storage term, which can be written:

$$S_{CO_2} = -L_{CO_2} \frac{dM_{CO_2}}{dt} \qquad (2.2)$$

L_{CO_2} is the latent heat of sublimation of CO_2; dM_{CO_2}/dt is the net rate of solid CO_2 accumulation within the boundaries of the study regions due to condensation. The instantaneous heat balance equation can be solved to yield S_{CO_2} if all the other terms in the equation can be determined.

3. Radiation Budget Measurements

The dominant measurable quantity in equation (2.1) is F_{Rad}, which can be written:

$$F_{Rad} = F_{Solar}(1 - A_P) - F\uparrow_{IR} \qquad (2.3)$$

where F_{Solar} is the flux of incident solar radiation at the top of the atmosphere corrected for the cosine of the solar zenith angle; A_P is the planetary albedo or the total combined reflectivity of the surface and atmosphere; $F\uparrow_{IR}$ is the outward flux of emitted radiation at all wavelengths at the top of the atmosphere. Since the north and south study regions experience no significant diurnal variations in insolation, their thermal and reflectance properties are purely seasonal. This makes them significantly easier targets for satellite radiation balance measurements than other regions of the planet.

The IRTM instruments aboard the two Viking orbiters (VO-1 and VO-2) obtained sufficient spectral, temporal and angular coverage to determine F_{Rad} for the north and south study regions with reasonable accuracy and excellent time resolution throughout a Martian year. They operated in six wavelength bands which included a broad-band solar reflectance channel (λ = 0.3 to 3 μ) and five broad infrared channels centered on $\lambda \approx$ 7, 9, 11, 15 and 20 μ. During clear atmospheric conditions, the 7, 9, 11 and 20 μ channels measured surface brightness temperatures. The 15 μ channel, with spectral response centered on a strong CO_2 absorption feature, measured atmospheric temperatures over a broad range of altitudes with maximum sensitivity near the 0.6 mbar pressure level. Fig. 2-2 shows the IRTM spectral response. The design and operation of the IRTMs are described more completely elsewhere (8).

The observing geometry for single IRTM observations can be characterized by three angles, φ, ϑ, and ψ, where φ is the incidence angle measured from the local zenith to the sun; ϑ is the emission angle measured from the local zenith to the spacecraft and ψ is the solar azimuth angle or the projected angle from the sun to the spacecraft measured on the local planet tangent plane. The IRTMs obtained more than 250,000 separate observations within the boundaries of the study regions over a wide range of observing geometries. The full-width at half-maximum fields of view or 'spot

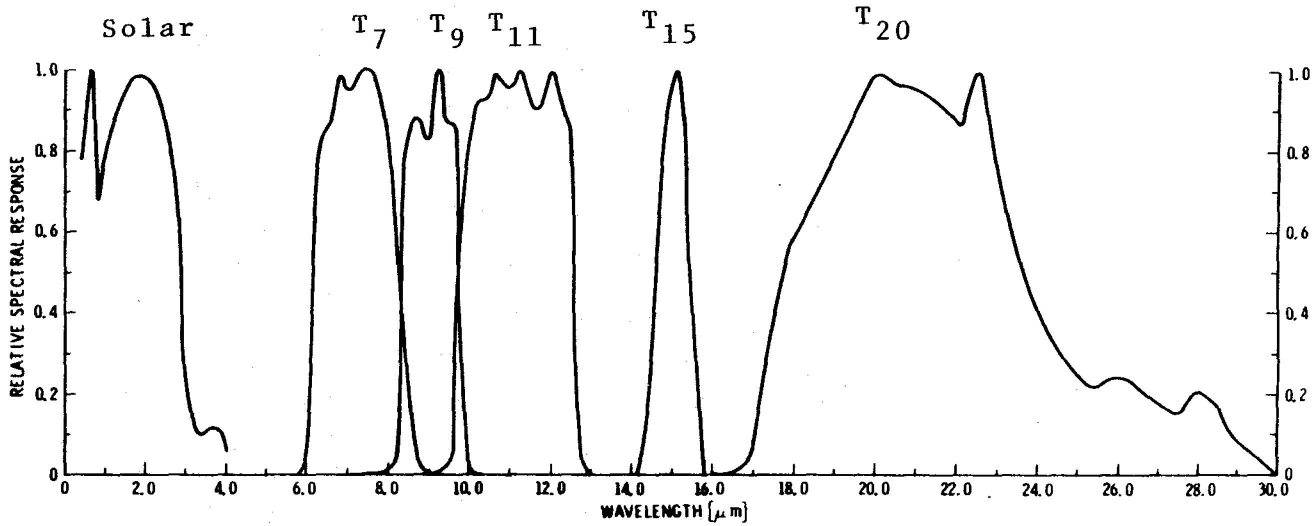

Fig. 2-2. The spectral response of the IRTM instruments.

diameters' of single IRTM observations that were used in this study varied widely, but always corresponded to less than two degrees of latitude on the planet near the poles.

Figs. 2-3 a,b and 2-4 a,b are a partial compilation of the IRTM infrared emission and solar reflectance measurements of the north and south study regions. They are intended to show the general character of the data with a minimum of processing. These parts of the figures were constructed by discarding observations that were obtained at emission angles greater than 60° for brightness temperatures and 30° for solar reflectances to reduce the effects of varying spacecraft viewing geometries. The remaining data were binned, averaged and then plotted with ten-day time resolution. The abscissa scales are Julian date since 2,440,000 and L_s, the areocentric longitude of the sun, an angular measure of Martian season measured from spring equinox in the north. Note that the south polar winter data were obtained prior to the spring data. Figs. 2-3a and 2-4a show radiance-weighted average brightness temperatures in the IRTM infrared channels designated T_7, T_9, T_{11}, T_{15} and T_{20}. Figs 2-3b and 2-4b show averaged IRTM solar reflectances in terms of Lambert albedo, which is the ratio of the measured reflected intensity at a given observing geometry to the intensity that would be obtained if the study regions were ideal, perfectly reflecting, uniformly diffusing surfaces. Gaps in the data are due to incomplete coverage of the study regions at the specified observing geometries and times. T_7 and T_9 were not plotted during most of the fall and winter seasons because of low signal-to-noise ratios for T_7 below 165 K and T_9 below 147 K. The approximate durations of two Martian great dust storms that occurred during 1977 are also shown.

Figs. 2-3c and 2-4c show upper and lower limits for $F\uparrow_{IR}$ for the north and south study regions. They were constructed by first separating all the 10-

Fig. 2-3. IRTM observations and heat balance quantities for the north study region for one Mars year. (A) IRTM brightness temperatures T_7, T_9, T_{11}, T_{15}, and T_{20} for emission angle $\vartheta \leq 60°$ and surface temperature estimates T_S. (B) IRTM Lambert albedos A_L for $\vartheta \leq 30°$ and upper and lower limits for planetary albedos A_P. (C) Radiation budget quantities at the top of the atmospere. Insolation rates F_{Solar} and upper and lower limits for solar absorption rates $F_{Solar}(1 - A_P)$ and emission rates $F\uparrow_{IR}$. (D) Upper and lower limits for derived CO_2 latent heat storage rates S_{CO_2} and calculated upward subsurface conductive heat fluxes F_{Cond}.

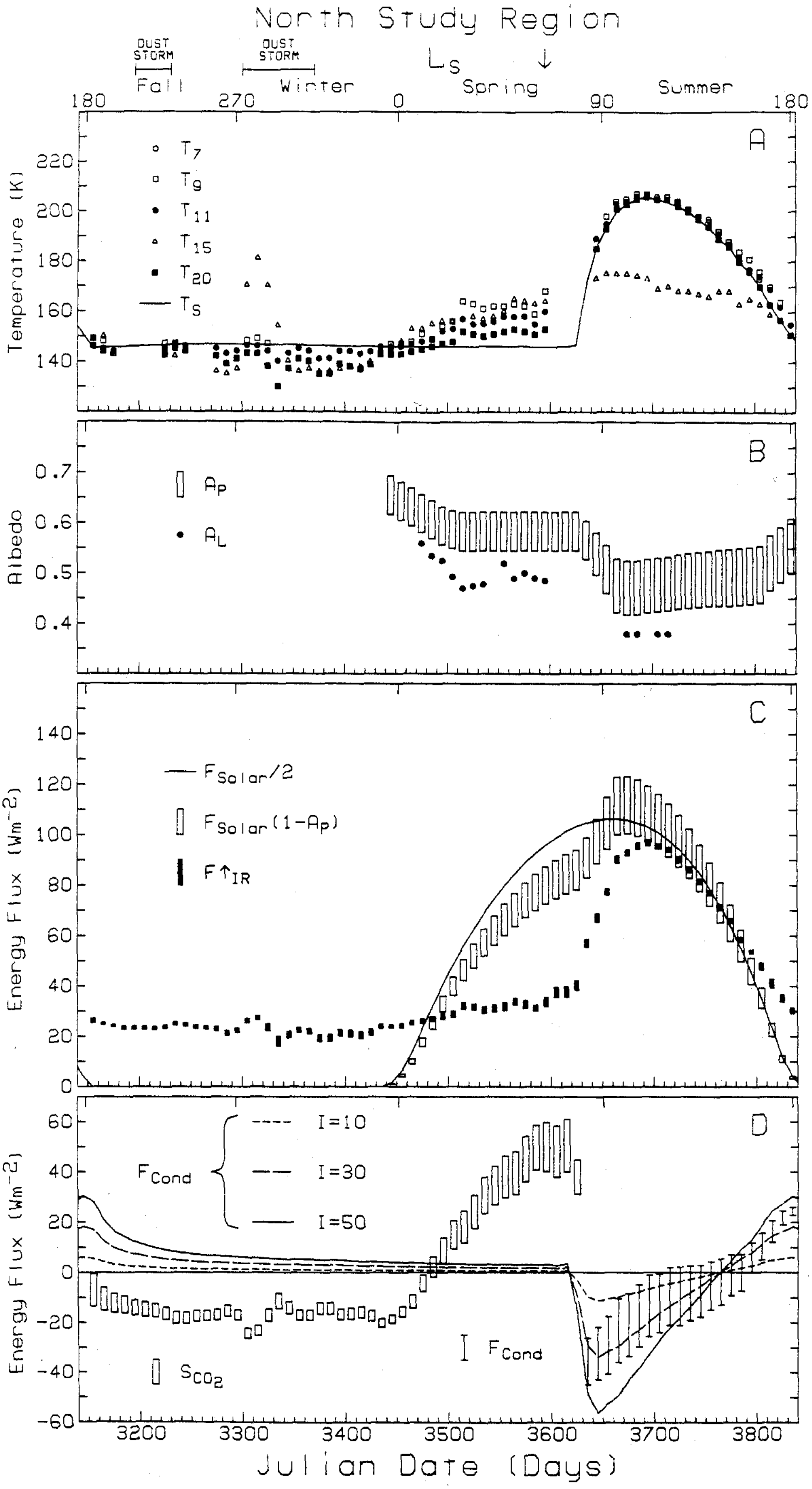
North Study Region
DUST STORM
DUST STORM
Ls
Fall
Winter
Spring
Summer
180
270
0
90
180
A
Temperature (K)
220
200
180
160
140
T_7
T_9
T_{11}
T_{15}
T_{20}
T_S
B
Albedo
0.7
0.6
0.5
0.4
A_P
A_L
C
Energy Flux (Wm^{-2})
140
120
100
80
60
40
20
0
$F_{Solar}/2$
$F_{Solar}(1-A_P)$
$F\uparrow_{IR}$
D
Energy Flux (Wm^{-2})
60
40
20
0
-20
-40
-60
F_{Cond}
I=10
I=30
I=50
F_{Cond}
S_{CO_2}
3200
3300
3400
3500
3600
3700
3800
Julian Date (Days)

Fig. 2-4. Same as Fig. 2-3 for south study region, $F_{Cond} = 0$.

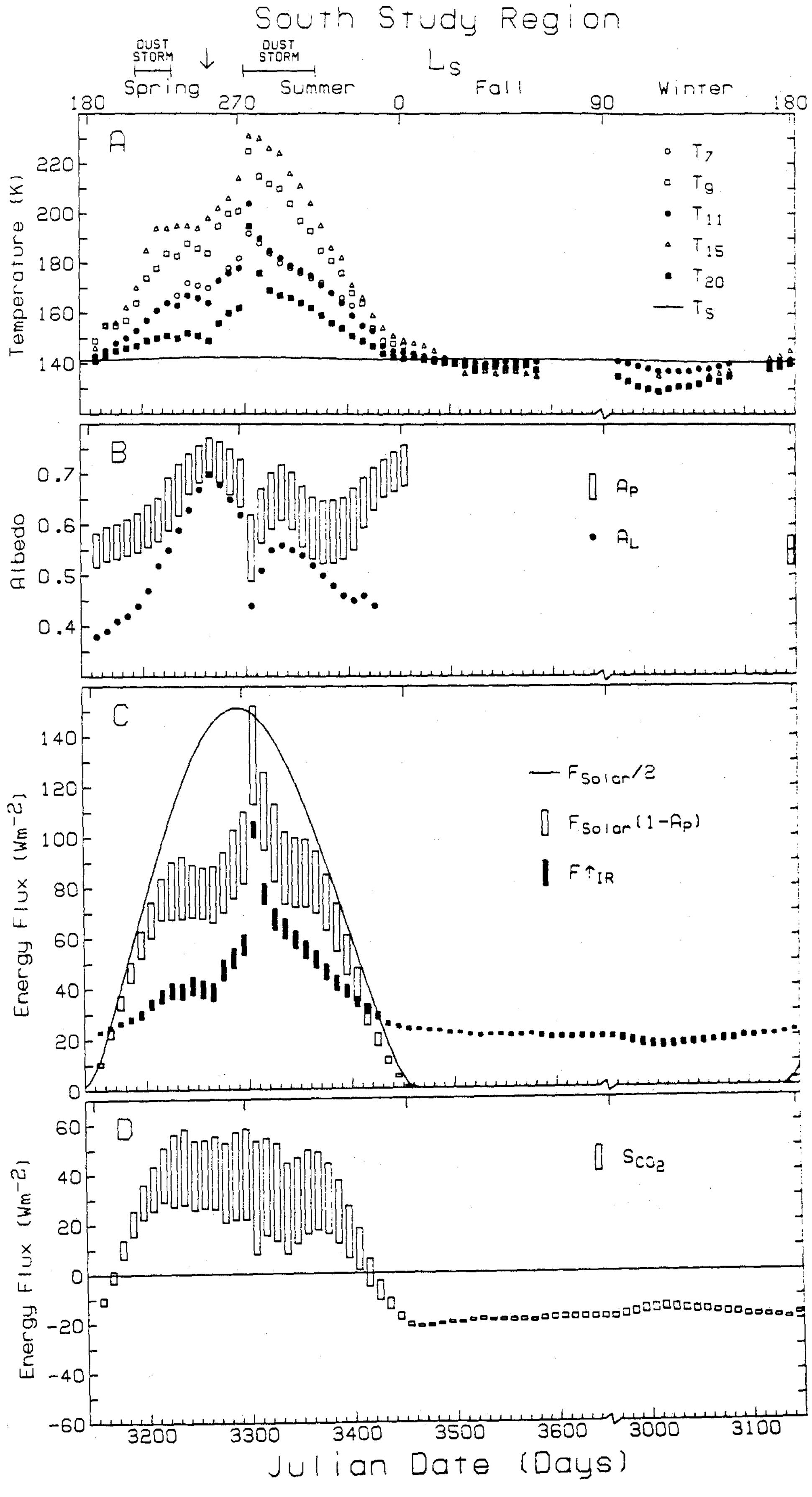
South Study Region
DUST STORM
DUST STORM
Ls
Spring
Summer
Fall
Winter
180
270
0
90
180
A
Temperature (K)
220
200
180
160
140
T_7
T_9
T_{11}
T_{15}
T_{20}
T_S
B
Albedo
0.7
0.6
0.5
0.4
A_P
A_L
C
Energy Flux (Wm^{-2})
140
120
100
80
60
40
20
0
$F_{Solar}/2$
$F_{Solar}(1-A_P)$
$F\uparrow_{IR}$
D
Energy Flux (Wm^{-2})
60
40
20
0
-20
-40
-60
S_{CO_2}
3200
3300
3400
3500
3600
3000
3100
Julian Date (Days)

day averaged radiances in the five IRTM infrared channels into two emission angle bins; $0° \leq \vartheta < 60°$ and $60° \leq \vartheta < 90°$. Standard deviations for the radiances within each bin were generally the equivalent of ≈3K, while differences between the average temperatures in the high and low emission angle bins ranged from 0 to ≈10K. An empirical spectral model was used to synthesize complete emission spectra by computing brightness temperatures at all wavelengths from linear combinations of the equivalent average brightness temperatures in the two emission angle bins (see Appendix 1). Uncertainties in $F\uparrow_{IR}$ are primarily due to potential variations in the unmeasured emission spectrum at wavelengths beyond the sensitivity of the IRTM 20 μ channel. To account for these uncertainties, brightness temperatures for $\lambda > 30\ \mu$ were assumed to be bracketed by $T_{20} \pm (T_{11} - T_{20})$, thus making $F\uparrow_{IR}$ most uncertain during periods of high spectral contrasts. The upper and lower limits for the emission rates of the north and south study regions shown in Figs. 2-3c and 2-4c contain additional ±1% uncertainties for absolute calibration.

Solar absorption rates are more difficult to determine than emission rates due to the complex geometries of reflected radiation fields. The instantaneous planetary albedo is the measured Lambert albedo averaged over the emission hemisphere, or:

$$A_P = \frac{1}{\pi} \int_0^{2\pi} \int_0^{\pi/2} A_L(\vartheta,\psi) \cos\vartheta \sin\vartheta \, d\vartheta \, d\psi \qquad (2.4)$$

where $A_L(\vartheta,\psi)$ is the Lambert albedo at a particular emission angle and azimuth angle. Time-dependent planetary albedos for the study regions were determined by constructing bidirectional reflectance plots of successive groups of approximately 40 days of IRTM Lambert albedo measurements as a function of ϑ and ψ. The plots were hand-contoured and then averaged according to equation (2.4) to yield planetary albedos (see Appendix 1). The reflected radiation fields were assumed to be bilaterally symmetric. Fig. 2-5 shows late springtime bidirectional reflectance plots for the north and south study regions and a bidirectional reflectance plot for aged terrestrial snow that was measured at a comparable solar zenith angle *(10)* and normalized to $A_P = 0.6$. Throughout the spring and summer seasons, the study regions preferentially redirected sunlight to high emission angles and high azimuth angles, making their planetary albedos significantly higher than their low emission angle Lambert albedos. The Lambert albedos shown in Fig. 2-4b also show a strong apparent correlation with φ.

The angular coverage obtained by the IRTMs was never complete but was usually sufficient to define the bidirectional reflectance of the study regions such that A_P could be estimated with few ambiguities. To estimate the potential uncertainties in A_P during those 40-day periods in which the angular coverage was marginal, the available data were contoured twice, once to yield a minimum A_P and once to yield a maximum A_P. During the most marginal periods, the assumed bidirectional reflectance patterns ranged from nearly isotropic to the most specular observed (see Appendix 1). Uncertainties in A_P are further compounded by ±5% uncertainties in the absolute calibrations of the IRTM solar reflectance channels. Fig. 2-3b and 2-4b show upper and lower limits for the planetary albedos of the north and south study regions.

Figs. 2-3c and 2-4c show F_{Solar} for the north and south study regions, computed at their average latitudes using a solar constant of 1370 Wm^{-2} at 1 AU. The curves are not symmetric because Mars' orbit is eccentric. Perihelion passage currently occurs about 31 days before summer solstice in the south, causing the sunlit seasons in the south to be shorter but more intense than their northern counterparts. Annually averaged insolation rates for both study regions were essentially identical. Upper and lower limits for the solar

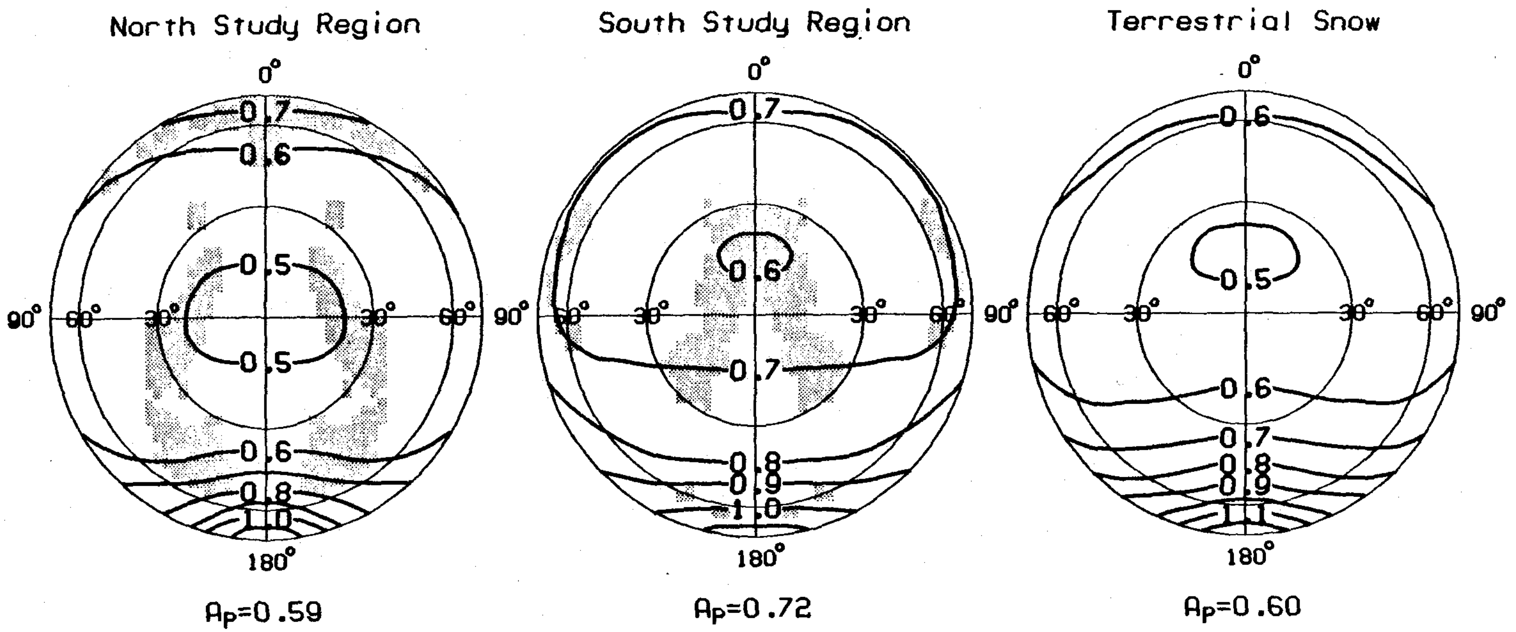

Fig. 2-5. Bidirectional reflectance plots showing contours of Lambert albedo vs. emission angle ϑ (radial) and solar azimuth angle ψ (azimuthal). The sun is at $\psi = 0$. IRTM angular coverage is shaded. (Left) North study region, Julian date 3560 to 3600 (L_s 50.0 to 67.6) for solar zenith angles ϑ of 60° to 70°. (Center) South study region, Julian date 3240 and 3280 (L_s 235.7 to 261.1) for $60° < \vartheta \leq 70°$. (Right) Measured bidirectional reflectance of aged terrestrial snow for $\vartheta = 64.1°$ from Dirmhirm and Eaton (1975) normalized to $A_P = 0.60$.

absorption rates for the study regions are shown in the same figures. Upper and lower limits for F_{Rad} were determined by assuming that the uncertainties in the solar absorption and infrared emission rates were additive.

4. Smaller Heat Balance Quantities

The rest of the terms in the heat balance equation must be determined by less direct means. This is not as serious as it might sound, since near the Martian poles, the magnitudes of S_{Atm}, F_{Horiz} and F_{Cond} are generally much smaller than those of F_{Rad} and S_{CO_2}, which are of order 20 Wm $^{-2}$.This makes proportionately larger uncertainties in the smaller terms almost always less important than uncertainties in the radiation budget measurements for determining CO_2 latent heat storage rates for the study regions.

The smallest and easiest of the three small terms to estimate is S_{Atm}, the atmospheric total potential energy storage rate. The total potential energy of an atmospheric column is the sum of its internal thermal and gravitational potential energies *(11)*. To estimate S_{Atm}, the atmospheric columns within the boundaries of the study regions were assumed to be hydrostatic with constant surface pressures of 4.64 mb in the north and 2.54 mb in the south. The surface pressures are from estimates of surface frost temperatures that will be presented later. Changes in atmospheric temperatures at all levels were assumed to be equal to the measured changes in T_{15}. The calculated magnitudes of S_{Atm} were typically less than 0.5 Wm^{-2}, and never exceeded 3 Wm^{-2}. The total potential energy of the atmosphere within the boundaries of the study regions also underwent seasonal variations due to changes in the mass of the Martian atmosphere caused by the global condensation and sublimation of CO_2 frost *(16)*. Although changes in total atmospheric potential energy due to these seasonal mass variations were of the same order as those due to seasonal temperature variations, the mass variations were not used to estimate S_{Atm} because they were likely to have been balanced during most seasons by equivalent variations in F_{Horiz} with no strong direct effects on S_{CO_2}.

A more difficult term to estimate is F_{Horiz}, the instantaneous net horizontal heat flux into the study regions at their boundaries. The results of general circulation model (GCM) calculations show that although the Martian atmosphere is expected to transport some heat from lower-warmer latitudes to the polar regions, the effects of dynamic heat transport on the current heat balance at the Martian poles are small when compared to those of radiation. Martian GCM calculations for seasons near L_s=270, L_s=0 *(12)* and L_s=90 *(13)* all give vertically integrated polar atmospheric advective heating rates ranging from 0 to 10 Wm^{-2}. Similar advective heating rates are required by a 10-layer one-dimensional polar radiative model to explain the IRTM 15 μ channel observations of the north and south study regions during the fall and winter seasons (see Chapter 3).

The annually averaged upper and lower limits for F_{Rad} are approximately +3 and -7 Wm^{-2} for both the north and the south study regions. If one assumed that each region behaved identically from year to year and there was no net flux of solid CO_2 into or out of the regions, then the annually averaged values of F_{Cond}, S_{Atm} and S_{CO_2} would be zero and the annually averaged value of F_{Horiz} would be $\approx 2 \pm 5$ Wm^{-2} from equation 2.1.

Two lines of quantitative evidence support the notion that the heat budgets of the study regions are nearly repeatable from year to year. The first is that the IRTM observations of the north residual cap during the summer season used in this study and those from one Mars year earlier *(1)* show no discernible interannual variations in thermal or reflectance behavior. This suggests that the permanent water ice cap in the north was exposed within ten days of the same Martian date and heated at the same rates both years. The second line of evidence comes from comparisons between Viking and Mariner 9 images of the receding south seasonal cap. The Viking images show that the cap nearly receded to its residual configuration by Julian date 3353 (L_s 306), whereas the Mariner 9 images that were obtained three Mars years earlier show that the cap receded to the same point approximately 17 days earlier *(4)*. The same seasonal lag would correspond to approximately 9 days on earth. Results presented later in this chapter will show that S_{CO_2} for the south study region could range from between 20 and 50 Wm^{-2} during this season. In 17 days, this would result in the sublimation of 5 to 12.4 g cm^{-2} of CO_2 frost, assuming a latent heat of sublimation of 590 Jg^{-1}. To produce such a frost later in one year would only require an annually averaged perturbation to the heat balance of the south study region of 0.5 to 1.2 Wm^{-2}.

Unfortunately, there are no firm constraints on the magnitude or direction of latitudinal frost transport near the poles. Little is known about the microphysical properties of Martian seasonal frosts, or whether they can be transported effectively over large horizontal distances. Viking orbiter images show bright frost streaks associated with impact craters at latitudes ranging from 55°S to 80°S. The streaks persisted up to 70 days after the passage of the receding south seasonal cap. It has been suggested that the streaks are accumulations of wind-blown frost in the lees of craters, implying that Martian seasonal frosts may be effectively redistributed by winds *(14)*. An alternate, viable explanation for these streaks is that they are the result of local variations in the properties and processes that determine the rates of seasonal frost condensation and sublimation at these latitudes. The simplest explanation for the annually-averaged radiation budget measurements is that $\overline{S_S}$, $\overline{S_A}$, and $\overline{S_{CO_2}}$ are all close to zero and $\overline{F_H}$ is a small positive quantity at both poles in accordance with the GCM and one-dimensional radiative model results.

For the purpose of estimating S_{CO_2}, F_H will be assumed to equal 2 Wm^{-2} for both study regions throughout the year. Although this procedure may introduce significant uncertainties during some seasons, it is the simplest and least *ad hoc* method of correcting the instantaneous heat budget results for the hopefully minor effects of atmospheric heat transport. Any effects that this assumption may have on subsequent results will be discussed.

5. North Polar Subsurface Heat Conduction and Permanent CO_2 Reservoir

The last term in the heat balance equation to consider is F_{Cond}, the upward subsurface conductive heat flux at the top boundaries of the permanent caps. It will be useful to first consider the case of the north study region.

The relative magnitudes of seasonal variations in F_{Cond} can be derived from solutions to the one-dimensional heat diffusion equation if the temperature at the top of the permanent cap can be determined throughout the year. Since the polar atmosphere was relatively clear during northern summer when the permanent cap was exposed, its temperature can be taken directly from the measured brightness temperatures in the IRTM surface-sensing channels since water ice is an excellent blackbody emitter. During other seasons, the top of the permanent cap is in direct thermal contact with seasonal CO_2 frost deposits. If the frost deposits are in solid-vapor equilibrium with CO_2 gas in the atmosphere, then their temperatures will not vary with depth and the temperature at the top of the permanent cap will equal the surface temperature

T_s.

The temperatures of Martian CO_2 frost deposits are determined by the local partial pressure of CO_2. Most previous studies have assumed that polar frost deposits lie close to the 6.1 mbar pressure level - giving CO_2 frost temperatures near 148K, but the IRTM observations suggest that the study regions lie somewhat higher. Figs. 2-3a and 2-4a show that during early fall and late winter, the IRTM brightness temperatures in the available channels were nearly coincident. This occured in both the north and south study regions and was especially apparent during early fall in the south. The simplest and most likely explanation for this behavior is that the spectral emissivities of seasonal frost deposits in the north and south study were very close to unity during these seasons, making the measured brightness temperatures close to actual surface frost temperatures (see Chapter 3). Frost temperatures can be used to determine surface CO_2 equilibrium vapor pressures and estimate approximate altitudes for the study regions relative to the 6.1 mbar reference aeroid. Using T_s=146±1k for the north study region at Julian date 3430 (L_s=348.6) and T_s=142±1K for the south study region at Julian date 3490 (L_s=18.2) gives altitudes of +2.5±2km in the north and +8±2km in the south assuming a hydrostatic atmosphere of uniform composition with a scale height of 9km. Although the true uncertainties of these inferred study region elevations are difficult to gauge, they are in good agreement with the general trends displayed by radio occultation altitude determinations at lower latitudes *(15,20)*.

T_s was calculated for all other seasons in which CO_2 was present by assuming that CO_2 partial surface pressures at the study regions were proportional to the seasonally varying surface pressures measured at Viking Lander 1 *(16)*. Figs. 2-3a and 2-4a show estimated values of T_s for the north and south study regions throughout the year. The day that the north permanent cap was exposed was determined from high emission angle observations that are not shown in Fig. 2-3a.

With year-long surface temperatures in hand, F_{Cond} can be calculated by treating the north permanent cap as a semi-infinite homogeneous half-space in annual equilibrium. With boundary conditions that surface temperatures equal T_s and that temperature gradients at great depths equal zero; i.e., no heat flow from the Martian interior, the one-dimensional heat diffusion equation was solved to yield F_{Cond} throughout the year. (The heat flow from the Martian interior has been estimated to be of order 10^{-2}Wm^{-2} *(17)*.) The solutions are such that the magnitude of F_{Cond} at any given time is proportional to the thermal inertia $I = (k\rho c)^{1/2}$ where k is the thermal conductivity, ρ is the density and c is the heat capacity of the permanent polar cap material. The thermal inertia of the permanent cap is not expected to exceed 50×10^{-3} cal cm^{-2} sec$^{-1/2}$, the value for solid water ice or rock. Fig. 2-3d shows calculated values for F_{Cond} throughout the year for $I = 10 \times 10^{-3}$, 30×10^{-3} and 50×10^{-3} cal cm^{-2} sec$^{-1/2}$.

Values for I in the north can be determined from the IRTM observations by considering the heat balance equation during the summer season when the permanent water ice cap is exposed. Since high surface temperatures preclude the stability of solid CO_2 during this season, and H_2O latent heat terms are always small on Mars because of the limited water vapor holding capacity of the atmosphere, equation 2.1 can be solved to yield upper and lower limits for F_{Cond} during northern summer since upper and lower limits for F_{Rad} and values for S_{Atm} and F_{Horiz} have been determined. Observationally constrained limits for F_{Cond} during northern summer are shown as vertical bars in Fig 2-3d. Comparing these with the values of F_{Cond} that were calculated from the heat diffusion equation in the same figure shows that the the two can be consistent if the thermal inertia of the north permanent cap is in the neighborhood of 30 ×

10^{-3} cal cm^{-2} sec$^{-½}$. The goodness of fit provides not only an estimate in the uncertainties in I, but independent confirmation that possible systematic errors in A_P and $F\uparrow_{IR}$ are not large. Upper and lower limits for calculated year-long values of F_{Cond} for the north study region will be estimated by using permanent cap thermal inertias of 40×10^{-3} and 20×10^{-3} cal cm^{-2} sec$^{-½}$.

Since the skin depths for the attenuation of Martian seasonal temperature waves are on the order of meters, the derived range of thermal inertias are a composite measure of the physical properties of the north permanent cap to these depths. The derived thermal inertias are very consistent with the notion that the north permanent cap is a coarse grained or nearly solid admixture of water ice, rock and dust. Figure 2-6 shows calculated year-long north study region subsurface temperatures as a function of the thermal skin depth β^{-1}, where $\beta = \sqrt{\frac{\pi \rho c}{kP}}$ and P is the length of a Martian year.

While the Viking IRTM observations of the north residual cap during summer have completely ruled out the possibility that solid CO_2 could have survived on the surface *(1)*, it is still not inconceivable that CO_2 could have survived within the north permanent cap in the form of carbon dioxide-water clathrate ($CO_2{-}6H_2O$). The dissociation temperatures of $CO_2{-}H_2O$ clathrates on Mars are 4 to 5 K higher than those of pure CO_2 frosts *(18)*. For a CO_2 partial pressure of 4 mb, the dissociation temperature of $CO_2{-}H_2O$ clathrates is 149.1 K. It has been proposed that the mass of the Martian atmosphere may currently be determined over annual time scales by the CO_2 vapor pressure of permanent clathrate deposits at one or both poles *(19)*. These deposits would have to be close enough to the surface to exchange CO_2 with the atmosphere over annual time scales but deep enough not to be significantly affected by the penetration of the seasonal temperature wave. A confident lower limit for the temperature

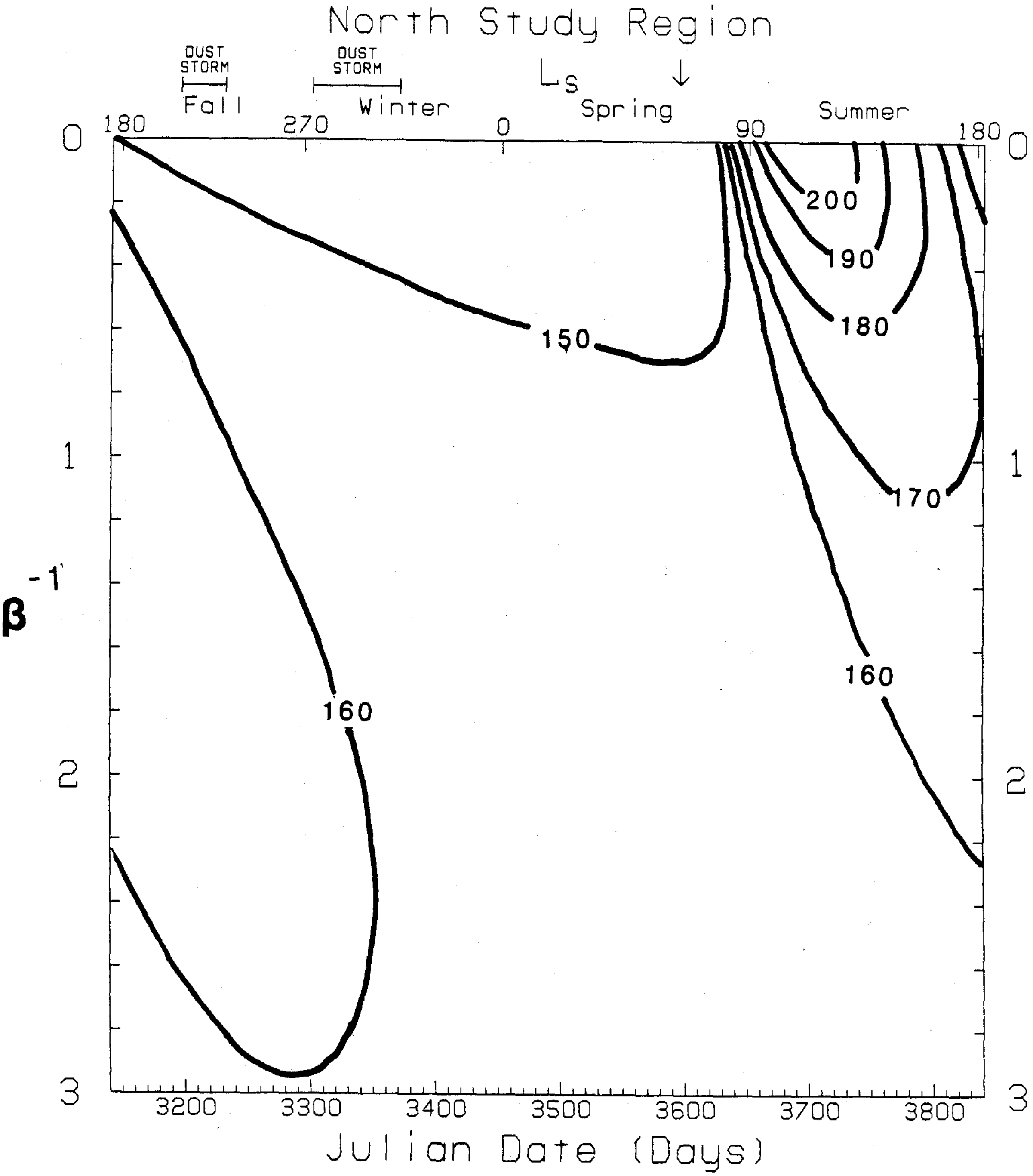

Fig. 2-6. **Calculated north study region subsurface temperatures using the values of T_S shown in Fig. 2-3 and the one-dimensional heat diffusion equation. β^{-1} is the skin depth for the penetration of the seasonal temperature wave.**

of any permanent clathrate reservoir in the north can be obtained by simply determining the average value of T_s over the year, since this will be the seasonally invariate temperature at great depths assuming zero heat flux from the Martian interior. The annually averaged value of T_s from Fig. 2-3a is 158.7 K. This precludes the stability of a permanent clathrate reservoir in the north over annual time scales by a wide margin. These arguments against permanent clathrate reservoirs apply even more strongly to possible buried reservoirs of solid CO_2 *(20)*.

6. South Polar Subsurface Heat Conduction and Permanent CO_2 Reservoir

In the south, the magnitude of F_{Cond} is directly tied to the important question of whether or not solid CO_2 remained on the surface of the south residual cap throughout the summer season. If the entire south study region was covered with solid CO_2 throughout the year, then F_{cond} would be close to zero. An analysis of the Viking orbiter images of the receding south polar cap suggests that some CO_2 frost may have been left on the outskirts of the residual cap area at the end of summer, but the images alone provide few clues as to the extent of CO_2 cover within the south study region itself towards the end of summer because the rate of change of frost coverage was extremely slow *(4)*. The IRTM observations of the south residual cap during the Martian summer of 1977 can provide additional constraints, but the data can not be interpreted as easily as the corresponding data in the north.

One factor that complicates the interpretation of the IRTM southern summer observations is the observed gradual exposure of thin lanes of dark surface materials within the south study region soon after summer solstice *(4)*. Although dark lanes visible in the Viking images never comprised more than 10%

of the area of the south study region, they are a strong indication that the surface properties of the region were not spatially homogeneous. Since the dark lanes in the south were not resolved by the IRTMs, they do not degrade the accuracy of the radiation budget measurements of the south study region.

Another set of complicating factors during southern summer arise from the radiative effects of dust in the south polar atmosphere. At solar wavelengths, the dust obscured surface features *(4)* and caused marked changes in the planetary albedo of the south study region (Fig. 2-4b). At infrared wavelengths, emission from the hot dust particles resulted in elevated brightness temperatures in the IRTM surface-sensing channels. The severity of this latter effect was particularly evident in the greatly elevated IRTM brightness temperatures during southern spring, when the Viking Images showed that the surface of the south study region was completely covered with CO_2 frost (Fig. 2-4a).

These complicating factors make it impossible to use the measured IRTM brightness temperatures to unambiguously confirm or exclude the possible presence of solid CO_2 throughout the summer in the south in a straightforward fashion. Using the brightness temperatures as measures of emitted energy for heat balance measurements can provide more concrete results.

The best evidence for a permanent CO_2 cap in the south has come from Kieffer's analysis of IRTM spring and summer south polar data *(3)*. In his study, he used observations of the interior of the residual cap at Julian date 3362 (L_s=311) to estimate that the net flux of solar and infrared radiation at the top of the atmosphere was on the order of 60 Wm^{-2}. Kieffer argued that a large fraction of this energy flux must have been going into sublimating surface CO_2 deposits. This result, along with the absence of any unequivocal evidence ***for*** an exposed water ice cap in the south (i.e., large atmospheric water vapor abundances over the cap *(21)*, or any abrupt increases in the IRTM brightness temperatures during late summer) led him to conclude that the south residual cap contained solid CO_2 throughout the first Viking year of observations.

The IRTM observations and heat balance statistics presented in this paper provide additional support for Kieffer's conclusion. It is instructive to observe the behavior of F_{Rad} (the difference between $F_{Solar}(1-A_P)$ and $F\uparrow_{IR}$) during the early spring seasons when the surfaces of both the north and the south study regions were completely covered with CO_2 frost (Figs. 2-3c and 2-4c). As the insolation rate increased in early spring, F_{Rad} underwent a rapid transition from negative to positive values in both the north and the south study regions. Since F_{Cond} is small during this season, this behavior can be readily interpreted as a quick transition from CO_2-condensing to CO_2-sublimating conditions within both study regions. In the south, F_{Rad} stayed positive until late in the summer season and then underwent a rapid transition to negative values as the insolation rate decreased. This behavior is in sharp contrast to the slow transition that was observed in the north and is exactly what would be expected if a large fraction of the surface of the south study region contained sublimating and then condensing CO_2 frost during late summer.

To investigate the quantitative implications of the above argument, the same subsurface thermal conduction model that was used in the north was applied in the south. Fig. 2-7a shows the same IRTM brightness temperatures that were shown in Fig. 2-4a with the addition of two hypothetical scenarios for the spatially averaged surface temperature of the south study region designated T_{S1} and T_{S2}. During the seasons when the Viking images definitely show that the surface of the south study region was at least partially covered with CO_2 frost, surface temperatures were determined via solid-vapor phase

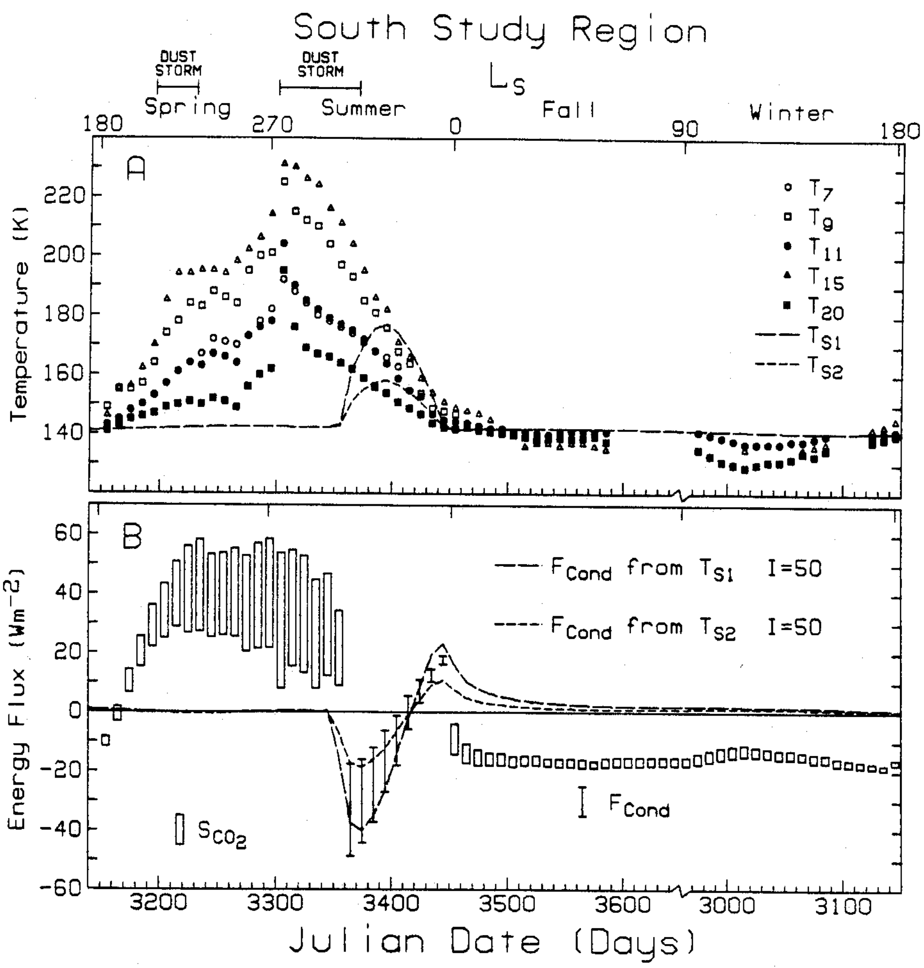

Fig. 2-7. (A) Hypothetical south study region average surface temperatures T_{S1}, and T_{S2} and the IRTM brightness temperature observations. (B) Hypothetical CO_2 sublimation rates and conductive heat fluxes at the surface using T_{S1}, and T_{S2}.

relationships and the VL-1 pressure data, using the measured, coincident IRTM brightness temperatures during early fall and late winter as surface frost temperatures as was done in the north. During the rest of the year, the hypothetical surface temperatures were made to vary in such a way as to make the calculated values of F_{Cond} for $I = 50 \times 10^{-3}$ cal cm^{-2} sec$^{-½}$ balance the other terms in the instantaneous heat balance equation on the assumption that the south study region contained no solid CO_2 and S_{CO_2} was zero. Fig. 2-7b shows calculated values of F_{Cond} from T_{S1} and T_{S2}, and upper and lower limits on F_{Cond} from the instantaneous heat balance equation on the assumption that S_{CO_2} was zero from Julian Date 3360 to 3450. Since an exposed permanent cap in the south is not likely to have a thermal inertia greater than that of solid water ice, the hypothetical surface temperatures shown in Fig. 2-7a represent the minimum changes in average surface temperatures that are required to balance the instantaneous heat balance equation without CO_2 latent heat storage terms after the assumed date of exposure. Despite this very generous assumption, the hypothetical average surface temperatures for both cases are still higher than the IRTM observations allow. Fig. 2-7a shows that T_{20} was lower than T_{S1} and T_{S2} during late summer. Since bare soil and water ice have high spectral emissivities at these wavelengths, the measured 20μ channel brightness temperatures require the presence of emitting material within the region that was colder than the hypothetical average surface temperatures. The colder emitting material (the CO_2 frost) must have been on the surface, since T_{15} indicates that the atmosphere was at least as hot as the the hypothetical surface temperatures and the atmosphere was not optically thick at $\lambda = 20_{\mu}$.

The above arguments for the presence of CO_2 frost within the south study region during late summer are the most direct and least assumption-ridden that could be found. Any argument that relies on heat balance measurements can not positively exclude a nearly instantaneous absence of CO_2 frost just as F_{Rad} changes from positive to negative values in late summer. Future efforts to determine if CO_2 frost is present on the south residual cap would be greatly simplified by the availability of accurate surface temperatures with high spatial resolution or by the direct spectroscopic identification of solid CO_2.

7. Annual Behavior of CO_2 Frost

With the necessary terms in the heat balance equations accounted for, it is now possible to present derived CO_2 frost accumulation rates for the north and south study regions over the course of a Martian year. Upper and lower limits for S_{CO_2} for the north study region (Fig. 2-3d) were computed from equation 2.1 by assuming that the estimated uncertainties in F_{Rad} and F_{Cond} were additive. Upper and lower limits on S_{CO_2} for the south study region (Fig. 2-4d) reflect uncertainties in F_{Rad} alone.

Before comparing the behavior of CO_2 frost in the north and south, it is important to point out that there is no obvious reason to expect permanent CO_2 frost deposits at only one Martian Pole. This is true for elliptical orbits as well as circular ones since the total annual insolation at both poles will always be equal *(20,22)*. Elliptical orbits complicate comparisons between the behavior of CO_2 in the north and south because the durations of seasons and the distributions of incident solar energy within them are not symmetric. Currently, if CO_2 accumulation rates in the absence of sunlight were the same at both poles, then approximately 30% more CO_2 would be expected to accumulate in the south over the course of a year because its polar night season is longer than the north's. If the properties of the north and south polar surfaces and atmospheres were identical, then the south's apparent advantage during the fall and winter seasons would be completely cancelled out during the spring and summer because the distribution of insolation with time is such that more total sublimation would take place in the south. The results in Figs. 2-3d and 2-4d are especially useful for understanding the current asymmetric behavior of seasonal frost at the Martian poles because they make it possible to compare the behavior of CO_2 season by season.

On the whole, the north and south study regions behaved symmetrically during their respective fall and winter seasons. Figs. 2-3d and 2-4d show that the rates of CO_2 condensation within both regions were generally quite comparable during this period except during early northern winter and during the first half of the second global dust storm in the north. The elevated rates of CO_2 condensation that are inferred during the first part of the storm could well be an artifact of the assumption that F_{Horiz} remained constant throughout the year *(24)*. Upward heat conduction from the permanent cap played and important role in the heat balance of the north study region during fall as a large fraction of F_{Cond} probably resulted in CO_2 frost sublimation at the base of the accumulating seasonal frost layer. Since the net vertically integrated rates of CO_2 condensation within the north and south study regions were comparable, CO_2 accumulation rates at the top of the seasonal frost layer in the north must have been slightly higher than they were in the south. Higher combined surface and atmospheric CO_2 condensation rates are not unexpected in the north because of its lower elevation. Subsituting the upper and lower limits for S_{CO_2} into equation 2.2 and then integrating these rates over the periods in which net frost accumulation occurred yields total annual frost accumulations of 75±12 gcm^{-2} in the north and 110±7 gcm^{-2} in the south for $L_{CO_2}=590Jg^{-1}$. Although these derived annual CO_2 accumulations should contain additional uncertainties for F_{Horiz}, they do not suggest that the absence of CO_2 frost in the north during summer was primarily due to north-south asymmetries during fall and winter.

The north and south study regions behaved very asymmetrically during their respective spring seasons. Figs. 2-3b, 2-4b and 2-5 show that during late spring, planetary albedos in the south were significantly higher than they were in the north. Comparison between Figs. 2-3d and 2-4d shows that by mid-spring, CO_2 sublimation rates in the north were at least as high as they were in the south despite the fact that insolation rates in the south were over 50% greater. Since the north and south study regions experienced similar CO_2 accumulation rates during fall and winter, the absence of permanent CO_2 frost deposits in the north can be primarily attributed to the north study region's ability to convert a significantly greater fraction of its available incident solar energy into CO_2 frost sublimation.

An important question concerning the asymmetric behavior of CO_2 frost at the Martian poles is whether this behavior was primarily due to north-south differences in surface properties, atmospheric properties or both. It has been suggested that differences in the dust contents of the polar atmospheres or the seasonal frost deposits themselves may play an important role in the asymmetry since global dust storms presently occur only during southern spring and summer and the radiative effects of dust in the atmosphere and on the surface could be large *(24,7,25)*. The results presented so far have shown that the most important north-south asymmetries occurred during the spring seasons. The next section describes how the observed late spring season heat balance quantities can be interpreted in terms of surface and atmospheric properties with the aid of a polar radiative model.

8. Simplified Polar Radiative Model

The model described here is similar to the simplified 1-dimensional radiative equilibrium model used by Davies to investigate the effects of atmospheric dust on Martian surface and atmospheric heating rates *(25)*. By treating the atmosphere's thermal response as instantaneous (see Appendix 2), the model calculates surface CO_2 sublimation rates and observable radiative fluxes at the top of the atmosphere from an assumed set of aerosol optical properties, surface properties and atmospheric dynamical heating rates. By comparing the model calculated values of A_P and $F\uparrow_{IR}$ with the observations, the surface and atmospheric properties that are responsible for the contrasting behavior of the north and south study regions during the spring seasons can be identified.

An important task for the model is to calculate the fraction of incident solar energy that is deposited on the surface and in the atmosphere. The planetary albedo, a key observable can be written $A_P=1-(H_s+H_A)/F_{Solar}$ where H_s is the surface solar heating rate and H_A is the vertically integrated atmospheric solar heating rate. In the model, the fraction of solar energy absorbed by gaseous CO_2 at near infrared wavelengths is calculated from formulae presented by Pollack *et al (13)*. The remaining solar energy (typically 99%) is then assumed to be available for broad-band multiple scattering and absorption by atmospheric aerosols and the surface. Scattering calculations are performed using a two-stream δ-Eddington code that yields calculated radiative fluxes that are in good agreement with the results of exact solutions to the equation of radiative transfer for the range of aerosol optical properties considered in this chapter *(26)*. H_s and H_A are determined by the values of six model input parameters: A_s, τ, $\tilde{\omega}_0$, g, F_{Solar} and φ where A_s is the solar spectrum averaged surface albedo[1] ,τ is the spectrum averaged vertical aerosol optical depth or opacity, $\tilde{\omega}_0$ is the solar spectrum averaged aerosol single scattering albedo[2] and g is the solar spectrum averaged aerosol scattering phase function asymmetry parameter.[3]

The model's infrared calculations are greatly simplified by the fact that north and south polar atmospheres respond almost instantaneously to thermal forcings. Since S_{Atm} is small and elevated polar atmospheric temperatures preclude the stability of condensed atmospheric CO_2, the model's instantaneous heat balance equation for the atmospheric columns within the study regions during late spring is:

$$H_A + F_{Horiz} = F\uparrow_{IR} - \varepsilon_s \sigma T_s^4 + \varepsilon'_s F\downarrow^{*}_{IR} \qquad (2.5)$$

where ε_s is the Planck weighted average emissivity of the surface frost, σ is the Stefan-Boltzman constant, $F\downarrow^{*}_{IR}$ is the downward flux of infrared radiation at the surface and ε'_s is the fraction of $F\downarrow^{*}_{IR}$ absorbed by the surface. ε'_s and ε_s are not the same quantities because the spectral distributions of the downward infrared fluxes and the upward emitted fluxes at the surface are not necessarily the same. Equation 2.5 makes no allowance for vertical convective heat transport between surface and atmosphere because spring season polar atmospheric temperature profiles are very stable. The effects of heat conduction from atmosphere to surface are also small under these circumstances *(12)* and are ignored in this model. $F\downarrow^{*}_{IR}$ is not calculated explicitly in this model but is evaluated in terms of a new free parameter f where $f = F\downarrow^{*}_{IR} / (H_A + F_{Horiz})$. f is a measure of the atmosphere's tendency to re-radiate its absorbed solar and dynamically transported energy to the surface. During late spring in the north

---

1. Surface bidirectional reflectances are assumed to be isotropic.
2. $\tilde{\omega}_0$ is the ratio of scattered to scattered and absorbed radiation in a single scattering event. $\tilde{\omega}_0$ equals one for non-absorbing particles.
3. g is the difference between the fractions of singly scattered radiation redirected into the forward and rearward hemispheres; g equals zero for isotropic scattering, g equals one for totally forward scattering.

and south, f should be greater than zero and less than $(\varepsilon'_s)^{-1}$ since $(H_A + F_{Horiz})$ is likely to be greater than zero and $F\uparrow_{IR}$ is greater than $\varepsilon_s \sigma T_s^4$ (see eq. 2.5). A series of more elaborate 10 layer 1-dimensional radiative equilibrium model calculations show that f is primarily determined by the vertical distributions of advective heating and aerosol opacity and is relatively insensitive to all other surface and atmospheric properties. In these calculations, f was found to be greater than 0.45 and less than 0.7 even when all aerosol particles were assumed to be concentrated at the top of the atmosphere or just above the surface (see Appendix 3). If T_s is known, then $F\uparrow_{IR}$ can be calculated from equation 2.5 given the the values of H_s, H_A, F_{Horiz}, f, ε'_s and ε_s.

Figs. 2-8 a,b and c show some important aspects of the model's behavior for one of the many possible combinations of model input parameters. Fig 2-8a shows calculated values of A_P as a function of A_s and τ for φ=66.5°, $\tilde{\omega}_0$=0.86 and g=0.79. These values for $\tilde{\omega}_0$ and g were derived from analyses of Viking lander imaging observations of the sun and sky *(27)* and are frequently used to characterize the solar spectrum averaged optical properties of Martian dust. The contours in Fig. 2-8a show that for this choice of aerosol optical properties, A_P is a lower limit for A_s as long as A_P is greater than 0.3. Fig. 2-8b shows calculated values of S_{CO_2} as a function of A_s and τ for the polar insolation conditions that occur during late southern spring. S_{CO_2} can be determined by using model calculated values of A_P and $F\uparrow_{IR}$ in equation (2.3) and then assuming F_{Cond}=0 in equation (2.1). Model input parameters were F_{Solar}=290.7 Wm^{-2}, φ=66.5°, $\tilde{\omega}_0$=0.86, g=0.79, T_s=142.5K, $\varepsilon'_s=\varepsilon_s=1$, F_{Horiz}=2 Wm^{-2} and f=0.55. The contours in Fig 2-8b redemonstrate Davies' conclusion that the addition of atmospheric dust can either result in increased or decreased surface sublimation rates depending on the surface albedo, but also show that spring season surface CO_2 sublimation rates are much stronger functions of A_s than of

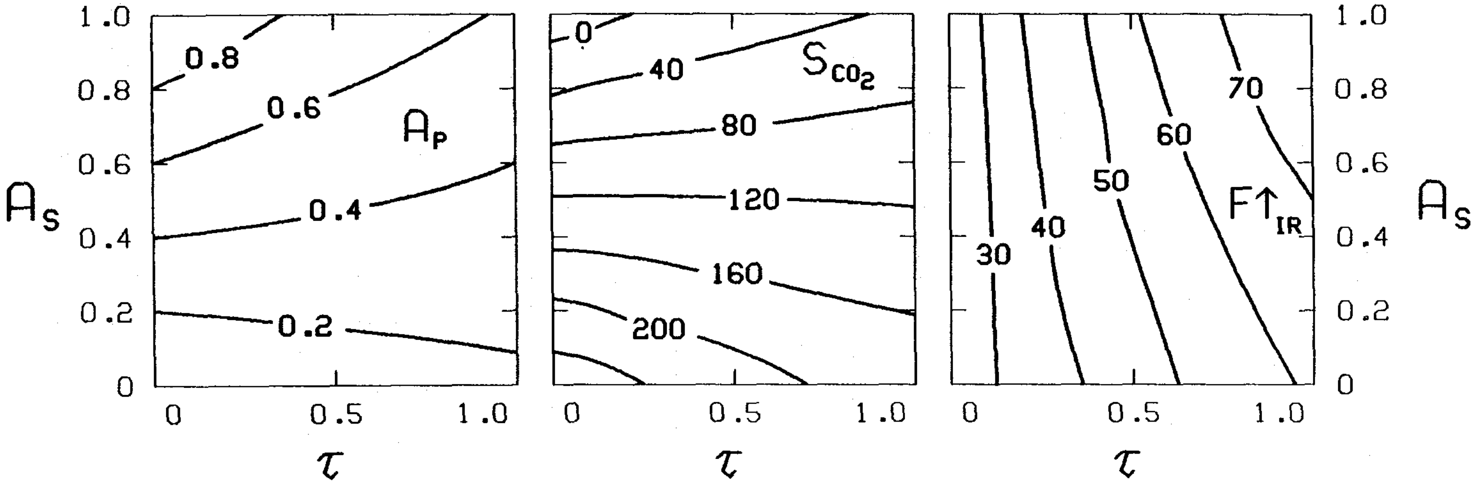

Fig. 2-8. Simplified polar radiative model results for one set of model input parameters. (A) Calculated spring season planetary albedos A_P, (B) south study region surface CO_2 latent heat storage rates S_{CO_2}, and (C) upward infrared fluxes at the top of the atmosphere $F\uparrow_{IR}$. Axes are surface albedo A_S and solar spectrum averaged dust opacity τ.

τ. This strong dependence makes A_s the key property of the study regions during spring.

Fig. 2.8c shows calculated values of $F\uparrow_{IR}$ as a function of A_s and τ for the same set of input parameters used in Fig. 2.8b. Comparison between Figs. 2.8a and 2.7c shows that for this set of model input parameters, contours of $F\uparrow_{IR}$ versus A_s and τ are nearly orthogonal to contours of A_p versus A_s and τ. This is very important because it means that measurements of A_P and $F\uparrow_{IR}$ can impose strong constraints on the values of A_s and τ during this season.

A complete set of model calculations for all possible combinations of model input parameters were performed for the insolation conditions at Julian Date 3265 (L_s=251.6) for the south study region and Julian Date 3595 (L_s=65.4) for the north study region (see vertical arrows above Figs. 2-3a and 2-4a). These particular dates were chosen for comparing the model results with the IRTM observations for a number of reasons. First, insolation rates at the tops of the atmospheres in the north and south were near their maximum values with average solar zenith angles near 66.5° for both study regions. Second, the Viking orbiter images show that the surfaces of both study regions were plainly visible and completely covered with seasonal CO_2 frost *(4,28)*. Also, the diameters of both seasonal polar caps were approximately 20° of latitude and the planetary albedos of both regions were well constrained. On these dates, observed upward infrared fluxes at the top of the atmosphere in the north and south were similar while observed planetary albedos at the top of the atmosphere in the south were distinctly higher ($0.54 \leq A_P \leq 0.62$ and $32.0 \leq F\uparrow_{IR} \leq 35.6$ for the north study region versus $0.69 \leq A_P \leq 0.77$ and $35.3 \leq F\uparrow_{IR} \leq 42.0$ for the south study region).

The calculations were performed by varying each of the model input parameters A_s, τ, ϖ_0, g, F_{Horiz}, ε_s and f over a wide range in every possible combination and then recording only those combinations of parameters that yielded model calculated values of A_P and $F\uparrow_{IR}$ that were within their measured upper limits on the chosen dates in the north and the south. ε'_s was assumed to equal ε_s for all calculations. Table 2-1 shows two sets of constraints on the model input parameters $\tilde{\omega}_{zero}$, g, F_{Horiz}, ε_s and f. Set 1 covers a likely range of dust optical properties and study region surface and atmospheric properties. Set 2 covers a much wider range, including nearly all possible water ice, dust and soot optical properties and a very wide range of study region surface and atmospheric properties. Fig. 2-9 shows all combinations of A_s and τ that yielded calculated values of A_p and $F\uparrow_{IR}$ that were within their measured upper and lower limits when the two sets of constraints on the model input parameters in Table 2-1 were imposed. The model calculations show that the late spring season IRTM observations are consistent with the first set of input parameters only if dust opacities in the north and south are similar and surface frost albedos in the south are distinctly higher. When the wider ranging second set of model input parameters are employed, the observations still require surface frost albedos in the south to be higher than those in the north for almost every combination of input parameters as long as τ is less than 1.0. This last condition is guaranteed by the Viking orbiter images of the study regions during these seasons.

9. Discussion

It appears then that the contrasting behavior of CO_2 frost at the north and south poles of Mars during the Viking year can be attributed almost entirely to spring season frost albedos being approximately 25% lower in the north than in the south. Experience from terrestrial snow and water ice studies has shown that albedo variations of this magnitude can arise from variations in frost

Table 2-1

		Model Input Parameters				
		ϖ_0	g	ε_s	F_{Horiz} (Wm^{-2})	f
Set 1	min	0.84	0.69	0.90	0	0.5
	max	0.88	0.89	1.0	4.0	0.6
Set 2	min	0.4	0.4	0.65	-2.0	0.45
	max	0.99	0.99	1.00	8.0	0.70

Table 2-1. Two sets of constraints on the remaining model input parameters used in Fig. 2-9.

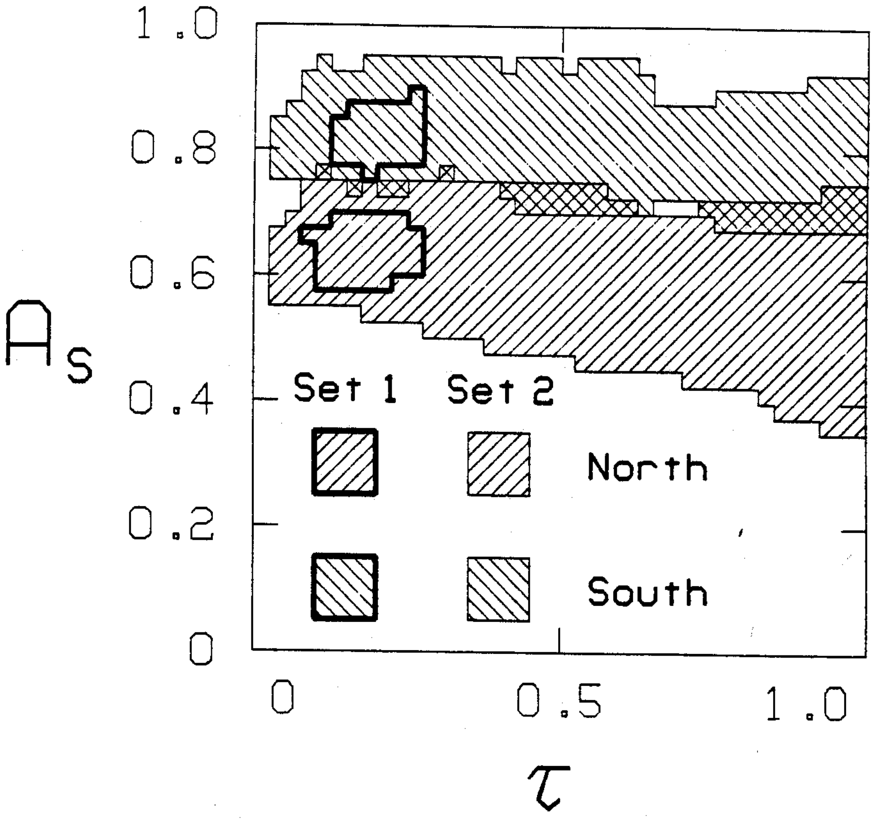

Fig. 2-9. Inferred surface albedos and aerosol opacities for the north study region at Julian date 3595 (L_s = 65.4) and for the south study region at Julian date 3265 (L_s = 251.6) for all combinations of two sets of model input parameters.

microphysical properties such as grain size and from variations in the concentrations of absorbing contaminants such as dust *(29)*. In view of the extreme sensitivity of pure frost reflectivities to the addition of minute quantities of absorbing materials *(30)* and the ready supply of dust in the Martian atmosphere, preferential dust contamination of the seasonal frost deposits that overlie the north residual cap seems a very likely explanation for the behavior and properties that have been documented in this study.

If dust contamination is responsible for the low reflectivities of the seasonal frost deposits at the north pole, then it will be important to establish whether they are contaminated primarily during global dust storms in the fall and winter or during local dust storms at the cap edge in early spring *(31)*. If global dust storms are primarily responsible, then the north permanent cap should become exposed much later in the season during years in which no global dust storms occur.

In the south, the very high surface frost albedos derived in the last section suggest that seasonal frost deposits within the south study region contained *no* significant quantities of dust during late spring despite the occurrence of a major global dust storm earlier in the season. In addition, the results in Figs. 2-4b and 2-4d suggest that south study region surface albedos continued to be high even during the second global dust storm of 1977 as evidenced by the sharp rebound in planetary albedos and the continued low surface CO_2 sublimation rates after the initial intense phase of the storm. Understanding exactly how the seasonal frost deposits at the south residual cap are able to maintain their high reflectivities through the dusty spring and summer seasons could be very important since the vapor pressures of these deposits could well be determining the present mass of the Martian atmosphere.

The Viking results have made it clear that the annual heat balance at the Martian poles is not a purely local phenomenon, but may be strongly influenced by the complex, global scale geologic and atmospheric processes that bring dust to the polar regions each year. In 1991, the Mars Geochemistry-Climatology Observer (MGCO) is scheduled to arrive at Mars, enter into a low polar orbit and begin surveying its surface, atmosphere and magnetosphere for one Mars year. By better defining the global circulation of dust in the Martian atmosphere, the surface topography of the Martian polar regions and the behavior and properties of Martian CO_2 frosts on the surface and in the atmosphere, MGCO could provide a new and more detailed understanding of the Martian polar caps and their relation to the Martian climate.

10. Conclusions

The major conclusions of this chapter can be summarized as follows:

1. An analysis of detailed heat balance measurements provides further evidence that solid CO_2 was present on the south residual polar cap throughout the year of Viking observations.

2. The observed absence of CO_2 frost at the north pole during the summer season was primarily due to enhanced springtime sublimation rates.

3. Spring season CO_2 sublimation rates at the poles are primarily determined by the reflectivities of the seasonal frost deposits, with the radiative effects of atmospheric aerosols being of secondary importance.

4. Mid-spring surface reflectivities of seasonal frost deposits at the south residual cap were approximately 0.82 while the reflectivities of seasonal frost deposits at the north residual cap at the same season were approximately 0.65. This difference can account for the asymmetry.

References

1. H. H. Kieffer, S. C. Chase, E. D. Miner, F. D. Palluconi, *Science* **194** , 1341 (1976).

2. C. B. Farmer, D. W. Davies, D. D. La Porte, *ibid.* pp. 1339.

3. H. H. Kieffer, *J. Geophys. Res.* **84**, 4249 (1976).

4. P. B. James, G. Briggs, J. Barnes, A. Spruck, *ibid.* **84**, 2889, (1979).

5. R. B. Leighton and B. C. Murray, *Science* **153**, 136, (1966).

6.F. P. Fanale, F. R. Salvail, W. B. Banerdt, S. Saunders, *Icarus* **50**, 381 (1982).

7. O. B. Toon, J. B. Pollack, W. Ward, J. A. Burns, K. Bilski, *Icarus* **44** , 552 (1980).

8. Kieffer *et al.* [*J. Geophys. Res.***82**, 4249 (1977), Chase *et al. Appl. Opt.* **17**, 1243 (1978).

9. C. W. Snyder, *J. Geophys. Res.* **82**, 3971 (1977), C. W. Snyder, *J. Geophys. Res.* **84**, 7917 (1979),

10. I. Dirmhirn and F. D. Eaton, *J. Appl. Meteor.* **14**, 275 (1975).

11. J. T. Houghton, *The Physics of Atmospheres* (Cambridge University Press, Cambridge, 1977), pp. 20-22.

12. C. B. Leovy and Y. Mintz, *J. Atmos. Sci.* **26**, 1167 (1969).

13. J. B. Pollack, C. B. Leovy, P. W. Greiman, Y. Mintz, *ibid.* **38**, 3 (1981).

14.P. J. Thomas, J. Veverka, R. Campos-Marquetti, *J. Geophys. Res.* **84**, 4621 (1979).

15. G. F. Lindal, H. B. Holtz, D. N. Sweetnam, Z. Shippony, J. P. Brenkle, G. V. Hartsell, R. T. Spear, W. H. Michael, *J. Geophys. Res.* **84**, 8443 (1979).

16. Year-long atmospheric pressure records from the Viking landing sites are presented by C. W. Snyder [*J. Geophys. Res.* **84**, 8487 (1979)].

17. F. P. Fanale, J. R. Salvail, W. B. Banerdt and R. S. Saunders, *Icarus* **50**, 381 (1982).

18. S. L. Miller and W. D. Smythe, *Science* **170**, 531 (1970).

19. A. Dobrovolskis and A. P. Ingersoll, *Icarus* **26**, 353 (1975).

20. B. C. Murray and M. C. Malin, *Science* **182**, 437 (1973).

21. D. W. Davies and L. A. Wainio, *J. Geophys. Res.* **84** 216 (1979).

22. R. W. Ward, B. C. Murray M. C. Malin, *J. Geophys. Res.* **79**, 3187 (1974).

23.T. Z. Martin and H. H. Kieffer, *J. Geophys. Res.* **84**, 2843 (1979).

24. H. H. Kieffer and F. D. Palluconi, Abstracts from The Second International Colloquioum on MARS, NASA Conference Publication 2072 (1979)

25. D. W. Davies, *J. Geophys. Res.***84**, 8,289 (1979).

26. H. J. Joseph, W. J. Wiscomb and J. A. Weinman, *J. Atmos. Sci.* **33**, 2452 (1976).

27. J. B. Pollack, D. S. Colburn, F. M. Flasar, R. Kahn, C. E. Carlston, D. Pidek, *J. Geophys. Res.* **84**, 2,929 (1979).

28. J. A. Cutts, K. R. Blausius, J. Roberts, *J. Geophys. Res.* **84**, 2,9755 (1979).

29. S. G. Warren and W. J. Wiscomb, *J. Atmos. Sci.* **37**, 2734 (1980).

30. R. N. Clark, *Icarus* **49**, 244 (1982).

31. R. W. Zurek, *Icarus* **50**, 288 (1982).

CHAPTER 3

AN ANALYSIS OF IRTM POLAR NIGHT OBSERVATIONS

1. Introduction

During the fall and winter seasons, the Martian polar regions are shrouded in continual darkness. The IRTM instruments aboard the Viking orbiters were the first to observe the polar regions during the polar night and almost all that is known about the behavior of the polar regions during these seasons has come from these observations.

The first glimpse of the south polar area by IRTM during mid-winter turned out to be a shock. Measured brightness temperatures in the 20 μ channel showed considerable structure poleward of $-70°$ latitude, with minimum brightness temperatures of 134 K or less at the pole (Kieffer et al., 1976). Figure 3-1 shows an IRTM 20 μ channel brightness temperature map of the south polar region from the original paper. These brightness temperatures are considerably lower than 147.7 K, the expected physical temperature of surface CO_2 frost in solid-vapor equilibrium with an atmosphere with a surface CO_2 partial pressure of 6.1 mb as predicted by the Leighton and Murray model (1966). In the "discovery" paper, Kieffer et al. defended the accuracy of these observations and listed several mechanisms that could be invoked to explain them. These included low surface emissivity, the presence of high altitude clouds or depressed solid-vapor equilibrium CO_2 frost kinetic temperatures due to reduced atmospheric CO_2 partial pressures at the surface. This latter effect could be caused by high surface elevations, dynamic meteorological phenomenon, or reduced CO_2 mixing ratios over the condensing cap.

In a later paper, Kieffer et al. (1977) examined the unexpectedly low brightness temperatures in greater detail. Newly processed mid-winter

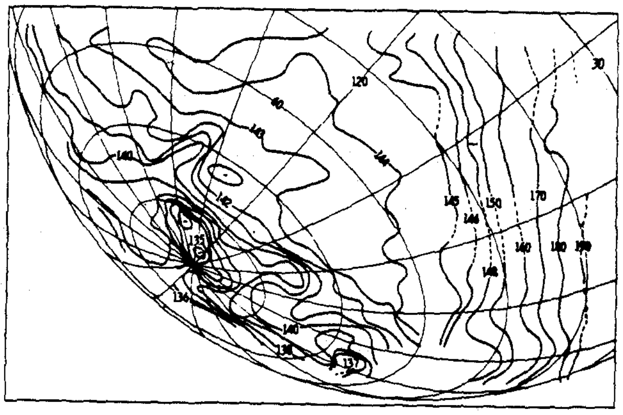

Fig. 3-1. A perspective view of IRTM 20 μ channel mid winter south polar brightness temperatures during the polar night from the original paper (Kieffer et al., 1976). Contour intervals are 1 K below 145 K and 10 K above 150 K. Latitude lines are spaced by 10°.

brightness temperature maps gave fragmented evidence that the positions and intensities of some of the lowest of the low brightness temperature regions were not constant. This led Kieffer et al. to suggest that the unexpectedly low brightness temperatures were due to a combination of causes. They proposed that the low spatial frequency, non-time-varying components of the brightness temperatures were due to surface effects such as low frost emissivity or topography, whereas the high spatial frequency time-varying components of the brightness temperatures were due to atmospheric effects. In this second paper, they strongly favored the hypothesis that the lowest of the low brightness temperature regions were caused by the local depletion of near surface atmospheric CO_2 and enrichment of near surface atmospheric layers in lighter non-condensable species. Hess (1979) cast some doubt on the feasibility of this explanation by showing that vertical and horizontal gradients in the average molecular weight of the Martian polar atmosphere could only be stable under special circumstances.

In 1979, Ditteon and Kieffer (1979) published infrared transmission spectra of thick solid CO_2 samples grown in the laboratory. They showed that in wavelength regions away from strong CO_2 absorption features, the transmissivity of their samples was quite high, and concluded that both components of the IRTM low brightness temperature observations in the south polar night could be explained entirely by low surface frost emissivity. Warren and Wiscomb (1981) have used Ditteon and Kieffer's laboratory data in conjunction with scattering models to show that the spectral emissivities of Martian CO_2 frosts could take on almost any value from 0 to 1 depending on CO_2 grain size, dust and water ice content, or viewing angle.

Hunt (1980) has shown that the low polar night brightness temperatures could also be explained by the radiative effects of CO_2 clouds. Scattering calculations based on the laboratory data of Ditteon and Kieffer show that the single scattering albedos of solid CO_2 spheres with radii of 1 or 10 μ are near unity in the wavelength regions defined by the IRTM surface sensing channels (Hunt et al., 1980). CO_2 clouds composed of conservatively scattering particles can significantly reduce upward radiative fluxes at the top of the Martian atmosphere during the polar night by redirecting photons emitted by the surface back down to the surface where they will ultimately be absorbed. Hunt showed that brightness temperatures at the top of the atmosphere at $\lambda = 20\ \mu$ could be significantly lowered by the presence of CO_2 clouds of only modest optical thickness. Figure 3-2 shows some of the results of his calculations. Since CO_2 cloud particles emit almost no radiation themselves, Hunt's basic results are insensitive to their assumed altitudes or temperatures. In his paper, Hunt argued that CO_2 clouds were most likely to be present at high altitudes during the polar night.

Although the analyses performed to date have eliminated some of the possibilities, much disagreement remains as to the true cause(s) of the low brightness temperatures observed by IRTM during the polar night. Understanding this phenomena is of importance because its net effect is to reduce the net rates of CO_2 condensation during the polar night (Kieffer et al 1976, Chapter 2).

Another interesting polar night phenomena observed by IRTM was an extremely rapid rise in measured 15 μ channel brightness temperatures at the north pole during the initial phase of the second global dust storm of 1977 (Martin and Kieffer, 1979). The dynamical heat transport processes that must be responsible for this behavior are not well understood. Martin and Kieffer show that the radiative effects of elevated atmospheric temperatures during this season could significantly retard the rate of CO_2 condensation at the

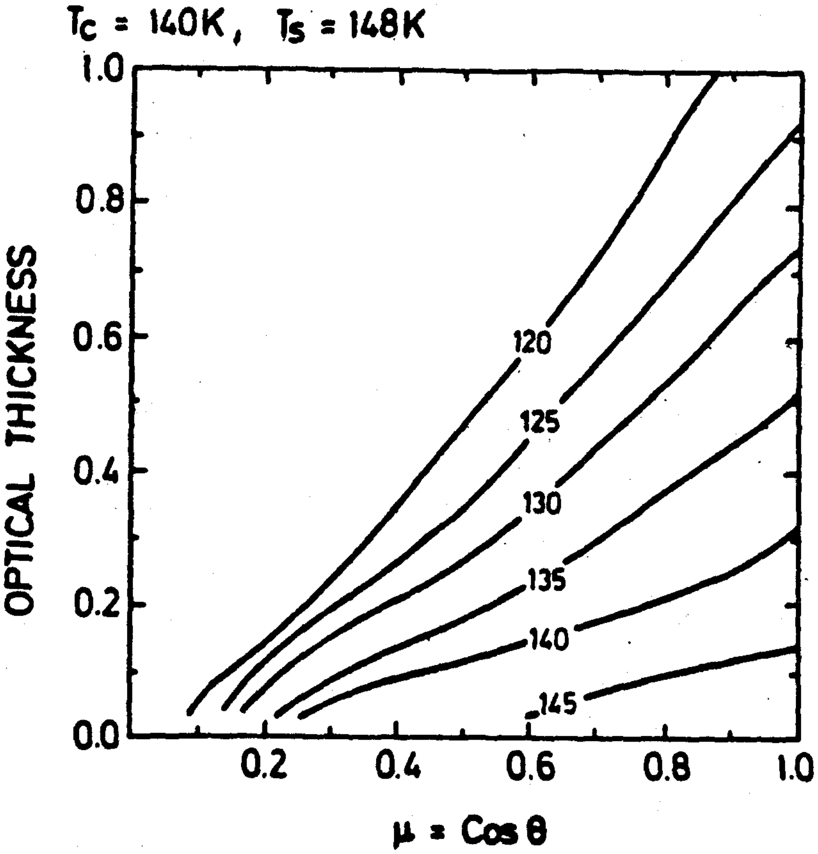

Fig. 3-2. Calculated effects of CO_2 clouds composed of particles of 10 μ radius on brightness temperatures at the top of the atmosphere at $\lambda = 20\ \mu$ from Hunt (1980). μ is the cosine of the emission angle, optical depth refers to optical depth at $\lambda = 20\ \mu$. T_S and T_c are the assumed surface and cloud temperatures.

surface.

One unanswered question associated with the IRTM polar night observations in the north is whether or not significant quantities of dust are transported to and deposited within the accumulating north seasonal polar cap during global dust storms as suggested by Kieffer and Palluconi (1979) and Pollack et al. (1979). This question is of obvious significance when considering the current asymmetric behavior of CO_2 frost at the poles (see Chapters 1 and 2); but it may also be important for understanding Mars' past geologic and climatologic history. Layered deposits within the residual polar caps have long been interpreted as evidence for variations in the rates of deposition of water ice and dust at the poles triggered by large amplitude variations in Mars' orbital elements (Ward, 1974; Carr, 1982). Pollack et al. (1979) have adopted the view that layer formation in the north is an ongoing, contemporaneous process. Jakosky (1983b), on the other hand, has argued that significant quantities of dust and water do not reach the north residual cap during global dust storms and that the net annual flux of water on Mars is southward toward the cold finger at the south residual cap. There must be a famous quote somewhere about the tendency for disagreement concerning things that can't be seen.

This chapter presents an analysis of the IRTM observations of the north and south residual caps during the polar night seasons. The principal data employed here are the same 10-day averaged brightness temperatures used to determine annual radiation budgets for the north and south study regions in Chapter 2. These data form a convenient time history of the behavior of the important residual cap areas during the Viking year. IRTM polar night data from lower polar latitudes are employed to illustrate certain points, but the main goal of this work is to explain the observations at the locations of the north and south residual caps. What emerges is a fairly cohesive picture of the properties of the surface and atmosphere at the poles during the polar night seasons.

2. Coincident Brightness Temperatures

One aspect of the IRTM polar night observations that has not received much attention (except in Chapter 2) is the tendency for T_{11}, T_{15} and T_{20} to be nearly coincident during the early fall and late winter seasons. This behavior is demonstrated in Figures 3-3a,b, which show 10-day averaged brightness temperatures in the IRTM channels for emission angles $\vartheta < 60°$ for the north and south study regions. Periods with coincident brightness temperatures are highlighted with vertical arrows. The figures show that the only periods in which T_{11} equaled T_{20} were during the summer season in the north when the residual water ice cap was exposed, and during the early fall and late winter seasons at both poles where T_{11} and T_{20} also tended to equal T_{15}. I will now argue that the coincident brightness temperatures during the early fall and late winter seasons are due to the high spectral emissivities of Martian seasonal CO_2 frosts.

First, during the early fall and late winter seasons, the polar atmosphere is at nearly the same temperature as the surface. Figures 3-3a,b show that T_{15}, which measures atmospheric temperatures over a wide range of altitudes near the 0.6 mbar pressure level, is always close to the expected physical temperatures of surface CO_2 frost deposits whenever coincident brightness temperatures are observed. Since the results of Chapter 2 show that seasonal CO_2 frost is always accumulating within the study regions when the coincident brightness temperatures are observed, temperature contrasts between surface and atmosphere during these seasons are small.

Second, when thermal contrasts between surface and atmosphere are small, measured brightness temperatures at the top of the atmosphere in the 11 and 20 μ channels are much more sensitive to the spectral emissivity properties

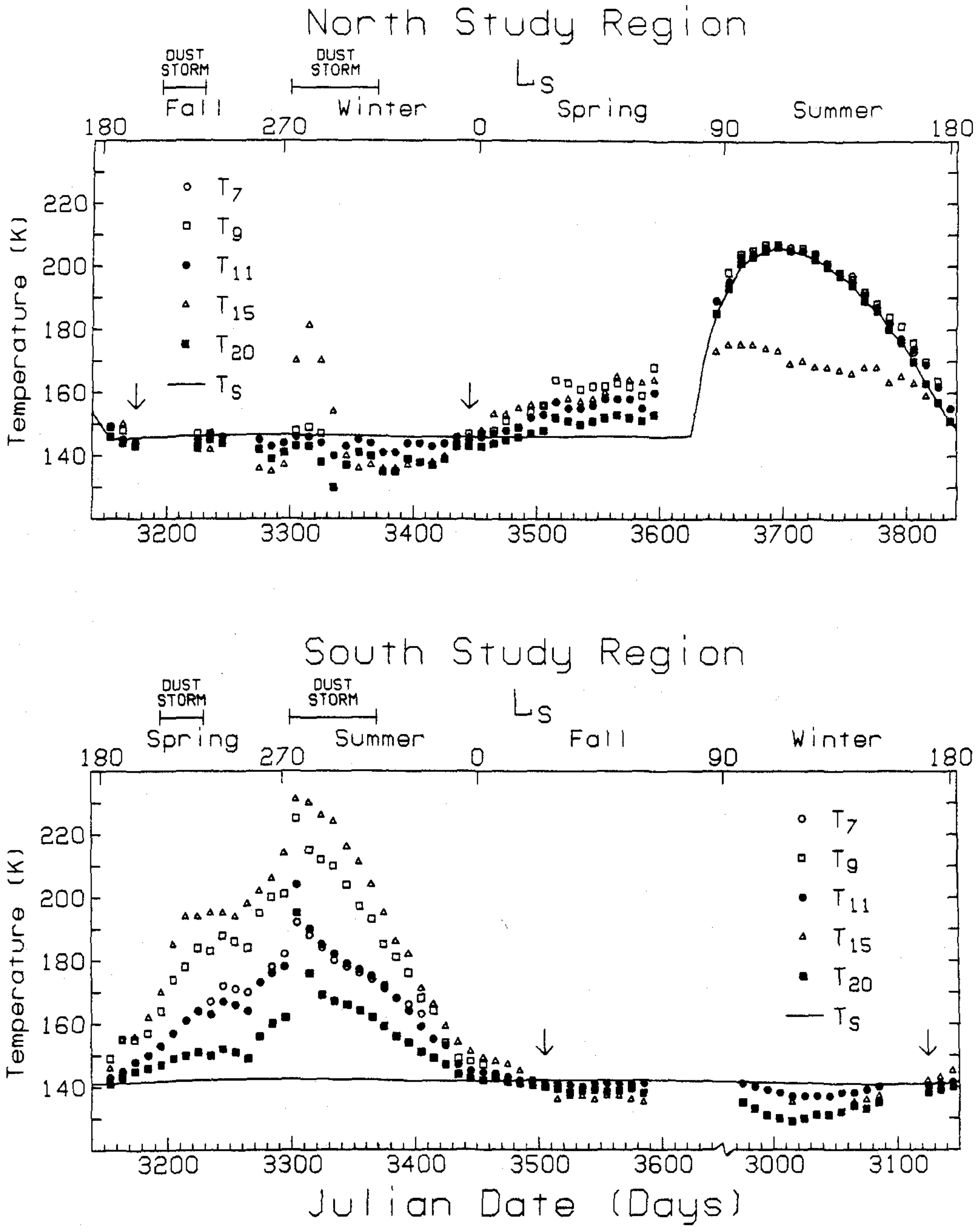

Fig. 3-3. IRTM brightness temperatures and inferred surface temperatures for the north (A) and south (B) study regions. The arrows denote coincident brightness temperatures during the early fall and late winter seasons.

of the surface than to the presence of absorbing aerosols in the atmosphere. This is demonstrated in Figure 3-4, which shows calculated values of T_{11} and T_{20} at the top of a single layer isothermal atmosphere using the δ-Eddington approximation (see Appendix 2). In these calculations, the surface physical temperature, T_s, and the atmospheric temperature, T_A, were both assumed to equal 144.7 K. Similar results were obtained using infrared optical properties for basalt and water ice spheres.

Third, the fact that T_{11} and T_{20} converge to nearly the same values is most easily explained by spectral emissivities of near unity at these wavelengths. The brightness temperatures of greybody emitters (emitters with constant spectral emissivity with wavelength) change with wavelength. This is demonstrated in the clear atmospheric case in Figure 3-4. Greybodies that give the same measured brightness temperatures over a wide range of wavelengths are therefore blackbodies. If the seasonal frost deposits are not good blackbodies during these seasons, then their spectral emissivities near $\lambda = 11$ and $\lambda = 20\ \mu$ must assume special combinations of values. Figure 3-5 shows the combinations of Planck weighted emissivities in the IRTM 11 and 20 μ channels that yield coincident brightness temperatures for surface physical temperatures ranging from 135 to 151 K under clear atmospheric conditions. This argument could be even stronger had brightness temperatures in the 7 and 9 μ channels not been below their noise-limiting thresholds during these seasons.

The last argument for high surface frost emissivities is that T_{11} and T_{20} are quite reasonable if interpreted as true surface temperatures during these seasons. If the possible effects of near surface CO_2 depletion and atmospheric pressure variations due to dynamical motions are ignored, then the temperatures of CO_2 frost deposits should be related to their aeropotential

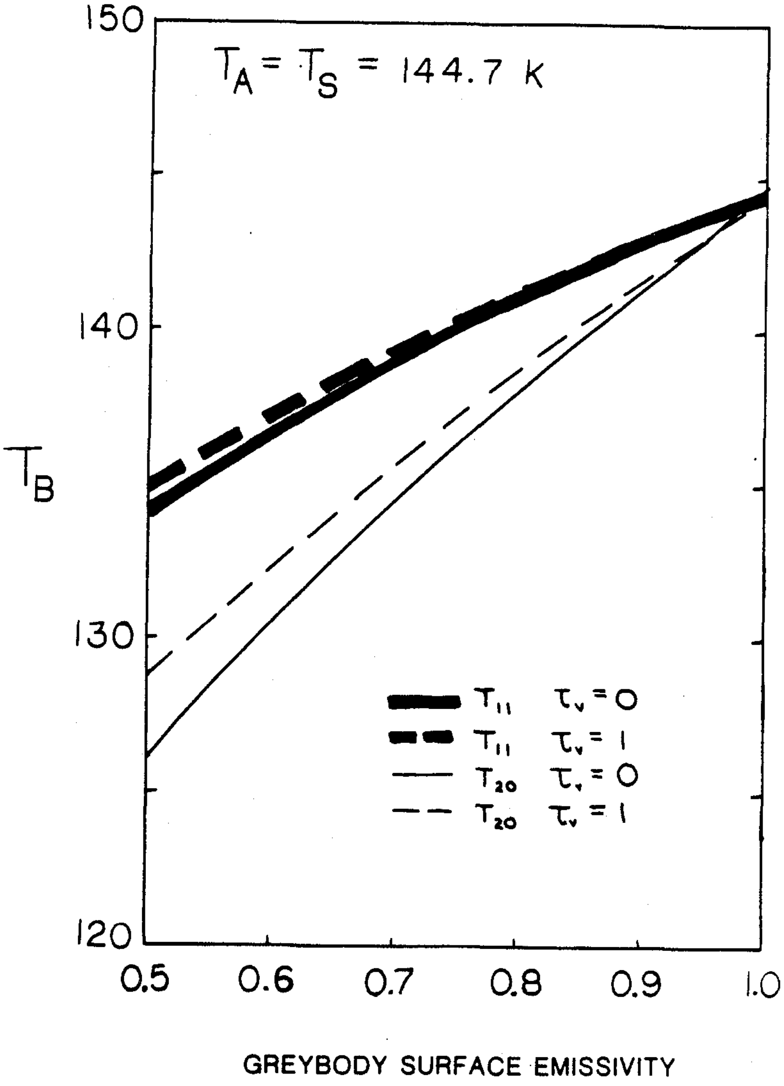

Fig. 3-4. Calculated effects of surface emissivity variations on early fall or late winter IRTM 11 and 20 μ channel brightness temperatures at the top of the atmosphere for clear and dusty atmospheric conditions. Greybody surface emissivities and surface temperatures of 144.7 K were assumed in both cases. The $\tau_v = 1$ case assumed montmorillonite 219b dust (size distribution 1) at the same temperature as the surface.

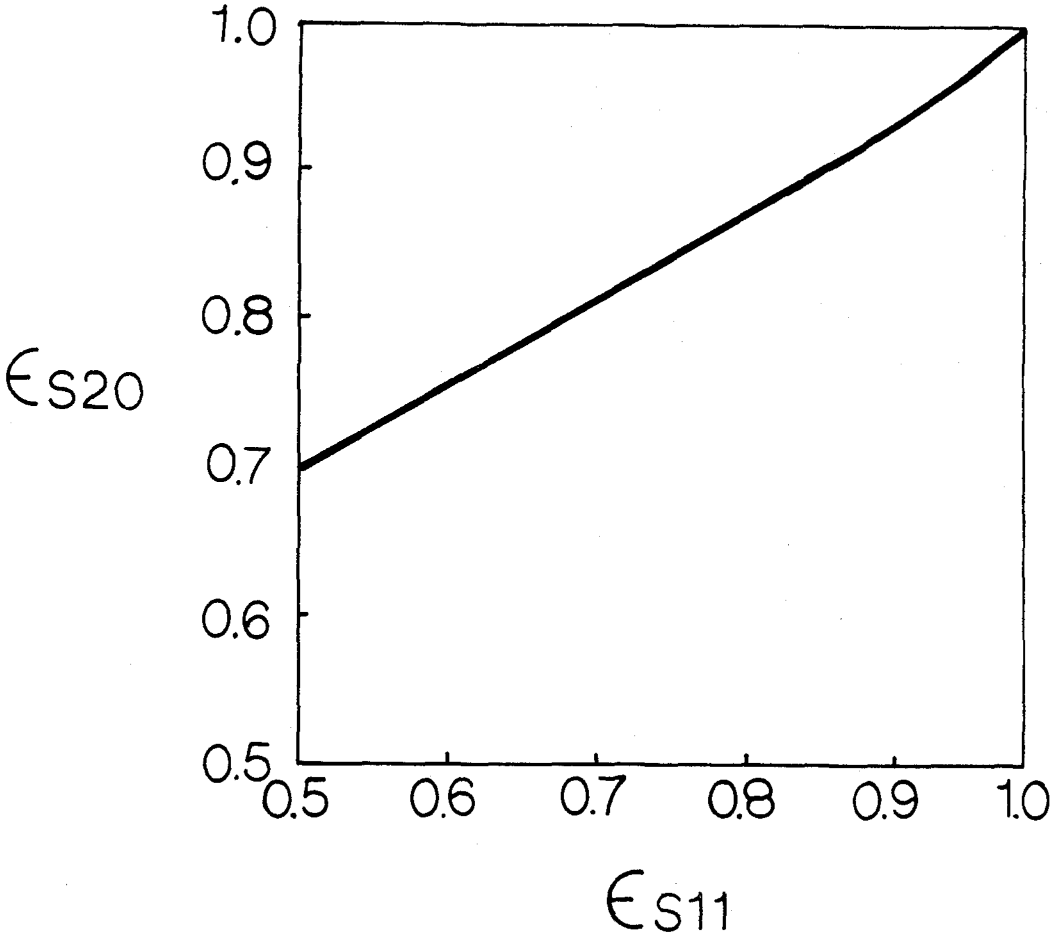

Fig. 3-5. Combinations of Planck weighted spectral emissivities in the IRTM 11 and 20 μ channels that will give coincident brightness temperatures in these channels under clear atmospheric conditions for surface temperatures ranging from 135 to 150 K.

(geopotential) altitudes since they are in solid-vapor equilibrium with CO_2 gas in the Martian atmosphere. Using T_s = 146 ± 1 K for the north study region at Julian date 3430 (L_s = 348.6) and T_s = 142 ± 1 K for the south study region at Julian date 3490 (L_s = 18.2) gives altitudes of +2.5 ± 2 km in the north and +8 ± 2 km in the south relative to the 6.1 mbar reference aeroid assuming a hydrostatic atmosphere of 95% CO_2 with a scale height of 9 km. The accuracy of these inferred elevations can not be determined because the absolute elevations of the north and south residual caps have not been measured. Murray and Malin (1973) present Mars radii in the polar regions derived from Mariner 9 radio occultation profiles (Kliore et al., 1973) which indicate that both polar regions are above the 6.1 mbar level, with the south polar area being higher. These data are reproduced in Fig. 3-6. To this extent, the derived elevations are quite consistent with what is currently known. Another observation that supports this interpretation is that T_{11}, T_{15}, and T_{20} converge to approximately the same values during late winter as they did during early fall at each pole. Figures 3-3ab show expected year-long surface temperatures for the study regions assuming CO_2 partial surface pressures are proportional to the seasonally varying surface pressures at the Viking 1 landing site due to the global condensation and sublimation of seasonal CO_2 frost.

The fact that the emissivities of Martian seasonal frost deposits are high at $\lambda = 11$ and $\lambda = 20$ μ during some seasons is not too surprising. Warren and Wiscomb (1981) have shown that the spectral emissivities of pure CO_2 frost deposits at these wavelengths can be significantly increased by the addition of small quantities of absorbing contaminants such as water ice and dust. It is also quite likely that the microphysical properties of real Martian frosts are not at all like those of Ditteon and Kieffer's lab samples. Further theoretical and experimental work in this area should definitely be encouraged.

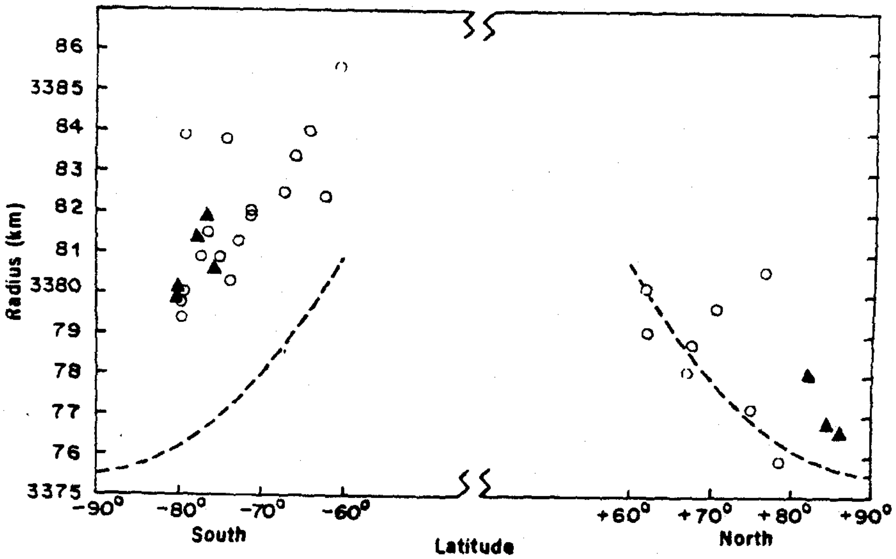

Fig. 3-6. Mars radii in the polar regions derived from Mariner 9 radio occultation data (Kliore et al., 1973) and the best fit tri-axial ellipsoid for the figure of Mars (from Murray and Malin, 1973).

If seasonal CO_2 frost emissivities are also near unity in regions away from the residual polar caps, then the IRTM polar night observations may be a new source of topographic information. On revolutions 490 and 497, the IRTM aboard Viking Orbiter 2 obtained high quality brightness temperature maps of the south polar area. A map of 20 μ channel brightness temperatures obtained on revolution 479 (Julian date = 3505, L_s = 25.6) is shown in Figure 3-7. The data shown in this map were binned on a rectilinear grid with pixel dimensions of 2° of latitude and then machine contoured. Each bin contained roughly 10 individual brightness temperature observations, so higher spatial resolution may be possible with future processing. Within the area shown, the difference between T_{11} and T_{20} within each boresighted field of view was typically 0 to 1 K and did not exceed 2.5 K at any point on the map. A simultaneously acquired map of T_{15} shows symmetric circular contours about the pole, with brightness temperatures of 150K at -73° latitude and 139K at the pole. Maps acquired 7 days earlier on revolution 490 agree with Fig 3-7 to within 1K in the region poleward of -75° latitude.

The spatial variations in 11 and 20 μ channel brightness temperatures observed during this season are very difficult to explain by spatial variations in surface emissivity. The 20 μ brightness temperatures in Figure 3-7 span a wide range. If one were to assume that the true physical temperature of the frost was 146 K at all points, then the fact that T_{11} equals T_{20} at all locations on the map would require that the spectral emissivities of the frost deposits at $\lambda = 20\ \mu$ and $\lambda = 11\ \mu$ vary with latitude and longitude in a well-defined, systematic fashion. The required variation is shown in Figure 3-8. This idea is clearly nonsense — the surface emissivities are high!

Figure 3-9 shows inferred surface aeropotential altitudes for the region south of −80° latitude derived from the data in Figure 3-7 using the formula

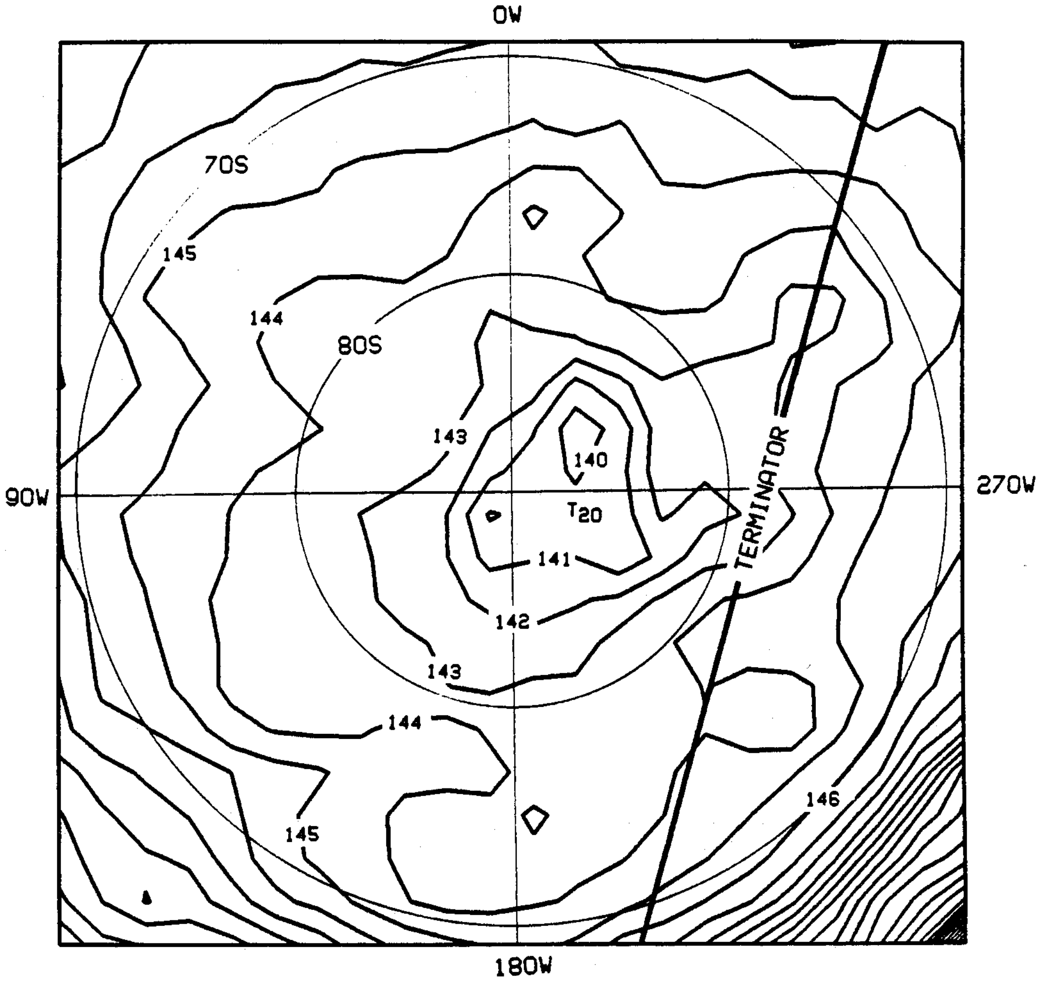

Fig. 3-7. An early fall season IRTM 20 μ channel brightness temperature map of the south polar region from data obtained on Viking Orbiter 2 revolution 479. The contour interval is 1 K. The terminater is also shown.

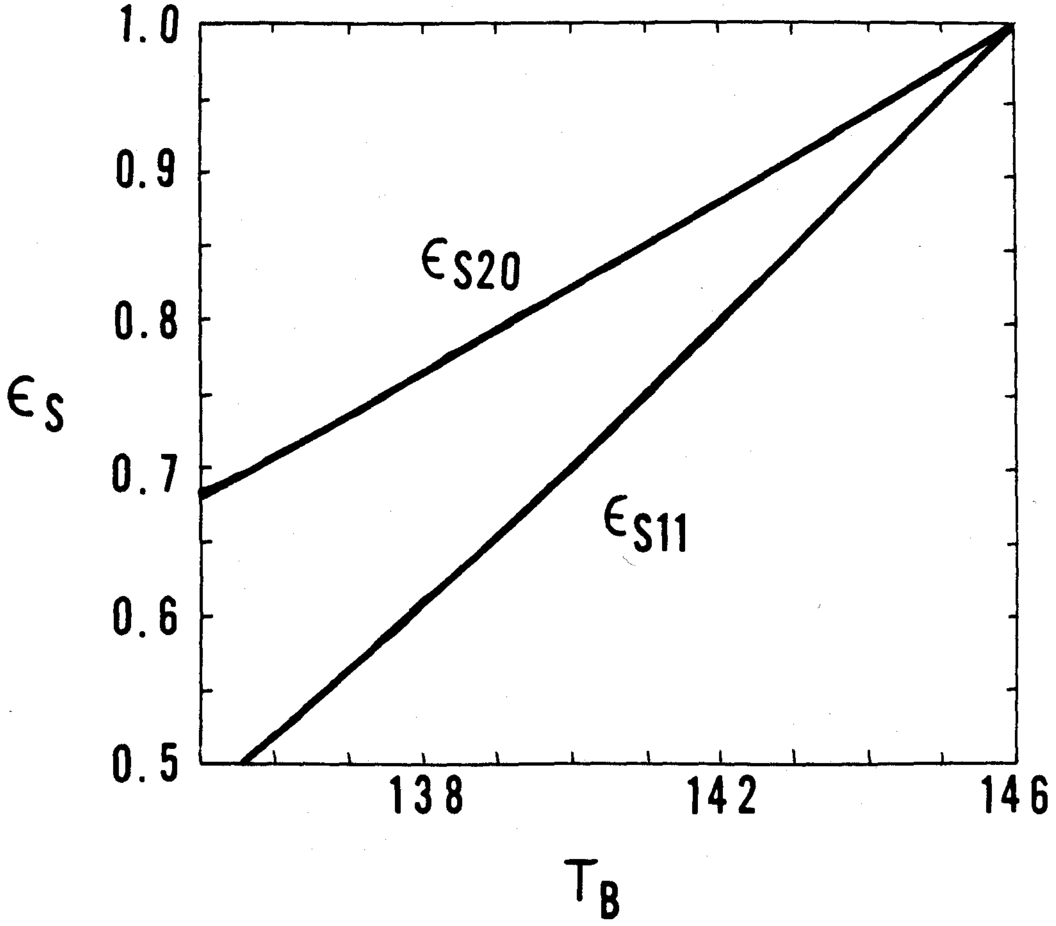

Fig. 3-8. Combinations of Planck weighted spectral emissivities of frost deposits at physical temperatures of 146 K that are required to give coincident brightness temperatures T_B in the IRTM 11 and 20 μ channels under clear atmospheric conditions.

$$A = -H\ln\left[\frac{P_{CO_2}(T_{20})}{f_{CO_2}6.1\mathrm{mb}}\right] \tag{3.1}$$

where H is the assumed atmospheric scale height of 7 km, f_{CO_2} is the assumed CO_2 mixing ratio of 0.95, $P_{CO_2}(T)$ is the equilibrium vapor pressure of solid CO_2 at temperature T, which is assumed to equal to T_{20}. Machine contours overlay a Mariner 9 shaded relief map of the south polar region. Because of the assumptions built into equation 3.1, the inferred elevations are not likely to be accurate in an absolute sense. The sense of curvature of the slopes may also be suspect.

The contours reveal a broad three-sided plateau area centered off the geographic pole. The plateau has a maximum elevation of 5 to 6 km above the surrounding terrain. The south residual cap lies on the slope of the plateau that is nearest to the pole. Unfrosted valleys within the south residual cap, and most every other valley in the plateau region show a strong tendency to run downhill, perpendicular to the contours. Although future exploration of Mars may eventually prove otherwise, this map can not be considered a joke at present.

A longstanding question is why the Martian south residual cap is offset from the geographical pole. One explanation that has been put forward is that the residual cap area may be tilted down towards the pole in such a way as to make its normal vector parallel with the spin axis. This would allow it to receive the minimum possible total annual insolation (Dzursin and Blasius, 1975). The results in Fig 3-9 suggest exactly the opposite. The potential importance of topography to the present stability of permanent CO_2 deposits at the south residual cap is demonstrated by observations of the retreating south seasonal polar cap. Fig. 3-10 shows a Viking Orbiter mosaic of the south polar area just

Fig. 3-9. Derived relative elevations in the south polar region using the brightness temperature data in Fig. 3-7 and equation (3.1). The contours are superposed on a 1:25 million scale Mariner 9 shaded relief map. The contour interval is 1 km.

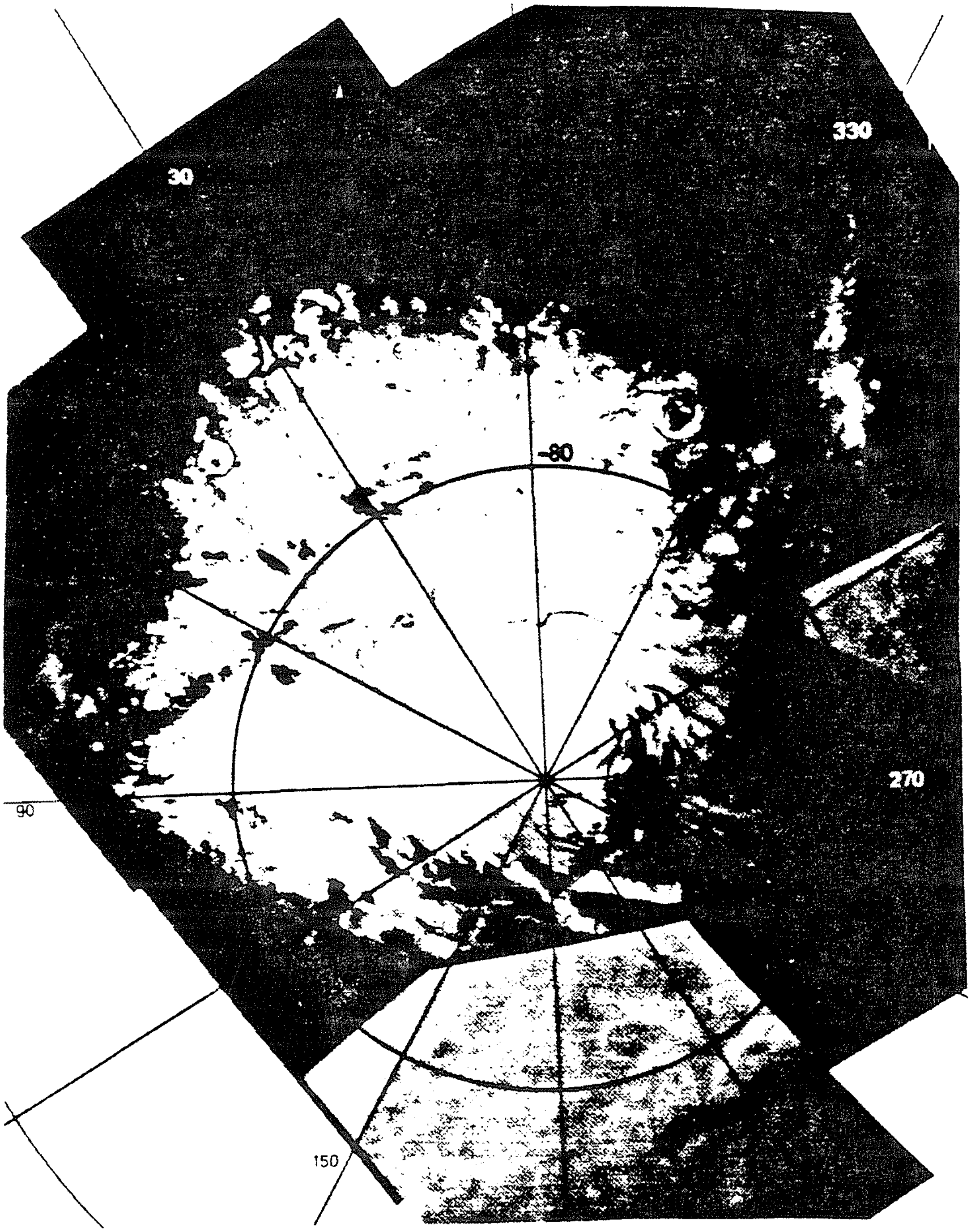

Fig. 3-10. A Viking Orbiter mosaic image of the retreating south seasonal cap obtained 5½ days before summer solstice (211-5615B) (reproduced from James et al., 1979).

before summer solstice (James et. al., 1979) The off-center boundaries of the seasonal cap during this season show that the highest regions of the plateau area and slopes that face away from the pole were not favorable locations for the persistence of seasonal frost during late spring. This could be an important clue to understanding the present stability of CO_2 deposits at the south residual cap.

Fig. 3-9 is very new, and the geologic implications of this new information have not been fully investigated. In further analyses, it will be important to examine the IRTM observations of coincident brightness temperatures during late winter in the south to make sure that the inferred topography did not change overnight. It will also be interesting to see if a similar analysis can be performed with the north polar data.

3. Low Brightness Temperatures

One aspect of the IRTM low brightness temperature observations during the polar night that does not favor the explanation that they are due to the dilution of near surface atmospheric CO_2 is that low 20 μ channel brightness temperatures are always accompanied by proportionately lower, but not identically lower 11 μ channel brightness temperatures. This effect is clearly evident in the brightness temperature histories of the north and south study regions in Figures 3-3a,b. This same effect is also seen in single brightness temperature maps of extended geographic regions. Figure 3-11 shows the correlation of T_{20} and $T_{11} - T_{20}$ for latitudes poleward of −80° latitude from a single IRTM brightness temperature map obtained during late southern fall by Viking Orbiter 2 on revolution 576 (Julian date = 3584, L_s = 61.0). Superimposed on these data are 10-day averages of the same quantities for the south study region during the entire polar night seasons taken from Figure 3-3b. This plot

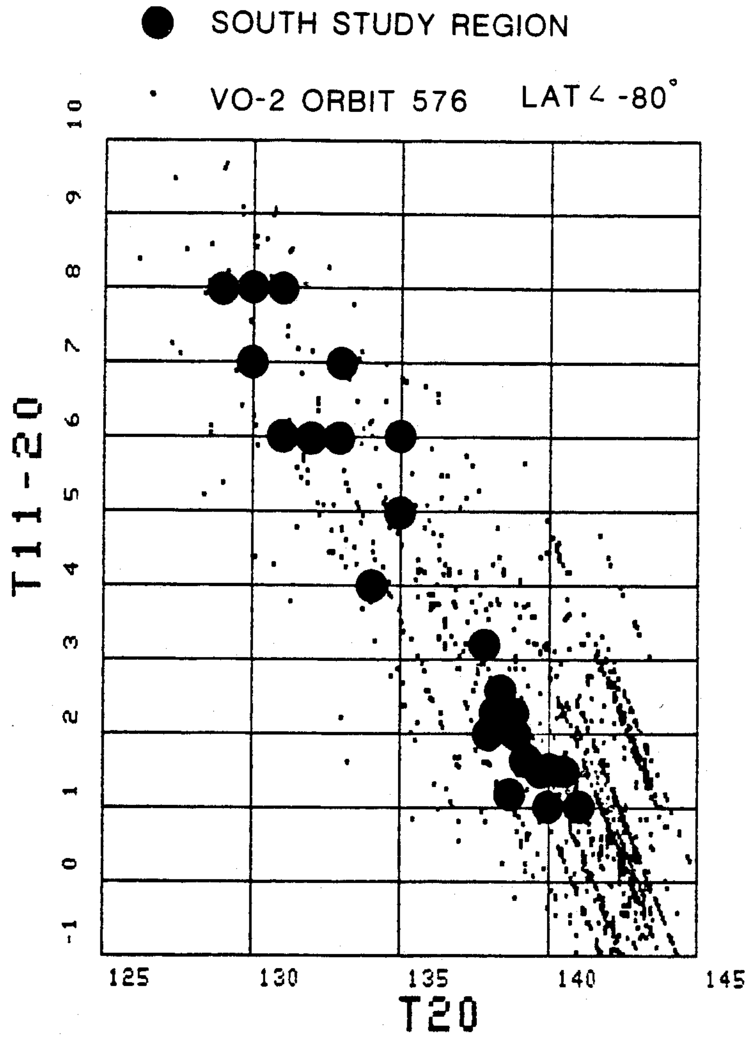

Fig. 3-11. Spatial and temporal correlations of T_{20} and $T_{11} - T_{20}$ in the south polar area during the polar night. The small squares correspond to single boresighted fields of view obtained during a single brightness temperature mapping sequence after mid fall. The large dots show the time history of correlations of these two quantities at the south study region during fall and winter from the data shown in Fig. 3-3b.

indicates that the spatial and temporal variations in these quantities share the same cause. One could argue that this effect could be attributed to a gross relative miscalibration of IRTM 11 and 20 μ channel brightness temperatures for fluxes below a certain threshold value. This is unlikely for two reasons. First, brightness temperature maps obtained by Viking Orbiter 1 show similar effects (Kieffer et al., 1976). Second, the divergence between T_{11} and T_{20} begins at $T_{20} \approx 145$ K in the north study region and $T_{20} \approx 141$ K in the south study region (see Figs. 3-3a,b). Also, the data in Figure 3-10 argue against temporal variations in the calibration of the IRTM aboard Viking Orbiter 2.

This leaves two possibilities; the low brightness temperatures are due to spatial and temporal variations in the surface emissivities of seasonal frosts or to spatial and temporal variations in the occurrence and properties of clouds. These two hypotheses are rather similar in that they both rely on the fact that solid CO_2 can be relatively transparent at infrared wavelengths, and it is difficult to differentiate between them on the basis of the numerical values of the brightness temperatures alone. I will now argue that the spatial and temporal variations of the IRTM brightness temperatures point to CO_2 clouds.

The possibility that CO_2 could condense in the Martian atmosphere was first investigated by Gierasch and Goody (1968). The conditions for the onset of atmospheric condensation on Mars are simple: the temperature must be at the local CO_2 frost point. The 10-layer one-dimensional polar radiative model described in Appendix 2 is a valuable tool for predicting when and were atmospheric condensation is most likely to occur.

The purpose of the model is to simulate radiative and dynamic heating and cooling rates in the Martian polar atmosphere and to calculate vertical thermal equilibrium temperature profiles for an assumed set of surface and atmospheric properties. For polar night conditions, the model can simulate the heating effects of horizontal eddies and meridional circulations and the cooling effects of infrared emission by atmospheric aerosols and by CO_2 gas in the strong 15 μ band. Solar heating terms are not required. The model accounts for the small effects of thermal conduction between surface and atmosphere, but does not deal with dry convection or atmospheric CO_2 condensation itself. Since the Martian atmosphere naturally achieves a state of thermal equilibrium in less than 10 days during the polar night, model calculated IRTM brightness temperatures at the top of the atmosphere can be compared directly with the real data.

Figure 3-12 shows model calculated thermal equilibrium polar atmospheric temperature profiles and atmospheric CO_2 condensation temperatures. All calculations assume a CO_2 mixing ratio of 0.95, a surface pressure of 4.0 mb, a fixed surface temperature of 144.7 K, a surface emissivity of unity, and an initially isothermal atmosphere at 145 K.

Profile 1 was computed assuming no atmospheric aerosols and no atmospheric heating due to dynamical motions. This type of profile could not occur in the real Martian atmosphere because atmospheric condensation would prevent temperatures from falling below the local CO_2 frost point. Supersaturation with respect to CO_2 is highly unlikely on Mars since CO_2 is the dominant atmospheric constituent and condensation nuclei should not be in short supply. Unlike the other profiles, Profile 1 is not a true radiative equilibrium profile because of the total absence of atmospheric heating and the tendency for the equivalent width of the CO_2 15 μ band to decrease with decreasing temperature. The calculations were stopped after the equivalent of 40 days. The model input parameters for Profile 2 were the same as for Profile 1, except that the atmosphere was assumed to contain dust. Dust optical properties at infrared wavelengths were assumed to be those those inferred by

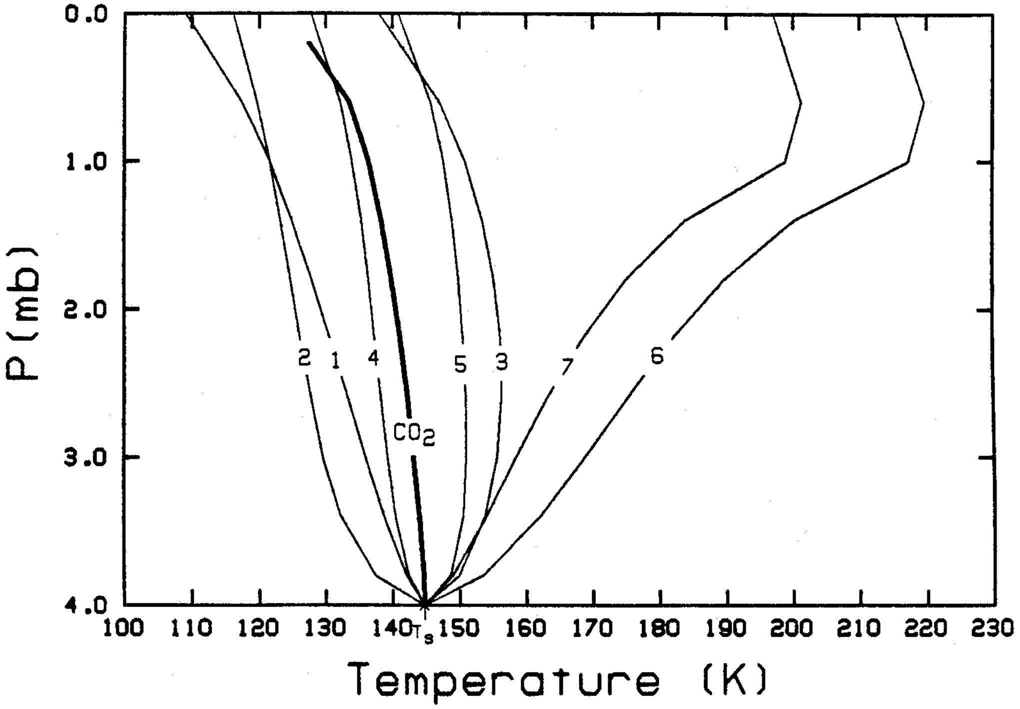

Fig. 3-12. Calculated thermal equilibrium temperature profiles for polar night conditions using the 10-layer model described in Appendix 2. CO_2 solid-vapor equilibrium temperatures are also shown. Seleced model input parameters and calculated IRTM brightness temperatures for these profiles are listed in Table 3-1.

Profile	τ_V	F_{Horiz}	T_9	T_{15}
1	0	0	-	-
2	1.0	-	-	-
3	0	2.3	-	145.8
4	0.5	2.3	-	-
5	0.5	6.5	-	145.0
6	0.3	40.0	167.1	214.0
7	0.2	20.0	155.0	196.6

Table 3-1. Model input parameters τ_V, the solar spectrum averaged dust opacity and F_{Horiz}, $(W m^{-2})$ the vertically integrated rate of atmospheric horizontal advective heating for the seven model calculated polar night atmospheric temperature profiles in Fig. 3-12. Where applicable, model calculated values of T_9 and T_{15} (K) at the top of the atmosphere for cos(ϑ) = 0.75 are also listed. For profiles 1 through 5, dust and advective heating were assumed to be distributed uniformly with pressure. For profiles 6 and 7, they were both assumed to be totally concentrated above the 1.2 mbar pressure level.

Toon, Pollack, and Sagan (1977) from Mariner 9 IRIS spectra (see Distribution 1 in Appendix 2). Dust optical depth is specified in terms of τ_V, the solar spectrum averaged optical depth. The ratios of dust optical depths at solar and infrared wavelengths are determined by Q_V, the solar spectrum averaged particle extinction efficiency. Following the recommendations of Pollack et al. (1979), Q_V was assumed to equal 2.74. This set of optical properties will be referred to as Toon-Pollack dust. Profile 2 assumes Toon-Pollack dust is uniformly distributed with pressure, with $\tau_V = 1.0$.

Profiles 1 and 2 are interesting because they show that Martian atmosphere will quickly begin to condense out during the polar night in the absence of horizontal advective heating from lower latitudes. Martian general circulation model results show that heat can be transported into the polar night by meridional circulation or by horizontal eddies (Leovy and Mintz, 1969; Pollack et al., 1981). The heating effects of horizontal eddies can be simulated in a one-dimensional model by allowing for net fluxes of energy through the "sides" of the atmospheric layers. The heating effects of meridional circulations be simulated by assuming fixed vertical velocities at each layer boundary (see Appendix 2). In Profile 3, the atmosphere was assumed to be free of aerosols, but the atmosphere was heated uniformly with pressure at a vertically integrated rate, F_{Horiz} of 2 Wm^{-2}. This profile is above the CO_2 frost point at all altitudes down to the surface and gives calculated IRTM 15 μ channel brightness temperatures at the top of the atmosphere that are very close to T_s. Similar results can be obtained by assuming zero eddy heating, but a sinusoidal sinking profile with zero downward velocity at $p = 0$ and $p = 4$ mb and maximum sinking velocity at $p = 2$ mb of 0.012 mb/hr. Either profile gives coincident brightness temperatures in the IRTM 11, 15, and 20 μ channels like those observed in the polar regions during early fall and late winter. The required horizontal advective heating rates provide further evidence that F_{Horiz} is a small positive quantity as assumed in Chapter 2.

Profile 4 demonstrates the effects of dust on atmospheric temperatures in the polar night. F_{Horiz} was assumed to be 2 Wm^{-2} as in Profile 3, but Toon-Pollack dust was assumed to be distributed uniformly with pressure with τ_V = 0.5. The marked cooling effect of the dust is easily understood: During the polar night, the atmosphere is in a state of thermal equilibrium. Thermal equilibrium temperature profiles during this season are determined by the competing effects of horizontal advective heating and infrared cooling. Since the addition of dust increases the efficiency with which the atmosphere can cool at infrared wavelengths, atmospheric temperatures must drop when dust is added if the rates of horizontal advective heating remain constant. A similar effect would be expected for the addition of other types of broad band infrared absorbers such as water ice clouds. Atmospheric temperatures were raised above the frost point in Profile 5 by raising F_{Horiz} to 6 Wm^{-2}.

The model calculations presented so far show that CO_2 clouds are most likely to form in places where horizontal advective heating rates are low or aerosol opacities are high. Although the current model is not set up to deal with what may happen after the onset of atmospheric condensation, it is still possible to make some general statements as to the expected behavior of CO_2 clouds once formed. Although the single scattering albedos of solid CO_2 spheres of radius 1 and 10 μ may be very high at wavelengths away from solid CO_2 absorption bands, it is probable that the total bolometric infrared absorptivity of an optically thick CO_2 cloud is at least that of the Martian polar atmosphere under clear atmospheric conditions. CO_2 clouds therefore not expected to dissipate simply because they are unable to radiate energy as efficiently as the surrounding atmosphere. Since CO_2 condensation temperatures are distinctly higher than pure radiative equilibrium temperatures in the polar night, energy conservation requires that the net outward radiative fluxes at the upper and lower boundaries of the clouds be balanced by the latent heat of condensing CO_2 within (Gierasch and Goody, 1968). This process will eventually lead to the production of CO_2 snow. Martian snow storms in the polar night should be very difficult to stop once they start because atmospheric temperatures cannot be raised above the CO_2 frost point until heating rates are high enough to halt CO_2 condensation. Since horizontal advection provides the only source of atmospheric heating in the polar night, CO_2 snow storms should persist until they happen into the sunlight.

The modeling results make it easy to explain the IRTM low brightness temperature observations presented thus far by the selective occurrence of CO_2 clouds. During the early fall seasons, the seasonal polar caps are just starting to grow. Polar atmospheric temperatures are maintained above the CO_2 frost point by relatively high rates of horizontal advective heating during these seasons due to the small diameters of the seasonal caps and the tendency for condensation winds to flow toward the poles (Kahn, 1984). By the start of the winter season, the seasonal polar caps have grown to the point where a broad expanse of nearly isothermal territory exists between the core regions of the seasonal caps and their peripheries. Radiative time constants in the polar atmosphere are short enough that warm air parcels starting out at the peripheries of the winter seasonal caps will radiate away much of their energies as they travel to the poles. This will cause near-polar atmospheric temperatures to be lower during winter than during fall, which favors the preferential occurrence of near-polar CO_2 clouds during mid-winter. The apparent tendency for south polar low temperature regions to vary in position and intensity (Kieffer et al., 1977) is quite consistent with the CO_2 cloud hypothesis as Hunt's results (1980) suggest that IRTM brightness temperatures at the top of the atmosphere are most likely to be affected by the optical properties of only the uppermost CO_2 cloud layers. The tendency of the low brightness temperature regions to persist is also well explained by the CO_2 cloud hypothesis. Figures 3-3a,b show that, once initiated, lower than expected north and south study region brightness temperatures were observed continuously until late in the winter seasons.

The available observations and modeling results suggest that Martian CO_2 clouds are predominantly a lower atmosphere or near surface phenomena. Since condensation temperatures are at their maximum near the surface, CO_2 clouds are easier to form at lower altitudes than at higher ones. The CO_2 condensation temperature at the center of the 15 μ channel weighting function (see Appendix 2) at p = 0.6 mb is approximately 133 K. Optically thick CO_2 clouds at pressures lower than p = 0.6 mbar should then be expected to give 15 μ channel brightness temperatures of lower than 133 K since they are likely to be excellent black bodies at $\lambda = 15\ \mu$. The results in Figures 3-3a,b show that values of T_{15} lower than 133 K are not observed. Also, simultaneously acquired brightness temperature maps show that T_{15} is completely unaffected by the presence of low brightness temperature regions at T_{20}.

At the Seventh Annual D.P.S. Meeting, Frank Palluconi (1977) presented a unique set of IRTM low brightness temperature observations. Figures 3-13 and 3-14 are reproduced from his paper. Figure 3-13 shows T_{20} vs. latitude from a high resolution scan of the north polar region just prior to the second global dust storm of 1977 by Viking Orbiter 2. The scan shows an extended low brightness temperature area near the north pole and two smaller low brightness temperature regions at lower latitudes. Careful study of Orbiter images and shaded relief maps showed that the position of the southernmost low brightness

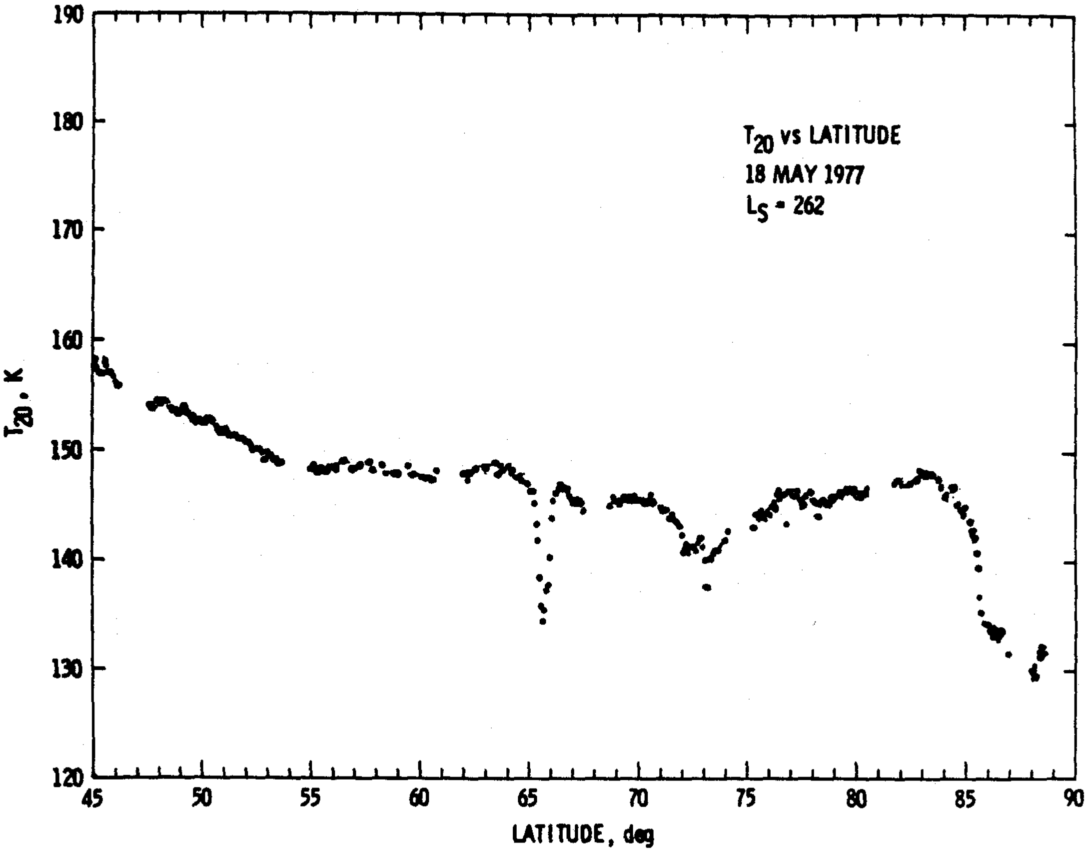

Fig. 3-13. T_{20} vs. latitude for a high resolution scan of the north polar region during late fall. Only data from one of the seven T_{20} detectors are plotted (from Palluconi, 1977).

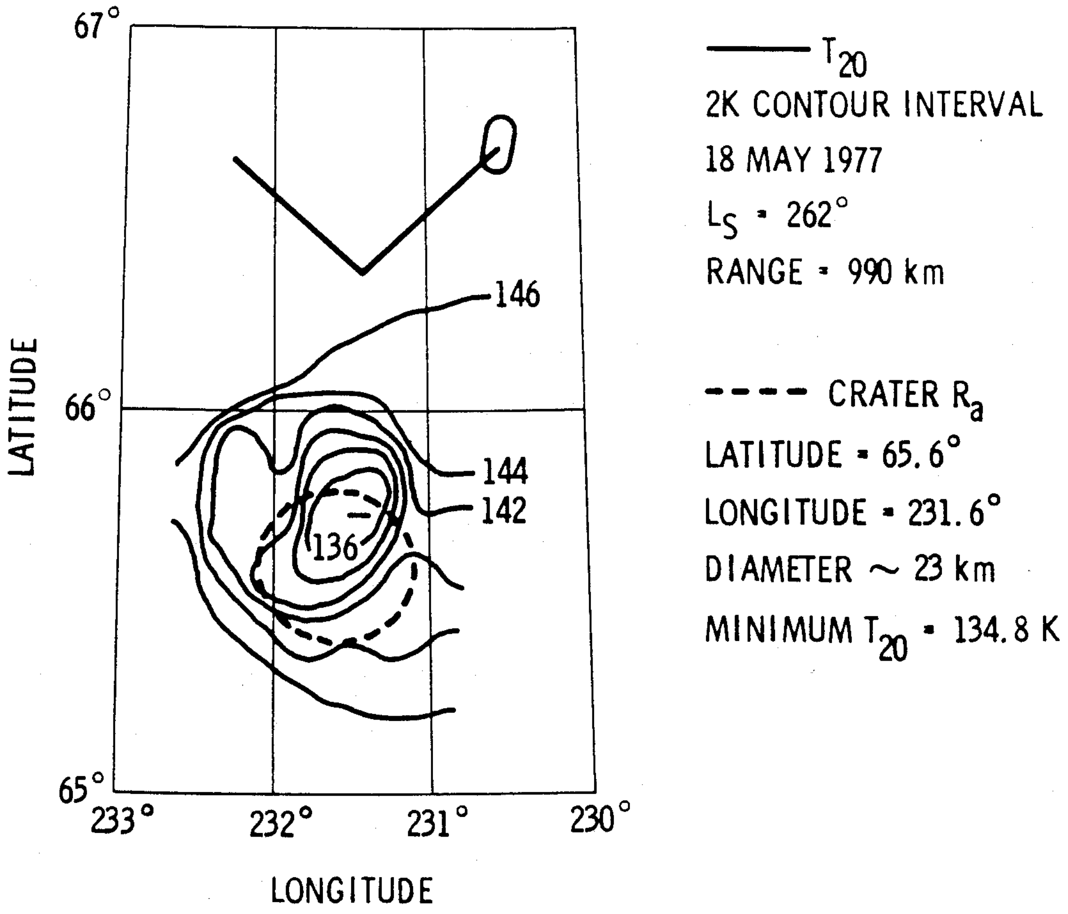

Fig. 3-14. A high resolution contour map of data from all seven T_{20} detectors in the region of the very sharp low brightness temperature spike near 65.6° latitude in Fig. 3-13. The 'V' and the elongated circle above the contours show the orientation of the IRTM detector array and the approximate width and length of the field of view of one of the detectors when an allowance is made for smear due to spacecraft motion. The location of the rim of an isolated impact crater is also shown. Uncertainties in the positions of the IRTM fields of view are greatest along the track of the spacecraft (from Palluconi, 1977).

temperature feature corresponds almost exactly with that of a medium-sized impact crater. This is shown in Figure 3-14. This observation can be explained quite simply by the hypothesis that the crater was filled with CO_2 fog. The ability of Martian topographic features such as impact craters, canyons, and calderas to hold morning water ice fogs is well known. The stagnant air within the walls of impact craters is a very likely site for the formation of CO_2 clouds because of the atmosphere's tendency to cool to the CO_2 frost point if horizontal advective heating rates are reduced. This can explain why this particular low brightness temperature feature was observed so close to the edge of the polar night.

In the future, it should be possible to simulate the development of CO_2 clouds and polar snow storms with more sophisticated models. The data in Figure 3-11 may provide constraints on parameters such as snow optical properties, size distributions, and opacities. Further analysis could lead to an understanding of the relative importance of surface vs. atmospheric condensation in the polar night and give clues to the local atmospheric motions that may be associated with these storms.

4. Dust Storm Brightness Temperatures

The elevated atmospheric temperatures in the north polar region during the initial phase of the second global dust storm of 1977 provide a rare opportunity to use the IRTM observations to "see" into the polar night. The sequence of events at the north pole are summarized by the 10-day averaged IRTM brightness temperatures of the north study region in Figure 3-3a. T_{15} rose rapidly during the initial phase of the storm, but then fell rapidly towards the middle of the storm, and achieved its pre-storm values soon after. The highest T_{15} values were accompanied by small sympathetic increases in T_9, T_{11}, and T_{20}. T_{11} and T_{20} fell precipitously towards the middle of the storm to their lowest recorded values, but then rebounded to their pre-storm values within 20 days. I will now argue that this sequence of events is excellent evidence for both the presence of significant quantities of dust in the north polar region and the deposition of dust onto the north seasonal polar cap during the storm.

The IRTM observations of the north polar region during this season are not in the form of maps, but in the form of high resolution scans that intersect the geographic pole. Figures 3-15 and 3-16 show IRTM 9, 15, and 20 μ channel observations during two of those scans. The first occurred on Julian date 3321 (L_s = 287.2) when T_{15} at the pole was near its highest value. The second occurred on Julian date 3332 (L_s = 294.1) when T_{20} at the pole was near its lowest value.

The 9 μ channel brightness temperatures in excess of 150K observed during Scan 1 provide clear evidence that dust was present. One-dimensional model results can provide quantitative estimates of the quantities of dust, but these estimates will be uncertain for three reasons. The first is that the radiative properties of the dust particles are not known. Toon-Pollack dust will be assumed for all calculations, but there is no guarantee that this will be correct. Infrared dust optical depths are proportional to the assumed ratio of dust optical depths in the IRTM 9 μ channel to those at visible wavelengths. This ratio is approximately unity for Toon-Pollack dust. It could be as low as 0.5 or as high as 1.5 for other types of dust. The second source of uncertainty is that the IRTM data contain little information as to the temperature structure of the atmosphere at low altitudes. T_{15} provides a good measure of atmospheric temperatures at high altitudes, but whether the atmosphere is hot or cold at low altitudes during this season is difficult to assess. The third source of uncertainty, the vertical distribution of dust in the atmosphere, is not known.

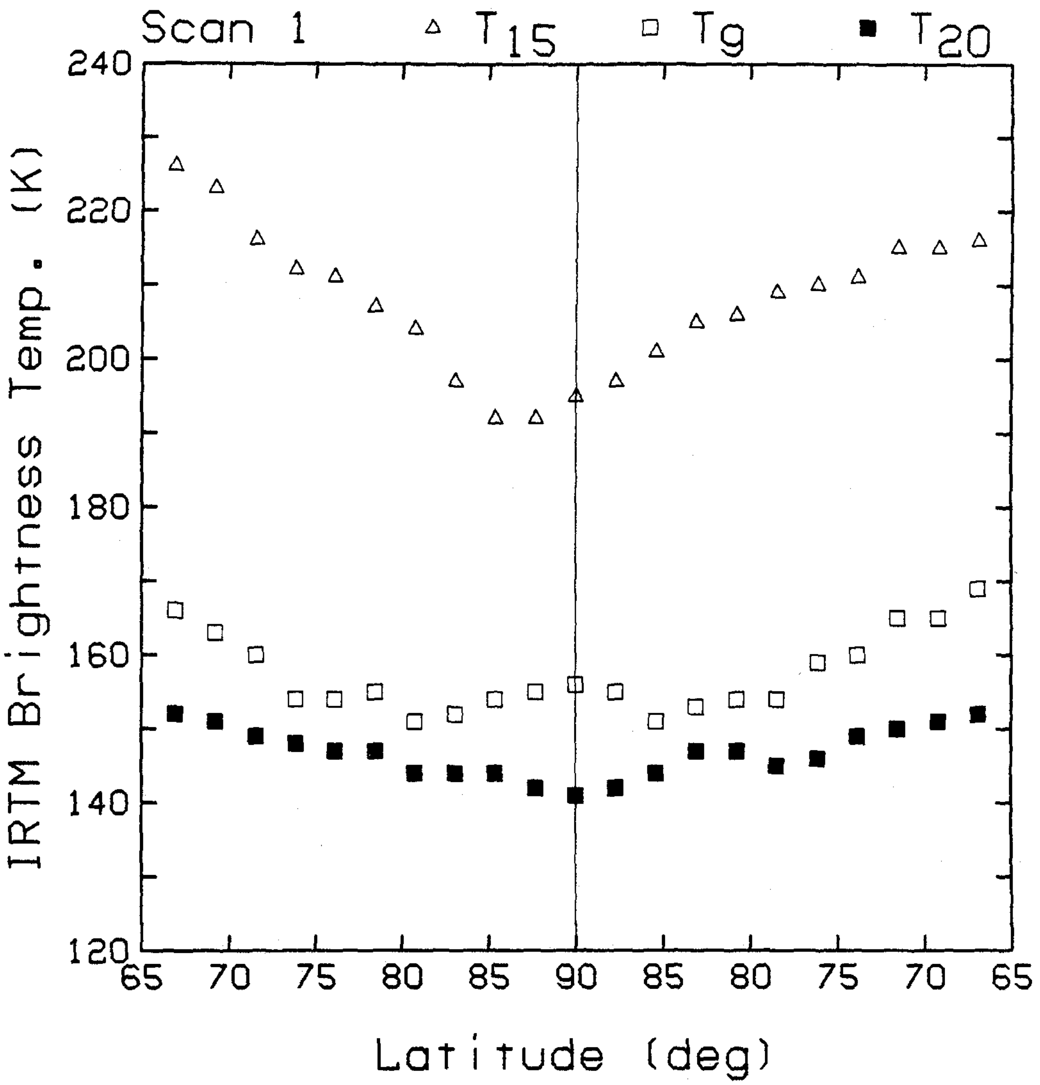

Fig. 3-15. Averaged IRTM 9, 15, and 20 μ channel brightness temperatures from a single cross polar scan from longitudes of 60°W (left) to 240°W (right) acquired by Viking Orbiter 2 on revolution 308 on Julian date 3321 (L_s = 287.2) when polar 15 μ channel brightness temperatures were near their maximum.

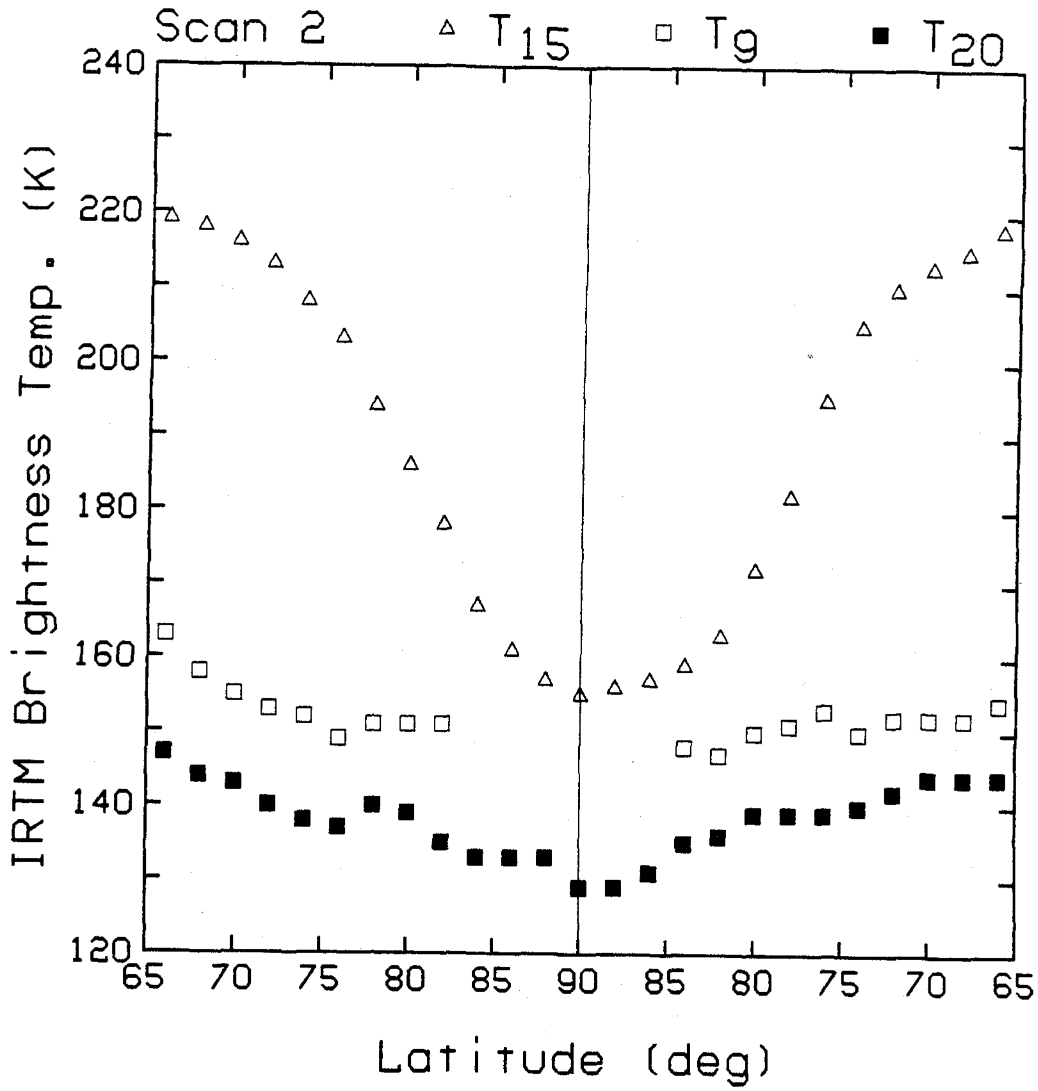

Fig. 3-16. Averaged IRTM 9, 15, and 20 μ channel brightness temperatures from a single cross polar scan from longitudes of 90°W (left) to 270°W (right) acquired by Viking Orbiter 2 on revolution 320 on Julian date 3321 (L_s = 294.1) when polar 20 μ channel brightness temperatures were near their minimum.

Lower limits for the dust content of the polar atmosphere during Scan 1 can be estimated with the model by assuming that all dust and all advective heating is concentrated in the highest three model layers above the 1.2 mb pressure level. In this mode, the model has two free input parameters, F_{Horiz} and τ_V, and two verifiable output parameters, T_9 and T_{15}. These can be compared with the IRTM observations in Scan 1 at any polar latitude. Profile 6 in Figure 3-12 gives calculated values of T_9 and T_{15} that are in good agreement with the observations in Scan 1 at 65° latitude. The required values of F_{Horiz} and τ_V were 40 Wm^{-2} and 0.3, respectively. T_9 and T_{15} for Profile 7 agree with the observations at the north pole. F_{Horiz} and τ_V for this case were 20 Wm^{-2} and 0.2.

The north polar atmosphere could have contained significantly more dust during the storm than the model derived lower limits might indicate for two reasons. The first is that only hot dust visible at $\lambda = 9\ \mu$. Cold, near-surface atmospheric layers could contain arbitrarily large quantities of dust during the height of the storm and produce no significant increases in T_9 at the top of the atmosphere. Second, the lower limit estimates of dust opacity apply only during the initial phase of the storm when T_{15} was high. Comparison with solar extinction measurements at Viking Lander 1 (Pollack et al., 1979) shows that although the timing of the rapid rise in observed dust opacities at the Lander agrees quite well with the rapid rise in T_{15} at the pole, dust opacities of greater than 2 were observed at the Lander for over fifty days after T_{15} had reached its maximum. Since the area covered by the north seasonal cap is not expected to be a source region for the dust raised during the storm, atmospheric mixing processes could well bring more dust to the north polar region during the latter phases of global dust storms than their initial phases.

Martin and Kieffer (1979) have used IRTM observations during the initial phase of the storm to show that down-going atmospheric radiation during this period could briefly retard or even stop CO_2 condensation at the surface near the periphery of the north seasonal cap. The more sophisticated 10-layer model calculations used here support this conclusion in that calculated surface heating rates for Profile 6 are -6.6 Wm^{-2} compared to -22.9 for Profile 3. This implies a 70% reduction in the rate of CO_2 accumulation at the surface at 65° latitude for this set of model input parameters.

The explanation of the IRTM north polar observations following the initial phase of the dust storm in Figures 3-3a and 3-16 draws on many of the results and ideas that have been presented so far. Figure 3-3a shows that T_{20} became extremely low for a brief period during the middle of the storm. Brightness temperatures as low as 126 K were recorded during this period (Palluconi, 1977). The data from Scan 2 in Figure 3-16 show that lower than expected 20 μ channel brightness temperatures were observed over a broad region poleward of 80° latitude. The data show T_{15} had fallen considerably by this time, but was still higher than normal for this season at all polar latitudes. T_9 was also elevated equatorward of 75° latitude, but had fallen below its noise-limiting threshold near the pole. In view of what has already been presented in this chapter, the occurrence of these brightness temperatures in the middle of the dust storm fit in very nicely with the notion that they are caused by the radiative effects of CO_2 clouds and that dust may have been deposited onto the north seasonal polar cap during the storm.

Model profiles 1 through 5 in Figure 3-12 demonstrate that atmospheric CO_2 condensation is most likely to occur when horizontal advective heating rates are low and dust opacities are high. Figure 3-15 and profiles 6 and 7 demonstrate that dust was present during the initial phase of the storm. The rapidly decreasing values of T_{15} after the initial phase of the storm indicate that polar horizontal advective heating rates were also decreasing rapidly after the initial phase. These conditions are perfect for the onset of atmospheric CO_2 condensation. The condensation must have taken place near the surface since the elevated values of T_{15} in Scan 2 effectively preclude atmospheric CO_2 condensation in the upper atmosphere. The fact that the intensely low brightness temperatures lasted for only 10 or 15 days suggests that the cooling effects of the dust that was present in the atmosphere were short lived. This could easily occur if the dust particles were coated with solid CO_2 and fell to the surface.

It is not inconceivable that the formation of water ice clouds could also help explain these observations in that the hot polar atmosphere could have contained significant quantities of water vapor and water ice particles. Water ice, like dust, has significant absorption at infrared wavelengths. Pollack et al. (1979) have suggested that dust grains in the polar night could be coated with water ice. The return of water to the north residual cap and the surrounding area during dust storms may play a key role in the present Martian seasonal water cycle (Davies, 1981, Jakosky, 1983a).

The importance of dust sedimentation in the polar night with regard to the present Martian dust cycle remains somewhat uncertain. The analysis if the IRTM observations presented above suggests that this process is occurring, but whether a significant fraction of the dust raised globally during each major dust storm is eventually deposited in the north polar area as suggested by Pollack et al. (1979) remains to be seen. The results of this study definitely support the notion that dust sedimentation during global dust storms is presently leading to the formation of sedimentary deposits in the north polar area. It is interesting to note that the lowest 20 μ channel brightness temperatures confined to latitudes of within 10° of the pole. This corresponds quite well to the area covered by polar layered deposits. It is then possible that these deposits could have been formed by a long succession of storms very much like the one that was observed in 1977. This line of thinking can be carried even further by noting that polar layered deposits in the south are also generally confined to within about 10° of the pole. This may be one more piece of the Mars orbital forcing-climatic change-polar layered terrain puzzle.

5. Conclusions

The major conclusions of this chapter can be summarized as follows:

1. The spectral emissivities of Martian seasonal frost deposits are close to unity during the early fall and late winter seasons.

2. The south residual cap is located on the slopes of a broad plateau area centered off the geographic pole. It does not receive the minimum possible annual insolation.

3. The occurrence of lower than expected IRTM brightness temperatures in the polar night can be well explained by the presence of CO_2 clouds in the lower atmosphere.

4. Dust was deposited onto condensing seasonal frost deposits in the north residual cap area during the second global dust storm of 1977.

References

Davies, D.W. (1981), *Icarus* **45**, 398.

Ditteon, R. and H. H. Kieffer (1979) *J. Geophys. Res.* **84**, 8289.

Dzurisin, D. and K.R. Blasius (1975) *J. Geophys. Res.* **80**, 3286.

Carr, M.H. (1982) *Icarus* **50**, 129.

Gierasch, P. and R. Goody, (1968) *Planet. Space Sci* **16** 615.

Hess, S.L. (1979) *J. Geophys. Res.* **84**, 2969.

Hunt., G. E. (1980) *Geophys. Res. Let.* **7**, 481.

Hunt, G. E. et al. (1980) *J. Quant. Spectrosc. Radiat. Transfer* **24**, 141.

Jakosky, B.M., (1983a) *Icarus* **55**, 19.

Jakosky, B.M., (1983b) *B. Amer. Astron. Soc.* **15**, 846.

James, P.B., eal (1979) *J. Geophys. Res.* **84**, 2889.

Kahn, R. (1984) *J. Geophys. Res.* **89**, 6671.

Kieffer, H.H. et al. (1976) *Science* **143**, 780.

Kieffer, H.H. et al. (1977) *J. Geophys. Res.* **82**, 4249.

Kieffer, H.H. and F.D. Palluconi (1979) NASA Conference Publication 2072, 45.

Kliore, A.J., (1973) *J. Geophys. Res.* **78**, 4331.

Leighton, R.B. and Murray, B.C. (1966) *Science* **153**, 136.

Leovy, C.B. and Y. Mintz (1969) *J. Atmos. Sci.* **26**, 1167.

Martin, T.Z. and H.H. Kieffer (1979) *J. Geophys. Res.* **84**, 2843.

Murray, B.C. and M.C. Malin, (1973) *Science* **182**, 437.

Palluconi, F.D. (1977) *B. Amer. Astron. Soc.* **9**, 540.

Pollack, J.B. et al. (1979) *J. Geophys. Res.* **84**, 2929.

Pollack, J.B. et al. (1981) *J. Atmos. Sci.* **38**, 3.

Toon, O.B., J.B. Pollack, and C. Sagan (1977) *Icarus* **30**, 663.

Ward, W.R. (1974) *J. Geophys. Res.* **79**, 3375.

Warren, S. and W. Wiscomb (1981) Abstract, Workshop on Quasi-Periodic Climate Change on Mars and Earth, NASA Ames, Feb. 24-26.

CHAPTER 4

A NEW THEORY FOR THE ASYMMETRIC BEHAVIOR OF THE MARTIAN POLAR CAPS

The results of Chapter 2 showed that the asymmetric behavior of seasonal CO_2 frost at the Martian north and south poles during the first Viking year was due almost entirely to late spring season surface frost albedos in the north being approximately 20% lower than those in the south. This piece of information must be an enormous clue to what is causing the polar caps to behave so differently.

At the Third International Colloquium on Mars and in his review of the meeting published in *Nature*, Conway Leovy pointed out that something was very wrong with the hypothesis that the asymmetric behavior of the Martian polar caps was due primarily to the preferential occurrence of global dust storms during the southern spring and summer seasons (Leovy, 1981). Fig. 4-1 shows annual barograms at the Viking landing sites for parts of three Martian years. These data were compiled by J.E. Tillman (1981) and are reproduced from Leovy's review. The vertical grid lines in the figure correspond to exactly one-fourth of a Martian year. The data from Viking Lander 1 are more complete than those from Viking Lander 2 and are less affected by high frequency pressure variations caused by "weather". The seasonal pressure variations at both landing sites are due to the combined effects of CO_2 frost condensation by the north and south seasonal polar caps. The dominant peaks and valleys at L_s 260 and L_s 150 are due to seasonal variations in the mass of the south seasonal cap. The smaller peaks and valleys at L_s 330 and L_s 50 are due to seasonal variations in the mass of the north seasonal cap. Close examination of the Viking 1 lander pressure curves shows that they repeat almost exactly from year to year. This absence of interannual variations in these pressure records is almost

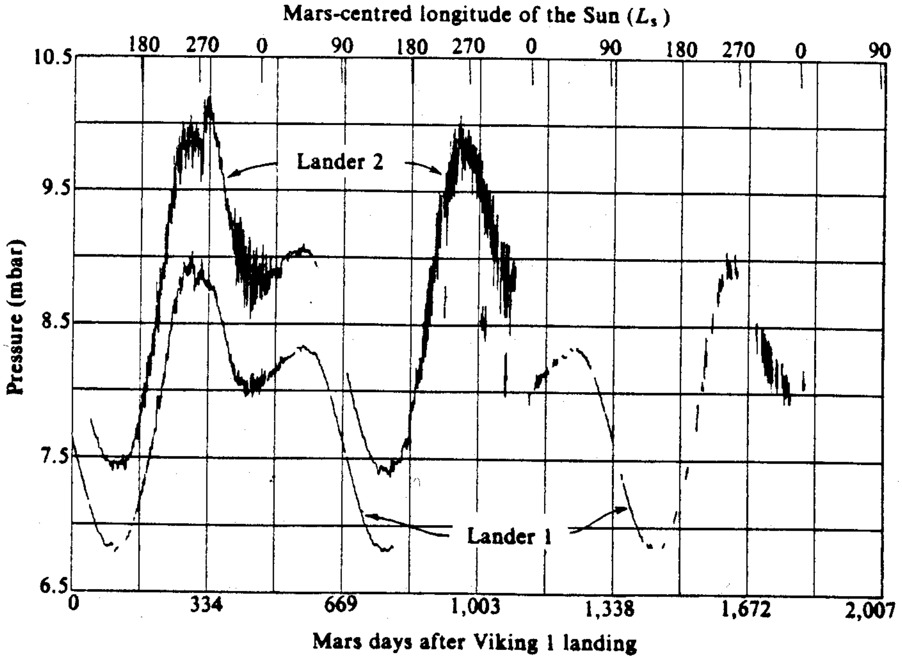

Fig. 4-1. Measured surface pressures at the Viking landing sites over three Mars years. The vertical grid lines correspond to exactly one-fourth of a Mars year. Gaps indicate missing data (from Leovy, 1981).

disturbing in view of the fact that two major global dust storms were observed during the first Viking year and no global dust storms were observed the second and third years. (J.E. Tillman, personal communication.)

The results of Chapter 2 showed that frost sublimation rates during spring are determined almost entirely by surface albedo, with the radiative effects of atmospheric aerosols being of only secondary importance. It is easy to show that even minor variations in seasonal frost albedos due to year to year variations in dust contamination should produce noticeable variations in the retreat rates of the seasonal polar caps and the surface pressures at the Viking landing sites. Changing the albedos of north seasonal cap frost deposits from 0.65 to 0.80 would result in an approximately two-thirds reduction in their rates of sublimation. Examination of Fig. 4-1 shows that the slope of the pressure increase due primarily to the sublimation of the north seasonal cap from L_s 330 to L_s 50 was essentially identical during the first two Viking years. This argues very strongly that dust contamination of north seasonal cap frost deposits during global dust storms is not the primary explanation for their early disappearance.

One way to explain the repeatability of the Viking lander pressure data would be to suggest that contamination of seasonal frost deposits does not occur primarily during global dust storms, but during local storms that are regularly observed at the edges of the retreating north and south seasonal polar caps during spring. This mechanism could also potentially explain the albedo difference between seasonal frost deposits at the north and south residual caps because the south seasonal cap has a larger diameter than the north seasonal cap during spring, so less dust might be able to reach the south residual cap. One set of observations that argue very strongly against this hypothesis are the Viking observations of the south residual cap during the second global dust storm of 1977. Figs. 4-2 and 4-3 show Viking orbiter mosaics of the south residual cap area from James et al. (1979) The first was obtained just before the start of the second global dust storm, the second was obtained 13 days later. Sophisticated data analysis techniques are not required to conclude that large quantities of dust were definitely present in the south polar atmosphere during the storm. The IRTM observations of the south study region during this period show that planetary albedos at the top of the atmosphere dipped sharply at the peak of the storm, but then rebounded soon afterwards (see Fig. 2-4). The heat balance results in Chapter 2 also show that CO_2 frost sublimation rates at the surface did not increase significantly after the storm. The same was true after the first global dust storm of 1977. One could always assert that not one speck of dust actually landed on the frost during these two storms, but I find this difficult to fathom.

The amazing repeatability of the Viking lander pressure curves and the dust storm observations at the south residual cap cast grave doubts on the notion that Martian seasonal frost deposits are darkened by contamination by dust. The results of Chapter 2 require that *something* caused frost albedos to be lower in the north than in the south during the first Viking year. The following analysis points to what it may have been.

One observation presented in Chapter 2 that was not discussed very thoroughly was the tendency for measured south study region Lambert albedos at low emission angles to increase sharply during spring and then decrease just as sharply during summer (see Fig. 2-4). The available north study region Lambert albedos also show a tendency to increase after mid-spring, but the effect is not as pronounced (see Figs. 2-3 and A1-12). This behavior could be due to a variety of factors including temporal variations in the dust or water ice content of the atmosphere, photometric variations in surface frost reflectivities with

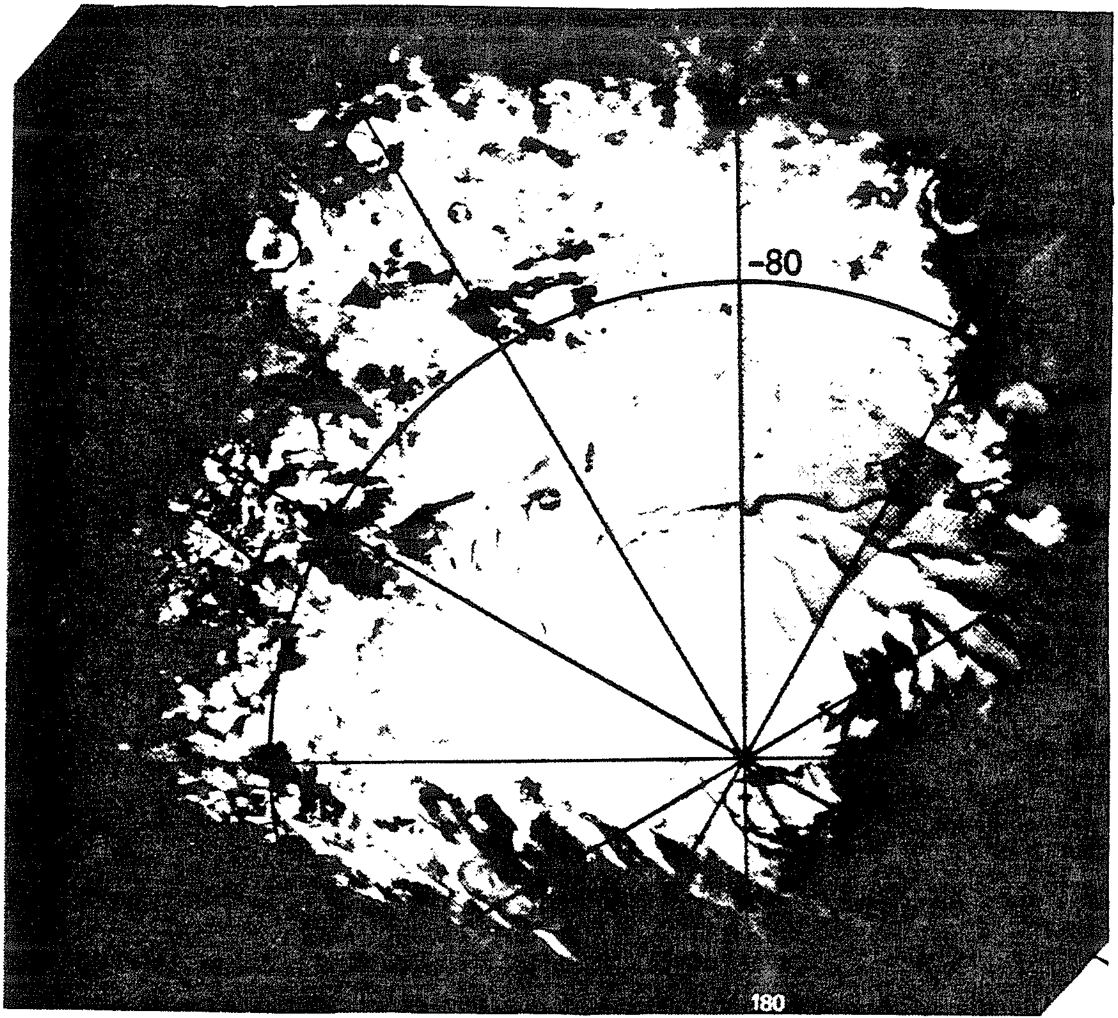

Fig. 4-2. A Viking Orbiter mosaic image of the retreating south seasonal cap just before the onset of the second global dust storm of 1977 (L_s=274.5) (211-5616B) (Reproduced from James et al., 1979).

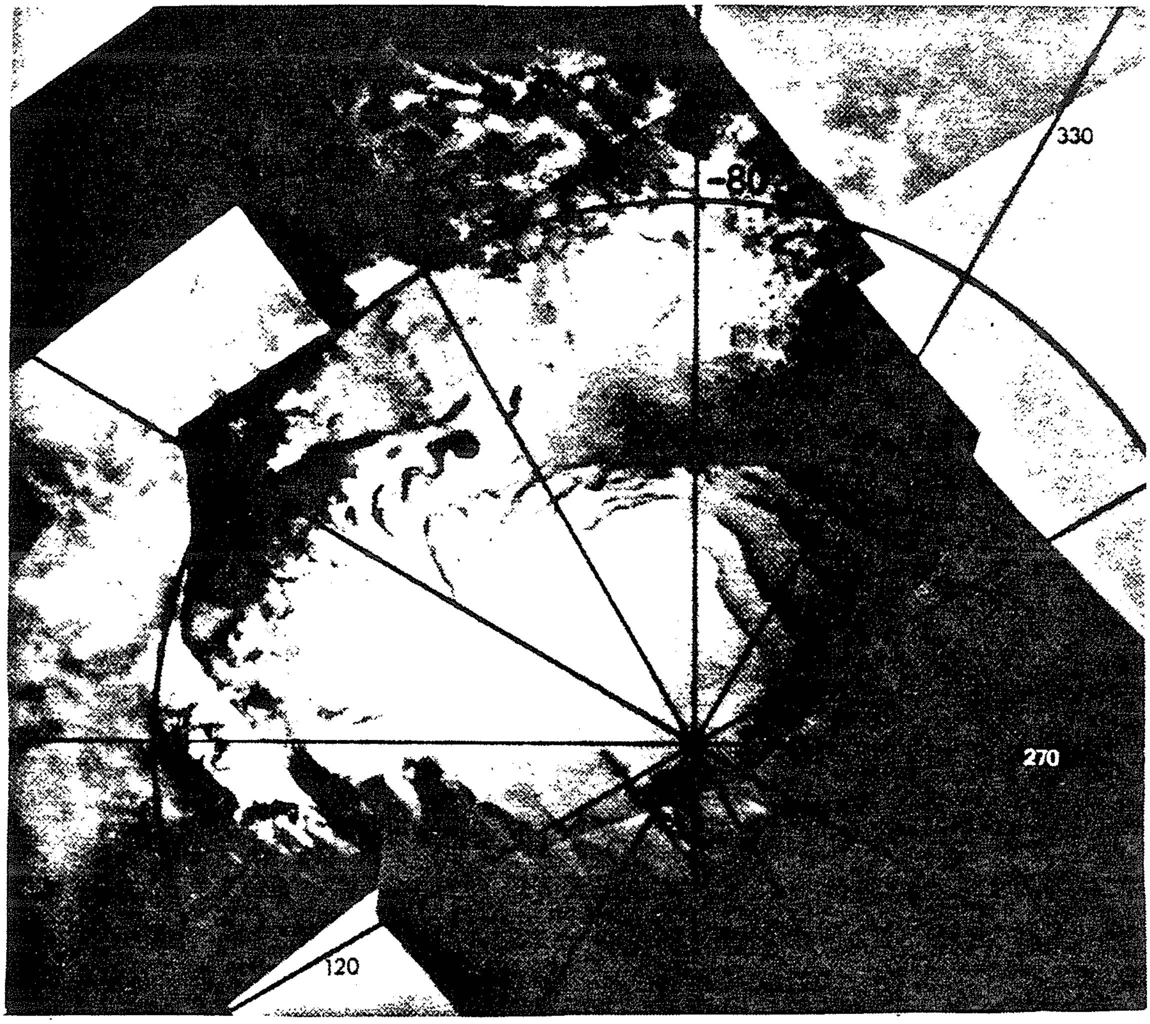

Fig. 4-3. A Viking Orbiter mosaic image of the retreating south seasonal cap 13 days after the onset of the second global dust storm of 1977 (L_s=282.2) (211-5617B) (Reproduced from James et al., 1979).

solar zenith angle or possibly due to actual variations in the albedos of the surfaces with the insolation rate or with time. This last possibility can be investigated by re-examining the annual heat budgets of the north and south study regions.

In Chapter2, the instantaneous heat balance equation for the seasonal frost deposits and the overlying atmosphere was written:

$$F_{Rad} + F_{Horiz} + F_{Cond} = S_{Atm} + S_{CO_2} \tag{4.1}$$

where F_{Rad} is the net radiative flux at the top of the atmosphere, F_{Horiz} is the net horizontal heat flux, F_{Cond} is the upward conductive heat flux from subsurface soil and ice layers, S_{Atm} is the rate of total potential energy storage in the atmospheric column and S_{CO_2} is the vertically integrated rate of latent heat storage in sublimating CO_2 frost. The results of Chapter 2 showed that F_{Horiz}, F_{Cond} and S_{Atm} were small during spring in the north and south, which leaves F_{Rad} to balance S_{CO_2} throughout most of these seasons. The results of Chapter 2 also showed that S_{CO_2} during spring was determined almost entirely by F_{Solar}, the incident solar flux at the top of the atmosphere and A_s, the albedo of the surface.

Figure 4-4 shows S_{CO_2} as a function of F_{Solar} for the north study region during spring and the south study region during spring and summer. This plot was made directly from the 10-day averaged results presented in Figs. 2-3 and 2-4.

Three very interesting things become apparent when the heat budget results are presented in this format. The first is that the inferred CO_2 sublimation rates in the south are not simple functions of the rate of insolation in that they clearly stop increasing after F_{Solar}>200Wm^{-2} . The second is that the inferred CO_2 sublimation rates for the north and south study region during their

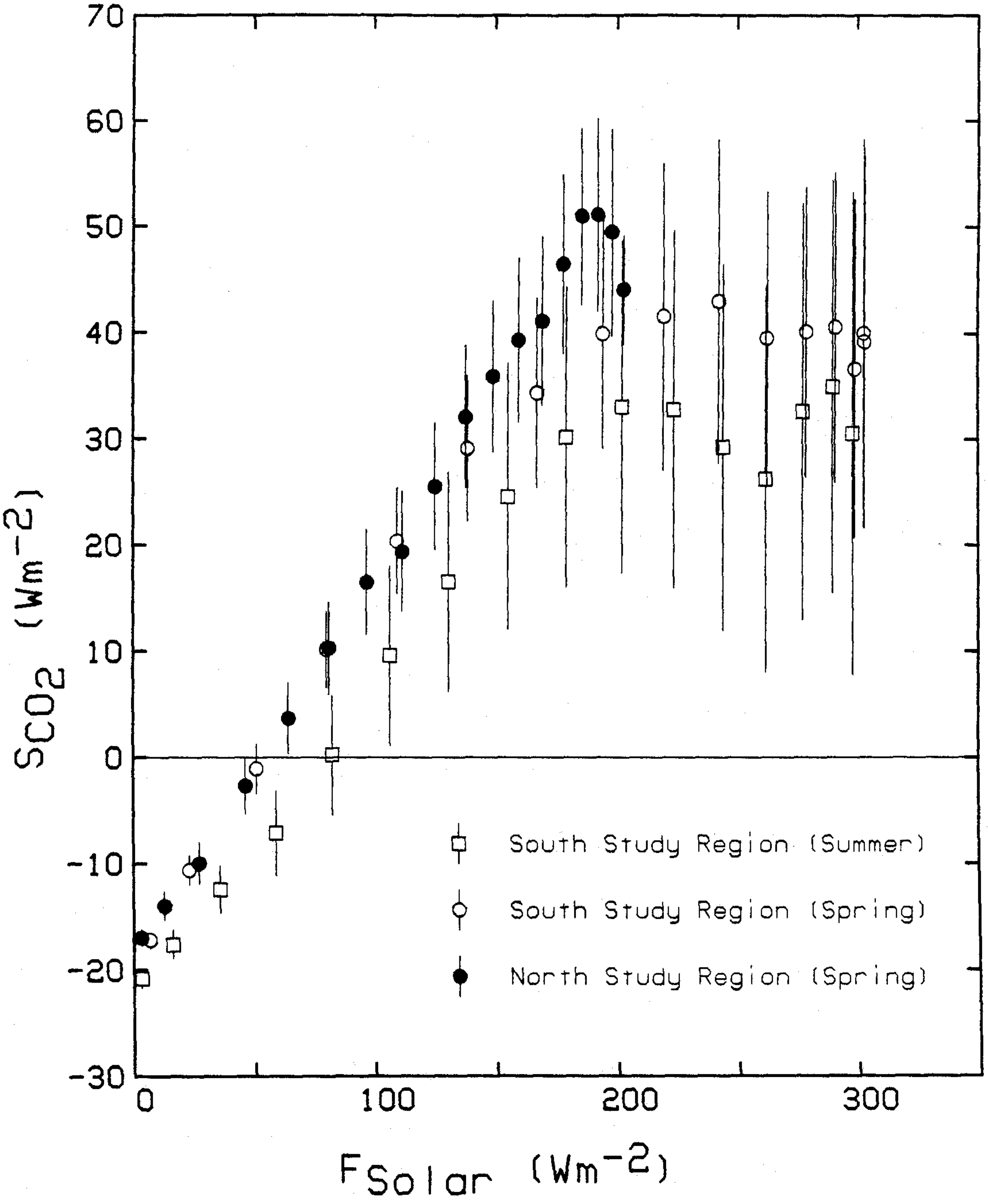

Fig. 4-4. Surface frost sublimation rates S_{CO_2} vs. the incident solar flux F_{Solar} for the north study region during spring and for the south study region during spring and summer.

respective spring seasons are very similar functions of F_{Solar} over the range in which comparisons can be made. The third is that the behavior of the south study region during summer mimics the behavior of the south study region during spring except that the inferred CO_2 sublimation rates during summer are uniformly lower.

This last effect can potentially be explained by the presence of dark lanes within the south study region during summer. Since the lanes contain no CO_2 frost and are likely to be in a state of near-radiative equilibrium, the fractional area that they cover contributes very little to the inferred values of S_{CO_2} for the study region as a whole. If the south study region contained CO_2 frost with behavior dependent solely on the rates of insolation during the spring and summer seasons, then the differences between S_{CO_2} during spring and summer are a rough measure of the fractional area of the south study region covered by dark lanes. The downturn in S_{CO_2} for the north study region at the end of spring can also be explained by fractional CO_2 coverage.

The modeling results presented in Chapter 2 showed that spring season CO_2 sublimation rates are determined primarily by the surface albedo, with the radiative effects of atmospheric aerosols being of only secondary importance (see Fig. 2-8b). The nonlinear relationship between S_{CO_2} and F_{Solar} shown in Fig. 4-4 suggests very strongly that that surface albedos of the study regions may be insolation dependent. This possibility can be investigated further by interpreting these results in terms of a simple polar heat balance model like that used by Leighton and Murray (1966).

If subsurface heat conduction and the radiative effects of atmospheric aerosols and gases are completely ignored, then the instantaneous heat balance equation for Martian seasonal frost deposits can be written:

$$F_{Solar}(1-A_s) + F_{Horiz} - \varepsilon_s \sigma T_S{}^4 = S_{CO_2} \tag{4.2}$$

where A_s is the surface albedo of the frost, ε_s is the greybody surface emissivity, σ is the Stefan-Boltzman constant and T_s is the temperature of the frost. If values for F_{Horiz}, ε_s and T_s are assumed, then upper and lower limits for S_{CO_2} can be converted to estimates of A_s.

Figure 4-5 shows estimates for spring season surface albedos for the north and south study regions derived from the data in Fig. 4-4 using equation 4.2. T_s was assumed to be 145K for the north study region and 142K for the south study region. ε_s was assumed to be unity and F_{Horiz} was assumed to be 2Wm^{-2} for all cases. Inferred surface albedos during the first twenty days of the spring seasons are extremely sensitive to the assumed values of these parameters and are not plotted in the figure.

The results in Fig. 4-5 are rather remarkable in that they show a nearly straight line correlation between insolation rate and inferred surface frost albedos. They also show the north study region data to be in near-coincidence with the south study region data. This suggests that the intrinsic properties of the seasonal frost deposits in the north and south may have been quite similar, but the differing rates of insolation in the north and south caused them to behave asymmetrically! It will be important to establish that this type of correlation could not be due to an undetected error in the calibration of the IRTM instruments or the subsequent data processing. It will also be important to search for a non-linear atmospheric effect that could account for this correlation, but I seriously doubt that one will be found.

If the albedos of Martian seasonal frost deposits are determined primarily by the instantaneous rates of insolation as suggested in Fig. 4-5, then this effect should also be apparent in regions away from the residual cap areas.

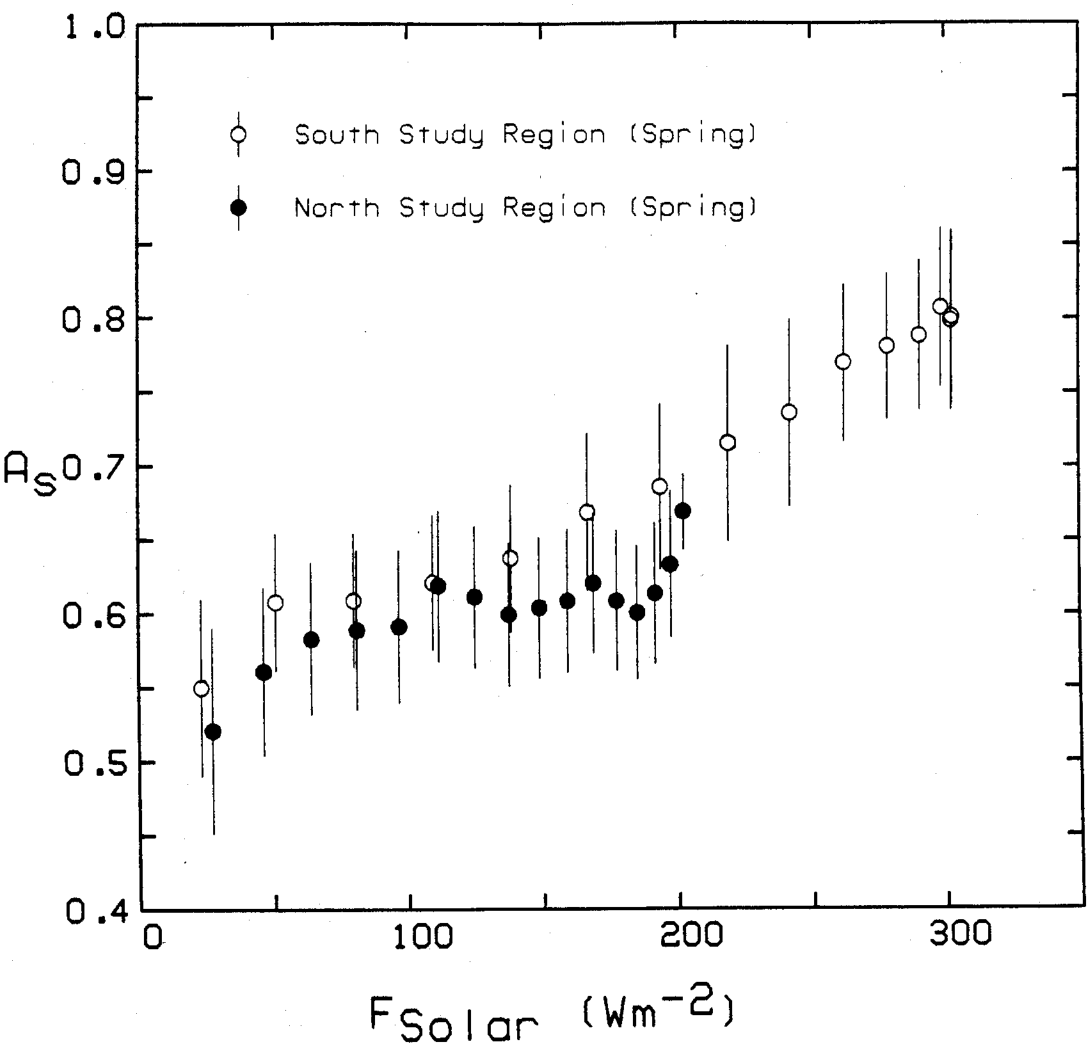

Fig. 4-5. Inferred surface albedos A_s vs. the incident solar flux F_{Solar} for the north and south study regions during spring.

Fig. 4-6 shows a Viking orbiter mosaic of the retreating south seasonal polar cap in early spring. Although these images were not processed to be photometrically accurate, there is a definite tendency for the cap to appear darker at its center than at its periphery. This same effect has been observed in earth based photographs of Mars and has been interpreted as evidence that the outer boundaries of the south polar cap may contain bright water-ice (Martin and James, 1984).

A similar brightening towards the edge of the south seasonal cap was observed by IRTM. Figs. 4-7ab show plots of simultaneously acquired T_{20} and Lambert albedo observations versus latitude reproduced from Kieffer (1979). The T_{20} plot defines the edge of the cap.

The albedo structure of the south seasonal polar cap becomes rather complicated during mid-spring and it is possible that the tendency for frost albedos to increase with increasing insolation may explain much of the observed structure. The cap exhibits small scale variations in frost brightnesses and the degree of frost coverage associated with topographic features and it will be interesting to examine the data more closely to see if these effects can be explained by the preferential brightening of frost deposits on sunlit slopes. "Frost streaks" observed on the northeast slopes of impact craters have been interpreted as evidence that seasonal frost deposits may be effectively redistributed by winds (Thomas et.al. (1979). The behavior suggested in Fig. 4-5 may be an alternative explanation for these features. It has also not escaped my attention that the apparent brightness of seasonal frost deposits at the south residual cap might also be explained by a similar effect, given the possible new topographic information in Chapter 3.

The brightening of Martian seasonal frost deposits with increasing insolation may also explain why Leighton and Murray-like thermal models are not

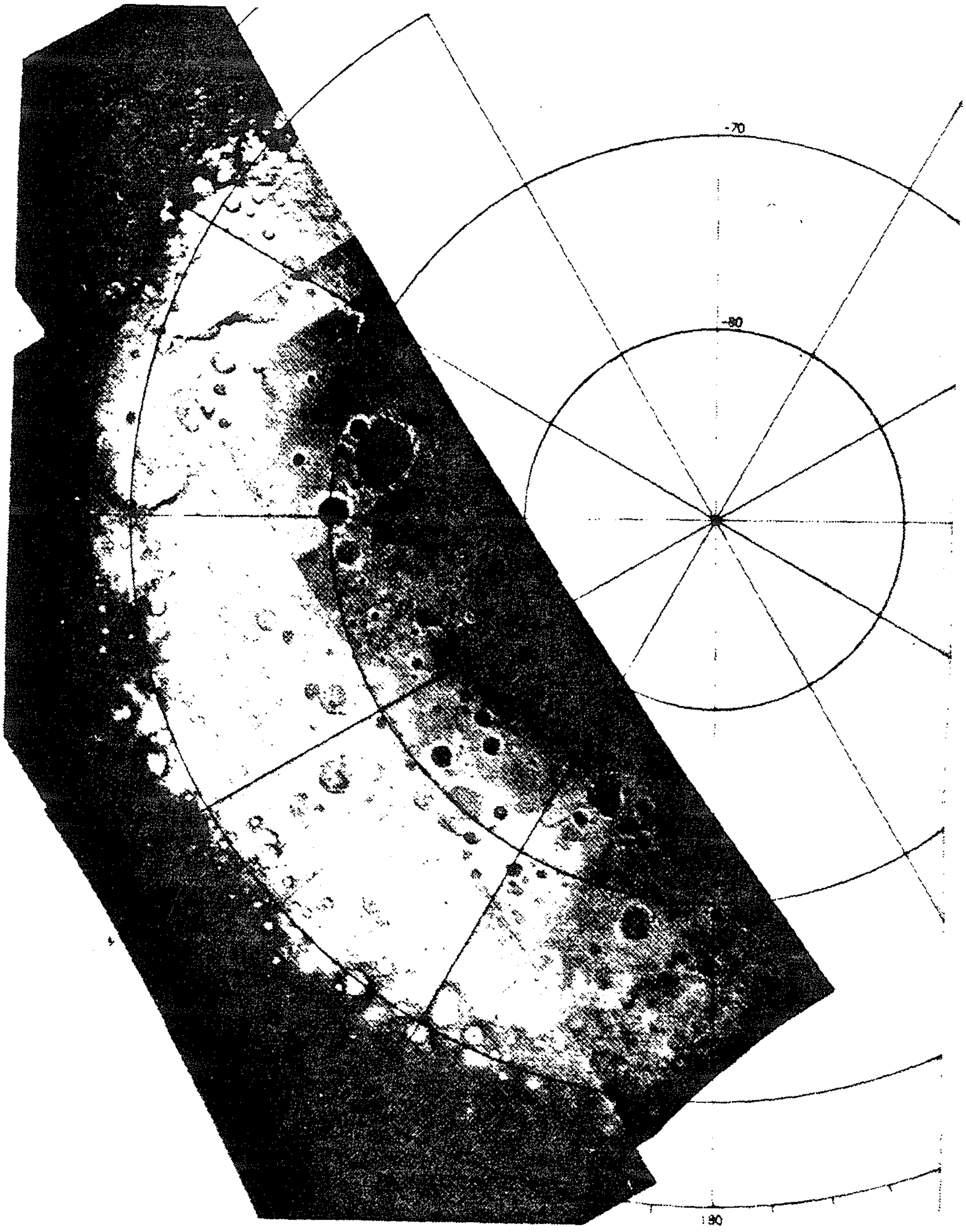

Fig. 4-6. A Viking Orbiter mosaic image of a portion of the retreating south seasonal polar cap obtained during early spring (L_s=196.5) (211-5625B) (Reproduced from James et al., 1979).

Fig. 4-7 T_{20} versus latitude and Lambert albedo versus latitude for a simultaneously acquired IRTM map of the south polar area at L_s=176. (Reproduced from Kieffer (1979)).

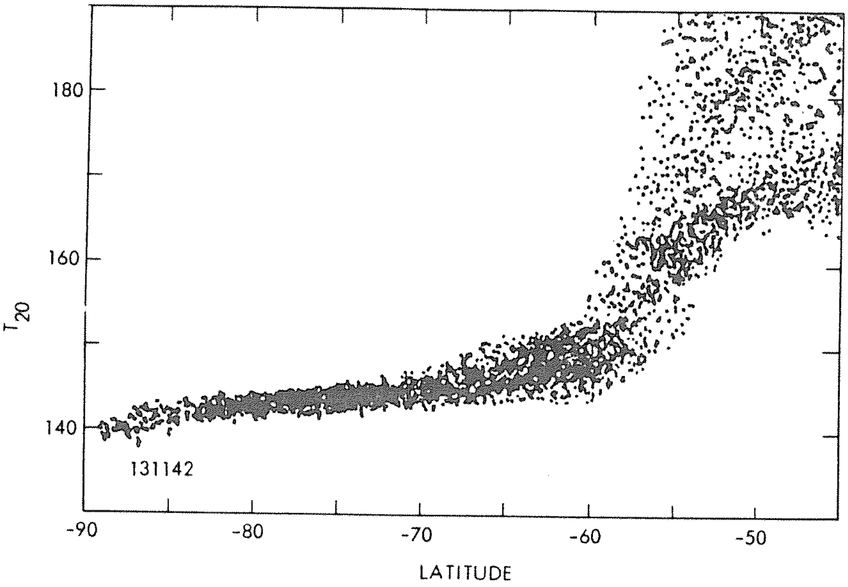
180
160
140
T_{20}
131142
-90
-80
-70
-60
-50
LATITUDE

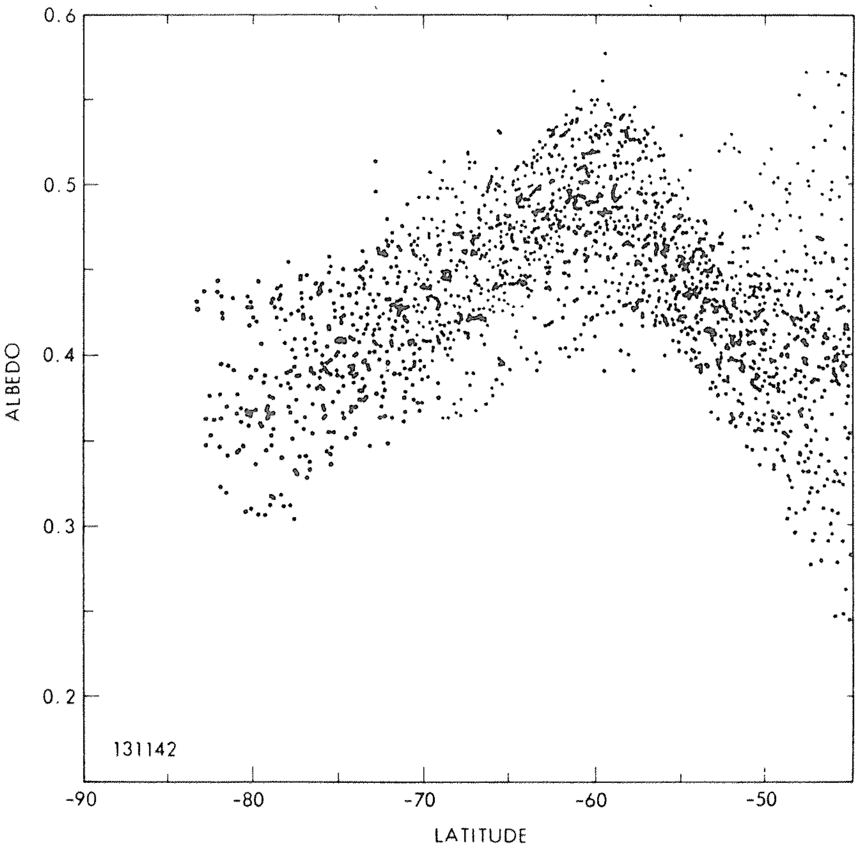
0.6
0.5
0.4
0.3
0.2
ALBEDO
131142
-90
-80
-70
-60
-50
LATITUDE

able to reproduce the retreat rates of the seasonal polar caps or the seasonal pressure oscillations at the Viking landing sites (James and North, 1982). The present models that use constant frost albedos have a great deal of difficulty explaining the slow rate of retreat of the south seasonal polar cap during summer and the possible tendency for the retreat rate of the north seasonal cap to vary with time (James, 1979). They also have difficulties explaining the observed directions of condensation winds in the north during spring (Kahn, 1984).

The apparent correlation of frost reflectivities with insolation rate and the possible insensitivity of frost reflectivities to bulk dust content suggest an interesting explanation for the behavior of seasonal CO_2 deposits on Mars. Hugh Kieffer may have been the first to suggest that dust grains landing on frost deposits might sublimate the CO_2 grains that support them and sink in to the frost. Although this phenomena has not yet been demonstrated to occur, it is possible that it could occur for the following reason: Laboratory measurements show that solid CO_2 is quite transparent at visible wavelengths and that small CO_2 particles ($r<100\mu$) are likely to be highly efficient scatterers of solar radiation (Warren and Wiscomb, 1981) and are not expected to absorb very much solar radiation themselves. Since dust grains are not perfectly scatterrers at solar wavelengths, a large fraction of the solar energy absorbed by a Martian seasonal frost deposit would actually be absorbed by the dust within the frost. Excess solar energy absorbed by dust particles could be converted to sublimation within a dusty CO_2 frost deposit through radiation and conduction.

One question that arises from this line of thinking is that if dust can sink into frost, how far will it sink and what will it do to the albedo of the frost deposit as a whole? The answer to this question is not immediately obvious and some careful theoretical and observational work will be required before a genuine understanding of the behavior of dust in Martian seasonal frost deposits is achieved. It is clear from an intuitive standpoint that the rate at which a dust grain can sink into frost will increase with the rate at which it can absorb solar energy, so the possibility that dust grains could organize themselves within the frost to produce the effect shown in Fig. 4-5 is very real. Whether the effect is completely insensitive to total amount of dust within the frost is not clear.

This idea may have many important implications for the theory of the Martian climate. The following discussion may easily miss some of the most important of them.

During the present epoch ϑ, the obliquity of Mars (the angle between its spin axis and its orbit normal) is 25°, ε, the eccentricity of the orbit of Mars is 0.09 and ω, the longitude of perihelion (the angle between the date of northern spring equinox and the time of perihelion passage) is 250°. Although both poles always receive the same total insolation over the course of a year, the present orbital configuration causes peak insolation rates to be higher at the south pole than at the north pole since Mars is closer to the sun during southern spring and summer. Since the albedos of seasonal CO_2 deposits increase with increasing rates of insolation, the south pole is currently the favored location for permanent CO_2 deposits. This situation would be expected to reverse in less than 50,000 years due to the precession of the Martian equinoxes.

The tendency for frost reflectivities to increase with increasing insolation rates should exert a powerful stablizing influence on the Martian climate system. Ward (1974a) has shown that ϑ and ε oscillate with periods on the order of 10^5 years and amplitudes of about ±13° and ±0.07 respectively. These variations can cause a two-fold variation in the annually averaged rates of insolation at the poles. Table 4-1 shows the results of annual Martian polar heat balance calculations for various combinations of ϑ, ε and ω. Instantaneous frost

	ϑ	ε	ω	$p(A_s=0.73)$	$p(A_s=A_s^*)$
1	25	0.09	250	2.93	2.91
2	25	0.09	0	2.93	4.49
3	15	0	0	0.21	1.14
4	25	0	0	2.82	4.76
5	35	0	0	12.84	6.52
6	15	0.14	270	0.25	0.81
7	25	0.14	270	3.30	1.96
8	35	0.14	270	15.02	1.04

Table 4-1. Calculated Martian atmospheric surface pressures for eight combinations of orbital elements ϑ, ε and ω. $p(A_s=0.73)$ is the calculated surface pressure assuming surface albedos are fixed, $p(A_s=A_s^*)$ is the calculated surface pressure assuming surface albedos increase with increasing insolation rates.

condensation and sublimation rates were determined throughout the year at each pole using Equation 4-2. F_{Horiz} was assumed to equal $2Wm^{-2}$ and ε_s was assumed to be unity for all calculations. T_s was assumed to be constant throughout the year, but was adjusted for each set of orbital parameters so that the annually averaged value of S_{CO_2} was zero at the coldest pole. This is equivalent to assuming that there is always enough CO_2 in the Martian cap-atmosphere system to maintain at least one permanent CO_2 deposit. Martian surface pressures can be calculated from this model by determining the vapor pressures of solid CO_2 at the temperature T_s at the coldest pole. The calculations were performed using two different assumptions concerning the albedos of Martian seasonal frost deposits. In the first case, A_s was assumed to be fixed at a value of 0.73. In the second case, A_s was assumed to be determined by A_s^* where

$$A_s^* = 0.52+0.000916F_{Solar}(Wm^{-2}) \tag{4.3}$$

This formula simulates the dependence of frost reflectivities on insolation rates suggested in Fig. 4-5.

Table 4-1 shows calculated Martian atmospheric pressures for the first case, $p(A_s=0.73)$ and for the second case, $p(A_s=A_s^*)$ for eight combinations of ϑ, ε and ω. The first combination of parameters simulates present Martian conditions, the second combination shows the behavior when ω becomes zero. Combinations 3,4 and 5 demonstrate the sensitivity of the system to variations in ϑ when ε is zero. Combinations 6,7 and 8 demonstrate the sensitivity when ε is 0.14 and ω is 270°.

The results show that $p(A_s=A_s^*)$ is much more sensitive to variations in ε and ω than is $p(A_s=0.73)$, but it is much less sensitive to variations in ϑ. The results also show that $p(A_s=0.75)$ varies by a factor of 70 over these combinations of orbital parameters, whereas $p(A_s = A_s^*)$ varies by only a factor of 8.

There are many assumptions built into these calculations that may prove to be incorrect. The most important of these is that the assumed relationship between A_s^* is valid over a fairly wide range of Martian climatic conditions. These calculations also do not take into account the possibly variable effects of CO_2 clouds during the polar night on CO_2 accumulation rates during fall and winter (see Chapter 3) and the distinct possibility that F_{Horiz} might also change. Another important assumption is that there has always been enough CO_2 in the cap-atmosphere system to support a permanent CO_2 deposit at the north or south poles. Fanale et.al (1981) have estimated that the south residual cap might contain enough solid CO_2 to support a Martian atmosphere with twice its present mass. The reduced range of pressure variations indicated by the results in Table 4-1 make the fact that the Martian cap-atmosphere system may currently contain just enough CO_2 to support a permanent CO_2 deposit seem much less of a coincidence.

Despite these assumptions, the picture of the Martian climate painted in Table 4-1 is solidly grounded in what is presently known about the seasonal behavior of CO_2 on Mars. In view of the crucial role that the Martian seasonal CO_2 cycle plays in determining the behavior of other Martian volatiles and dust, our present ideas concerning the geologic and climatologic history of Mars may be due for careful reexamination.

References

Fanale, F.P. et.al (1982) *Icarus* **50**,381.

James, P.B., etal. (1979) *J.Geophys. Res.* **84**,4249.

James, P.B., (1979) *J.Geophys. Res.* **84**,8332.

James, P.B and G. R. North, (1982) *J.Geophys. Res.* **87**,10271.

Leovy, C.B. (1981) *Nature* **294**, 310.

Kahn, R. (1984) *J. Geophys. Res.* **89**, 6671.

Kieffer, H.H., (1979) *J. Geophys. Res.* **84**, 4249.

Martin, L.J. and P.B. James, (1984) Abstracts from the MECA Workshop on Water on Mars.

Thomas, P.J. etal. (1979) *J. Geophys. Res.* **84**, 4621.

Tillman, J. E., (1981) Papers Presented at the Third Intl. Colloquium on Mars, LPI contribution 441, p. 267.

Ward, W.R. (1974a) *J. Geophys. Res.* **79**, 3375.

Ward, W.R. (1974b) *J. Geophys. Res.* **79**, 3387.

Warren, S.G. and W. J. Wiscomb, (1980) *J. Atmos. Sci.* **37**, 2734.

APPENDIX 1

POLAR RADIATION BUDGETS FROM IRTM OBSERVATIONS

Although the Martian polar regions were intensively studied by the Viking Infrared Thermal Mappers, it was not until after all the polar data were collected and processed that it was realized that the determination of year-long polar radiation budgets from the available observations might be feasible. This appendix describes the IRTM polar data set and the procedures that were used to determine the bolometric emission rates and planetary albedos presented in Chapter 2 in greater detail.

1. Bolometric Emission Rates

Bolometric rates of emission for the north and south polar regions were determined by using the measured fluxes in the five IRTM infrared channels in conjunction with an empirical spectral model. Model brightness temperatures were computed at 0.1 μ wavelength intervals by forming linear combinations of the measured IRTM brightness temperatures in selected wavelength intervals. Model parameters in the wavelength region of the 15 μ gaseous carbon dioxide absorption feature were determined by first convolving the IRTM spectral response with Mariner 9 IRIS spectra obtained under a variety of Martian conditions (Hanel *et al* 1972), and then determining the linear combinations of synthesized IRTM brightness temperatures that gave the best fit to the IRIS spectra in this region. Brightness temperatures outside the wavelength interval sensed by IRTM were assigned the measured brightness temperature from the nearest IRTM spectral band. Table A1-1 shows the wavelength intervals, and the formulas used to calculate brightness temperatures at their boundaries. Model brightness temperatures within each spectral interval were assumed to vary

Table A1-1. IRTM Bolometric Spectral Model

Wavelength Interval				Fraction of Total Radiated Power for Blackbodies at	
λ_{min} (μ)	λ_{max} (μ)	Brightness Temp at λ_{min} (K)	Brightness Temp at λ_{max} (K)	T=200K	T=140K
0	6.0	T_7	T_7	0.0021	0.0000
6.0	8.3	T_7	T_7	0.0225	0.0015
8.3	9.7	T_9	T_9	0.0329	0.0045
9.7	12.5	T_{11}	T_{11}	0.1031	0.0273
12.5	13.9	T_{11}	$\frac{6}{5}T_{11} - \frac{1}{5}T_{15}$	0.0620	0.0249
13.9	14.7	$\frac{6}{5}T_{11} - \frac{1}{5}T_{15}$	T_{15}	0.358	0.0171
14.7	14.9	T_{15}	$\frac{11}{10}T_{15} - \frac{1}{20}T_{11} - \frac{1}{20}T_{20}$	0.0090	0.0046
14.9	15.4	$\frac{11}{10}T_{15} - \frac{1}{20}T_{11} - \frac{1}{20}T_{20}$	T_{15}	0.0221	0.0119
15.4	16.2	T_{15}	$\frac{4}{5}T_{20} + \frac{1}{5}T_{15}$	0.352	0.0206
16.2	17.2	$\frac{4}{5}T_{20} + \frac{1}{5}T_{15}$	T_{20}	0.0428	0.0275
17.2	30.0	T_{20}	T_{20}	0.3675	0.3741
30.0	∞	T_{20}	T_{20}	0.2650	0.4860

Table A1-1. Spectral intervals and formulae used to synthesize complete emission spectra from IRTM brightness temperatures.

linearly between the values at their boundaries with wavelength. Also shown in Table A1-1 are the fractions of total radiated power contained within each wavelength interval for 200 K and 140 K blackbodies.

The angular coverage obtained by IRTM was such that near simultaneous observations of the polar regions at a wide range of emission angles ϑ occurred primarily during the sunlit spring and summer seasons. The IRTM emission angle coverage is summarized in Figs. A1-1 and A1-2, where T_7, T_9, T_{11}, T_{15} and T_{20} are the 10-day radiance weighted average brightness temperatures in the IRTM infrared channels for $0° \leq \vartheta \leq 60°$, and $T_{7H}, T_{9H}, T_{9H}, T_{11H}, T_{15H}$ and T_{20H} are the 10-day radiance weighted average brightness temperatures for $60° < \vartheta < 88°$. These brightness temperatures were used to synthesize 10-day average bolometric emission rates for $0° \leq \vartheta \leq 60°$ and $60° < \vartheta < 90°$ with the empirical spectral model. Total bolometric emission rates $F\uparrow_{IR}$ were then calculated by averaging the low emission angle bolometric rates with the high emission angle bolometric rates with weighting factors of 0.75 and 0.25, respectively, to account for the fractions of total emitted power expected within the two emission angle bins for an isotropically emitting blackbody. During periods in which high emission angle data were acquired intermittently, differences between the radiance weighted average brightness temperatures at high and low emission angles were assumed to be similar to those that were measured during nearby 10-day intervals. During seasons when high emission angle data were not acquired, no brightness temperature variations with emission angle were assumed.

Uncertainties in $F\uparrow_{IR}$ introduced by the empirical spectral model and the emission angle binning are difficult to assess because "real" bolometric spectra of the north and south study regions at all possible emission angles during the year of Viking observations are not available. Uncertainties in $F\uparrow_{IR}$ introduced

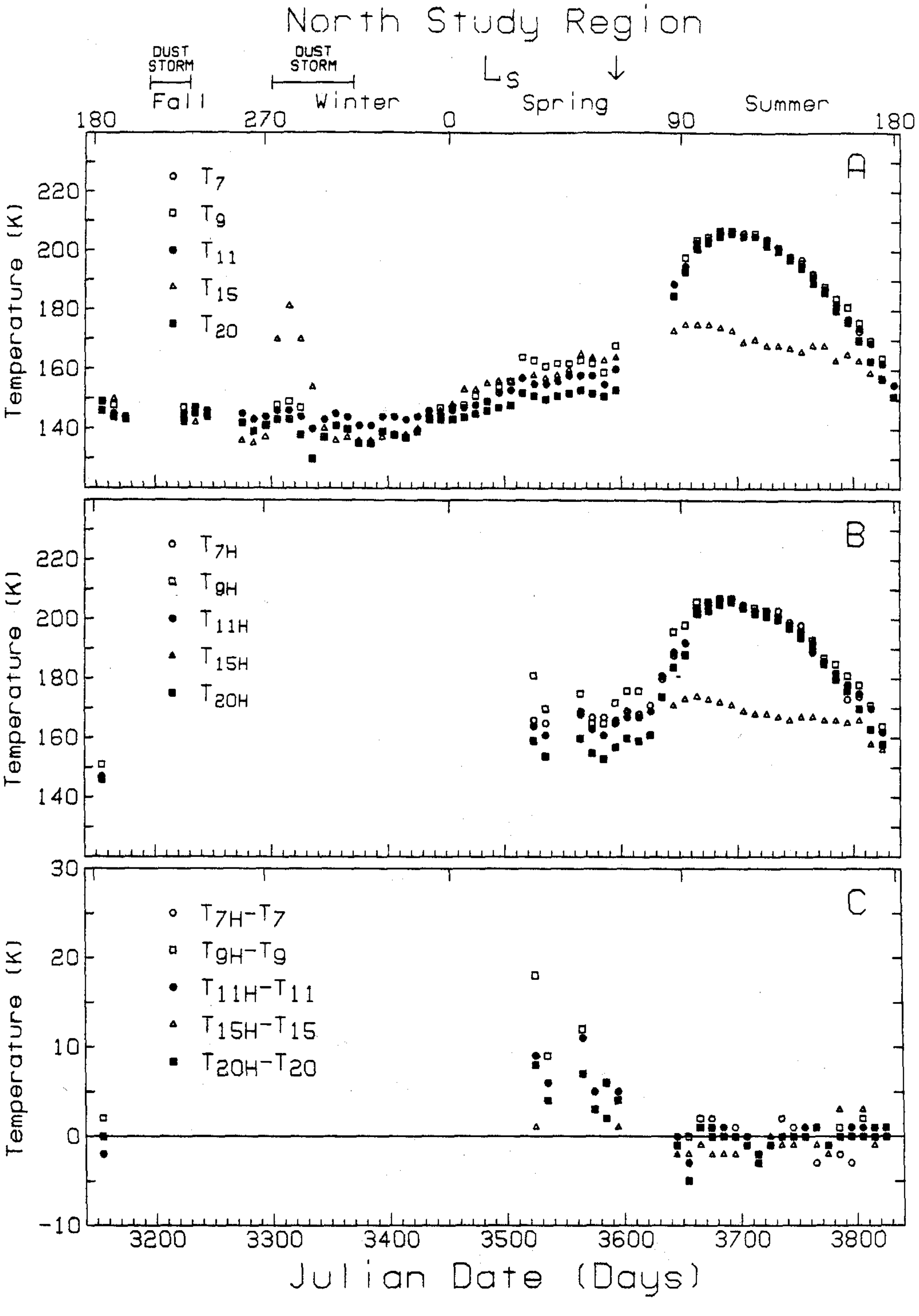

Fig. A1-1. 10-day averaged IRTM north study region brightness temperatures. (A) T_7, T_9, T_{11}, T_{15}, and T_{20} for emission angles $\vartheta < 60°$. (B) T_{7H}, T_{9H}, T_{11H}, T_{15H}, and T_{20H} for emission angles $\vartheta > 60°$. (C) Differences between the 10-day averaged IRTM brightness temperatures for $\vartheta < 60°$ and $\vartheta > 60°$.

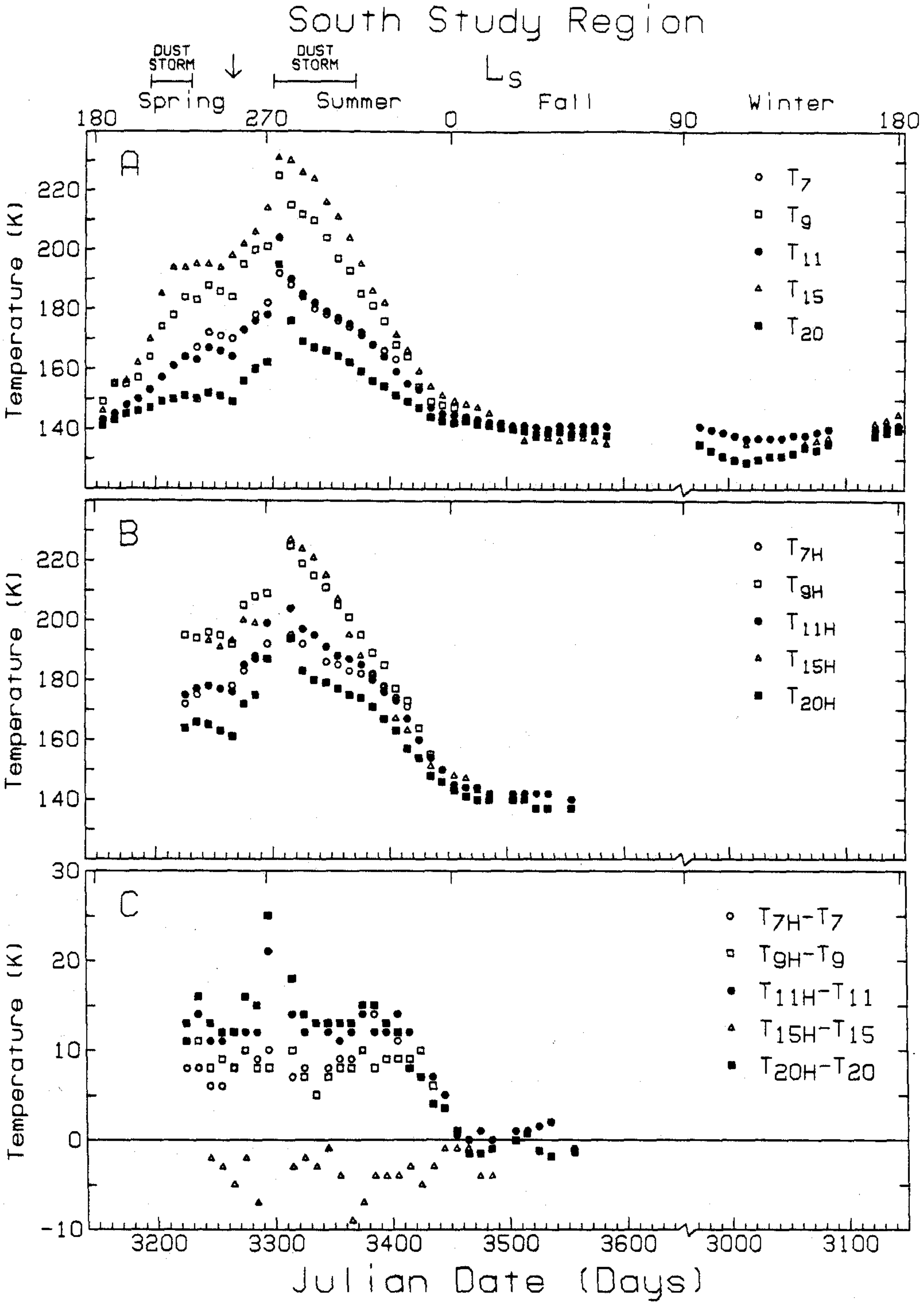

Fig. A1-2. Same as Fig. A1-1 for the south study region.

by the empirical spectral model for $\lambda < 30\ \mu$ are not reflected in the upper and lower limits in $F\uparrow_{IR}$ shown in Chapter 2 because of the likelihood that these errors are overshadowed by uncertainties in the unmeasured emission spectrum for $\lambda > 30\ \mu$. As shown in Table A1-1, the long wavelength part of the spectrum can contain up to one-half of the total emitted flux at the lowest polar temperatures that were recorded by IRTM. To account for these uncertainties, brightness temperatures for $\lambda > 30\ \mu$ were assumed to be bracketed by $T_{20} \pm (T_{11} - T_{20})$, thus making $F\uparrow_{IR}$ most uncertain during periods of high spectral contrasts. The upper and lower limits for the emission rates of the north and south study regions shown in Chapter 2. contain additional ±1% uncertainties for absolute calibration.

2. Planetary Albedos

The broadband spectral response, the spatial resolution and the absolute calibration of the IRTM solar reflectance channels would have made them almost ideal for measuring the planetary albedos of the Martian north and south polar regions, had the angular coverage been more complete. The characterization of the complex time-dependent bidirectional nature of reflected solar radiation fields from a limited set of spacecraft observations is the most difficult task in most radiation balance studies. One approach that is often employed in terrestrial work is to classify the target as land, ocean, clouds, snow or something else and then "fit" the available observations to a model for the bidirectional reflectance of that target to synthesize complete angular coverage. Bidirectional reflectance models vary widely in complexity and are generally formulated through the use of varying quantities of raw data, theory and guesswork. The modeling and fitting approach can work well in situations where the bidirectional reflectance patterns of the targets in question are well known in advance, but in situations where the bidirectional reflectance patterns are being measured for the first time (which is the case for this study), the original data provide much better guides to the true bidirectional reflectance of targets than models.

The procedure employed in this study was to create empirical, time-dependent bidirectional angular distributions directly from the IRTM solar reflectance measurements of the north and south study regions. This was accomplished by binning sucessive groups of approximately 40 days of IRTM Lambert albedo data as functions of emission angle ϑ and solar azimuth angle ψ. The data were divided in this way to minimize variations in measured Lambert albedos at constant emission angles and variations in solar zenith angles within each time period while retaining enough data to enable the bidirectional reflectance to be determined during each time period with the least ambiguity. Figs. A1-3a through A1-11a show all the original binned data for $\varphi<80^\circ$ where φ is the solar zenith angle. The data are projected so that distances from the origin are proportional to the sine of the emission angle, which makes the aerial average of the Lambert albedos in each plot equal to the average planetary albedo during that period. All bidirectional reflectance patterns were assumed to be bilaterally symmetric. Each plot shows simultaneously the number of Lambert albedos in each bin, the average Lambert albedo in each bin, the standard deviations of the Lambert albedos in each bin and an indication as to whether the bin contains data from Viking Orbiter 1 or Viking Orbiter 2. Almost all the plots show remarkably smooth, systematic variations in measured Lambert albedos with ϑ and ψ over the angles that were covered.

To determine $\overline{A_p}$, the average planetary albedos of the north and south study regions during each period, the data shown in Figs. A1-3a through A1-11a were contoured by hand and aerially averaged with the aid of a planimeter. The contours were constrained to match the original data as best as possible within the angles covered by IRTM. Outside the angles covered by IRTM, the contours were mostly a matter of taste but it must be kept in mind that it is not the shapes of the contours but the values of the functions defined by the contours integrated over the full bidirectional reflectance hemisphere that determine the $\overline{A_p}$. Experience from terrestrial studies (Dirmhirn and Eaton, 1975; Taylor and Stowe,1984) and from the data presented here shows that bidirectional reflectance patterns are generally slowly varying functions of ϑ and ψ except near the specular point ($\psi \approx 180°$, $\vartheta \approx \varphi$) where Lambert albedos can rapidly rise to unity and beyond. This phenomenon was definitely observed by IRTM during the spring seasons at both poles. To account for uncertainties in $\overline{A_p}$ during periods in which near specular point coverage was not available, the available data were contoured twice, once to give non-specular bidirectional reflectance patterns with "low" planetary albedos and once to give specular bidirectional reflectance patterns with "high" planetary albedos. Contoured bidirectional reflectance plots for the data in Figs. A1-3a through A1-11a and the resulting planetary albedos are shown in Figs. A1-3bc through A1-11bc. Fig. A1-12 and A1-13 show the period boundaries and derived values of $\overline{A_p}$ for the north and south study regions.

The last step in determining A_p, the 10-day averaged planetary albedos for the study regions was to account for observed temporal variations in the reflectances of the regions within each time period. In the south, a very fine set of continuous solar reflectance measurements for $\vartheta < 30°$ were obtained throughout the spring and summer seasons. Lambert albedos for $\vartheta < 30°$ are shown in Fig. A1-13. Unfortunately this type of data was not obtained with sufficient regularity in the north to provide a good indication as to temporal reflectance variations that may have occurred. A less useful alternative data

Figs. A1-3 through A1-11. Bidirectional reflectance observations and contours for the north and south study regions.

Figures designated "a" show binned Lambert albedos as a function of emission angle (radial) and solar azimuth angle (azimuthal). The sun is at 0° azimuth for all plots. The boundaries of the bins are designated by boxes. In the far left-hand corner of each box that contains data is the letter "A" or "B." "A" means the data in this bin were obtained by the IRTM aboard Viking Orbiter 1; "B" means the same for Viking Orbiter 2. The number at the top of each box is the average Lambert albedo of the observations within that bin times 1000. The number in the middle of each box is the standard deviation of the Lambert albedos in that bin from the mean times 1000. The number at the bottom of each box is the number of individual IRTM solar reflectance observations within each bin. The time periods covered by each map and the constraints on the solar zenith angle "phi" used to produce each map are shown in the upper right hand corner.

Figures designated "b" and "c" show hand drawn contours of Lambert albedo from the binned data in the corresponding "a" figure. The averaged value of the contoured Lambert albedos on each plot, $\overline{A_P}$ is also shown. In cases where the available binned data were judged insufficient to accurately characterize $\overline{A_P}$, two contour plots were made of the binned data — one to give "high" values of $\overline{A_P}$, one to give "low" values of $\overline{A_P}$.

NORTH STUDY REGION 3500<JD<3560 70<PHI<80

BINNED LAMBERT ALBEDOS

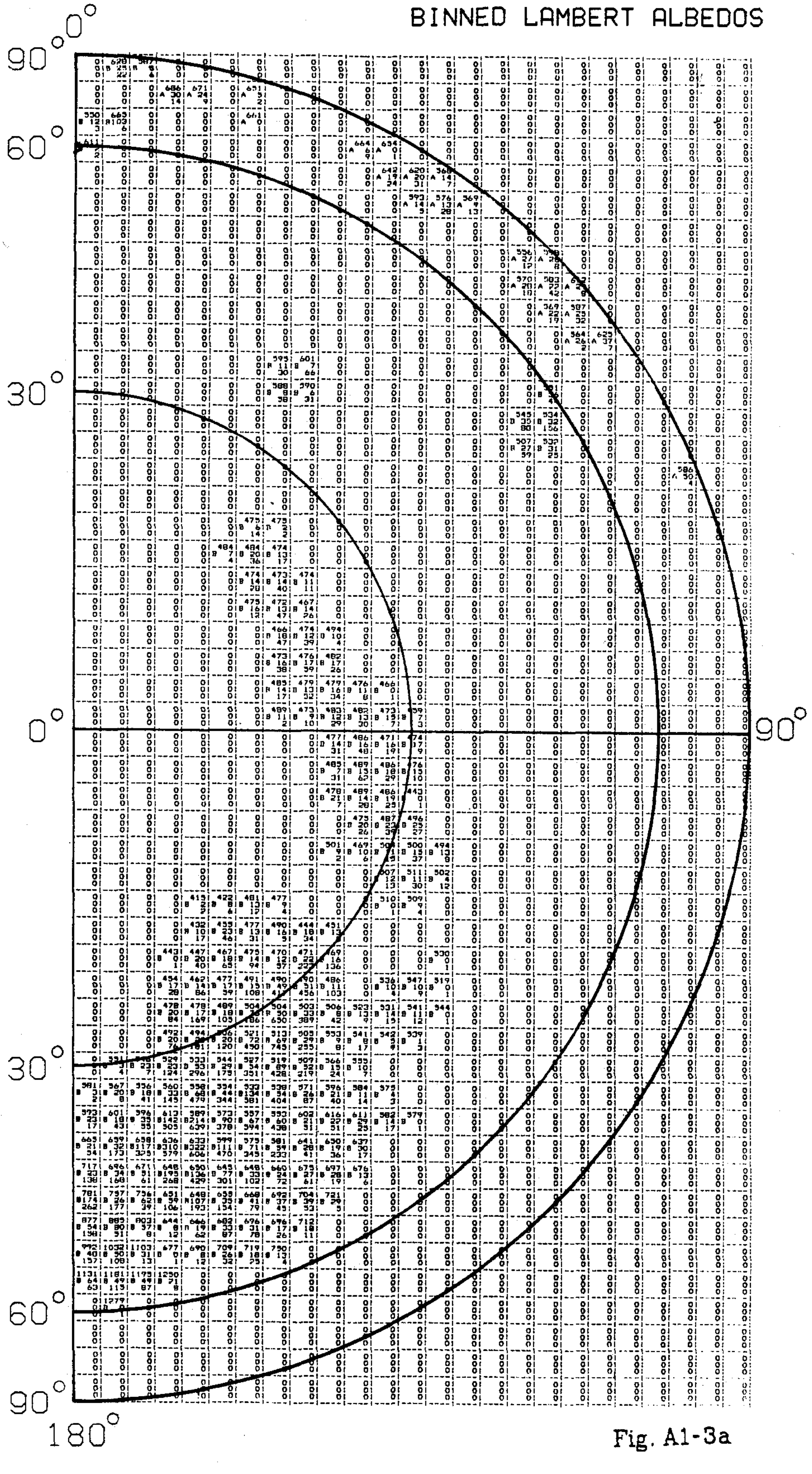

Fig. A1-3a

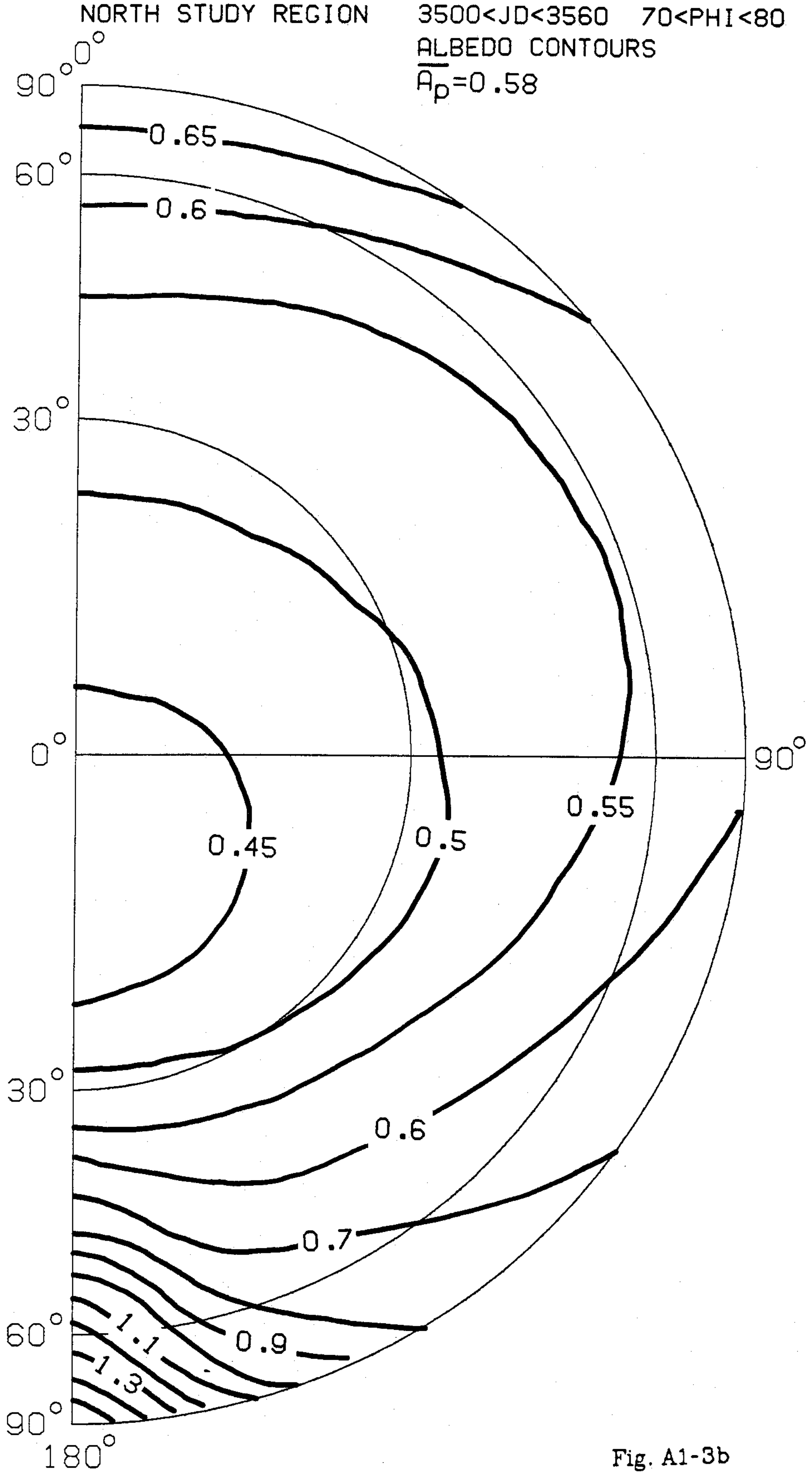
NORTH STUDY REGION
3500<JD<3560 70<PHI<80
ALBEDO CONTOURS
$\overline{A}_p$=0.58
90°
0°
60°
30°
0°
90°
30°
60°
90°
180°
0.65
0.6
0.45
0.5
0.55
0.6
0.7
0.9
1.1
1.3

Fig. A1-3b

NORTH STUDY REGION   3560<JD<3630   60<PHI<70
BINNED LAMBERT ALBEDOS

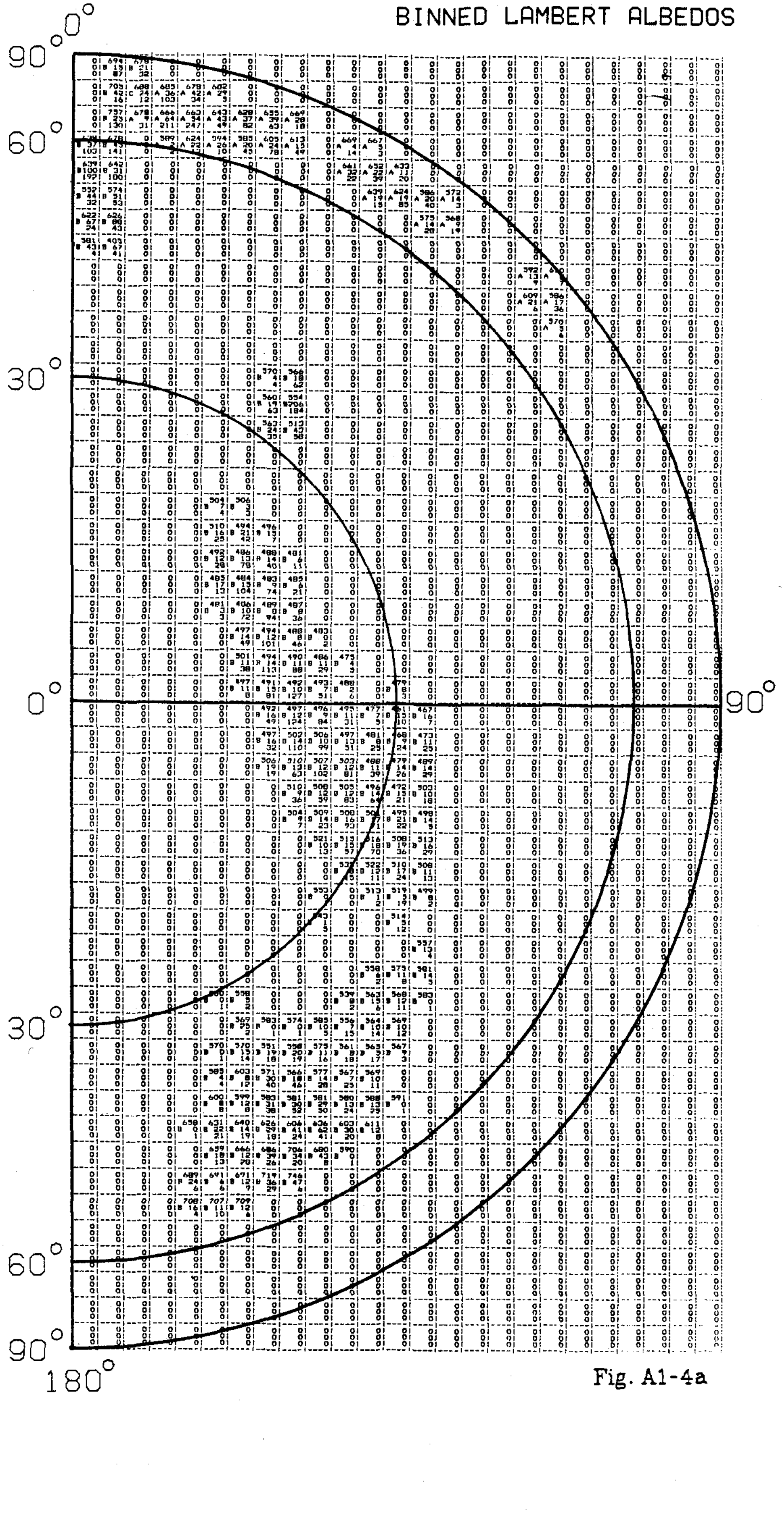

Fig. A1-4a

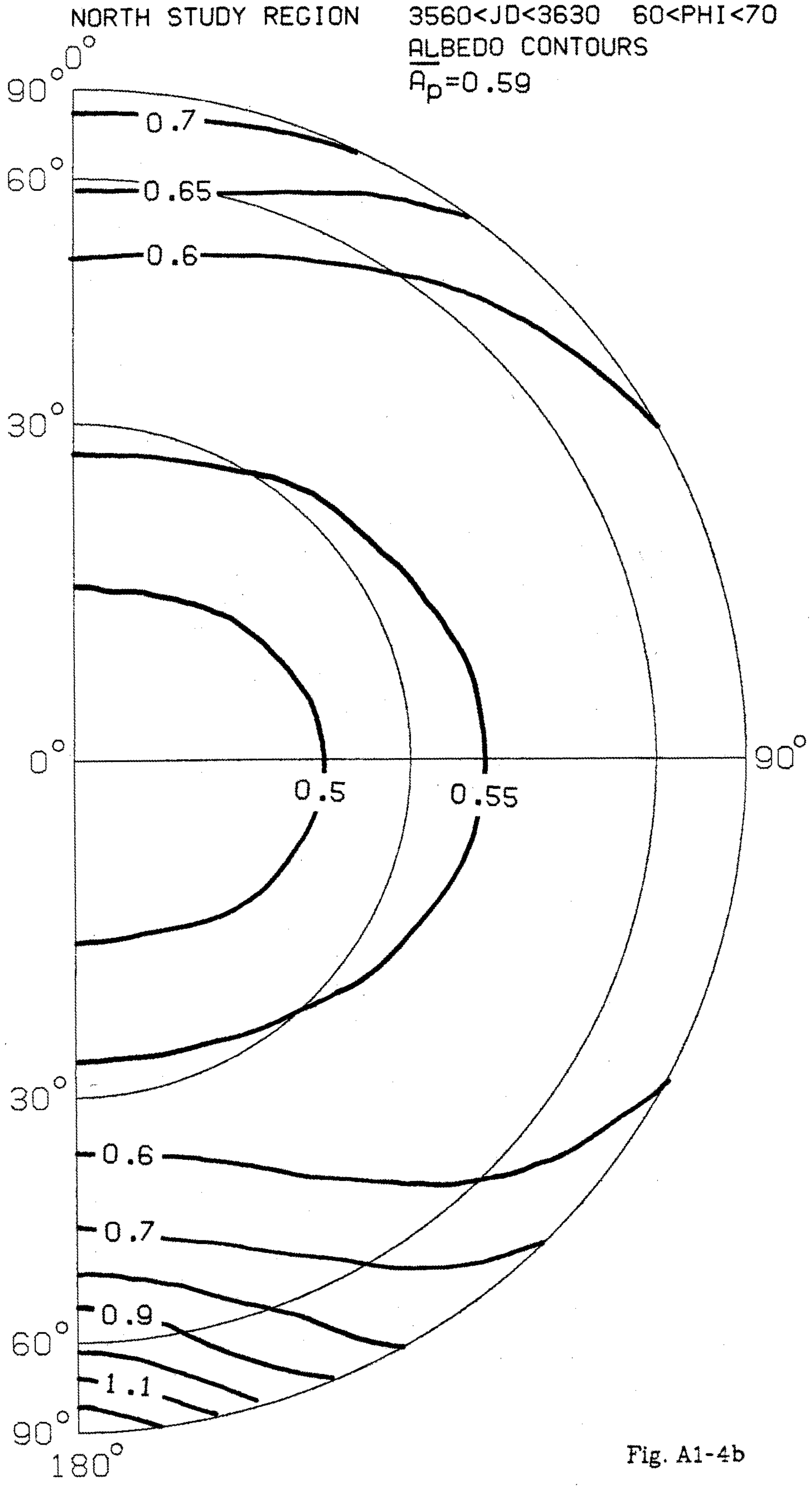
NORTH STUDY REGION 3560<JD<3630 60<PHI<70
ALBEDO CONTOURS
$\overline{A}_p$=0.59
0°
90°
60°
30°
0°
30°
60°
90°
180°
90°
0.7
0.65
0.6
0.5
0.55
0.6
0.7
0.9
1.1

Fig. A1-4b

NORTH STUDY REGION   3630<JD<3730   60<PHI<70
BINNED LAMBERT ALBEDOS

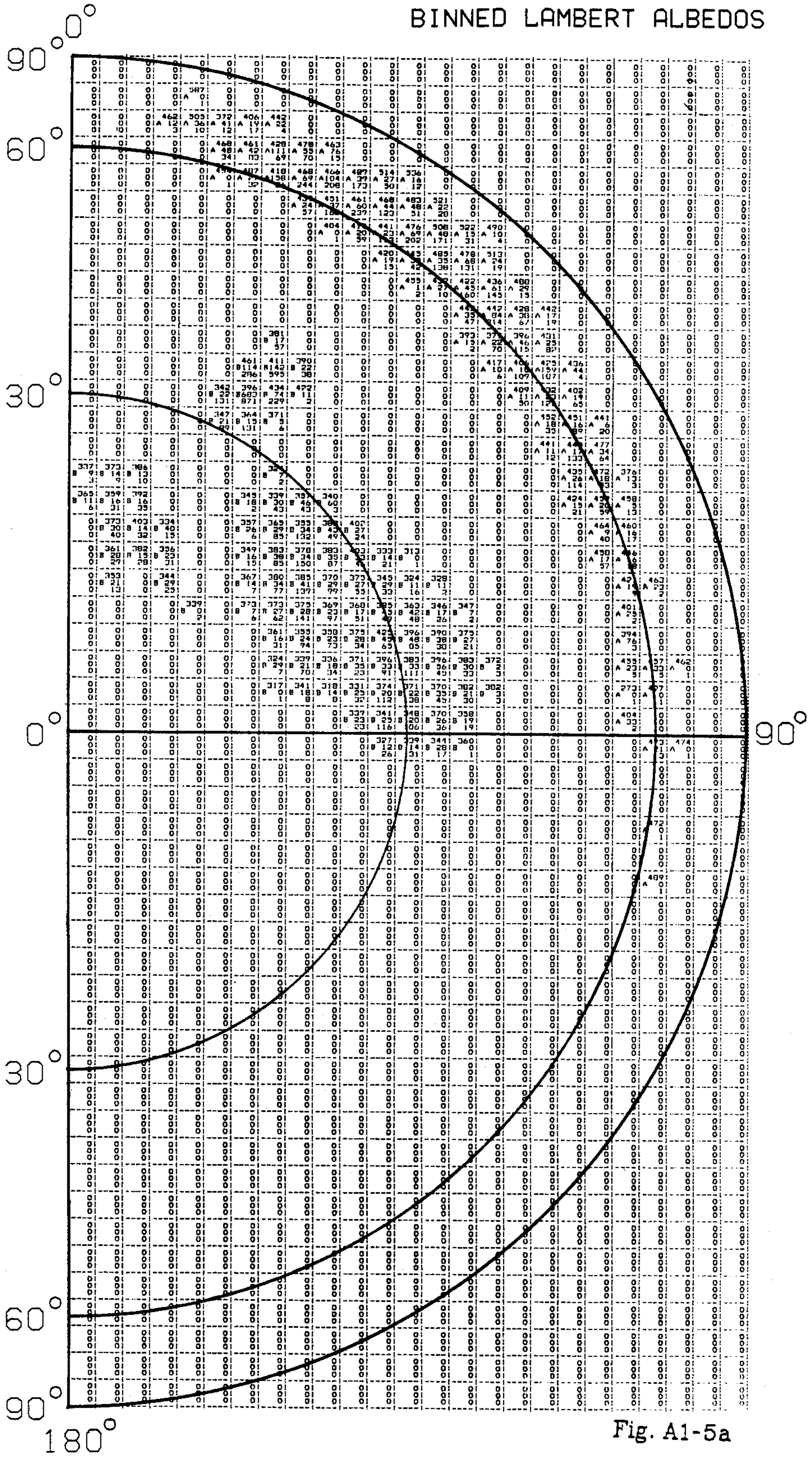

Fig. A1-5a

NORTH STUDY REGION   3630<JD<3730   60<PHI<70

LOW ALBEDO CONTOURS

$\overline{A_p}=0.45$

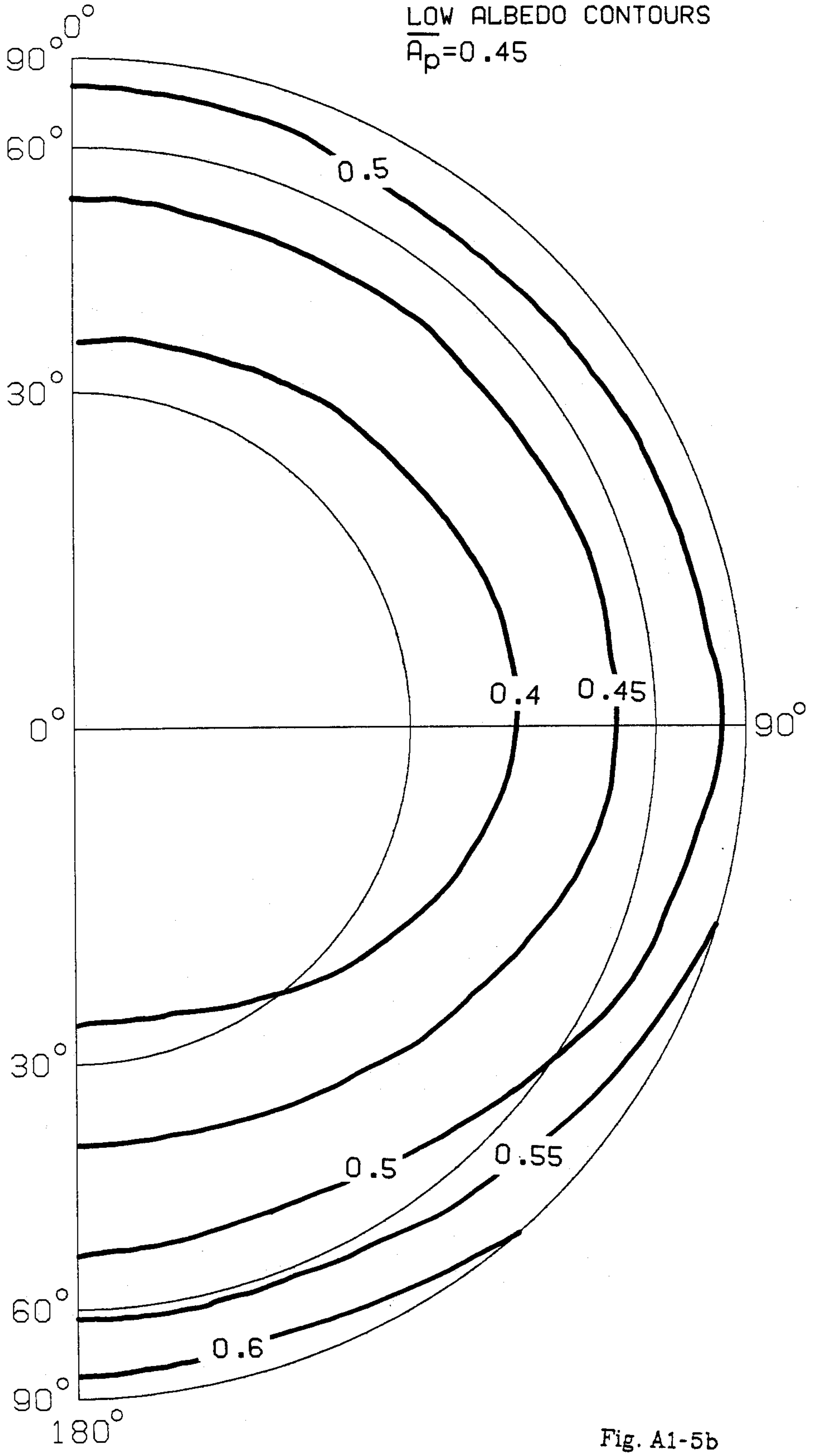

Fig. A1-5b

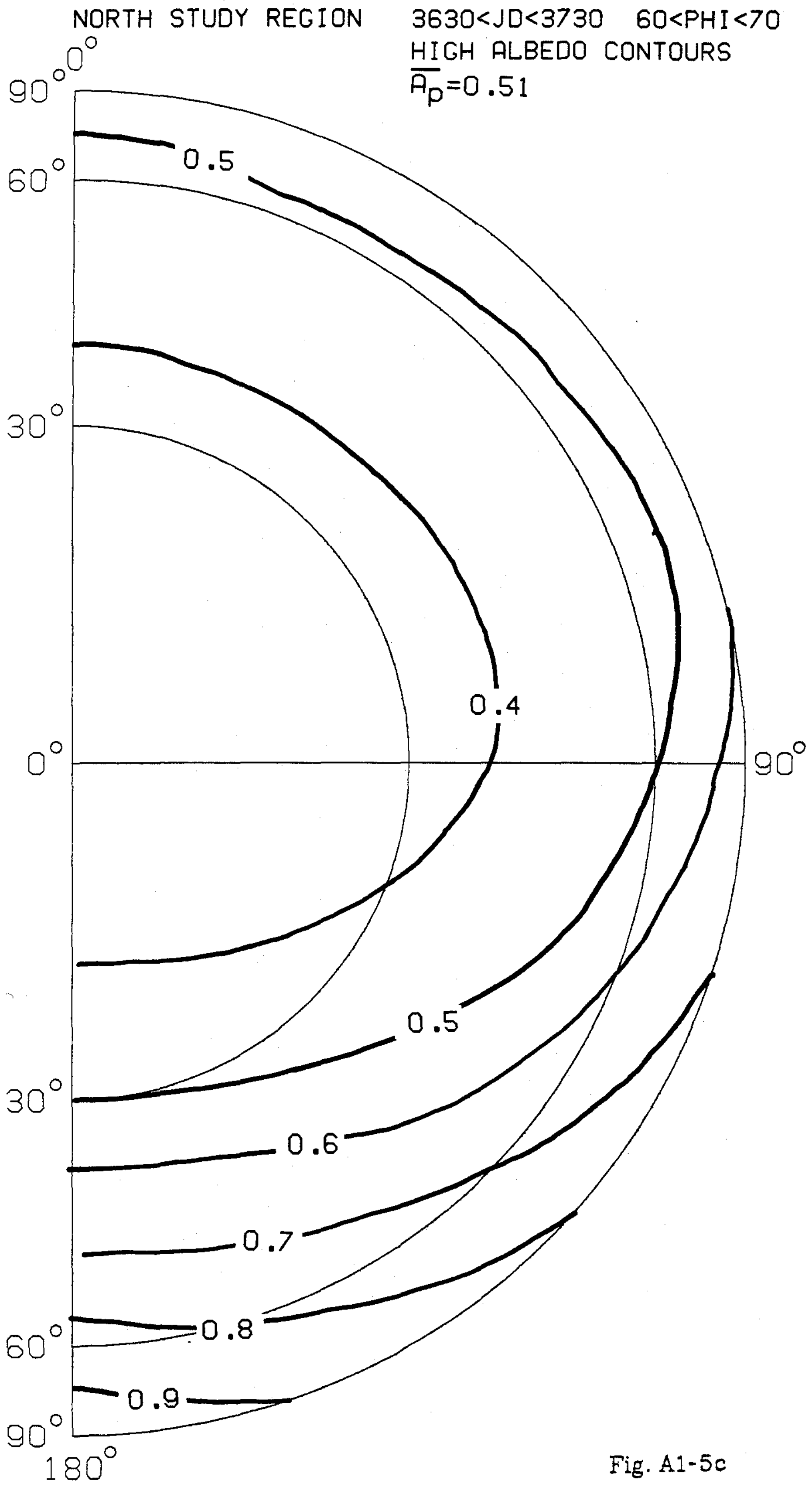
NORTH STUDY REGION 3630<JD<3730 60<PHI<70
HIGH ALBEDO CONTOURS
$\overline{A_p}$=0.51
0°
90°
60°
30°
0°
90°
30°
60°
90°
180°
0.5
0.4
0.5
0.6
0.7
0.8
0.9

Fig. A1-5c

NORTH STUDY REGION 3730<JD<3810 70<PHI<80
BINNED LAMBERT ALBEDOS

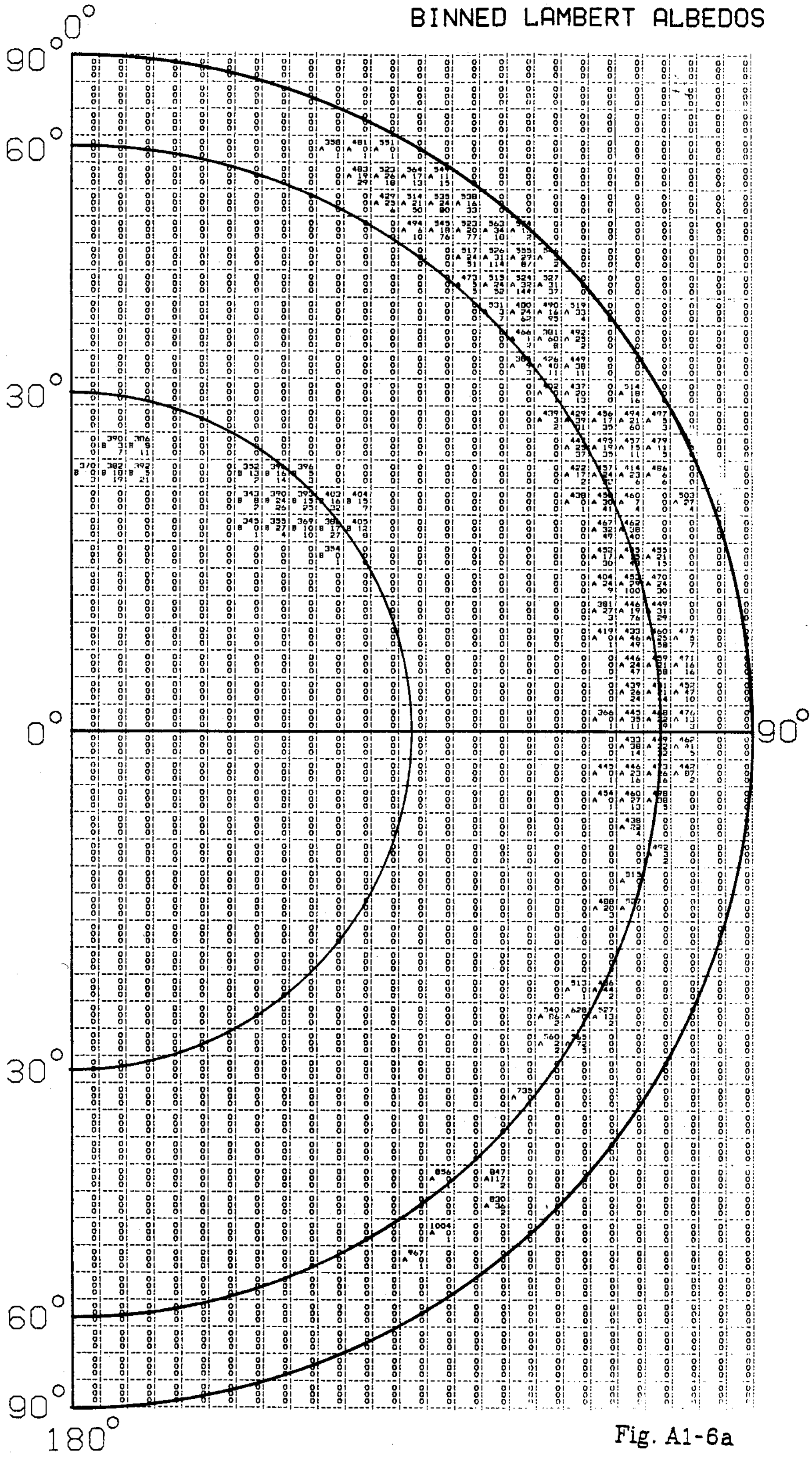

Fig. A1-6a

NORTH STUDY REGION 3730<JD<3810 70<PHI<80
<u>LOW</u> ALBEDO CONTOURS
$\bar{A}_p=0.46$

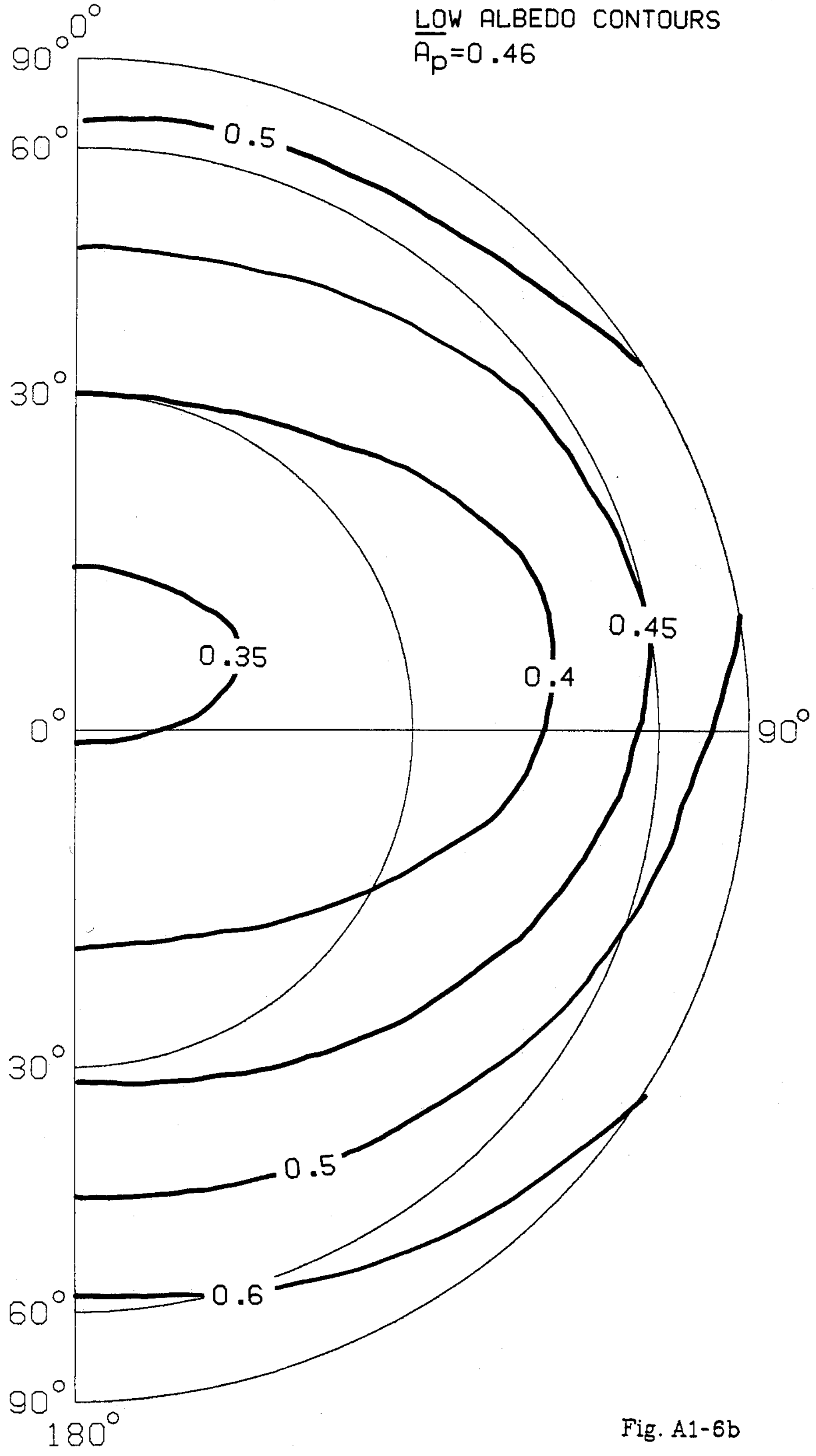

Fig. A1-6b

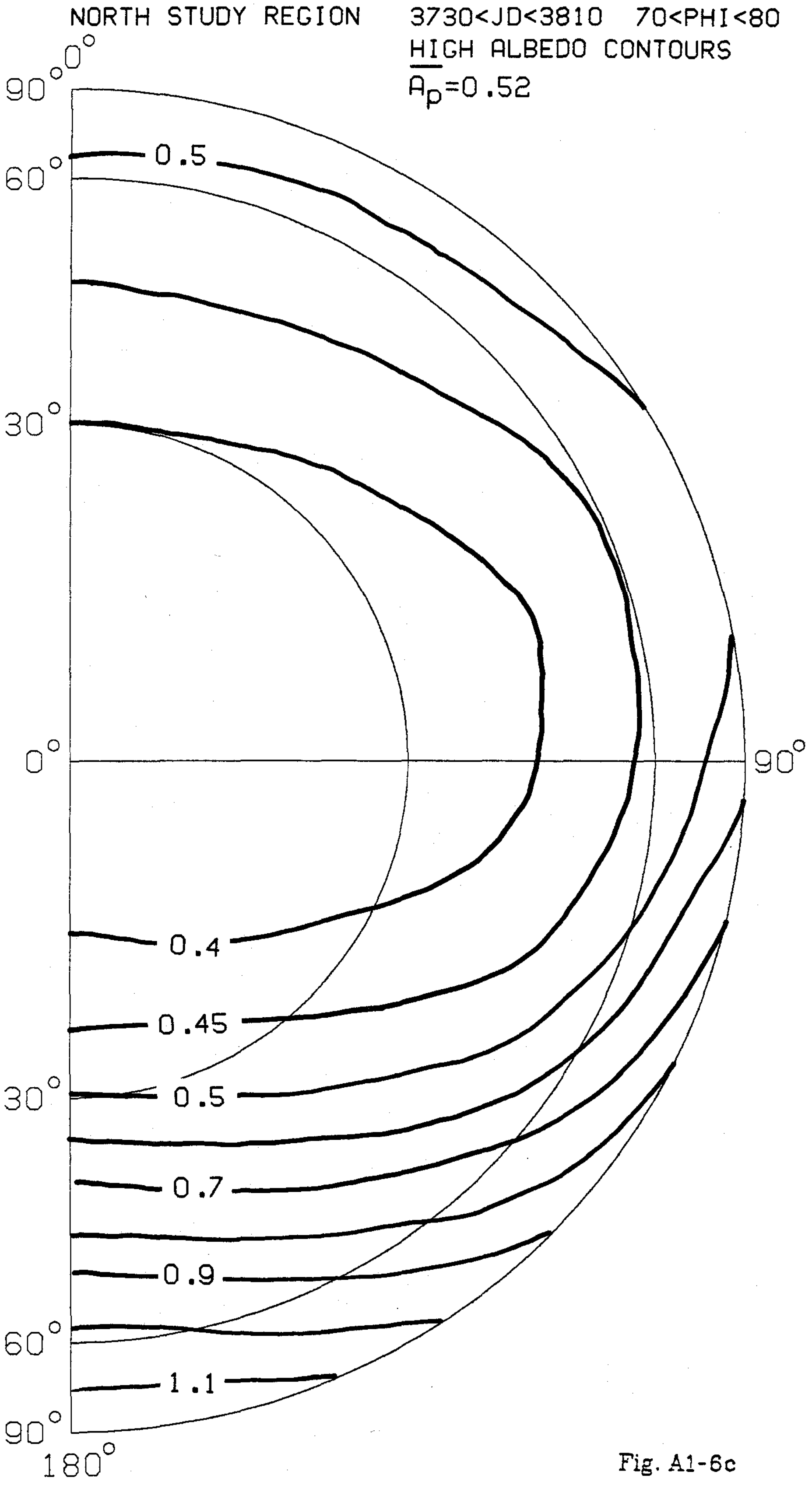
NORTH STUDY REGION
3730<JD<3810 70<PHI<80
HIGH ALBEDO CONTOURS
$\overline{A}_p$=0.52
0°
90°
60°
30°
0°
30°
60°
90°
180°
90°
0.5
0.4
0.45
0.5
0.7
0.9
1.1

Fig. A1-6c

SOUTH STUDY REGION 3190<JD<3240 70<PHI<80
BINNED LAMBERT ALBEDOS

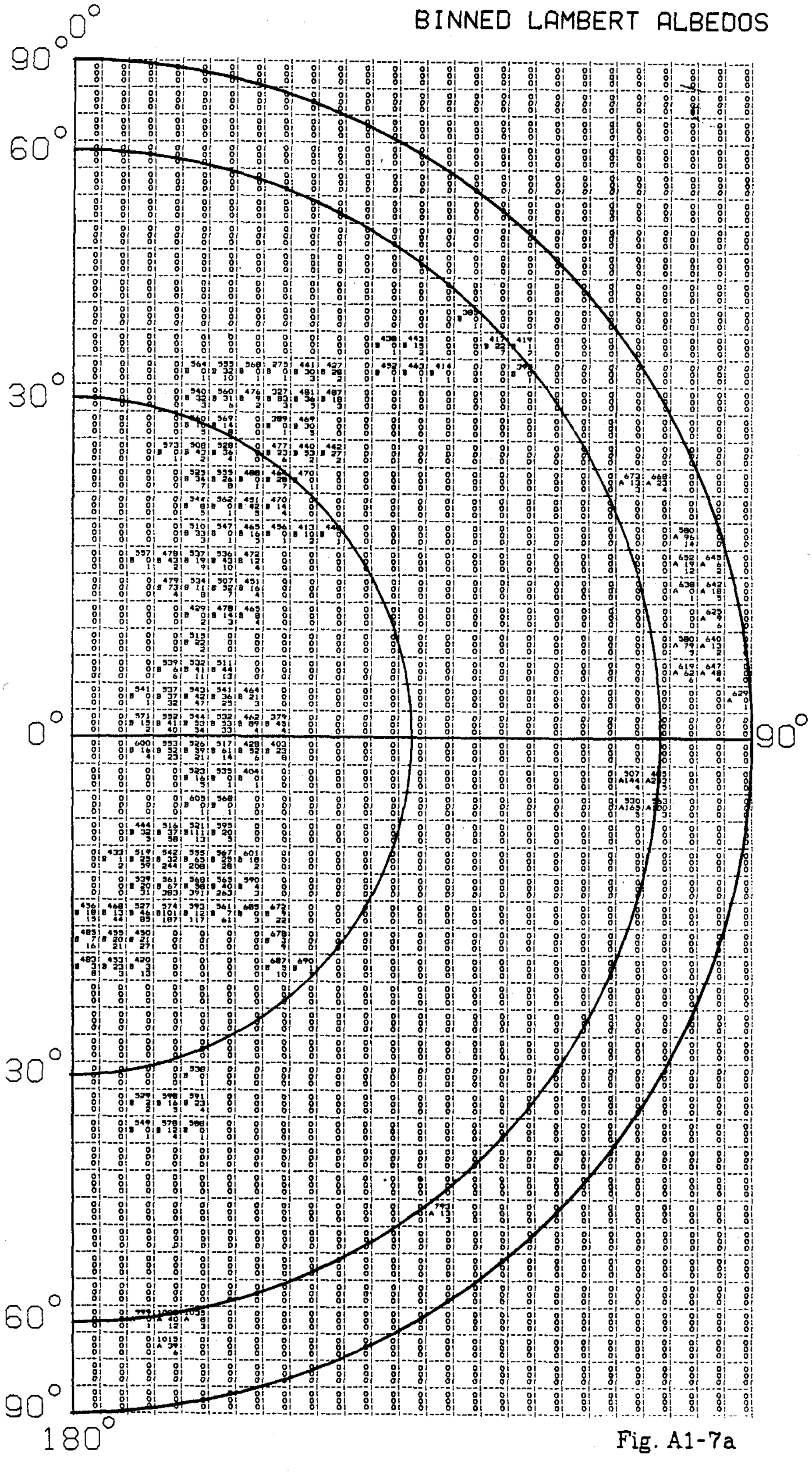

Fig. A1-7a

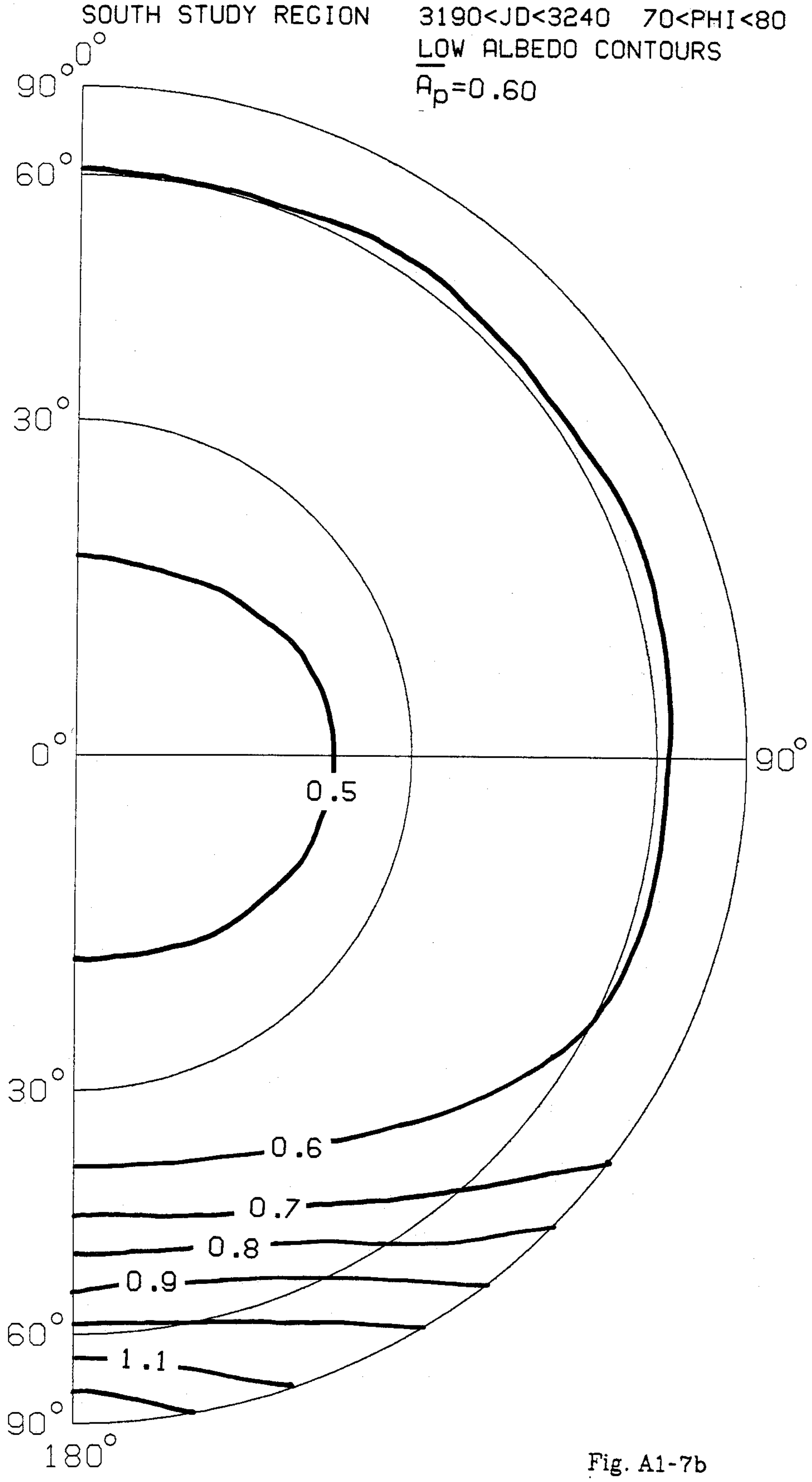
SOUTH STUDY REGION
3190<JD<3240 70<PHI<80
LOW ALBEDO CONTOURS
$\bar{A}_p$=0.60
90°
0°
60°
30°
0°
90°
0.5
30°
0.6
0.7
0.8
0.9
60°
1.1
90°
180°

Fig. A1-7b

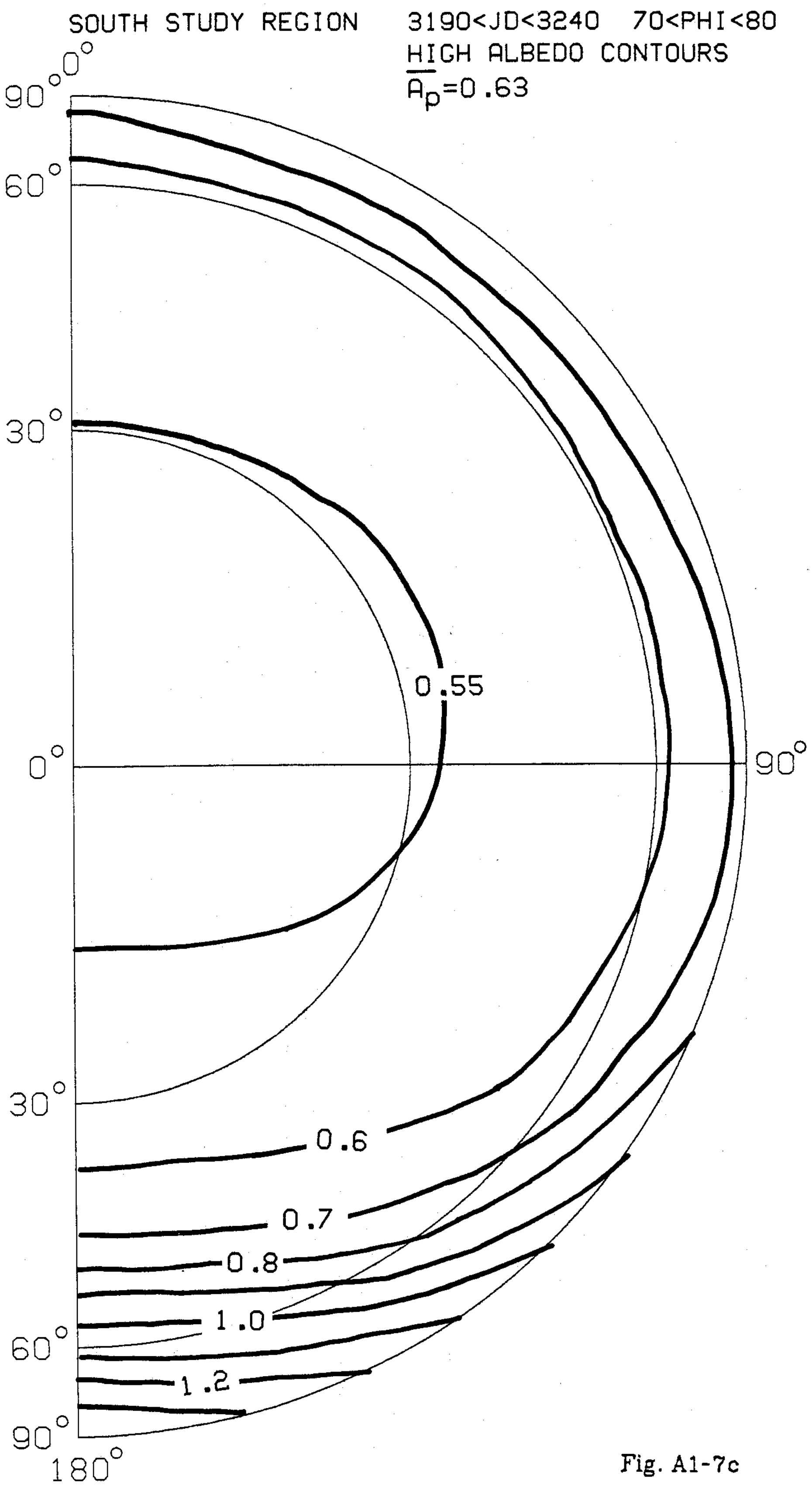
SOUTH STUDY REGION
3190<JD<3240 70<PHI<80
HIGH ALBEDO CONTOURS
$\overline{A}_p$=0.63
0°
90°
60°
30°
0°
90°
30°
60°
90°
180°
0.55
0.6
0.7
0.8
1.0
1.2

Fig. A1-7c

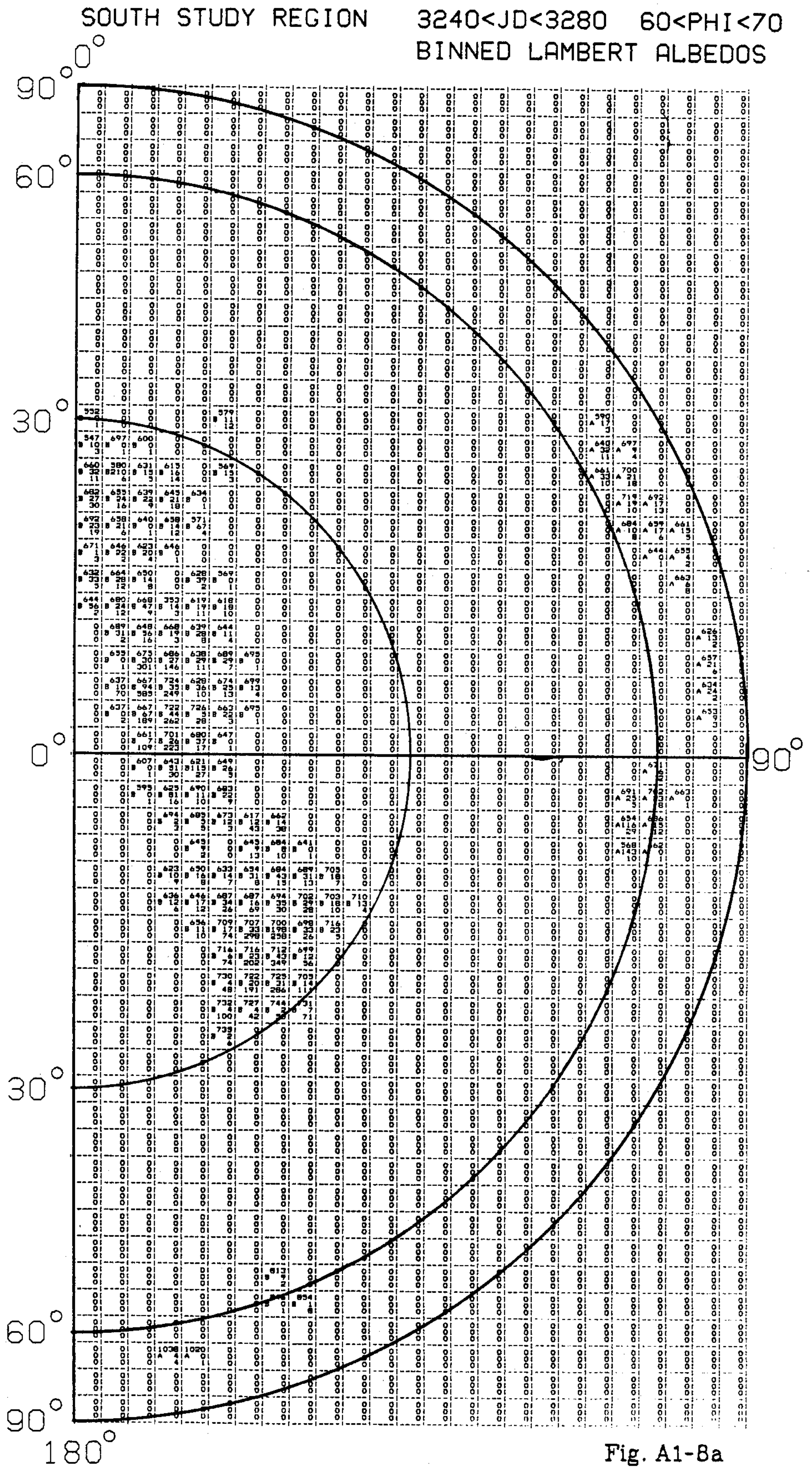
SOUTH STUDY REGION 3240<JD<3280 60<PHI<70
BINNED LAMBERT ALBEDOS

Fig. A1-8a

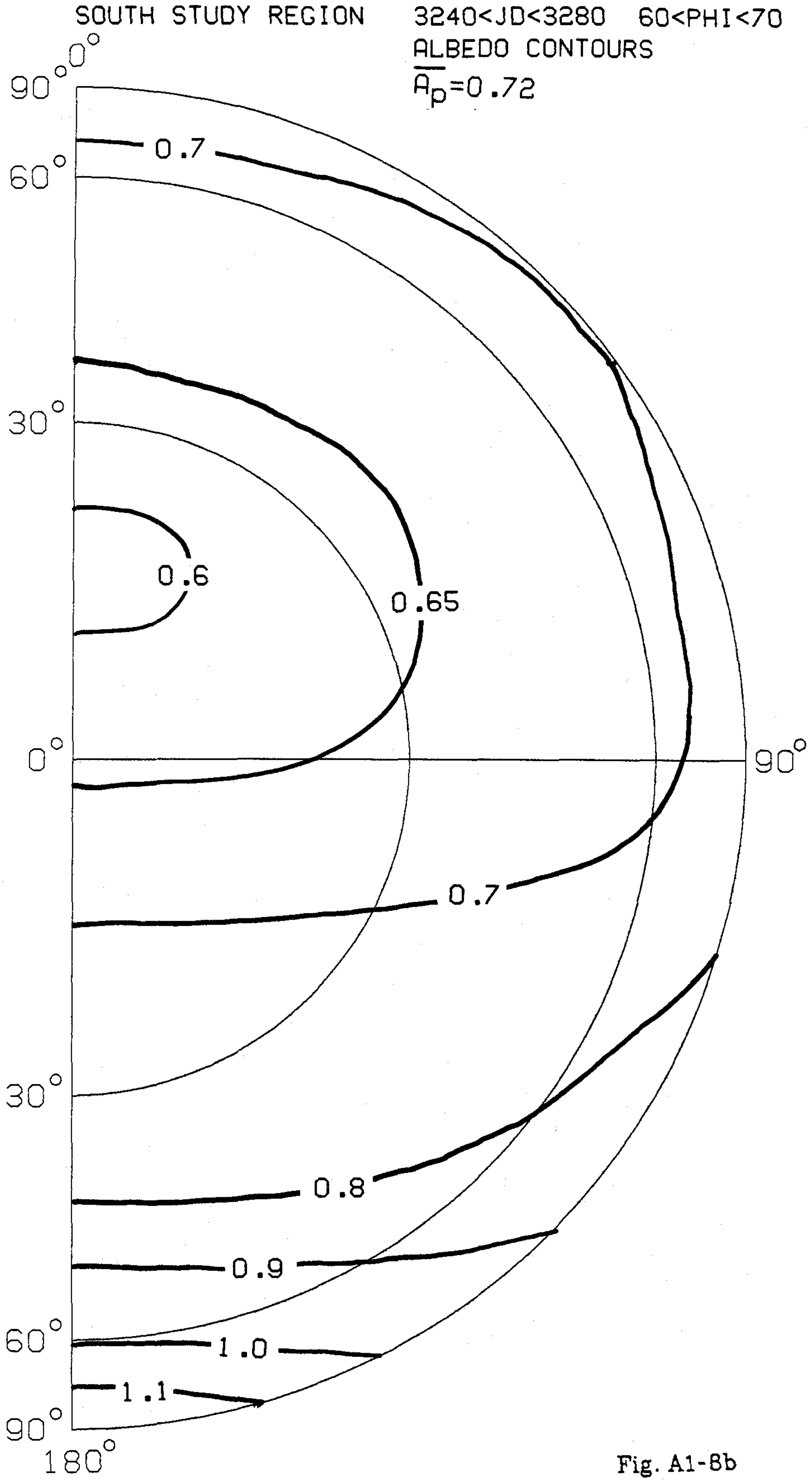
SOUTH STUDY REGION
3240<JD<3280 60<PHI<70
ALBEDO CONTOURS
$\overline{A}_p$=0.72
90°
0°
60°
30°
0°
90°
30°
60°
90°
180°
0.7
0.6
0.65
0.7
0.8
0.9
1.0
1.1

Fig. A1-8b

SOUTH STUDY REGION 3305<JD<3320 60<PHI<70
BINNED LAMBERT ALBEDOS

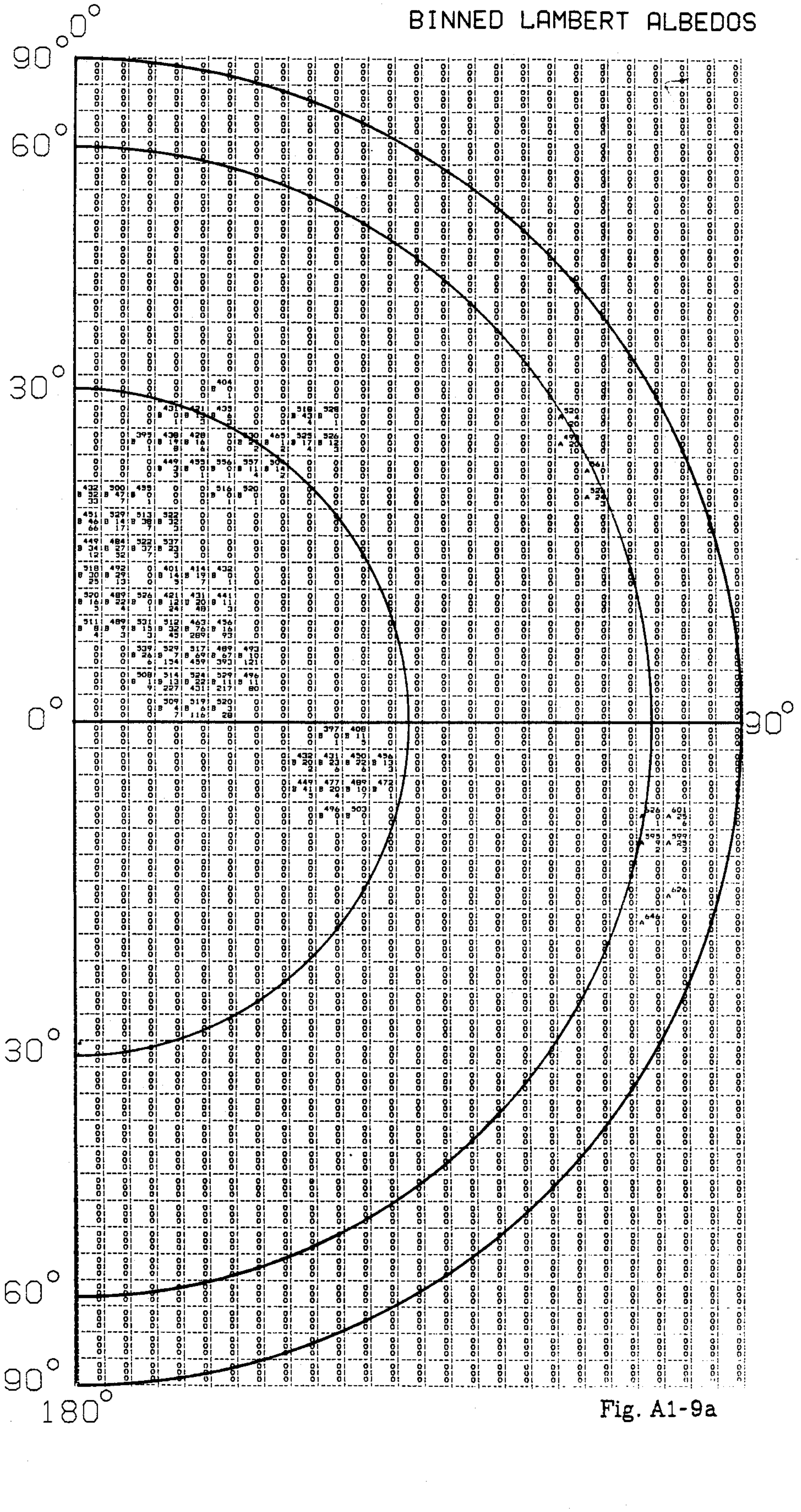

Fig. A1-9a

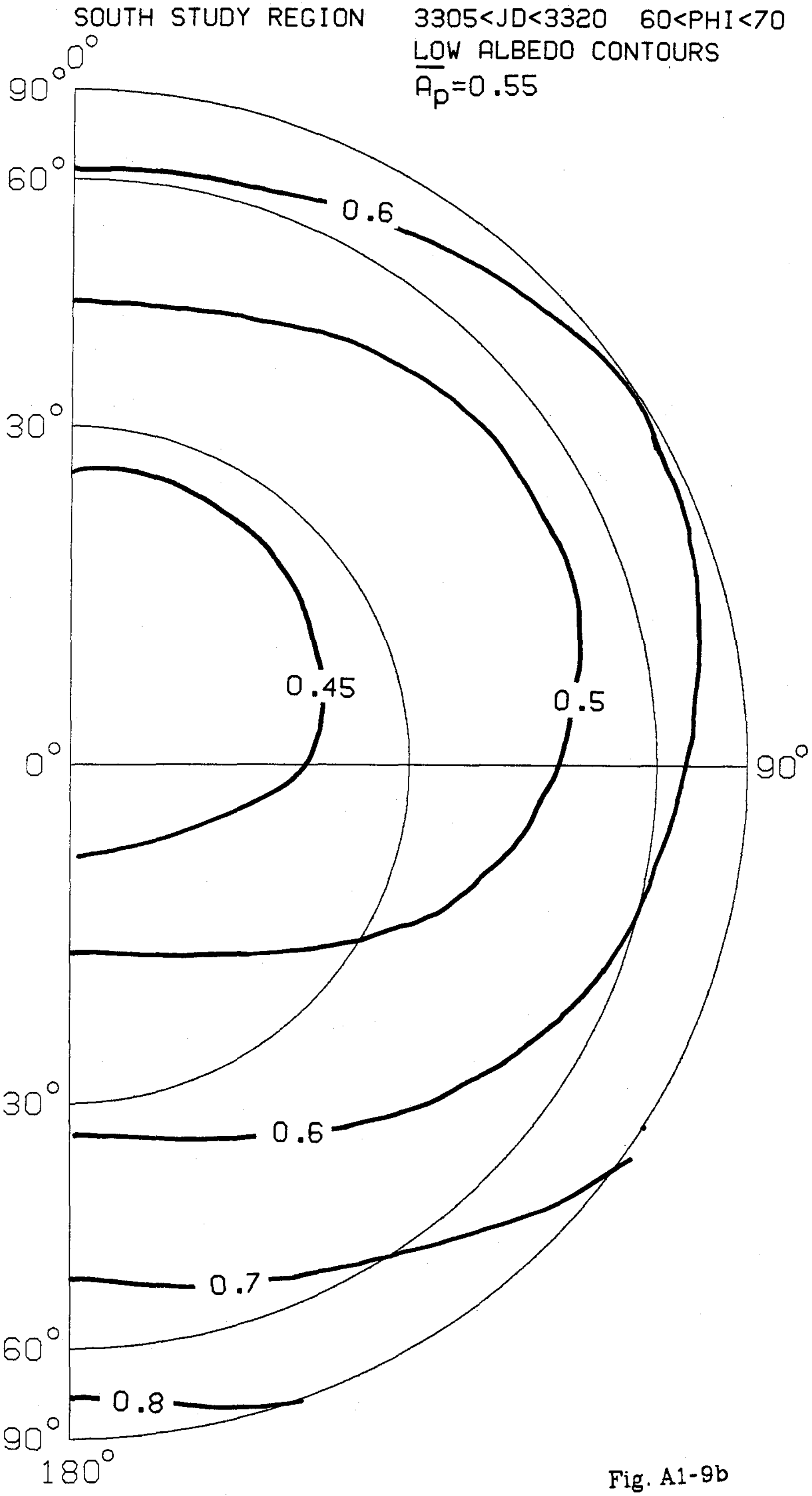

SOUTH STUDY REGION 3305<JD<3320 60<PHI<70

LOW ALBEDO CONTOURS

$\overline{A}_p=0.55$

Fig. A1-9b

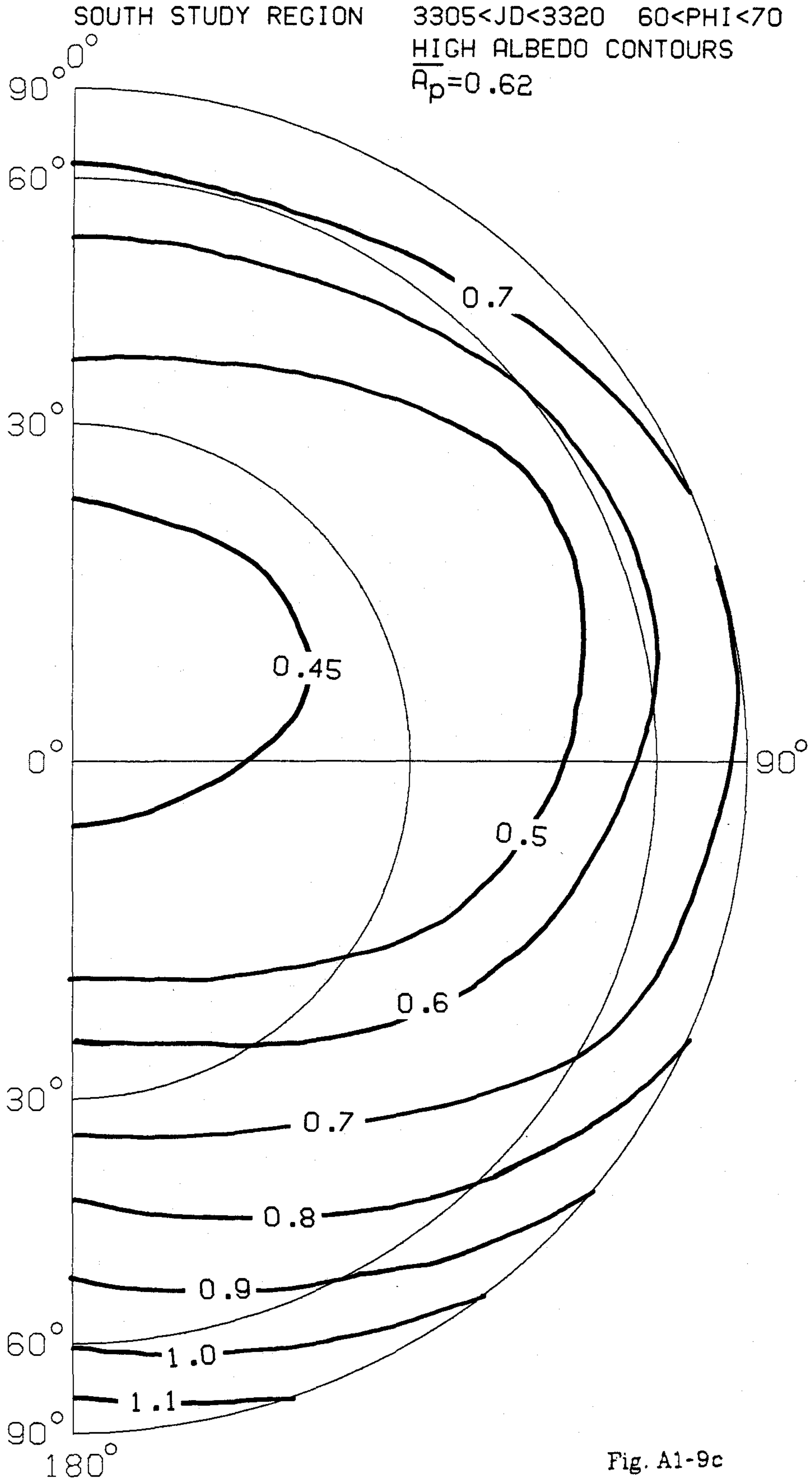
SOUTH STUDY REGION 3305<JD<3320 60<PHI<70
HIGH ALBEDO CONTOURS
$\overline{A_p}$=0.62
90°
0°
60°
30°
0°
90°
30°
60°
90°
180°
0.7
0.45
0.5
0.6
0.7
0.8
0.9
1.0
1.1

Fig. A1-9c

SOUTH STUDY REGION 3320<JD<3350 60<PHI<70
BINNED LAMBERT ALBEDOS

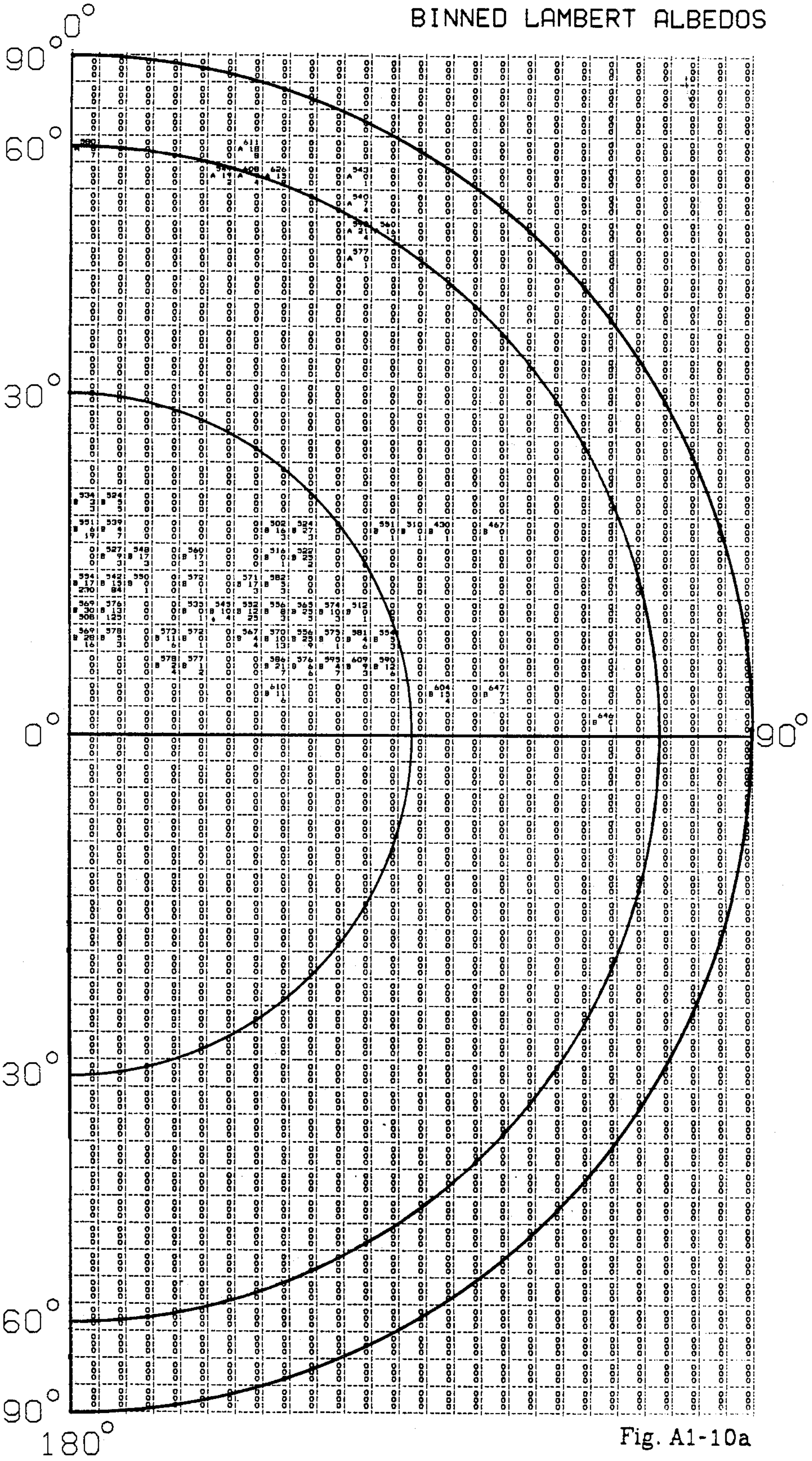

Fig. A1-10a

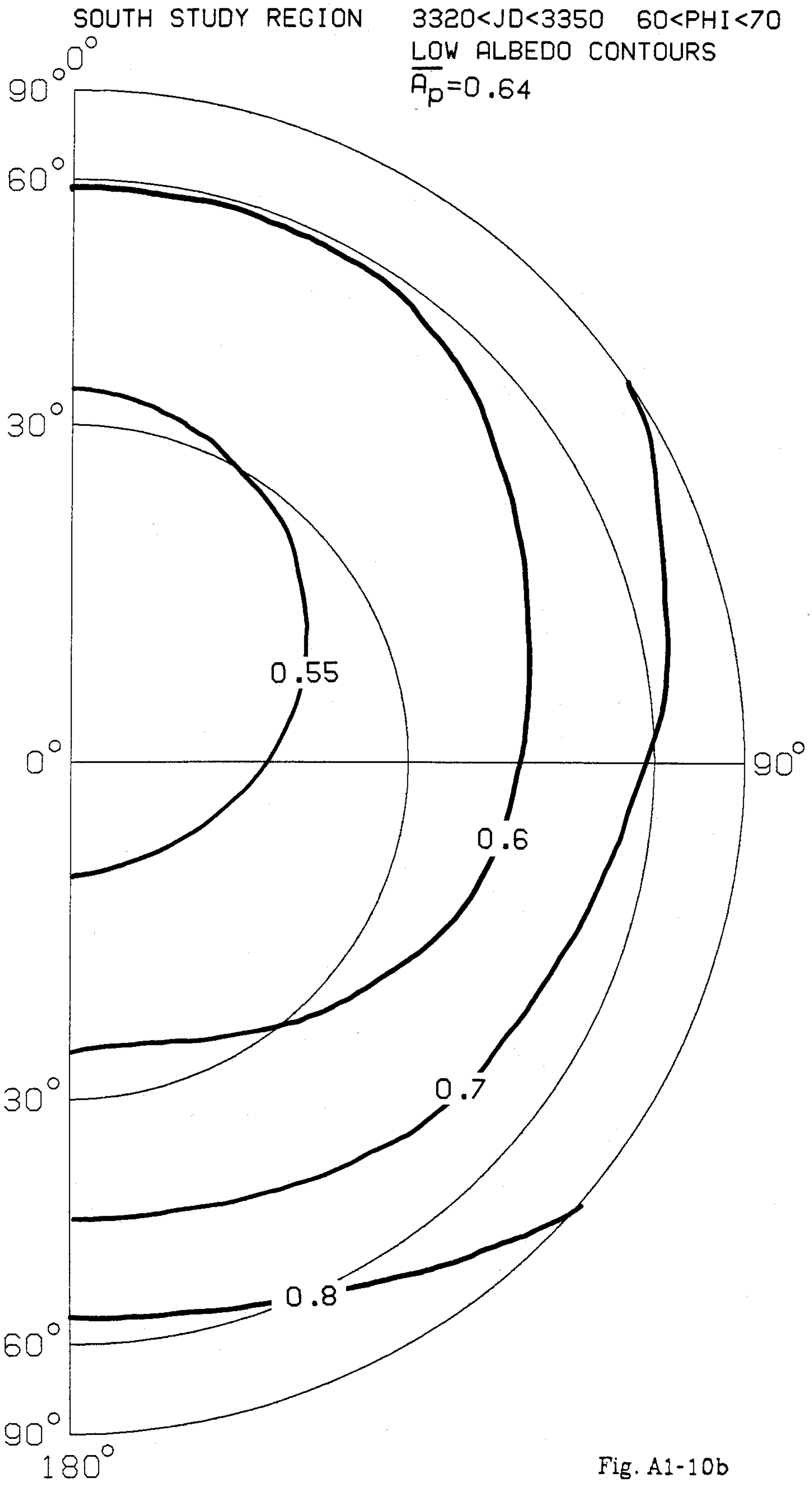
SOUTH STUDY REGION 3320<JD<3350 60<PHI<70
LOW ALBEDO CONTOURS
$\overline{A_p}$=0.64
90°
0°
60°
30°
0°
90°
30°
60°
90°
180°
0.55
0.6
0.7
0.8

Fig. A1-10b

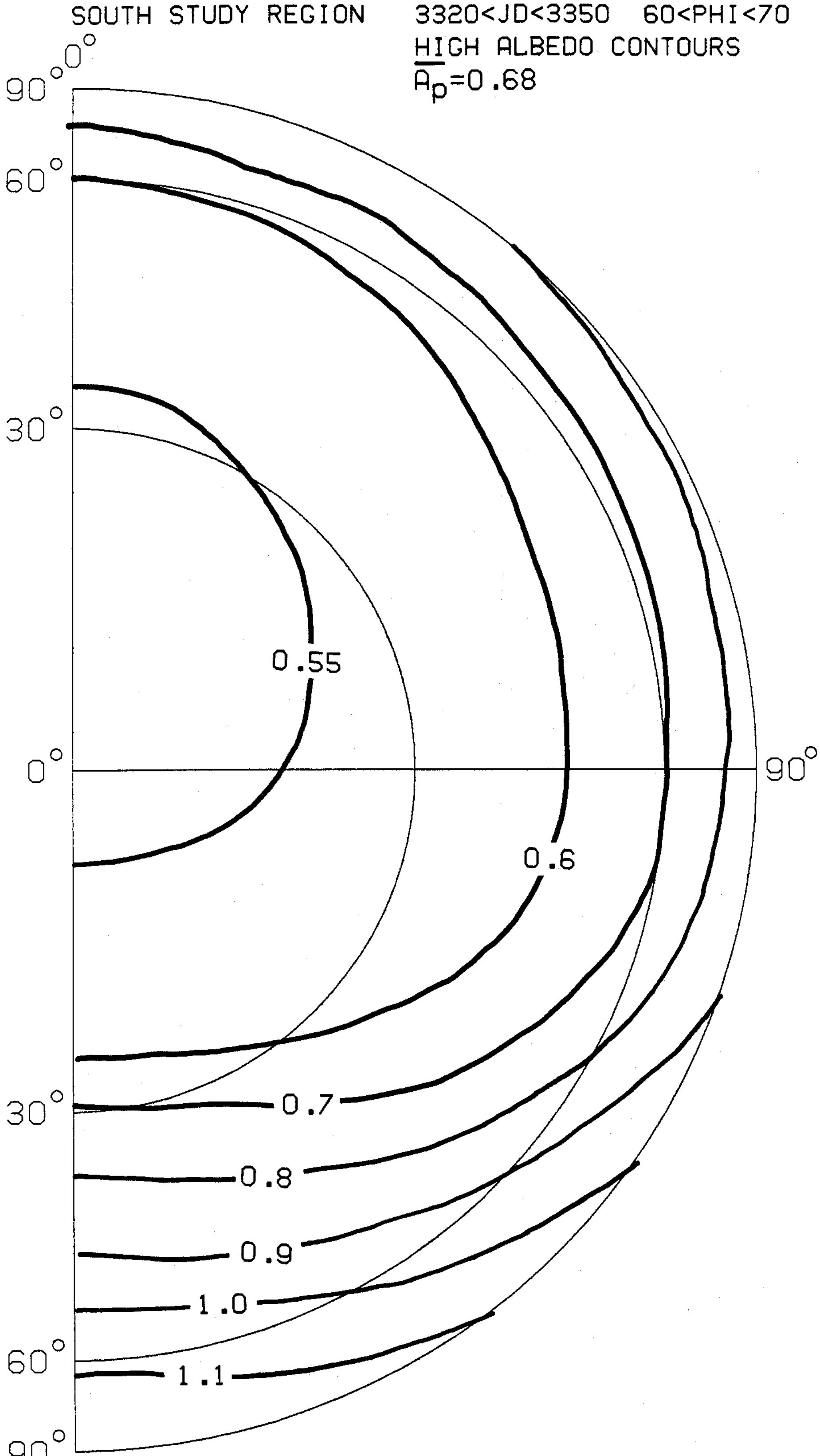
SOUTH STUDY REGION 3320<JD<3350 60<PHI<70
HIGH ALBEDO CONTOURS
$\overline{A}_p$=0.68
90°
0°
60°
30°
0°
90°
30°
60°
90°
180°
0.55
0.6
0.7
0.8
0.9
1.0
1.1

Fig. A1-10c

SOUTH STUDY REGION 3350<JD<3410 70<PHI<80
BINNED LAMBERT ALBEDOS

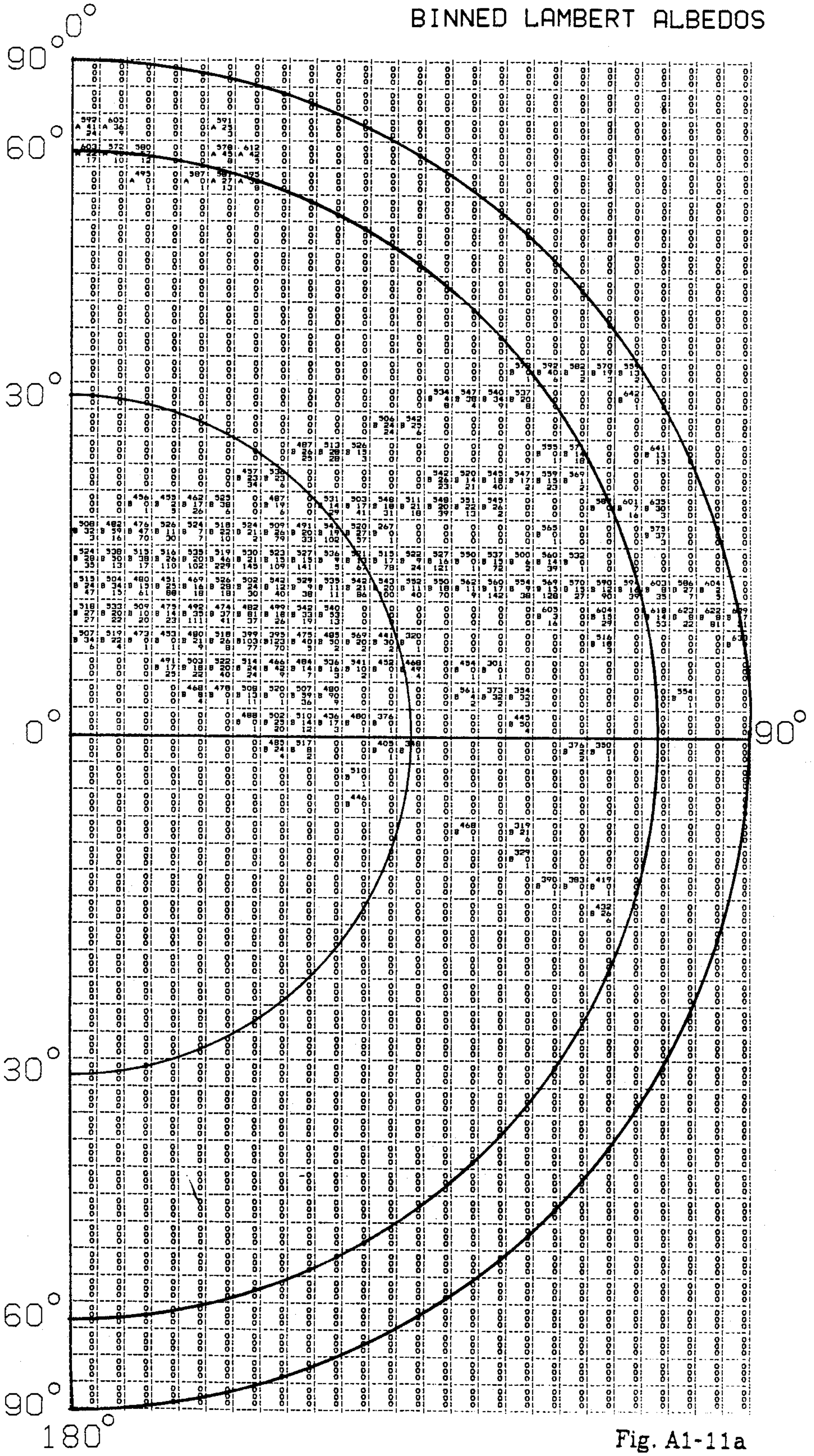

Fig. A1-11a

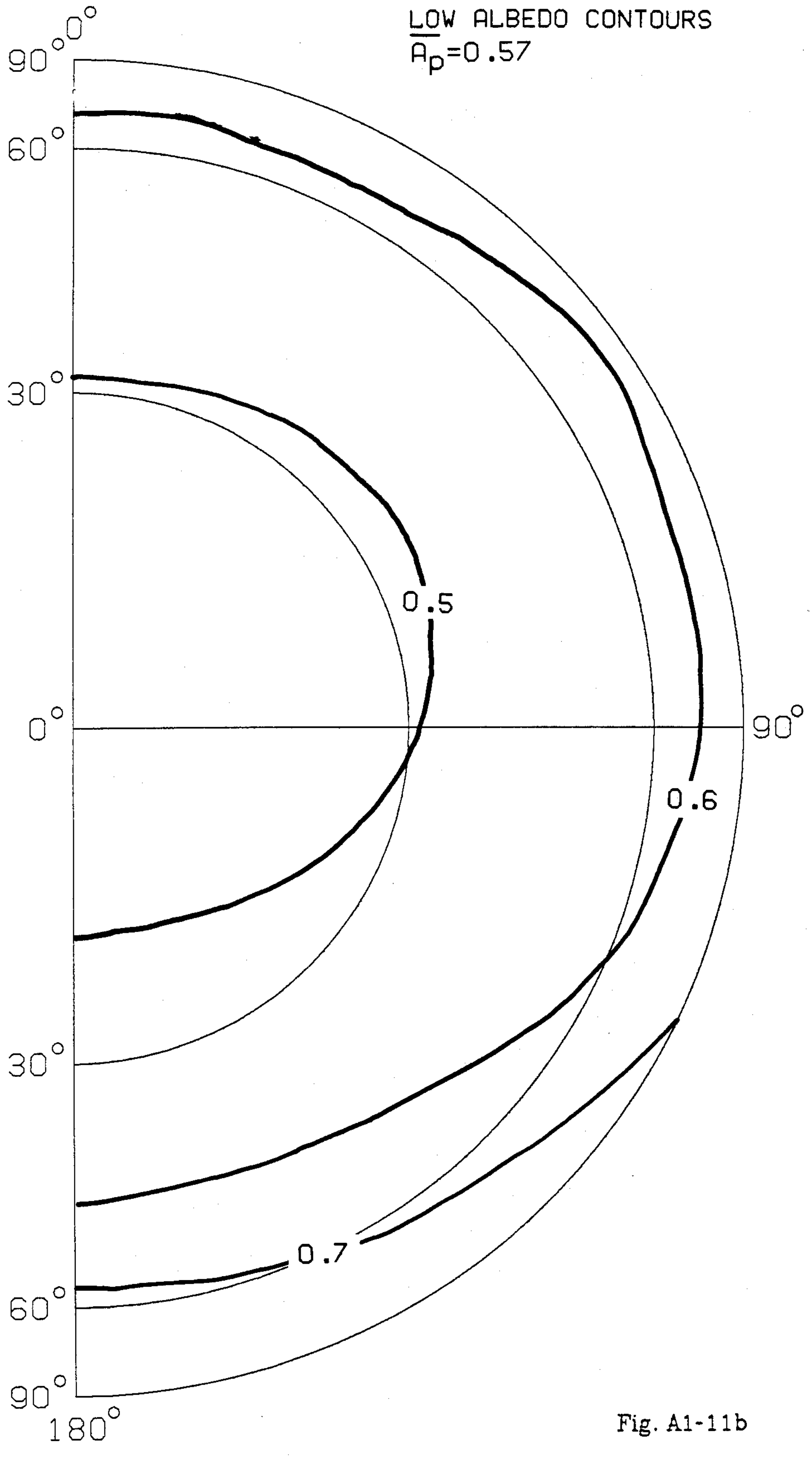

SOUTH STUDY REGION 3350<JD<3410 70<PHI<80
LOW ALBEDO CONTOURS
$\overline{A_p}=0.57$

Fig. A1-11b

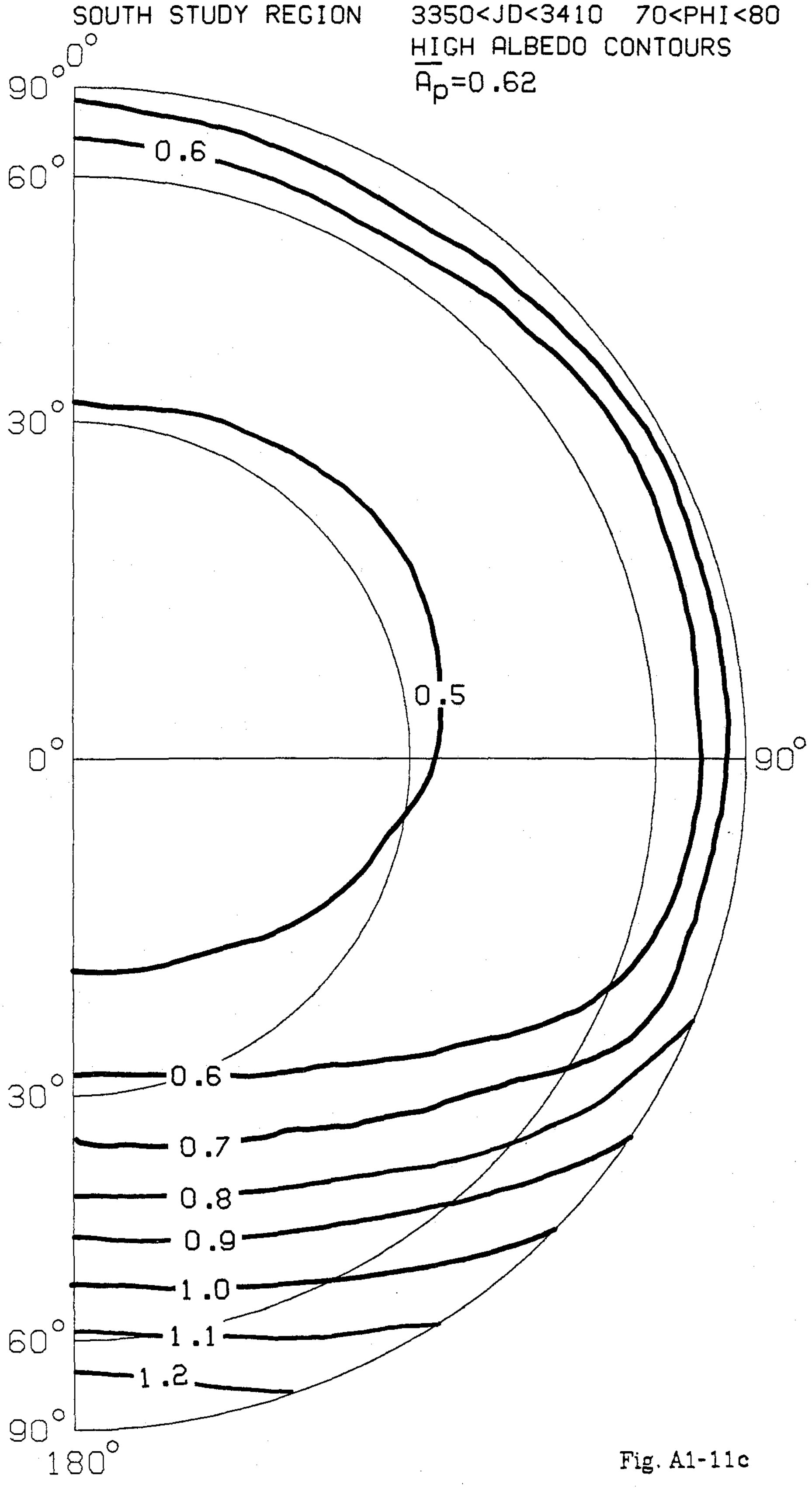
SOUTH STUDY REGION 3350<JD<3410 70<PHI<80
HIGH ALBEDO CONTOURS
$\overline{A}_p$=0.62
0°
90°
60°
30°
0°
30°
60°
90°
180°
90°
0.6
0.5
0.6
0.7
0.8
0.9
1.0
1.1
1.2

Fig. A1-11c

set in the north consists of solar reflectance measurements at $\vartheta > 60°$ and $\psi < 45°$. Lambert albedos for $\vartheta > 60°$ and $\psi < 45°$ are shown in Fig. A1-12. In the south, the final values of A_p were made to vary so that the time average of A_p within each peroid equalled the average of $\overline{A_p}$ and that variations in A_p within each time period were proportional to the measured Lambert albedos for $\vartheta < 30°$. In the north, the available observations suggest that temporal variations in A_P within each period were generally not as large as they were in the south, but the data are not good enough to put upper limits on the magnitudes of the variations that might have occured. The only definite conclusion that can be made concerning temporal variations is that the transition from high north study region reflectances during spring to low north study region reflectances during summer was not instantaneous. The final values of A_p in the north do not contain temporal variations in A_p within each time period except for the most general trends indicated by the values of $\overline{A_p}$. To partially account for other temporal variations in A_p that may have occured within each time period, the final values of A_p in the north were given additional uncertainties of ±1.5% at all seasons.

The final upper and lower limits for A_p for the north and south study regions are shown in Figs. A1-12 and A1-13. They contain uncertainties due to partial knowledge of bidirectional reflectance patterns as indicated by the upper and lower values of $\overline{A_p}$ during each time period, ±5% uncertainties for absolute callibration and ±1.5% uncertainties for unobserved temporal variations in A_p in the north. All sources of uncertainty were assumed to be additive.

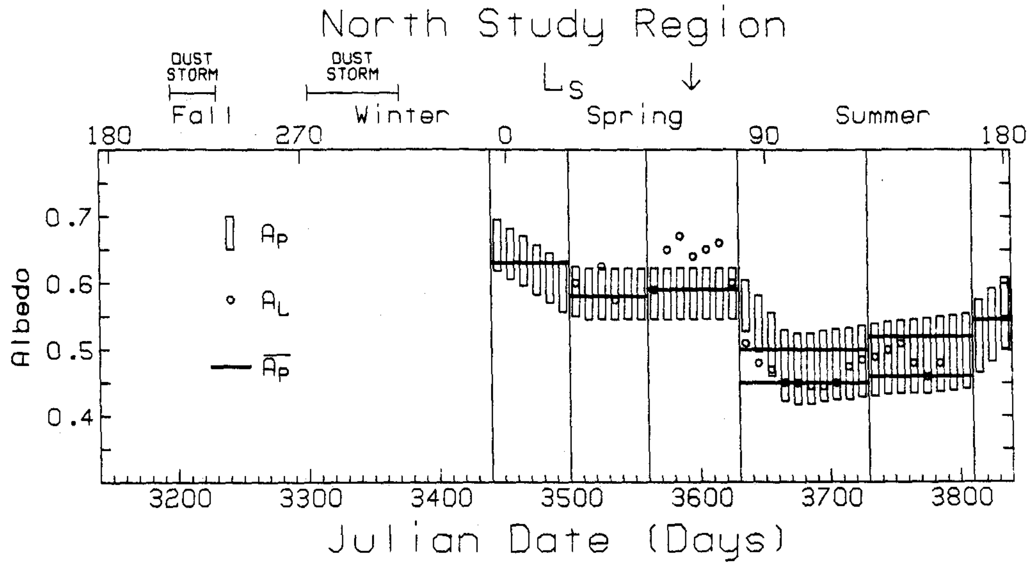

Fig. A1-12. The solar reflectance of the north study region from IRTM observations. The open circles show 10-day averaged Lambert albedos at relatively constant viewing geometries ($\vartheta > 60°$, $\psi < 45°$). Also shown are the derived values of $\overline{A_P}$ from the bidirectional reflectance contour plots in Figs. A1-3 through A1-12 and the estimated upper and lower limits for the instantaneous planetary albedos of the region A_P. The upper and lower limits for A_P include allowances for ambiguities in $\overline{A_P}$, possible rapid temporal variations in A_P within each time period and absolute calibration.

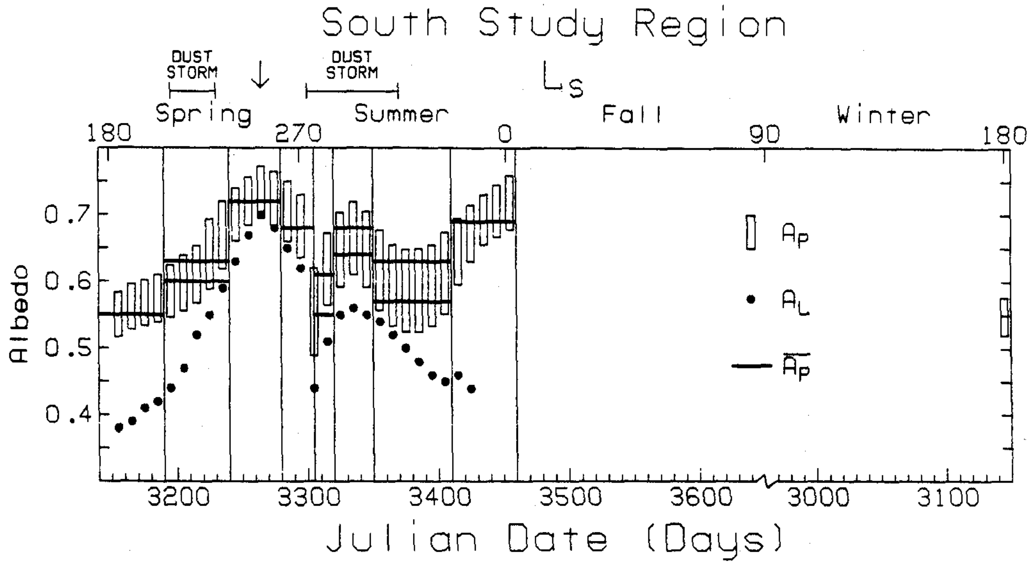

Fig. A1-13. Same as Fig. A1-12 except for the south study region. The closed circles are 10-day averaged Lambert albedos at relatively constant viewing geometries of $\vartheta < 30°$.

REFERENCES

Dirmhirn,I. and F. D. Eaton, (1975) *J. Appl. Meteor.* **14**, 275.

Hanel, R. *et al.* (1972) *Icarus* **17**, 423.

Taylor, R. V. and L. L. Stowe, (1984) *J. Geohys. Res.* **89**, 4996.

APPENDIX 2

A 10-LAYER ONE-DIMENSIONAL POLAR RADIATIVE MODEL

1. Overview

The model described here is similar in concept to the one-dimensional radiative-convective models that have been used to study the atmosphere and climate of the earth (Manabe and Wetherald, 1966; Hansen et al., 1981) and Mars (Pollack et al., 1979). Its specific purpose is to simulate the radiative and dynamic processes that occur in the Martian polar atmosphere and to determine how they affect the polar heat balance and observable radiances at the top of the atmosphere. The Martian polar regions are ideal places to apply one-dimensional models. Since they experience no significant diurnal variations in solar heating and the heat capacity of the Martian atmosphere is low, the north and south polar atmospheres are in a state of near thermal equilibrium throughout the year. This means that polar atmospheric temperatures are determined solely by the instantaneous rates of atmospheric heating and cooling at any given season.

The model accounts for all the major processes that determine vertical temperature profiles in the lowest two scale heights of the Martian north and south polar atmospheres, including anisotropic-nonconservative scattering by atmospheric aerosols and absorption by CO_2 gas at solar wavelengths, anisotropic-nonconservative scattering and emission by atmospheric aerosols at infrared wavelengths, emission and absorption by CO_2 gas in the strong 15μ band, heat conduction between surface atmosphere and atmospheric heating due to dynamical motions.

The model atmosphere consists of a stack of 10 isothermal layers of equal mass overlying a surface of known thermal and reflectance properties.

The radiative and dynamical properties of each layer are fixed but the temperature of each layer is not. The layers are numbered 1 through 10 with layer 10 being just above the surface.

There are levels at each layer boundary numbered 1 through 11 with level 1 at the top of the atmosphere and level 11 at the surface. The model layer structure is shown diagramatically in Fig. A2-1.

At the start of the model calculations, each layer is assigned an arbitrary temperature. During each model time step, net radiative fluxes at each level and the instantaneous heat balance of each layer are calculated and the temperature of each layer is adjusted accordingly. By the last model time step, the temperature change in each layer is negligible and a thermal equilibrium temperature profile has been established. The number of time steps that are required to achieve convergence depends on the properties of the model atmosphere, the season, and the duration of the time steps. The total equivalent length of time required to achieve convergence is generally less than five days. Once determined, the thermal equilibrium temperature profile can be used in conjunction with the radiative properties of each layer and the surface to calculate observable radiative fluxes at the top of the atmosphere.

The model consists of a collection of parts that were obtained from a variety of sources. Most of the parts were developed by others; a few of the parts were developed by me. This appendix describes how the model was put together and gives detailed descriptions of some of the more original modeling techniques. Efficient Fortran subroutines for performing many of the calculations described here will be made available to anyone upon request.

Pressure (mb)	Level		Altitude (km)
0.0	1		Space
		T(1)	
0.4	2		21.63
		T(2)	
0.8	3		15.12
		T(3)	
1.2	4		11.31
		T(4)	
1.6	5		8.60
		T(5)	
2.0	6		6.51
		T(6)	
2.4	7		4.80
		T(7)	
2.8	8		3.35
		T(8)	
3.2	9		2.09
		T(9)	
3.6	10		0.99
		T(10)	
4.0	11	Ts	0.00 (Surface)

Fig. A2-1. The layer structure of the 10-layer polar radiative model. Shown on the left are the pressures at each level for an atmosphere with surface pressure of 4 mb. Shown on the right are geopotential altitudes for an isothermal atmosphere at 180 K. Atmospheric temperatures within each model layer are assumed to be isothermal.

2. Solar Heating

Solar heating in the Martian atmosphere occurs primarily by absorption of solar energy at near infrared wavelengths by CO_2 gas and by the absorption of broad-band solar energy by atmospheric aerosols. These processes are accounted for as follows.

2.1 Near IR CO_2 Absorption

Pollack et al. (1981) present estimates of the solar absorption due to the weak bands of CO_2 at 1.316 μ, 1.455 μ, and 1.600 μ and of the strong bands of CO_2 at 2.020 μ, 2.759 μ, and 4.301 μ. They present the combined total fractional solar absorption due to all of these CO_2 bands as a function of the parameter $\hat{p}$ in graphical form.

$$\hat{p} \equiv \frac{p\left[1 + 0.405\left(\frac{\bar{T} - 200\mathrm{K}}{200\mathrm{K}}\right)\right]}{\left(2\mu_o\right)^{0.606}} \tag{A2.1}$$

where p is the atmospheric pressure at a given level in mb, $\bar{T}$ is the pressure weighted mean temperature down to that level, and μ_o is the cosine of the solar zenith angle. The total fractional solar absorption F_{CO_2} can be well approximated by

$$F_{CO_2} = \left(1.6747 \times 10^{-5}\hat{p}\right)^{0.4791} \tag{A2.2}$$

for $\hat{p} < 32$ mb. The total fractional absorption for each model layer was calculated by taking the difference between F_{CO_2} at its lower and upper boundaries. F_{CO_2} is typically 0.02 at the surface.

2.2 Broad-band Solar Scattering

Broad-band multiple scattering calculations are performed using a multi-layer, 2 stream, δ-Eddington code (Joseph, Wiscomb, and Weinman, 1976). This approximate method for calculating radiative fluxes and heating rates has proved to be extremely fast and yet highly accurate over the range aerosol optical properties considered in this study. The required model input parameters are μ_0, $\tau_V(j)$, the solar spectrum averaged optical depth at each level, $\tilde{\omega}_{0V}(j)$, the solar spectrum averaged aerosol single scattering albedo for each layer, $g_V(j)$, the solar spectrum averaged aerosol asymmetry parameter for each layer, and A_s, the solar spectrum averaged surface albedo.

2.3 Surface and Atmospheric Solar Heating Rates

Since less than 15% of the total incident solar flux is at wavelengths greater than 1.35 microns, possible interactions between near infrared CO_2 absorption and broad band solar scattering are not dealt with in this model. To conserve energy, the fraction of incident insolation absorbed by CO_2 is subtracted from the insolation that is assumed to be available for broad-band scattering. Model calculated planetary albedos at the top of the atmosphere are simply the fraction of incident solar radiation that is not absorbed at the surface or in the atmosphere.

3. Infrared Cooling

Infrared cooling in the Martian atmosphere occurs primarily in the strong 15 μ band of CO_2 and at all infrared wavelengths by scattering and emission by atmospheric aerosols. These processes are accounted for as follows:

3.1 The 15 μ Band of CO_2

For an N-layer atmosphere, the equations for the upward and downward fluxes of radiation in the strong 15 μ band of CO_2 at each level are:

$$F\!\downarrow_{15}(1) = 0 \tag{A2.3}$$

$$F\!\downarrow_{15}(i) = \sum_{j=2}^{i} B_{15}(T_j)\Big[E^*(i,j-1) - E^*(i,j)\Big] \tag{A2.4}$$

$$F\!\uparrow_{15}(N+1) = \pi B_{15}(T_s)\Delta\nu_{15} \tag{A2.5}$$

$$F\!\uparrow_{15}(i) = B_{15}(T_s)\Big[\pi\Delta\nu_{15} - E^*(i,N+1)\Big] + \sum_{j=i}^{N} B_{15}(T_j)\Big[E^*(i,j+1) - E^*(i,j)\Big] \tag{A2.6}$$

where $F\!\uparrow_{15}(i)$ and $F\!\downarrow_{15}(i)$ are the upward and downward fluxes in the 15 μ band at level i, $B_{15}(T_j)$ is the Planck function in the center of the band (ν = 667.3 cm^{-1}), T_j is the temperature of layer j, $B_{15}(T_s)$ is the same quantity for the temperature of the surface, $\Delta\nu_{15}$ is the nominal width of the 15 μ CO_2 band in cm^{-1} and $E^*(i,j)$ is the equivalent width for diffuse radiation of the 15 μ CO_2 band between levels i and j in cm^{-1}.

$E^*(i,j)$ is calculated with the exponential wide band model described by Crisp, Fels and Schwarzkopf (1985). This approximate method for finding the equivalent width of the 15μ band of CO_2 gives path absorbances within 20% of those determined by exact line by line calculations for model Martian atmospheres at temperatures ranging from 130K to 300K.

$F\!\uparrow_{15}$ and $F\!\downarrow_{15}$ can be fouled up by the choice of layer structure and the method of evaluation of path integrals. Fig. A2-2 shows thermal equilibrium temperature profiles generated by 5, 10, 20 and 40-layer radiative models for typical early fall or late winter polar conditions. In all cases, the surface was assumed to be a blackbody emitter at a fixed temperature of 144.7K. Total atmospheric pressure at the surface was assumed to be 4mb with a CO_2 mixing

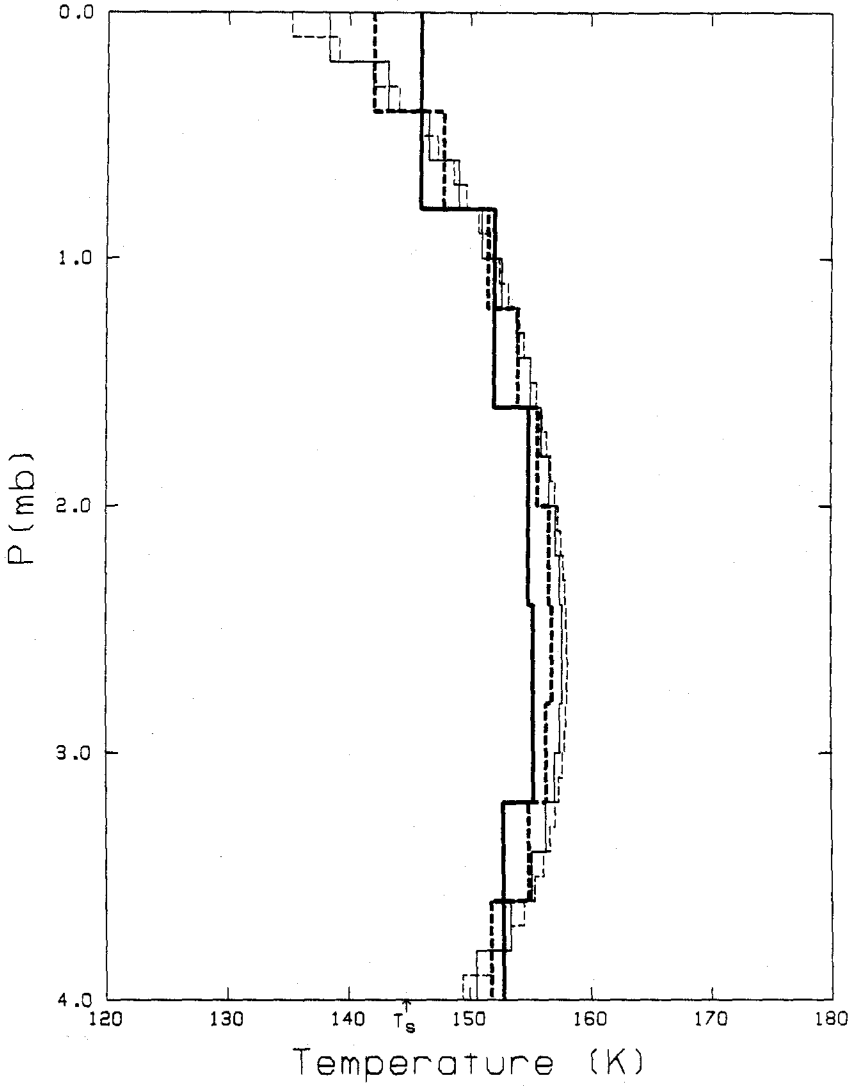

Fig. A2-2. The dependence of calculated thermal equilibrium temperature profiles under clear atmospheric conditions for model atmospheres with 5, 10, 20, and 40 model layers.

ratio of 0.95 at all altitudes. The atmosphere was assumed to be heated at a constant vertically integrated rate of $2.5 \mathrm{Wm}^{-2}$ and cooled only in the 15μ band according to the fluxes in equations A2.3 to A2.6. The equivalent widths generated by the exponential wide band model of Crisp, Fels and Schwarzpkof were used in all calculations. Each profile is shown after 180 timesteps of 2 hours duration. The results show that for this set of model input parameters and this type of layer structure, calculated thermal equilibrium temperature profiles in the lower two scale heights are not pathologically affected by the number of atmospheric layers assumed to be present. These effects seen in Fig. A2-2 are even smaller for cases in which atmospheric cooling is also assumed to occur at other wavelengths due to emission by atmospheric aerosols.

$F\uparrow_{15}$ and $F\downarrow_{15}$ can also be fouled up by incorrectly estimating $E^*(i,j)$. Pollack et al. (1981) present an approximate empirical formula for $E^*(i,j)$ derived from the data of Howard et al. (1955) and Burch et al. (1962):

$$E^*(i,j) = 2\pi\bar{\mu}d_0\left(\frac{\bar{T}}{T_0}\right)^{qd} \ln\left[1 + f_0\left(\frac{\bar{T}}{T_0}\right)^{qf} w^b \bar{p}^a\right] \qquad \text{(A2.7)}$$

where $\bar{\mu}$ is a diffusivity factor of 0.488, $d_0 = 54.4$, $\bar{T}$ is the pressure weighted average temperature between levels i and j, $T_0 = 300$ K, $qd = -.879$, $f_0 = 0.153$, $qf = -0.256$, w is the absorber path length in atmos-cm, $b = 0.566$, $\bar{p}$ is the average pressure between levels i and j, and $a = 0.323$. Haberle, Leovy and Pollack (1982) have used this same formula to calculate $E^*(i,j)$, except that they replace the variable $\bar{T}$ with 200K for all paths to give improved results at high altitudes for mid latitude temperature profiles.

Fig. A2-3 shows calculated early fall or late winter polar thermal equilibrium temperature profiles using the emperical 15μ band models of Pollack *et al* and Haberle *et al* and by the more accurate exponential wide band

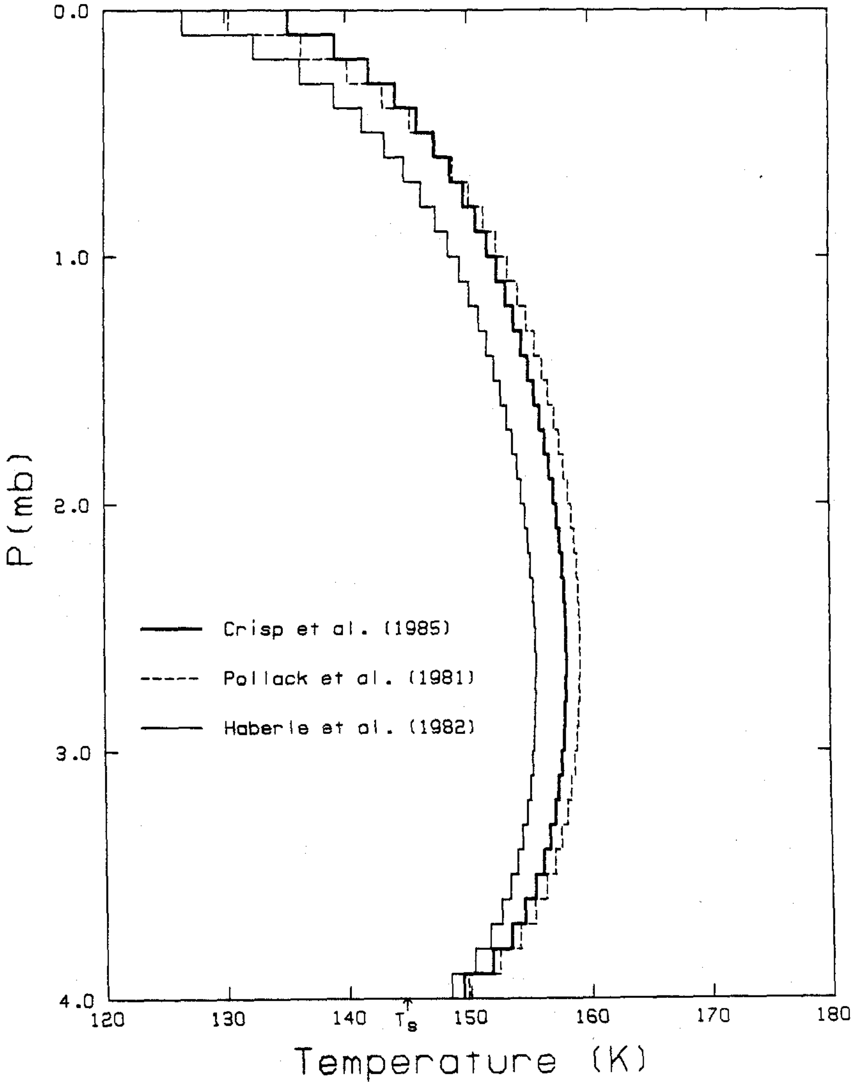

Fig. A2-3. Comparison between calculated thermal equilibrium temperature profiles for a 40 layer atmosphere using approximate CO_2 15 μ band equivalent widths from Crisp et al. (1985), Pollack et al. (1981), and Haberle et al. (1982).

model of Crisp *et al.* The input parameters and timesteps were the same as were used to generate the profiles in Fig. A2-2. A 40-layer atmosphere was assumed for all three cases. The results show that despite its simplicity, the Pollack *et al* model does quite well in the first two scale heights for this type of temperature profile. Above 0.4mb, the discrepancies between the Pollack *et al* model and the Crisp *et al* profiles are probably caused by the tendency for the Pollack *et al* model to overestimate path absorbances for transmission to space at low pressures (see Crisp *et al*, 1985). The results also show that for this type of profile, the Haberle *et al* model gives less accurate results than the original Pollack *et al* model. The tendency for the Haberle *et al* model to underestimate atmospheric temperatures at all levels can be directly traced to its disregard for the reduction of CO_2 15μ band path absorbances with decreasing temperature.

3.2 Two-stream δ-Eddington Code for IR Scattering

Broad-band multiple scattering calculations at infrared wavelengths are performed using a modified two-stream δ-Eddington code that accounts for emission by atmospheric aerosols. A similar code has been developed by Richard Zurek and has been used to study Martian north polar ice hazes (Christensen and Zurek, 1984), but the details have not been published.

In the standard Eddington approximation (Shettle and Weinman, 1970), the particle scattering phase function is approximated by

$$P_{edd}(\Omega) = 1 + 3g\cos(\Omega) \qquad \text{(A2.8)}$$

where Ω is the scattering angle and g is the original particle phase function. When this assumption is employed, the diffuse radiance within a plane parallel atmosphere can be written:

$$I(\tau,\mu) = I_0(\tau) + I_1(\tau)\mu \tag{A2.9}$$

where $I(\tau,\mu)$ is the azimuthally averaged radiance at vertical optical depth τ in the direction defined by μ, the cosine of the zenith angle. Following the conventions of Shettle and Weinman, $\mu>0$ for downward radiance. In this coordinate system, the upward flux is:

$$F\uparrow(\tau) = 2\pi\int_0^{-1}\mu\left[I_0(\tau) + \mu I_1(\tau)\right]d\mu = \pi\left[I_0(\tau) - \frac{2}{3}I_1(\tau)\right] \tag{A2.10}$$

The downward flux is:

$$F\downarrow(\tau) = 2\pi\int_0^{1}\mu\left[I_0(\tau) + \mu I_1(\tau)\right]d\mu = \pi\left[I_0(\tau) + \frac{2}{3}I_1(\tau)\right] \tag{A2.11}$$

The monochromatic equation of transfer for a single layer isothermal atmosphere with anisotropically non-conservative scattering and emitting particles with the Eddington approximation is:

$$\mu\frac{d(I_0 + \mu I_1)}{d\tau} = -(I_0 + \mu I_1) + \tilde{\omega}_0(I_0 + g\mu I_1) + (1 - \tilde{\omega}_0)B \tag{A2.12}$$

where $\tilde{\omega}_0$ is the particle single scattering albedo and B is the emitted intensity. Equation (A2.12) can be separated into two coupled equations in I_1 and I_0:

$$\frac{dI_1}{d\tau} = -3(1 - \tilde{\omega}_0)I_0 + 3(1 - \tilde{\omega}_0)B \tag{A2.13}$$

$$\frac{dI_0}{d\tau} = -(1 - \tilde{\omega}_0 g)I_1 \tag{A2.14}$$

whose general solutions are:

$$I_0 = C_1e^{-\kappa\tau} + C_2e^{+\kappa\tau} + B \tag{A2.15}$$

$$I_1 = P\left[C_1e^{-\kappa\tau} - C_2e^{+\kappa\tau}\right] \tag{A2.16}$$

where

$$\kappa = \sqrt{3(1-\tilde{\omega}_o)(1-\tilde{\omega}_o g)} \qquad \text{(A2.17)}$$

and

$$P = \sqrt{\frac{3(1-\tilde{\omega}_o)}{(1-\tilde{\omega}_o g)}} \qquad \text{(A2.18)}$$

and C_1 and C_2 are undetermined constant coefficients.

The first boundary condition is that at the top of the atmosphere, where $F(\tau=0) = 0$ or:

$$C_1(1 + \frac{2}{3}P) + C_2(1 - \frac{2}{3}P) = -B \qquad \text{(A2.19)}$$

The second boundary is that at the bottom of the atmosphere, where

$$F\uparrow(\tau=\tau^*) = \varepsilon_s B_s + (1-\varepsilon_s)F\downarrow(\tau=\tau^*)$$

where τ^* is the total atmospheric opacity, ε_s is the surface emissivity, and B_s is the surface emission or:

$$C_1 e^{-\kappa\tau^*}(1 - \frac{2}{3}P) + C_2 e^{+\kappa\tau^*}(1 + \frac{2}{3}P) + B =$$

$$\varepsilon_s B_s + (1-\varepsilon_s)\left[C_1 e^{-\kappa\tau^*}(1 + \frac{2}{3}P) + C_2 e^{\kappa\tau^*}(1 - \frac{2}{3}P) + B\right] \qquad \text{(A2.20)}$$

Equations (A2.19) and (A2.20) represent two linear equations with constant coefficients in C_1 and C_2 that can be rapidly solved by standard matrix methods.

For the case of an atmosphere consisting of multiple isothermal layers with different temperatures, C_1, C_2, and B can be replaced by $C_1(j)$, $C_2(j)$, and $B(j)$ where j indicates the layer number. The condition at each layer boundary is that I_o and I_1 be continuous, or:

$$C_1(j)e^{-\kappa\tau_j} + C_2(j)e^{+\kappa\tau_j} + B(j) = C_1(j+1)e^{-\kappa\tau_j} + C_2(j+1)e^{+\kappa\tau_j} + B(j+1) \tag{A2.21}$$

and

$$C_1(j)e^{-\kappa\tau_j} - C_2(j)e^{+\kappa\tau_j} = C_1(j+1)e^{-\kappa\tau_j} - C_2(j+1)e^{+\kappa\tau_j} \tag{A2.22}$$

where τ_j is the opacity at level j. This condition is fully equivalent to requiring that $F\uparrow$ and $F\downarrow$ be continuous at layer boundaries. For an N-layer atmosphere, $C_1(j)$ and $C_2(j)$ can be found by solving a system of $2N$ by $2N$ linear equations in $2n$ unknowns with at most four nonzero constant coefficients per row.

In the δ-Eddington approximation, the particle scattering phase function is approximated by the standard Eddington phase function with the addition of a Dirac delta function to better approximate the forward peak (Joseph, Wiscomb, and Weinman, 1976):

$$P_{\delta\text{-}Edd}(\Omega) = 2f\delta(1 - \cos(\Omega)) + (1 - f)(1 + 3g_E\mu) \tag{A2.23}$$

where f is the fractional scattering in the forward peak and g_E is the asymmetry parameter for the original truncated phase function used in the standard Eddington approximation. By assuming that $f = g^2$, the equation of transfer for the δ-Eddington phase function can be solved in exactly the same manner as the equation of transfer for the standard Eddington phase functions by replacing the variables g, $\tilde{\omega}_0$, and τ by the transformed variables g', $\tilde{\omega}_0'$, and τ' where:

$$g' = \frac{(g - f)}{(1 - f)} \tag{A2.24}$$

$$\tilde{\omega}_0' = \frac{\tilde{\omega}_0(1 - f)}{1 - f\tilde{\omega}_0} \tag{A2.25}$$

and

$$\tau' = (1 - f\tilde{\omega}_0)\tau \tag{A2.26}$$

3.3 Mie Calculations

Infrared calculations with the 2-stream δ-eddington code require knowledge of $\tilde{\omega}_0(\lambda)$, $g(\lambda)$, and $\tau(\lambda)$. $\tau(\lambda)$ can be expressed in terms of τ_V by the relation:

$$\frac{\tau(\lambda)}{\tau_V} = \frac{Q_{ext}(\lambda)}{Q_V} \quad \text{(A2.27)}$$

where $Q_{ext}(\lambda)$ is the particle extinction efficiency at wavelength λ and Q_V is the solar spectrum averaged particle extinction efficiency.

$Q_{ext}(\lambda)$, $\tilde{\omega}_0(\lambda)$, and $g(\lambda)$ were calculated for polydispersions of spheres using Mie theory (Hansen and Travis, 1979). Particle size distribution of the form:

$$N(r) = cr^{\alpha}\exp\left[-\left(\frac{\alpha}{\gamma}\right)\left(\frac{r}{r_m}\right)^{\gamma}\right] \quad \text{(A2.28)}$$

were used in all calculations, where r is the particle radius, r_m is the mode radius, and c, α, and γ are adjustable constants (Deirmendjian, 1969). Table A2-1 summarizes the calculations that were performed and the sources of data that were used to characterize the variations in real and imaginary reactive indices with wavelength. Size distributions 1, 2, and 3, which are the same as 4, 5, and 6, were originally used by Toon, Pollack, and Sagan (1977) to characterize the properties of the particles composing the Martian great dust storm of 1971-1972 from Mariner 9 IRIS spectra. Distribution 7 was used by Curran et al. (1973) to characterize the properties of Martian mid-latitude ice clouds from Mariner 9 IRIS spectra. Distribution 8 was originally used by Hunt (1979) to characterize the radiative properties of Martian water ice clouds composed of larger particles. Figures A2-4a,b,c,d through A2-6a,b,c show the results of the Mie calculations.

Table A2-1. Summary of Mie Calculations

Distribution	Particle Composition	Source of Refractive Index Data	r_m (μ)	α	γ	Wavelength Range (μ)	
						λ_{min}	λ_{max}
1	Montmorillonite 219b	Toon, Pollack, & Sagan (1977)	0.4	2	0.5	5.0	40.0
2	"	"	0.3	2	0.5	"	"
3	"	"	0.5	2	0.5	"	"
4	Basalt	Pollack, Toon, & Khare (1973)	0.4	2	0.5	6.0	50.0
5	"	"	0.3	2	0.5	"	"
6	"	"	0.5	2	0.5	"	"
7	Water ice	Schaaf & Williams (1973)	0.4	2	0.5	5.0	100.0
8	"	"	4.0	6	1	"	"

Table A2-1. Size distribution parameters and sources of refractive index data for 8 size distributions of dust and water ice spheres.

Fig. A2-4. (A) Montmorillonite 219b refractive indices from Toon et al. (1977). (B, C, D) Calculated MIE parameters Q_{EXT}, $\tilde{\omega}_o$, and g for these size distributions of montmorillonite 219b spheres. The size distribution numbers correspond to those in Table A2-1.

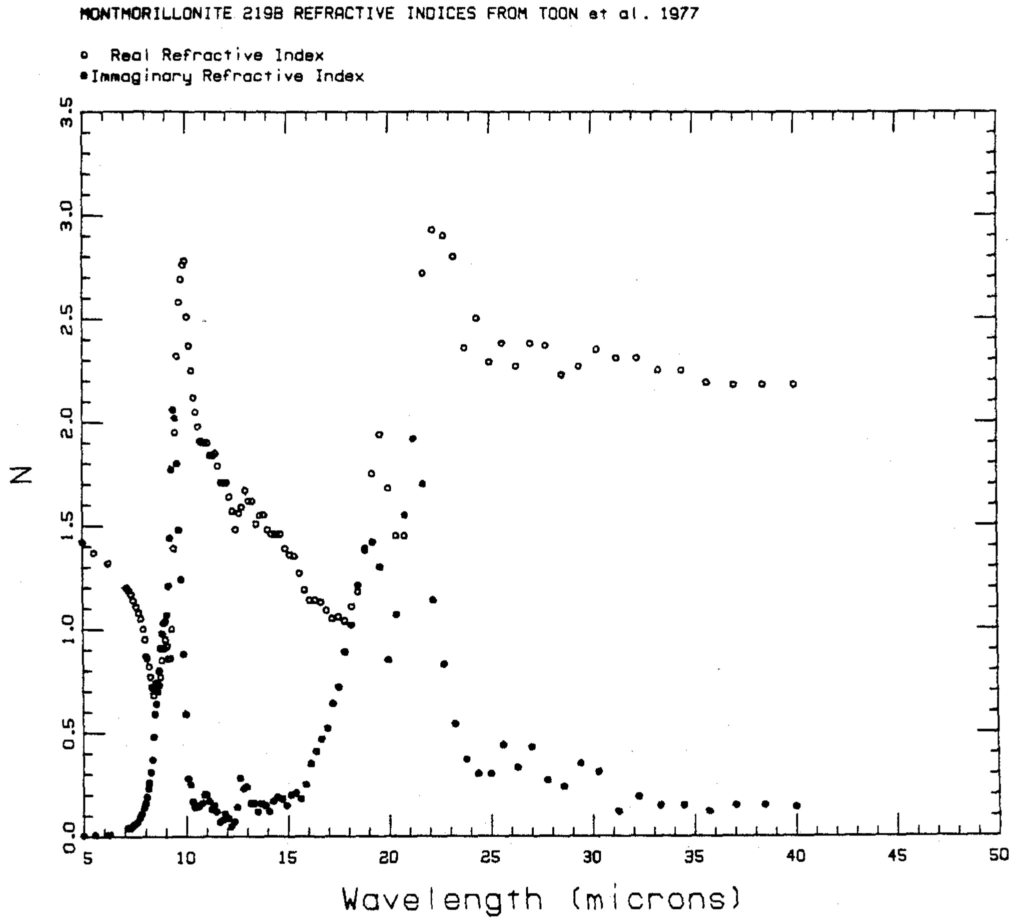

MONTMORILLONITE 219B REFRACTIVE INDICES FROM TOON et al. 1977

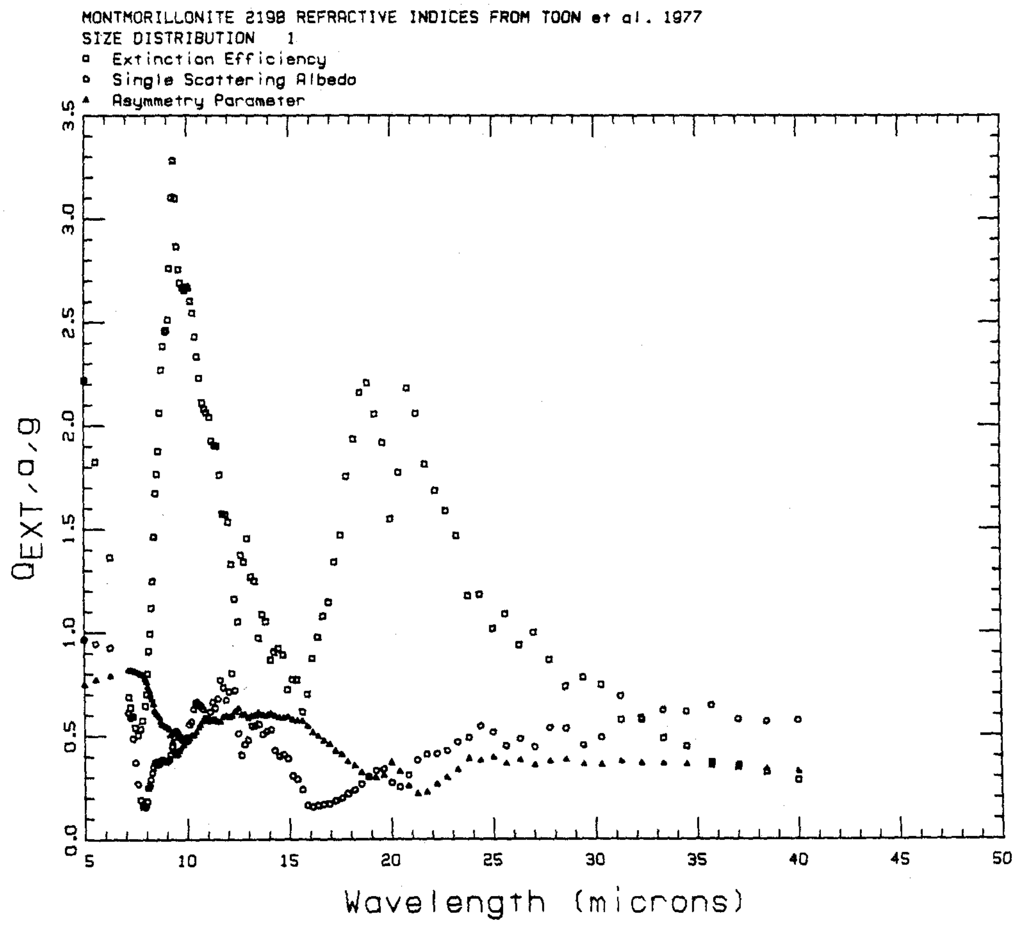
MONTMORILLONITE 2198 REFRACTIVE INDICES FROM TOON et al. 1977
SIZE DISTRIBUTION 1
□ Extinction Efficiency
○ Single Scattering Albedo
▲ Asymmetry Parameter
Q_EXT, a, g
0.0
0.5
1.0
1.5
2.0
2.5
3.0
3.5
5
10
15
20
25
30
35
40
45
50
Wavelength (microns)

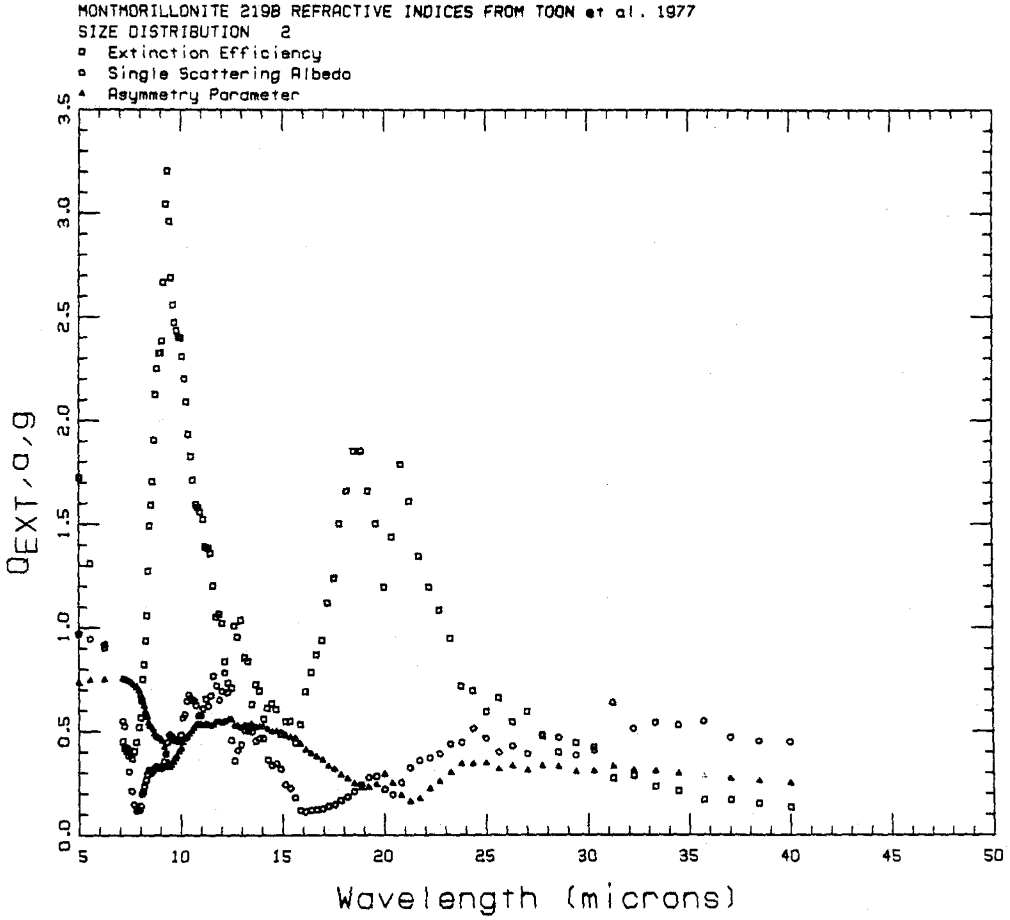
MONTMORILLONITE 219B REFRACTIVE INDICES FROM TOON et al. 1977
SIZE DISTRIBUTION 2
□ Extinction Efficiency
○ Single Scattering Albedo
▲ Asymmetry Parameter
Q_{EXT}, a, g
0.0
0.5
1.0
1.5
2.0
2.5
3.0
3.5
5
10
15
20
25
30
35
40
45
50
Wavelength (microns)

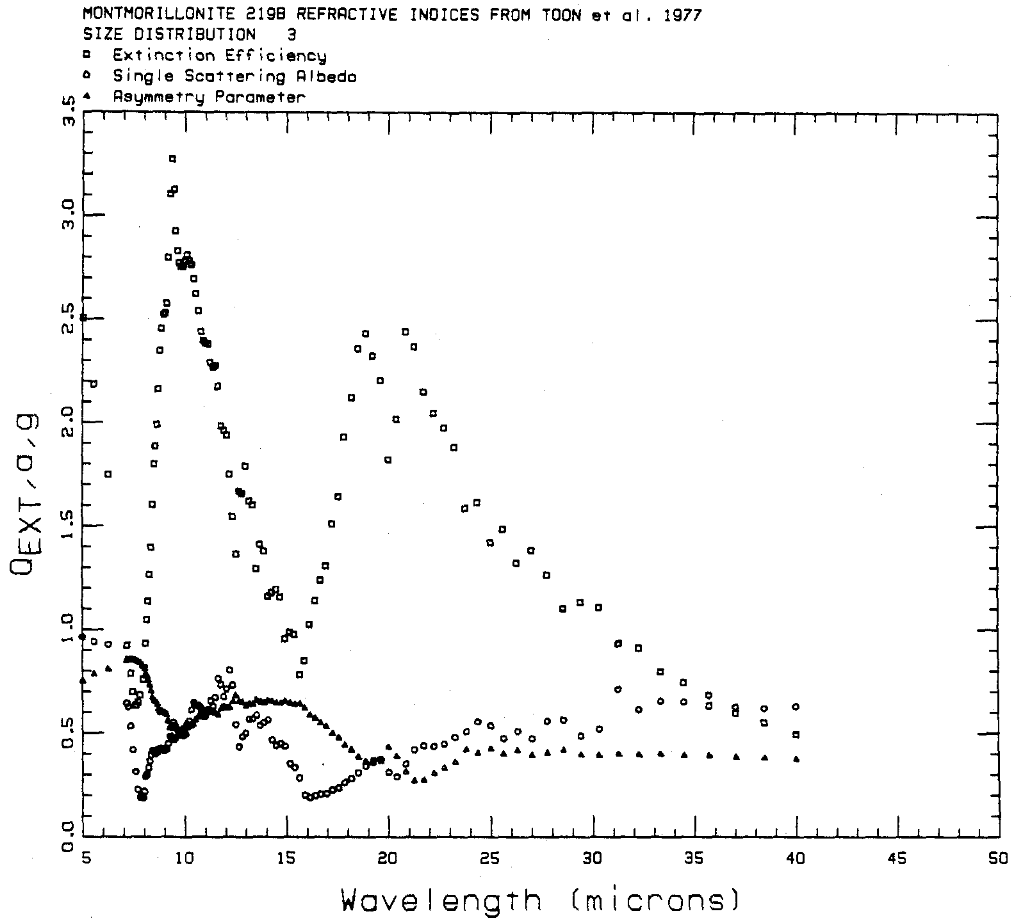
MONTMORILLONITE 219B REFRACTIVE INDICES FROM TOON et al. 1977
SIZE DISTRIBUTION 3
□ Extinction Efficiency
○ Single Scattering Albedo
▲ Asymmetry Parameter
Q_{EXT}, a, g
0.0
0.5
1.0
1.5
2.0
2.5
3.0
3.5
5
10
15
20
25
30
35
40
45
50
Wavelength (microns)

Fig. A2-5. (A) Basalt refractive indices from Pollack et al. (1973). (B, C, D) Calculated MIE parameters Q_{EXT}, $\tilde{\omega}_o$, and g for three size distributions of basalt spheres. The size distribution numbers correspond to those in Table A2-1.

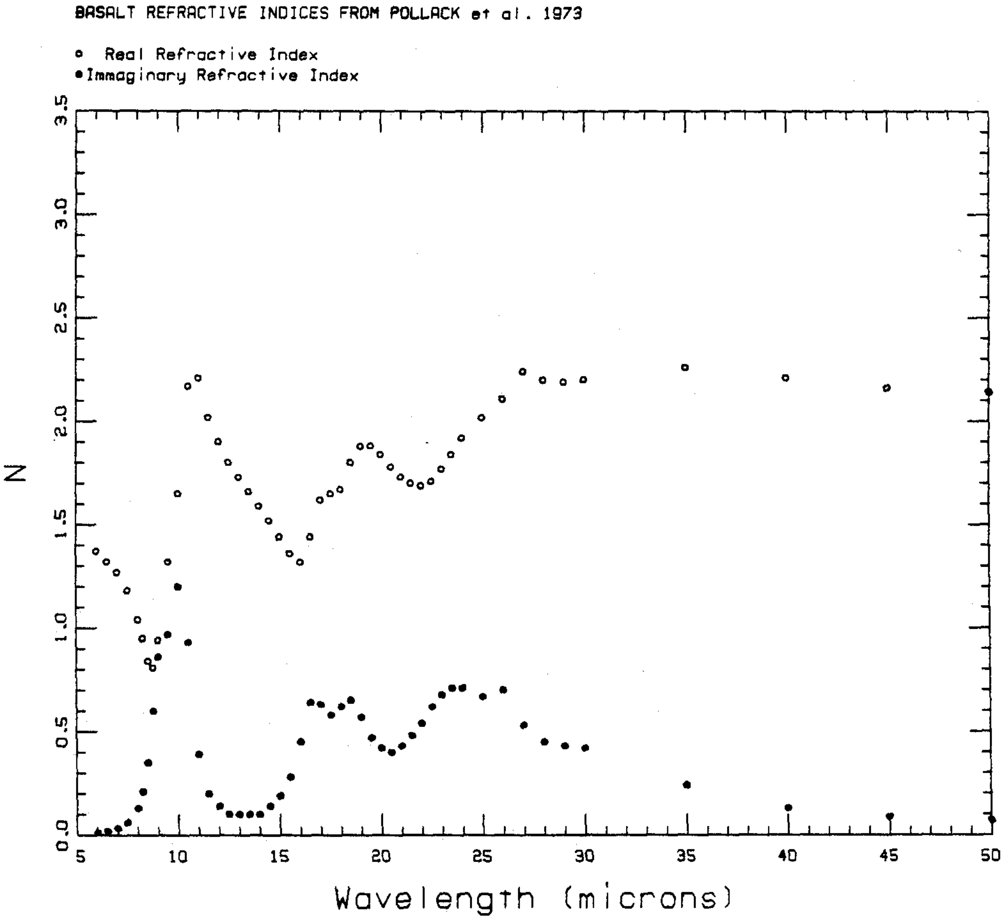
BASALT REFRACTIVE INDICES FROM POLLACK et al. 1973
○ Real Refractive Index
● Immaginary Refractive Index
N
0.0
0.5
1.0
1.5
2.0
2.5
3.0
3.5
5
10
15
20
25
30
35
40
45
50
Wavelength (microns)

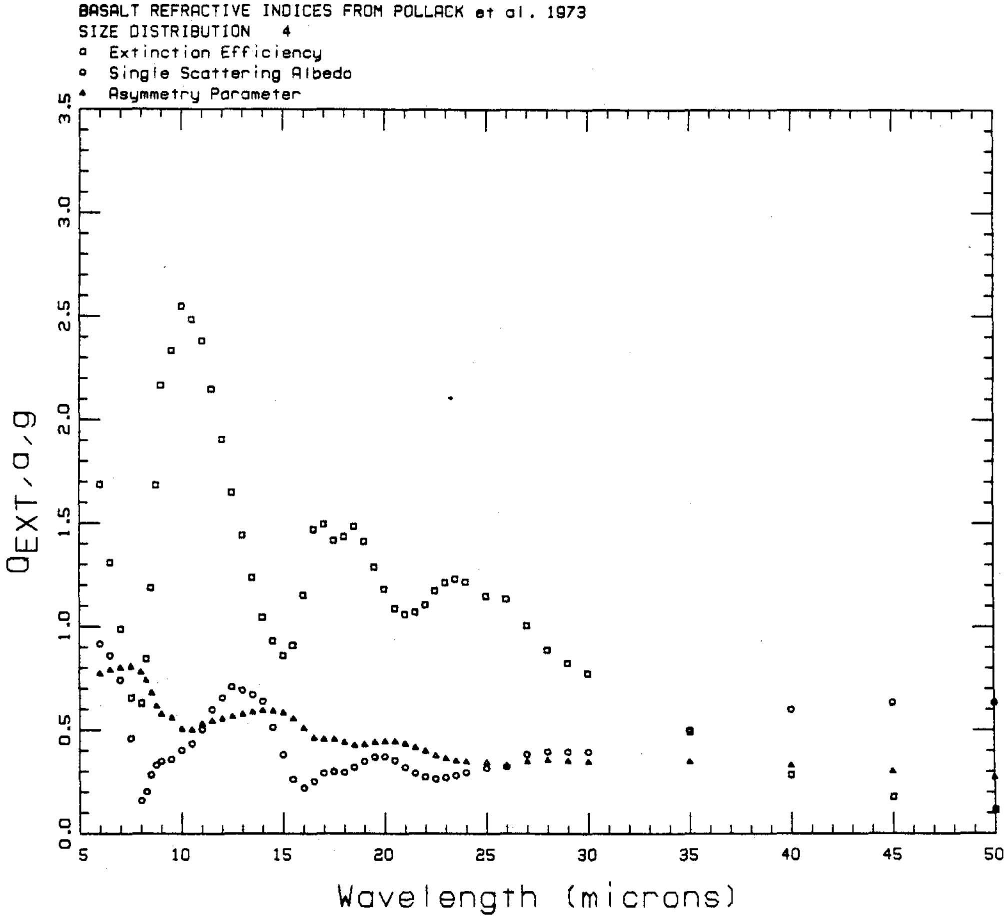
BASALT REFRACTIVE INDICES FROM POLLACK et al. 1973
SIZE DISTRIBUTION 4
□ Extinction Efficiency
○ Single Scattering Albedo
▲ Asymmetry Parameter
Q_EXT, a, g
0.0
0.5
1.0
1.5
2.0
2.5
3.0
3.5
5
10
15
20
25
30
35
40
45
50
Wavelength (microns)

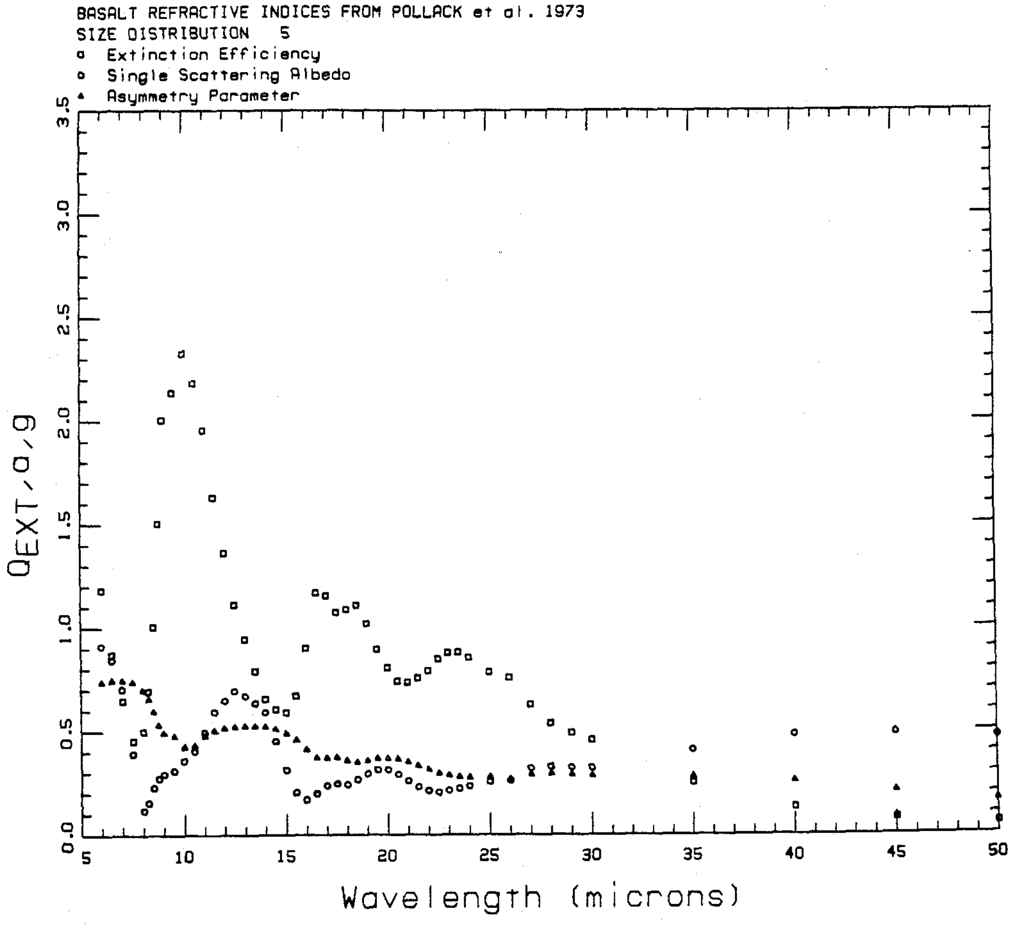
BASALT REFRACTIVE INDICES FROM POLLACK et al. 1973
SIZE DISTRIBUTION 5
□ Extinction Efficiency
○ Single Scattering Albedo
▲ Asymmetry Parameter
Q_{EXT}, a, g
0.0
0.5
1.0
1.5
2.0
2.5
3.0
3.5
5
10
15
20
25
30
35
40
45
50
Wavelength (microns)

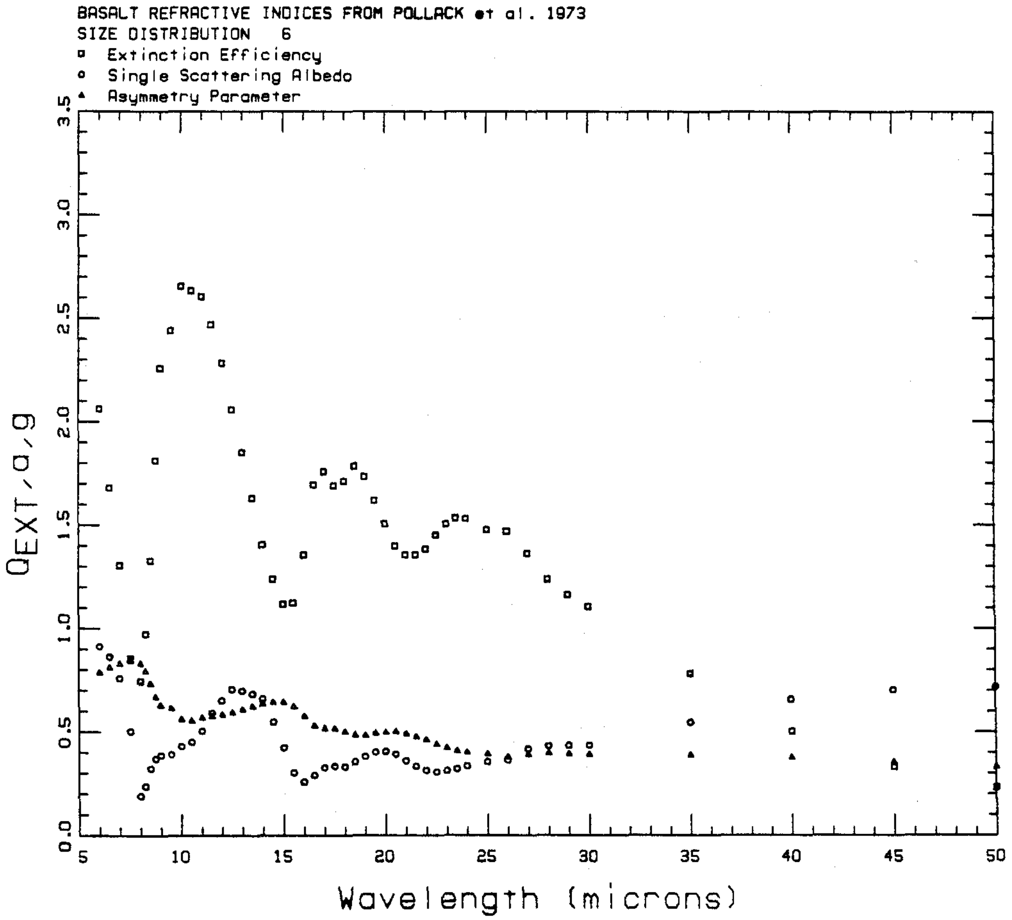
BASALT REFRACTIVE INDICES FROM POLLACK et al. 1973
SIZE DISTRIBUTION 6
▫ Extinction Efficiency
○ Single Scattering Albedo
▲ Asymmetry Parameter
Q_{EXT}, a, g
0.0
0.5
1.0
1.5
2.0
2.5
3.0
3.5
5
10
15
20
25
30
35
40
45
50
Wavelength (microns)

Fig. A2-6. (A) Water ice refractive indices from Schaaf and Williams (1973). (B, C) Calculated MIE parameters Q_{EXT}, $\tilde{\omega}_o$, and g for two size distributions of water ice spheres. The size distribution numbers correspond to those in Table A2-1.

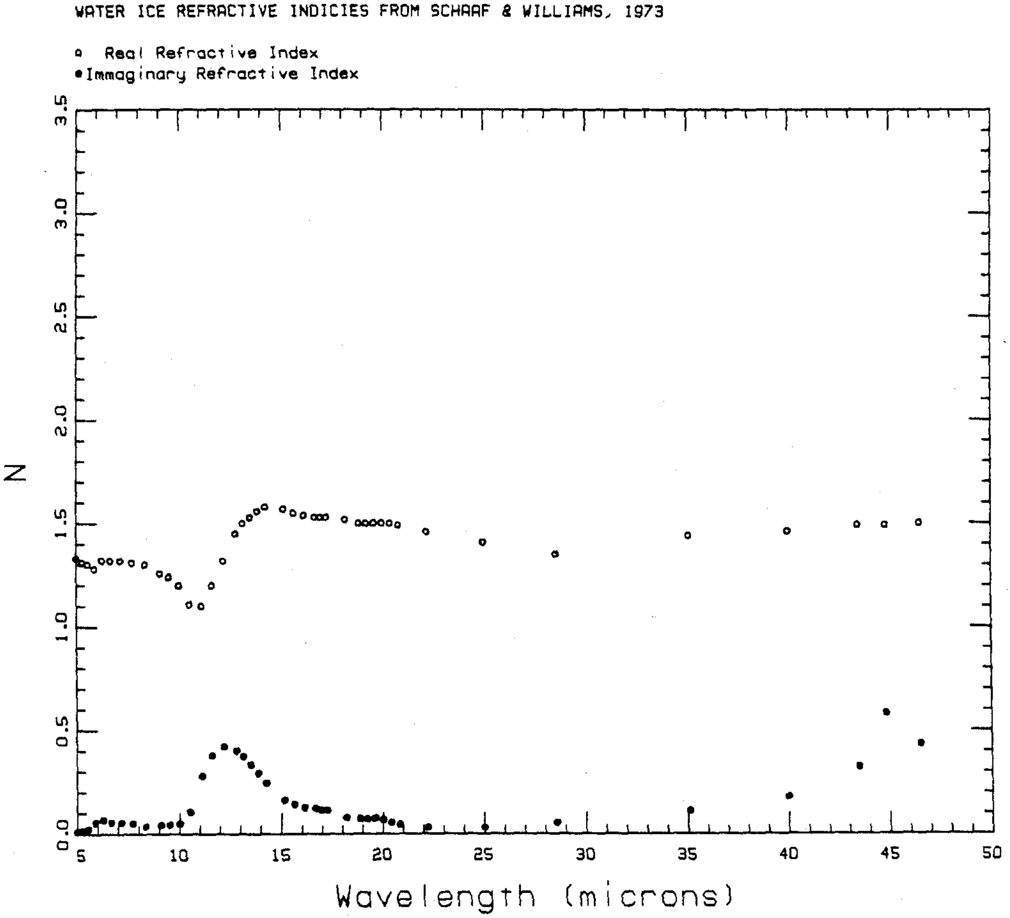
WATER ICE REFRACTIVE INDICIES FROM SCHAAF & WILLIAMS, 1973

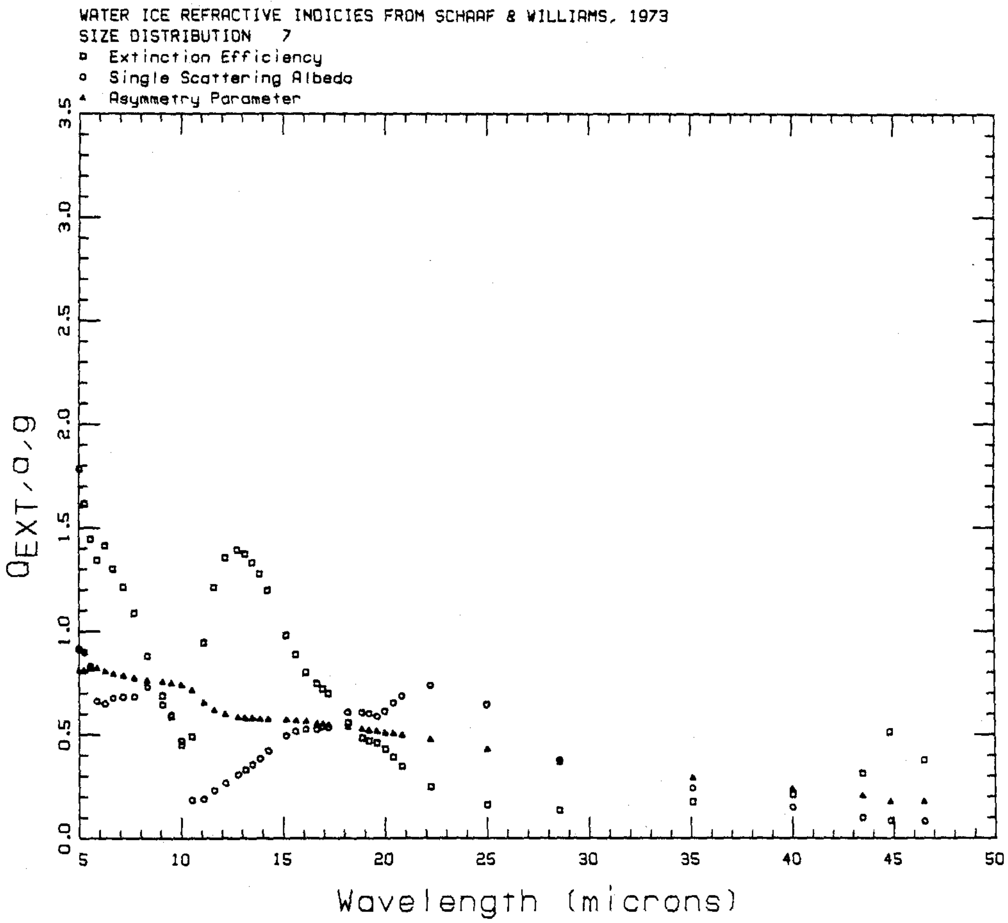
WATER ICE REFRACTIVE INDICIES FROM SCHAAF & WILLIAMS, 1973
SIZE DISTRIBUTION 7
□ Extinction Efficiency
○ Single Scattering Albedo
▲ Asymmetry Parameter
Q_{EXT}, a, g
0.0
0.5
1.0
1.5
2.0
2.5
3.0
3.5
5
10
15
20
25
30
35
40
45
50
Wavelength (microns)

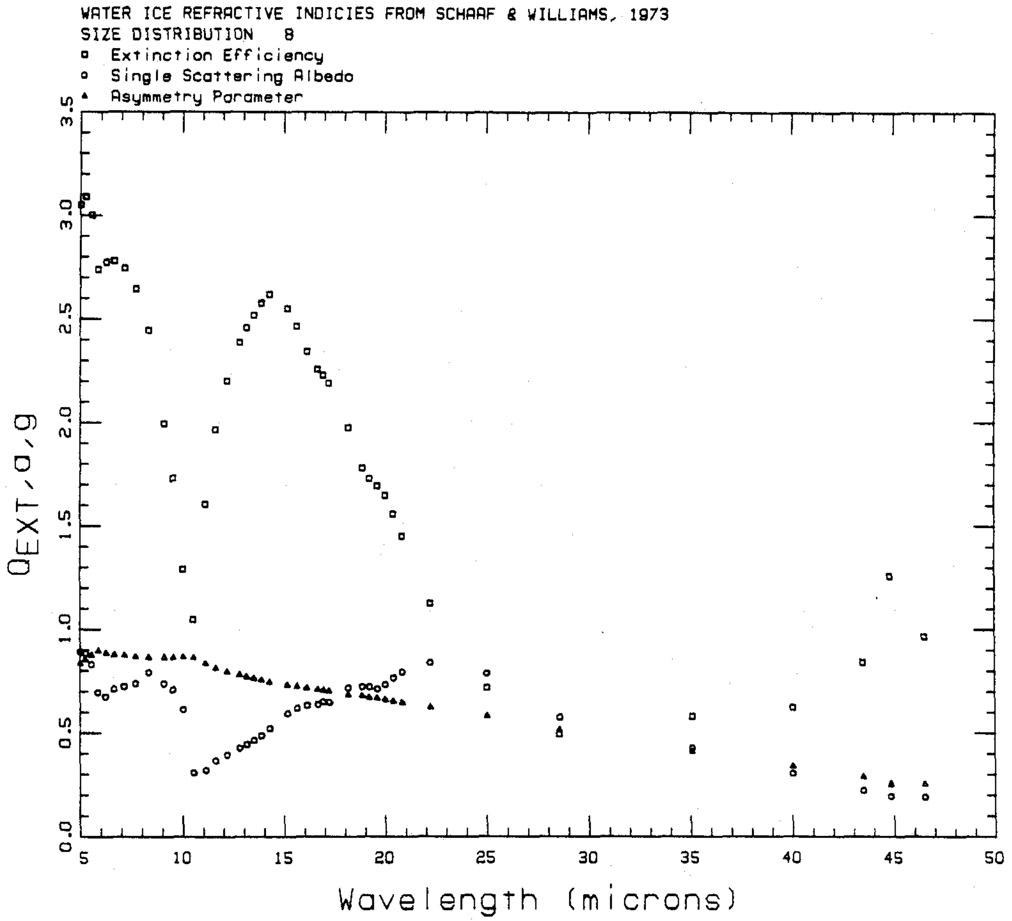
WATER ICE REFRACTIVE INDICIES FROM SCHAAF & WILLIAMS, 1973
SIZE DISTRIBUTION 8
□ Extinction Efficiency
○ Single Scattering Albedo
▲ Asymmetry Parameter
QEXT, a, g
0.0
0.5
1.0
1.5
2.0
2.5
3.0
3.5
5
10
15
20
25
30
35
40
45
50
Wavelength (microns)

3.4 IR Spectral Intervals

To calculate infrared cooling rates, the infrared spectrum is divided into 8 wavelength intervals. In intervals 1-3 and 5-8, infrared cooling rates are determined solely by aerosol scattering calculations, with no allowance for gaseous absorbers. In band 4, cooling rates are determined solely by emission in the strong 15 μ band of CO_2, with no allowance for aerosol scattering and absorption. The wavelength interval boundaries are at 0, 8.6, 11.0, 13.4266, 16.8126, 23.5, 35, 50, and 5000 μ. They were chosen to minimize variation in $Q_{ext}(\lambda)$ for size distributions of typical silicate materials over the most important parts of the Planck function at Martian atmospheric temperatures. Scattering calculations were performed by determining the Planck weighted averages of $Q_{ext}(\lambda)$, $\tilde{\omega}_o(\lambda)$, and $g(\lambda)$ in each relevant spectral interval, and replacing monochromatic emission rates in the δ-Eddington code with Planck function integrals. Efficient series representations of Planck function integrals are presented in Appendix 7 of Houghton (1977).

The model's inability to simultaneously deal with the effects of aerosol scattering and gaseous absorption is a serious shortcoming. Unfortunately, it is difficult to assess the effects of the assumptions employed here and much more work will have to be done before monochromatic infrared fluxes at all wavelengths can be calculated accurately. Interactions between aerosol scattering and gaseous absorption are likely to be most important in the wings of the CO_2 15μ band, which extend roughly from 12.0 to 13.5μ and from 17 to 20μ. For a blackbody emitter at 200K, this part of the spectrum accounts for less than 20% of the total emitted flux. Since model-calculated thermal equilibrium temperature profiles and surface CO_2 sublimation rates depend on integrated bolometric fluxes, large inaccuracies in calculating infrared fluxes in the wings of the 15μ band are not expected to cause large errors in surface and atmospheric heating rates. Also, $F{\downarrow}_{15}$ and atmospheric cooling rates in the fourth spectral interval are not affected by the assumed value of $\Delta\nu_{15}$ and dust tends to be relatively transparent in the 15μ region (see Figs A2-4 and A2-5).

4. Dynamics, etc.

In full general circulation models, atmospheric heating and cooling rates due to dynamical motions are calculated at all latitudes. In this model, atmospheric dynamic heating and cooling rates are either assumed at the start of calculations or are calculated from an assumed set of polar atmospheric motions.

The results of Martial general circulation models show that the polar atmosphere is heated by horizontal eddies and by sinking motions due to large scale meridional circulations (Leovy and Mintz, 1969; Pollack et al., 1981). In this model, the effects of horizontal eddies are simulated by simply adding an extra heating term to the instantaneous heat balance equation of each layer.

To simulate the heating effects of sinking motions, a fixed vertical velocity is specified at each layer boundary. Vertical velocities at the top of the atmosphere (Level 1) and at the surface (Level 11) are assumed to be zero. The "shape" of the sinking profile with pressure can be varied, but was usually assumed to take the form of a sinusoid, with maximum downward velocity in the middle of the atmosphere at level 6. Differences between the net fluxes of mass at each layer's upper and lower boundaries are assumed to be balanced by the advection of gas through the "sides" of each layer from or to lower latitudes assuming no local horizontal temperature gradients. For the case of a sinusoidal sinking profile, the required variation in horizontal velocities with height takes the form of a cosine curve, with maximum poleward velocities at high altitudes, zero horizontal velocity at mid altitudes, and maximum equatorward velocities at low altitudes. The horizontal and vertical velocity profiles for this case approximate those for a single thermally direct zonally symmetric Hadley cell at the pole. During each time step, heating rates for each layer due to vertical motions are determined by the net fluxes of potential temperature at its upper and lower boundaries.

Dry convection, which commonly occurs at lower Martian latitudes at midday does not occur at the poles because surface temperatures are low and the atmospheric temperature profiles are very stable during most of the year. Under favorable conditions, atmospheric temperatures can drop to the local CO_2 frost point during the polar night seasons (see Chapter 3). The current model does not attempt to deal with the many things that could occur after the onset of atmospheric CO_2 condensation.

For stable atmospheric conditions, the effects of heat conduction between atmospheric and surface are small. Following Gierasch and Toon (1973) and Leovy and Mintz (1969), surface heating rates due to convection are parameterized by:

$$H_c = p_s \frac{c_p C_H V_s}{R T_0} \left[T(10) - T_s \right] \tag{A2.29}$$

where H_c is the surface heating rate due to conductive heat transfer from atmosphere to surface, p_s is the surface pressure, c_p is the atmospheric specific heat at constant pressure, C_H is a heat transfer coefficient, V_s is the near surface wind velocity, R is the gas constant, T_0 is another constant, $T(10)$ is the temperature of the lowest atmospheric layer, and T_s is the surface temperature. Using the same values for c_p, C_H, V_s, R, and T_0 that were adopted by Gierasch and Toon and Leovy and Mintz gives $H_c = p_s K(T(10) - T_s)$ where $K = 6.5 \times 10^{-3}$ Wm^{-2}/mbK, $H_c = 0.52$ Wm^{-2} for $p_s = 4$ mb and $(T(10) - T_s) = 20$ K.

5. IRTM Brightness Temperatures

Once polar thermal equilibrium temperature profiles have been established, the model's final task is to calculate IRTM brightness temperatures at the top of the atmosphere as a function of emission angle ϑ.

For the IRTM 15 μ channel, Virgil Kunde has calculated weighting functions for constant atmospheric temperatures of 180 K (Kieffer et al., 1976b). These are shown for air masses of 1 through 6 in Figure A2-7. The effects of atmospheric temperature variations on these weighting functions are expected to be small. The effects of water ice, dust, and CO_2 clouds are more difficult to assess. Of the three, CO_2 clouds would be expected to cause the most trouble because optically thick CO_2 clouds should be excellent blackbody emitters at $\lambda = 15\ \mu$. The expected temperatures of CO_2 clouds residing above the top half of the IRTM 15 μ channel weighting functions are less than 133 K.

To calculate IRTM 15 μ channel brightness temperatures at the top of the atmosphere, atmospheric temperatures are assumed to vary linearly between their determined values at the centers of each layer. Atmospheric temperatures in the lower half of the lowest layer and the upper half of the highest layer are linearly extrapolated from the temperatures at the centers of the nearest two layers.

IRTM brightness temperatures in the 7, 9, 11, and 20 μ channels are calculated assuming no atmospheric opacity from gaseous absorbers. IRTM brightness temperatures in the 7, 9, 11, and 20 μ channels can be calculated as a function of emission angle using the formal solution to the the equation of radiative transfer.

In its most general form, the equation of radiative transfer can be written:

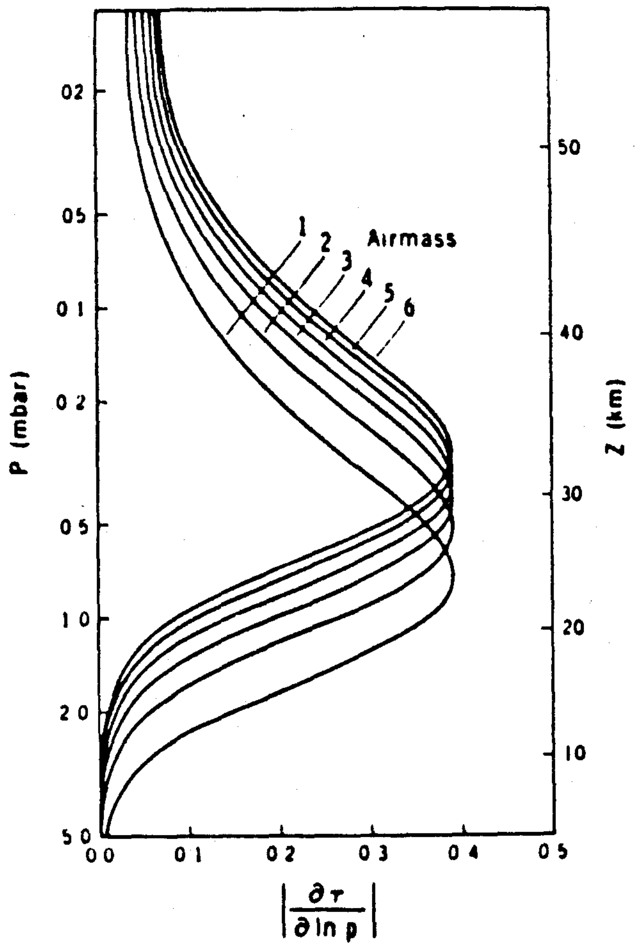

Fig. A2-7. IRTM 15 μ channel weighting functions as a function of airmass. Airmass = 1 corresponds to nadir viewing (from Kieffer et al., 1976).

$$\cos(\vartheta)\frac{dI(\tau,\vartheta,\psi)}{d\tau} = I(\tau,\vartheta,\psi) - J(\tau,\vartheta,\psi) \qquad \text{(A2.30)}$$

where ϑ is the emission angle and ψ is the azimuth angle and $J(\tau,\vartheta,\psi)$ is the source function (see Chandrasekhar, 1960, Ch. 1 Eq. 66.) The source function includes radiation that is scattered into the beam as well as radiation that is emitted into the beam. In this notation, $\cos(\vartheta) > 0$ for upward radiance. For an atmosphere with total optical depth τ^*, the emergent energy at the top of the atmosphere ($\tau = 0$) at emission angle ϑ and azimuth angle ψ can be found by integrating equation (A2-30) to yield:

$$I(0,\vartheta,\psi) = I(\tau^*,\vartheta,\psi)e^{-\tau^*/\cos\vartheta} + \int_0^{\tau^*} J(t,\vartheta,\psi)e^{-t/\cos\vartheta}\frac{dt}{\cos\vartheta} \qquad \text{(A2.31)}$$

This means that the emitted intensity at any emission angle can be determined if the source function can be accurately specified throughout the atmosphere. Toon, Pollack, and Sagan (1977) have generated theoretical Martian infrared spectra using source functions derived from a 2-stream approximation. In this model, source functions are derived from the δ-Eddington approximation.

In the δ-Eddington approximation, the azimuthally averaged equation of transfer is:

$$\mu' d\frac{(I_o - \mu' I_1)}{d\tau'} = (I_o - \mu' I_1) - \tilde{\omega}_o'(I_o + g'\mu' I_1) - (1 - \tilde{\omega}_o')B \qquad \text{(A2.32)}$$

This equation is the same as equation (A2.12) except that $\tilde{\omega}_o$, g, and τ have been replaced by the transformed variables $\tilde{\omega}_o'$, g', τ', and $\mu>0$ for upward radiance has been replaced by $\mu'>0$ for downward radiance. Having $\mu' = \cos(\vartheta) = -\mu$ avoids the inconvenience of having the cosine of the emission angle being negative for emergent intensities at the top of the atmosphere as is the case for the conventions used by Shettle and Weinman (1970). According to equation (A2.32) the δ-Eddington source function is:

$$J_{\delta-Edd} = \varpi_0' I_0 - \varpi_0' g' \mu' I_1 + (1 - \varpi_0')B \qquad \text{(A2.33)}$$

In this coordinate system:

$$F\uparrow(\tau) = 2\pi \int_0^1 \mu' \left[I_0(\tau) - \mu' I_1(\tau) \right] d\mu' = \pi \left[I_0(\tau) - \frac{2}{3} I_1(\tau) \right] \qquad \text{(A2.34)}$$

and

$$F\downarrow(\tau) = 2\pi \int_0^{-1} \mu' \left[I_0(\tau) - \mu' I_1(\tau) \right] d\mu' = \pi \left[I_0(\tau) + \frac{2}{3} I_1(\tau) \right] \qquad \text{(A2.35)}$$

which are the same as for the Shettle and Weinman conventions (see equations (A2.10) and (A2.11)). This means that the boundary conditions used to determine I_0 and I_1 in this new coordinate system will be the same as were used in the Shettle and Weinman coordinate system and $I_0(\tau)$ and $I_1(\tau)$ will have the same form and the same values in the two coordinate systems.

The first term in equation (A2.29) deserves special consideration for the case of non-unit emissivity. In Toon, Pollack, and Sagan's treatment, $I(\tau=\tau^*,\vartheta)$ is assumed to equal $\varepsilon_s B_s$ with no allowance for reflection of the down-going infrared flux of the bottom of the atmosphere by the surface. This same procedure was used by Kahn (1980). In this model, $I(\tau^*,\vartheta)$ is assumed to equal $\varepsilon_s B_s + (1 - \varepsilon_s)\ F\downarrow(\tau=\tau^*)/\pi = F\uparrow(\tau=\tau^*)/\pi$, which is equivalent to assuming isotropic emission and reflection at the surface. This procedure gives much more realistic calculated brightness temperatures at the top of the atmosphere for cases involving non-unit surface emissivity.

For the case of an isothermal single layer atmosphere, $I(\tau=0,\vartheta)$ can be determined analytically if the solutions for I_0 and I_1 (Eqs. A2.15 and A2.16) are used in $J_{\delta-Edd}$ and the resulting forms are used in (A2.31):

$$I(\tau=0,\mu') = e^{-\tau^*/\mu'}\left[C_1 e^{-\kappa\tau^*}(1 - \frac{2}{3}P) + C_2 e^{+\kappa\tau^*}(1 + \frac{2}{3}P) + B\right] +$$

$$\int_0^{\tau^*}\left[\frac{\tilde{\omega}_o}{\mu'}C_1 e^{(-\kappa-\frac{1}{\mu'})t}[1 - g'\mu'P] + \frac{\tilde{\omega}_o'}{\mu'}C_2 e^{(\kappa-\frac{1}{\mu'})t}[1 + g'\mu'P] + \frac{B}{\mu'}e^{-t/\mu'}\right] dt \quad \text{(A2.36)}$$

which upon integration yields:

$$I(\tau=0,\mu') = e^{-\tau^*/\mu'}\left[C_1 e^{-\kappa\tau^*}(1 - \frac{2}{3}P) + C_2 e^{+\kappa\tau^*}(1 + \frac{2}{3}P) + B\right] +$$

$$D(\tau^*) - D(0) \quad \text{(A2.37)}$$

where

$$D(t) = \frac{\tilde{\omega}_o'}{-\mu'\kappa - 1}C_1 e^{(-\kappa-\frac{1}{\mu'})t}[1 - g'\mu'P] +$$

$$\frac{\tilde{\omega}_o'}{\mu'\kappa - 1}C_2 e^{(\kappa-\frac{1}{\mu'})t}[1 + g'\mu'P] - Be^{-t/\mu'} \quad \text{(A2.38)}$$

For an N-layer atmosphere consisting of isothermal layers:

$$I(\tau=0,\mu') = e^{-\tau^*/\mu'}\left[C_1(N) e^{-\kappa\tau^*}(1 - \frac{2}{3}P) + C_2(N) e^{+\kappa\tau^*}(1 + \frac{2}{3}P) + B(N)\right] +$$

$$\sum_{i=1}^{N} D_i(\tau_{i+1}) - D_i(\tau_i) \quad \text{(A2.39)}$$

where D_i is the function $D(t)$ in layer i and τ_i is the optical depth at level i.

Fig.A2-8 shows a spot check of the accuracy of this method. In the figure, monochromatic intensities derived from δ-Eddington and two stream source functions (Toon, Pollack and Sagan 1977) are compared with exact solutions (Yamamoto *et al*, 1966) for a typical Martian infrared aerosol optical properties for infrared optical depths of 0.1 1.0 and 10.0. The results show that the δ-Eddington method is more accurate than the two-stream method for all

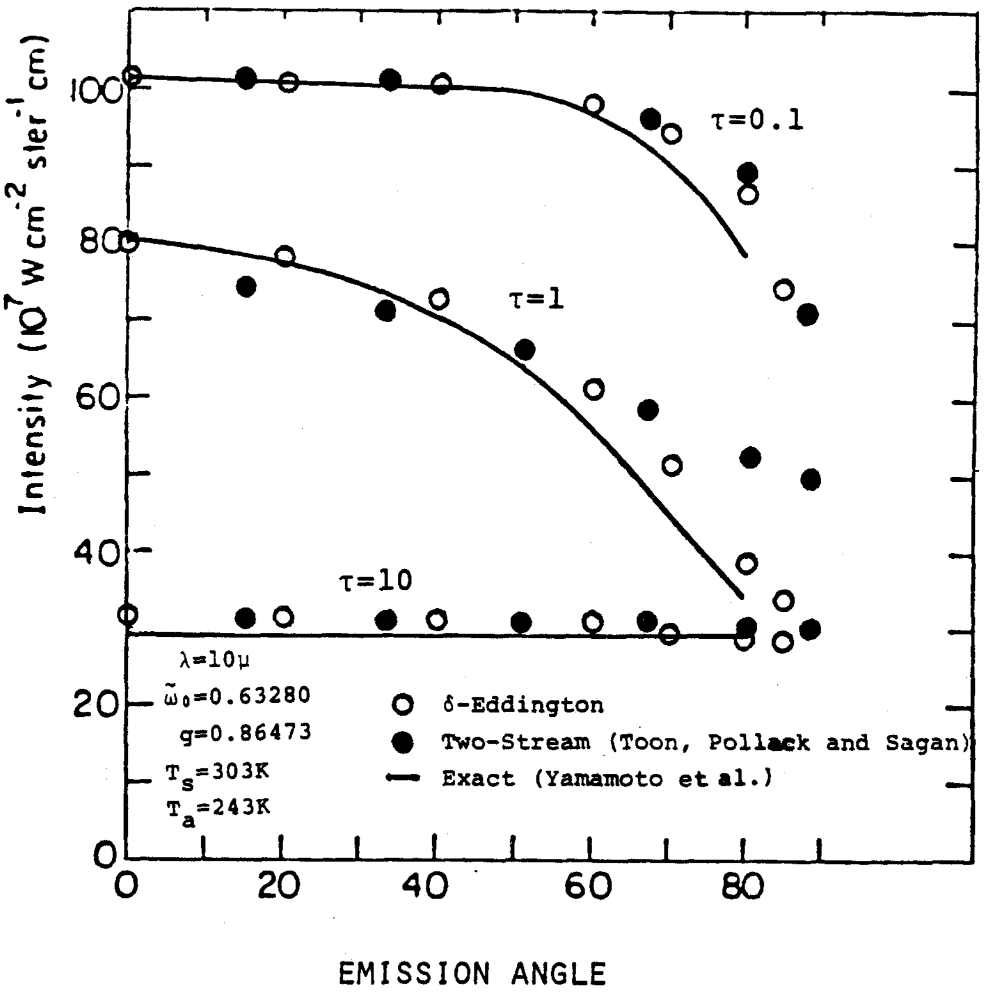

Fig. A2-8. Comparison between calculated outward infrared intensities at the top of the atmosphere as a function of emission angle and infrared opacity τ. Shown are results from the δ-Eddington code used in this study, Two-Stream approximation results from Toon, Pollack, and Sagan (1977), and exact calculations using a doubling code (Yamamoto et al., 1966). (This figure is after Toon, Pollack, and Sagan (1977).)

combinations of opacities and emission angles tested.

References

Burch, D.E. et al (1962) AFCRL report 62-698, [NTIS Ad-287406].

Chandrasekhar, S. (1960) *Radiative Transfer*, Dover.

Christensen, P.R. and R.W. Zurek, (1984) *J. Geophys. Res.* **89**, 4587.

Crisp. D., S.B. Fels and M.D. Schwarzkopf (1985) in preparation.

Curran, R.J., B.J. Conrath, R.A. Hanel, V.G. Kunde and J.C. Pearl (1973) *Science* **192**, 281.

Diermendjian, D. (1969) *Electromagnetic Scattering of Spherical Poydispersions*, Elsevier, N.Y.

Gierasch, P.J. and O.B. Toon (1973) *J. Atmos. Sci.* **30**, 1502.

Haberle, R. M., C.B. Leovy and J.B. Pollack (1982) *Icarus* **50**, 322.

Hansen, J.E. and L.D. Travis (1979) *Space Sci. Rev.* **16**, 527.

Hansen, J. *et al* (1981) *Science* **213**, 957.

Houghton, J.T., (1977) The Physics of Atmospheres, Cambridge University Press

Howard, J. *et al* (1955) AFCRL Report 55-213 [NTIS AD-087679]

Hunt, G.E. (1979) *J. Geophys. Res.* **84**, 2865.

Joseph, J.H., W.J. Wiscomb, and J.A. Weinman (1976) *J. Atmos. Sci.* **33**, 2452.

Kahn, R. (1980) Ph.D. Thesis, Harvard University.

Kieffer, H.H. et al (1976) *Science* **194**, 1346.

Leovy, C.B. and Y. Mintz (1969) *J. Atmos. Sci.* **26**, 1167.

Manabe, S. and R.T. Wetherald (1966) *J. Atmos. Sci.* **24**, 241.

Pollack, J.B., O.B. Toon and B.N. Kahre (1973) *Icarus* **19**, 372.

Pollack, J.B. et al (1979) *J. Geophys. Res.* **84** , 2929.

Pollack, J.B. et al. (1981) *J. Atmos. Sci.* **38**, 3.

Schaaf, J.W. and D. Williams (1973) *J. Opt. Soc. Amer.***63**, 726.

Shettle, E.P. and J.A. Weinman (1970) *J. Atmos. Sci.* **27**, 1048.

Toon, O.B., J.B. Pollack and C. Sagan (1977) *Icarus* **30**, 663.

Yamamoto, G. et al (1966) *J. Atmos. Sci.* **23**, 305.

APPENDIX 3

10-LAYER MODEL CALCULATIONS OF THE PARAMETER f

In Chapter 2, Viking IRTM radiation balance measurements at the top of the atmosphere were used in conjunction with a simplified polar radiative model to show that seasonal frost albedos were lower in the core region of the north residual cap during late spring than they were in the core region of the south residual cap during the same season. In order to test this conclusion for a wide range of possible surface and atmospheric properties, infrared calculations that could have been performed with the 10-layer model (see Appendix 2) and the many model input parameters these calculations require, were replaced by a single parameter f

$$f = \frac{F{\downarrow}^{*}_{IR}}{H_A + F_{Horiz}} \tag{A3.1}$$

where $F{\downarrow}^{*}_{IR}$ is the downward bolometric flux of the infrared radiation at the surface, H_A is the vertically integrated atmospheric heating rate due to the absorption of solar energy, and F_{Horiz} is the vertically integrated atmospheric heating rate due to dynamical motions.

For an arbitrary atmosphere, f could take on a wide range of both positive and negative values. For the special case of the Martian polar atmosphere during spring, the range of f is likely to be limited. The purpose of this appendix is to establish these limits.

In Davies' simplified polar radiative model (1979), he assumed that one-half the solar energy absorbed by atmospheric aerosols is ultimately absorbed by the surface at infrared wavelengths. This assumption would be 100% correct if the spectral emissivity of the surface were unity and the atmosphere was transparent to its own radiation at all infrared wavelengths. In reality, the Martian polar atmosphere is not transparent near the strong 15 μ band of CO_2 nor is it transparent at other infrared wavelengths if significant quantities of dust are present. There is also a significant possibility that surface emissivities at infrared wavelengths may be less than unity and that aerosols could be concentrated in the upper atmosphere or near the surface. All these phenomena could affect f.

To establish limits for potential variations in f, the 10-layer polar radiative model was used to calculate f for a number of combinations of model input parameters for the insolation conditions that exist at the poles during late spring. Limited computer resources, patience, and imagination made it impossible to calculate f for every conceivable combination of model input parameters. What is presented here is, I hope a thorough and representative spot check.

Insolation rates and basic surface and atmospheric properties used in the calculations were chosen to lie roughly midway between their likely values at the core regions of the north and south residual caps during late spring. Table A3-1 shows the values of the input parameters F_{Solar}, the constant insolation rate at the top of the atmosphere, φ, the constant solar zenith angle, p_s, the surface pressure, and T_s, the fixed surface frost temperature used in all calculations. Modest variations in these parameters should not affect calculated values of f.

The 10-layer model was run for three sets of combinations of input parameters. The sets are shown in Tables A3.2a,b,c. Sets A and B have 1620 possible combinations. Set C has 1024. The variables τ_V, A_s, $\tilde{\omega}_{0V}$, g_V - the solar spectrum averaged aerosol opacity, surface albedo, aerosol single scattering albedo and asymmetry parameter are perfectly analogous to the input parameters to the simplified polar radiative model in Chapter 2. Aerosol optical properties at infrared wavelengths are determined by Q_V, the solar spectrum averaged

TABLE A3-1

Fixed Model Input Parameters

Parameter	Units	Value
F_{Solar}	Wm^{-2}	241.325
φ	degrees	66.5
p_s	mb	4
T_s	K	144.7

Table A3-1. Fixed 10-layer model input parameter used to calculate f.

TABLE A3-2a

Parameter Set A

Parameter	Values			
τ_V	0.1	0.25	0.4	1.0
A_s	0.5	0.75	1.0	
ϖ_{oV}	0.76	0.86	0.96	
g_V	0.69	0.79	0.89	
ε_s	0.6	0.8	1.0	
F_{Horiz} ($\mathrm{Wm^{-2}}$)	2			
Q_V	2.74			
IRDIST	2	3	4	7
IVDUST	3			
IVHEAT	3			

Table A3-2a. 10-layer model input parameter values in parameter set A.

TABLE A3-2b

Parameter Set B

Parameter	Values				
τ_V	0.1	0.25	0.4	1.0	
A_s	0.5	0.75	1.0		
ϖ_{oV}	0.86				
g_V	0.79				
ε_s	1.0				
F_{Horiz} (Wm^{-2})	0.0	2.0	5.0		
Q_V	1.0	2.74	4.0		
IRDIST	1				
IVDUST	1	2	3	4	5
IVHEAT	1	3	5		

Table A3-2b. 10-layer model input parameter values in parameter set B.

TABLE A3-2c

Parameter Set C

Parameter	Values	
τ_V	0.25	1.0
A_s	0.5	1.0
$\tilde{\omega}_{oV}$	0.76	0.96
g_V	0.69	0.89
ε_s	0.6	1.0
F_{Horiz} (Wm^{-2})	0.0	5.0
Q_V	1.0	4.0
IRDIST	2	3
IVDUST	1	5
IVHEAT	1	5

Table A3-2c. 10-layer model input parameter values in parameter set C.

aerosol extinction efficiency and IROPT, which represents $Q_{Ext}(\lambda)$, $\tilde{\omega}_o(\lambda)$, and $g(\lambda)$ calculated from Mie theory for various size distributions of Montmorillonite 219b, Basalt, and Water Ice spheres in Appendix 2. IRDIST corresponds to the distribution number in Table A2-1. The ratios of aerosol opacities at visible and infrared wavelengths can be adjusted by changing Q_V. The remaining parameters IVDUST and IVHEAT refer to assumed vertical profiles of aerosol opacities and atmospheric advective heating rates. These are shown in Figure A3-1. Profile 1 assumes almost total concentration of aerosol opacity or advective heating in the uppermost atmospheric layer. Profile 3 assumes uniform distribution with pressure. Profile 5 assumes almost total concentration in the lowest atmospheric layer. Profiles 2 and 4 assume linearly increasing or decreasing concentrations with pressure.

The values in parameter set A were chosen to test the sensitivity of f to variations in τ_V, A_s, $\tilde{\omega}_{oV}$, g_V, ε_s, and IRDIST. The values in parameter set B test the sensitivity of f to τ_V, A_s, F_H, Q_V, IVDUST and IVHEAT. With the exception of τ_V (see later in the text), the values in parameter set C represent the extrema of the parameter values in sets A and B.

Model calculations were performed by initially assuming an isothermal atmosphere at 150 K and then calculating thermal equilibrium temperature profiles of f. The criterion for convergence was ±0.021K/1.2 hrs in the least thermally equilibrated layer. Superadiabatic lapse rates were not encountered at any point in the calculations.

Calculated values of f for parameter sets A, B, and C are shown as histograms in Figs. A3-2a,b,c. The results show that the most frequently calculated values of f were generally greater than 0.45 and less than 0.7 for all three sets of model input parameters. A small percentage of the calculated values of f

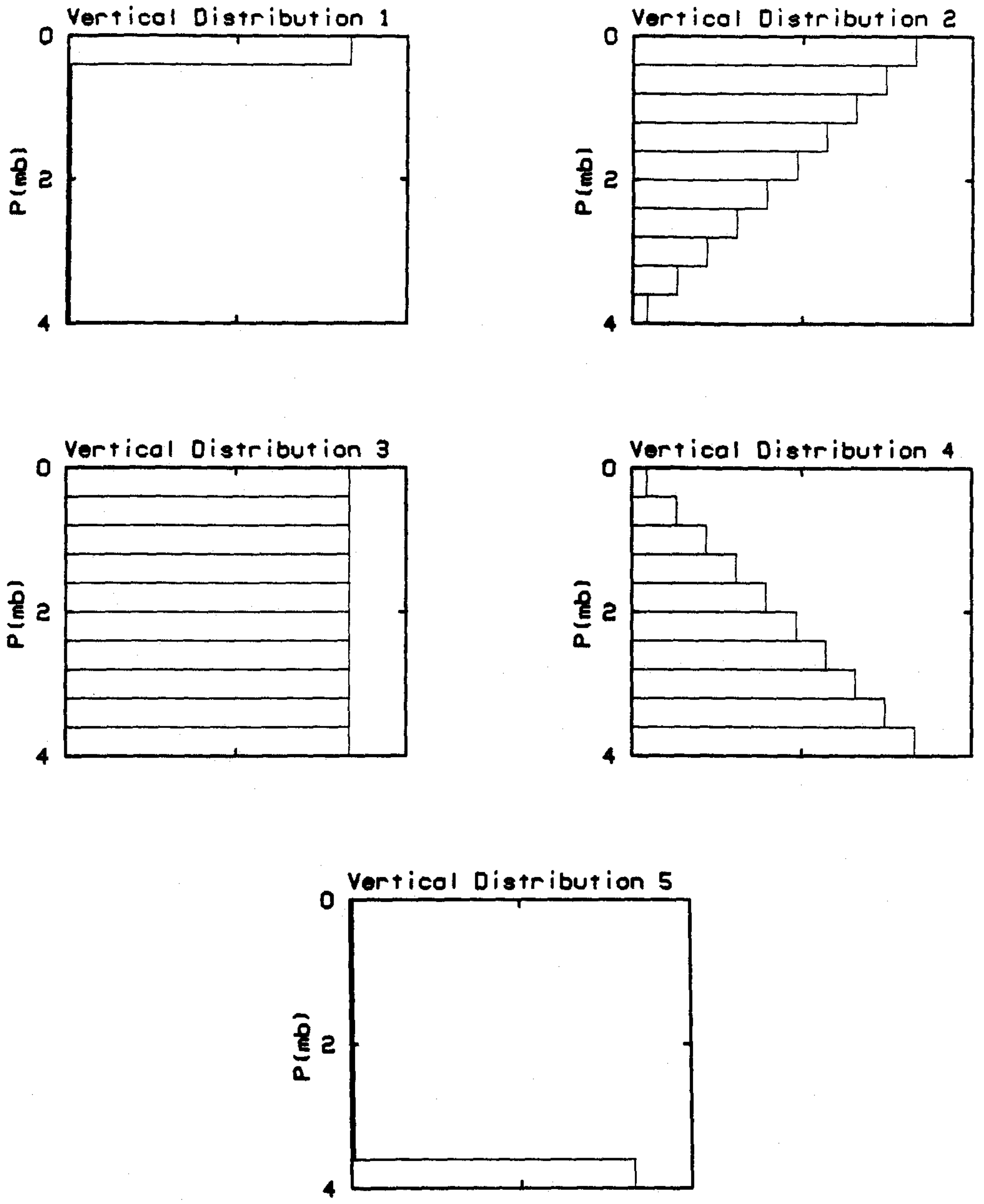

Fig. A3-1. Five assumed distributions of aerosol optical depths with pressure used in these model calculations. The abscissa scales are linear and have arbitrary units.

Fig. A3-2. 10-layer model calculated values of the parameter f for all combinations of model input parameters in parameter sets A, B, and C. N is the number of model calculated thermal equilibrium profiles that gave calculated values of f within the specified ranges. Shaded areas show the number of profiles that yielded calculated values of $F\uparrow_{IR}$ that were less than 32 Wm^{-2} which makes them inconsistent with the IRTM radiation balance observations of the north and south study regions during the late spring seasons.

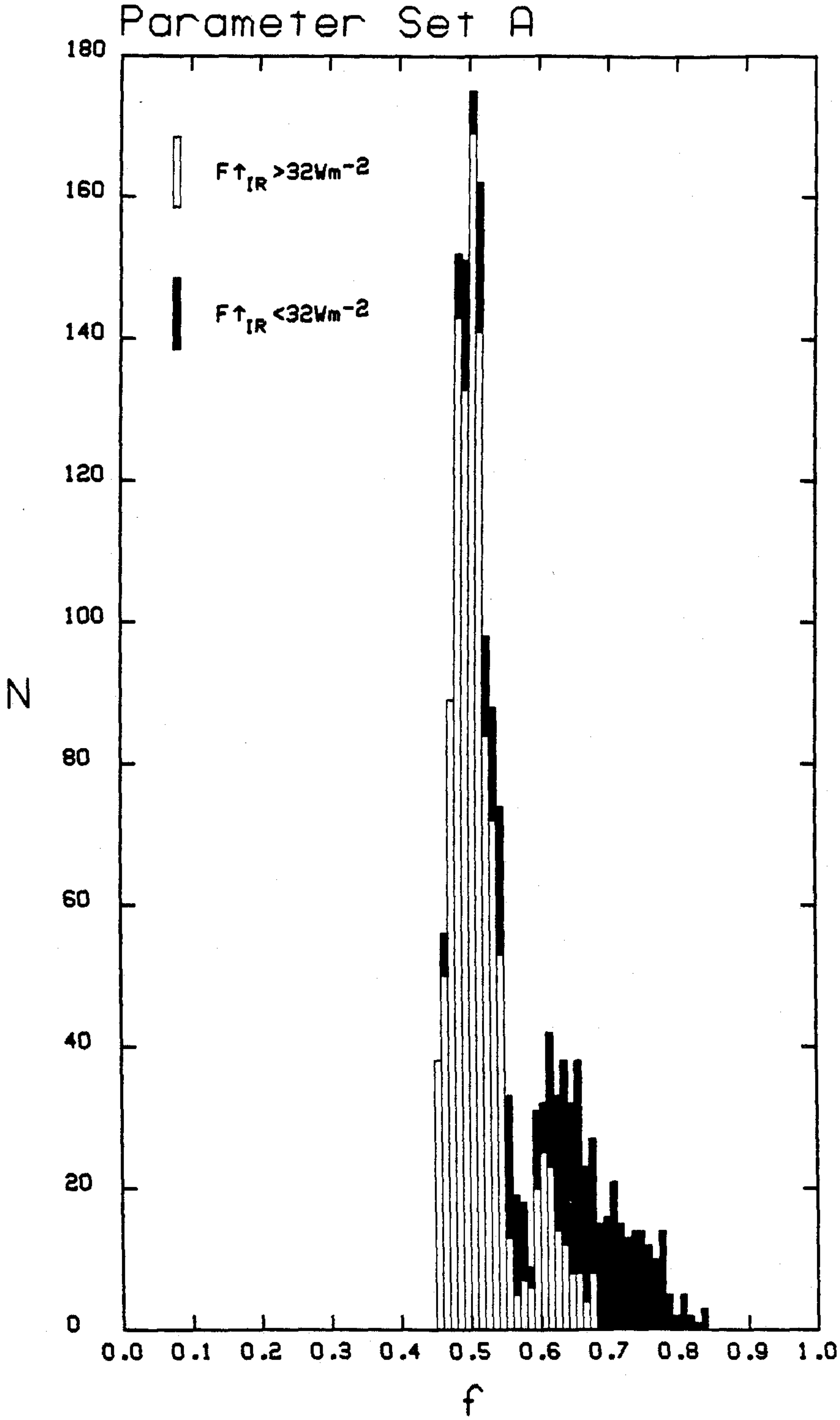
Parameter Set A
N
f
0
20
40
60
80
100
120
140
160
180
0.0
0.1
0.2
0.3
0.4
0.5
0.6
0.7
0.8
0.9
1.0
F↑IR >32Wm⁻²
F↑IR <32Wm⁻²

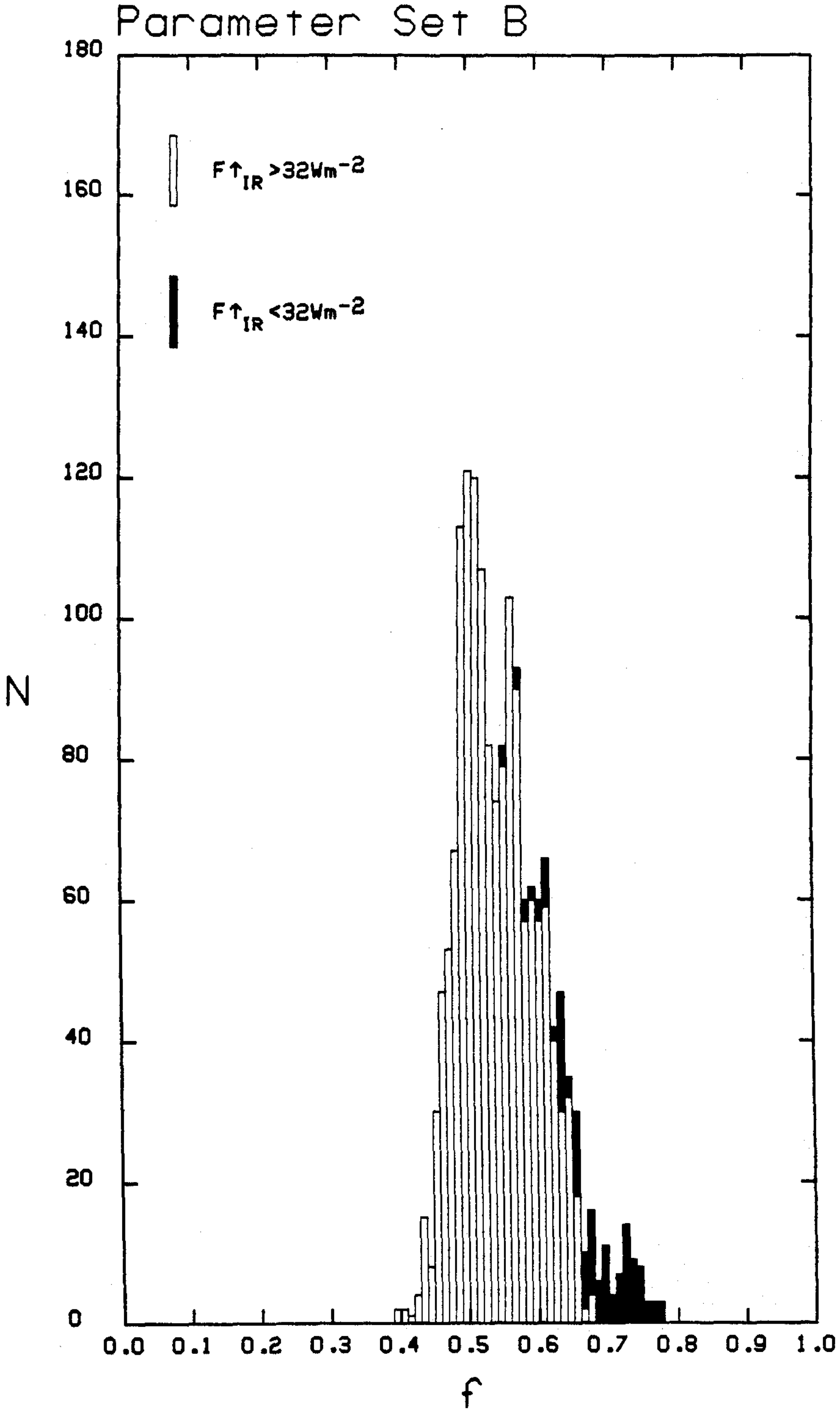
Parameter Set B
$F\uparrow_{IR} > 32 Wm^{-2}$
$F\uparrow_{IR} < 32 Wm^{-2}$
N
180
160
140
120
100
80
60
40
20
0
0.0
0.1
0.2
0.3
0.4
0.5
0.6
0.7
0.8
0.9
1.0
f

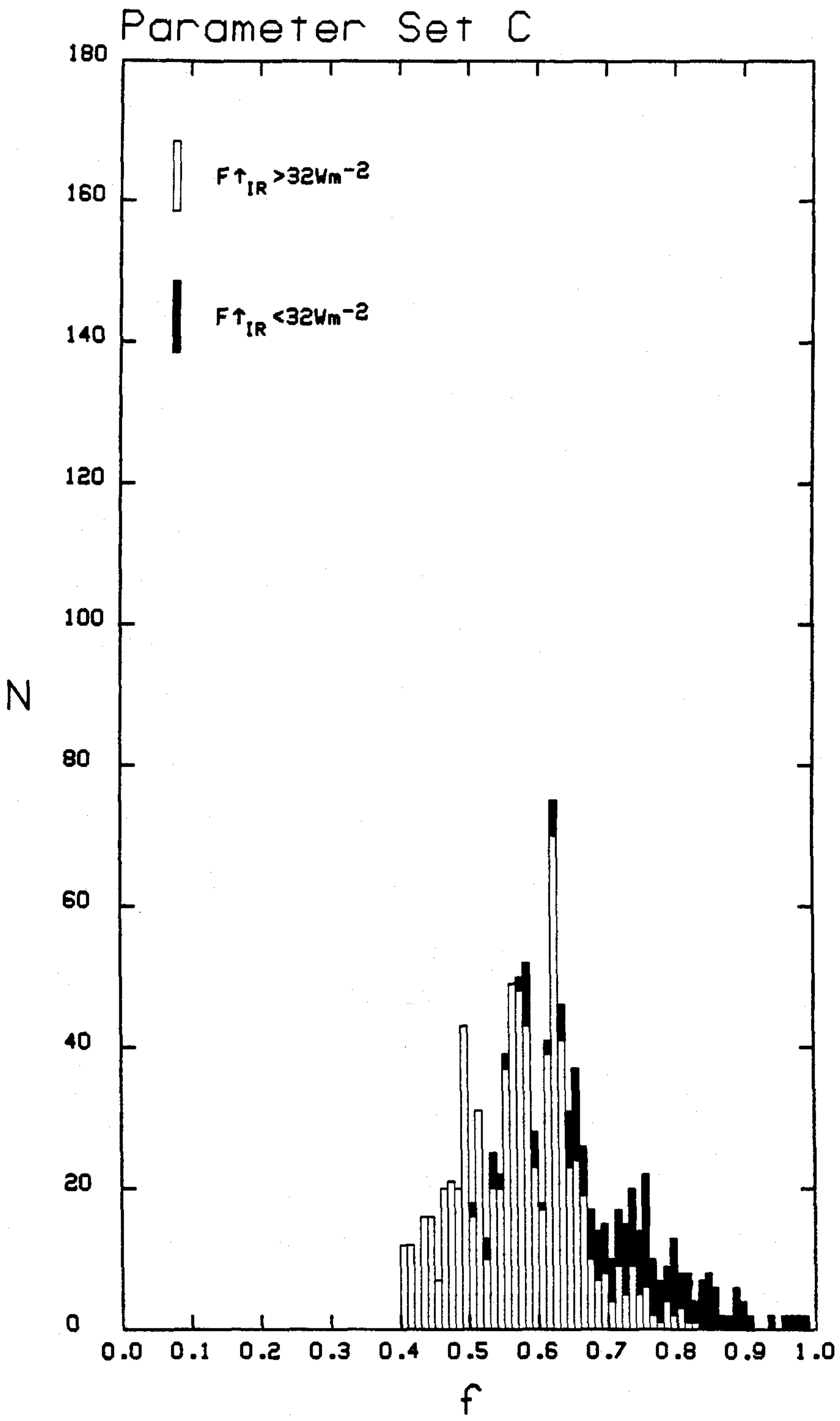
Parameter Set C
180
160
140
120
100
80
60
40
20
0
N
$F\uparrow_{IR}$ >32Wm^{-2}
$F\uparrow_{IR}$ <32Wm^{-2}
0.0
0.1
0.2
0.3
0.4
0.5
0.6
0.7
0.8
0.9
1.0
f

were outside these bounds, but it is fairly easy to show that most of the combinations of model input parameters that produced them could not have occurred during late spring at the north and south poles.

Since f is not a single physical quantity but a ratio, f can become large if its denominator becomes small. A large fraction of the calculated values of f greater than 0.7 occured when τ_V was assumed to be 0.1 and $\tilde{\omega}_0$ was assumed to be 0.96. f became small under these circumstances because H_A became small and yet $F\downarrow_{IR}^{*}$ remained significant due to atmospheric emission in the 15μ band of CO_2. One way to show that most of the calculated values of f greater than 0.7 are not realistic is to compare model calculated values of $F\uparrow_{IR}$, the upward infrared flux at the top of the atmosphere with values of $F\uparrow_{IR}$ determined from the IRTM observations. (see Chapter 2). $F\uparrow_{IR}$ will increase with increasing (H_A+F_{Horiz}) and increase with decreasing f. Figs. A3-2abc show that the range of model calculated values of f can be significantly reduced if model calculated values of $F\uparrow_{IR}$ are constrained to be greater that $32 wm^{-2}$

Of course, additional observational constraints could be used to constrain f even further, but for the purpose of showing that late spring season surface frost albedos at the north residual polar cap were lower than they were at the south residual cap, the material presented in this appendix and in Chapter 2 should be sufficient. One very important task that will be left to future studies will be to use the 10-layer model to better understand the IRTM spring season polar brightness temperatures. Since the unique geometry of the polar regions makes it possible to calculate thermal equilibrium temperatues and IRTM brightness temperatures at the top of the atmosphere in a self consistent manner, it may turn out that the IRTM data at the poles can be interpreted with greater ease and confidence than has been possible thus far at lower latitudes (Hunt 1979, Kahn 1980, Christensen and Zurek 1984). Possible payoffs of this type of study could include a better understanding of the optical properties of Martian aerosols at infrared wavelengths and a comparison between north and south polar atmospheric conditions during the crucial spring seasons.

References

Christensen, P.R. and R.W. Zurek, (1984) *J. Geophys. Res.* **89**, 4587.

Davies, D.W., (1979) *J. Geophys. Res.* **84**, 8289.

Hunt, G.E. (1979) *J. Geophys. Res.* **84**, 2865.

Kahn, R. (1980) Ph.D. Thesis, Harvard University.